Snow observations from Arctic Ocean Soviet drifting stations: legacy and new directions

Robbie D.C. Mallett

A dissertation submitted in partial fulfillment

of the requirements for the degree of

Doctor of Philosophy

of

University College London.

Department of Earth Sciences

University College London

December 11, 2022

I, Robbie D.C. Mallett, confirm that the work presented in this thesis is my own. Where information has been derived from other sources, I confirm that this has been indicated in the work.

Abstract

The Arctic Ocean is one of the most rapidly changing regions on the planet. Its warming climate has driven reductions in the region's sea ice cover which are likely unprecedented in recent history, with many of the environmental impacts being mediated by the overlying snow cover. As well as impacting energetic and material fluxes, the snow cover also obscures the underlying ice from direct satellite observation. While the radar waves emitted from satellite-mounted altimeters have some ability to penetrate snow cover, an understanding of snow geophysical properties remains critical to remote sensing of sea ice thickness. The paucity of Arctic Ocean snow observations was recently identified as a *key knowledge gap and uncertainty* by the Intergovernmental Panel on Climate Change's Special Report on Oceans and Cryosphere in a Changing Climate. This thesis aims to address that knowledge gap.

Between 1937 and 1991 the Soviet Union operated a series of 31 crewed stations which drifted around the Arctic Ocean. During their operation, scientists took detailed observations of the atmospheric conditions, the physical oceanography, and the snow cover on the sea ice. This thesis contains four projects that feature these observations. The first two consider a well known snow depth and density climatology that was compiled from observations at the stations between 1954 & 1991. Specifically, Chapter two considers the role of seasonally evolving snow density in sea ice thickness retrievals, and Chapter three considers the impact of the climatological treatment itself on satellite estimates of sea ice thickness variability and trends. Chapter four presents a statistical model for the sub-kilometre distribution of snow depth on Arctic sea ice through analysis of snow depth transect data. Chapter five then compares the characteristics of snow melt onset at the stations with satellite observations and results from a recently developed model.

Impact Statement

The Arctic Ocean is warming faster than any other region on earth, at more than three times the global average. Climate changes in the region have driven rapid reductions in the coverage and thickness of the floating sea ice, with knock-on effects for the underlying oceanography, ecology, and the people that live and work in the region. The effects of diminishing sea ice extend outside the region itself as sea ice regulates global temperatures through its high reflectivity, and its loss potentially impacts the Northern Hemisphere jet-stream, midlatitude weather and ocean circulation. As well as an indicator of Arctic change, sea ice is therefore a key mediator of change, with direct impacts on other systems. This means that how sea ice is changing is critical to a full understanding of how the region and the world is changing.

The first two of the four projects in this thesis focus on improving retrievals of sea ice thickness from satellite-mounted radar altimeters. Improved sea ice thickness retrievals will improve the output of climate models which assimilate the retrievals, and will allow more precise evaluation of the models which do not. Chapter three of this thesis focuses specifically on trends and variability in the sea ice thickness of the marginal Arctic seas which contain the North East passage. This essential shipping route is becoming increasingly passable by conventionally-constructed ships in winter due to diminishing sea ice, with profound impacts on flows of trade between Europe and East Asia.

Chapter four of this thesis investigates the sub-kilometre scale distribution of snow on sea ice: this is important to the retrievals of sea ice thickness from satellite-mounted laser altimeters such as IceSat-2, but also allows improved modelling of in- and under-ice light flux. This modelling reflects the changing light availability for in- and under-ice primary producers, which underpin the Arctic food web. A

better understanding of the snow distribution on sea ice may also improve the representation of heat fluxes and resulting thermodynamic ice growth in complex sea ice models. The final chapter of this thesis compares the melt onset timing at NP stations to satellite observations and results from a recently developed model. These comparisons improve our understanding of the different satellite products, and lead to improvements in the model's performance. Output from this model was instrumental in recent work to model the under-ice light field and establish a year-round satellite record of sea ice thickness.

Because this thesis is organised around observations by Soviet *Arctic Ocean* drifting stations, consideration is not given here to Antarctic sea ice. It is also the case that the snow model deployed in Chapter 3 has not yet been run in the Southern Hemisphere because of challenges involving the flooding of sea ice. Snow on Southern Hemisphere sea ice is also different in other ways: for instance it is less prone to forming melt ponds, and typically exists in warmer air temperatures due to generally lower latitudes. Furthermore, fewer in-situ validation campaigns have been performed on Antarctic sea ice. As such, it is not straightforward to port the findings of this thesis to the Southern Hemisphere, although these results may inform future, dedicated studies of Antarctic sea ice.

Acknowledgements

I have been extremely lucky during my academic career. I have generally been surrounded by supportive and expert colleagues, but have also benefited from a series of fortunate encounters and discoveries that have made my PhD worthwhile. I would like to thank not just those people who always believed in me, but also those who took a gamble on me. I will mention just a few of them here, in more-or-less chronological order.

I would first like to express gratitude to my school maths and physics teachers: Phillip Cooper, Emma Coy, Mehdi Behnoudnia and Irwin Deepchand. I'd especially like to thank Dr. Anthony Langdon, without whom I would not have conceived or written Chapter 4 of this thesis. I'm also grateful to Profs. Stephen Tucker and Laure Zanne for their instruction and encouragement while at Oxford. I imagine I was a fairly small feature in their lives, but their patience and belief made a big difference to me at a difficult time. I'd like to acknowledge the impact of Profs. Chris Brierley and David Thornalley, who (perhaps inadvertently) convinced me to continue in science. My experience on their courses showed me that I could do research, and that doing it could be enjoyable. I'm incredibly grateful for that.

Thank you to my supervisors, Prof. Julienne Stroeve and Dr. Michel Tsamados. Their guidance, support and patience during my PhD made a huge difference. They always took my ideas seriously and supported me to explore the research avenues of my interest. In particular, I'd like to thank Julienne for incorporating me into two field campaigns, with another coming up next year. Being able to follow your interests as a PhD student is a massive privilege, and does not just require supportive supervisors but also a permissive funding source. I'd therefore like to acknowledge the impact of the London NERC Doctoral Training Partnership in allowing me to

conduct the research of my choosing. The flexibility afforded by my funding has allowed me to collaborate widely and address research questions as they appeared, rather than focusing on grant deliverables set several years prior. I'd also like to thank the members of the KuKa radar team for fully including me from our very first meetings: to Rosie, Vishnu and Tom, thank you for molding me into a scientist.

I'm grateful to those who have taught and inspired me in the field. In particular I'd like to thank the participants of the MOSAiC School and the PS129 expedition to the Weddell Sea. These campaigns presented huge challenges, both personal and scientific. I'm indebted to Jeremy Wilkinson, Povl Abrahamsen, Mareike Bach, Sam Cornish, Lisa Craw, and Thomas Rackow among others for helping me adapt and rise to the challenges where I could.

As well as professionally, many people have contributed personally to my PhD project's completion. I'd like to thank my friends in cohort five of the NERC DTP. Having a network of sympathetic and supportive friends in academia made a big difference at some important junctures. I'd particularly like to thank those in the Earth Sciences department - Lucia, Bobby and Rachel. Thank you to the CPOM PhD students Diarmid, Tom, Connor, Ali, and most of all Carmen for all your friendship and companionship. I'd also like to thank Lottie Ritchie for her support and encouragement for so many years. To my parents, thank you for all the advising, the driving, the cooking, the packing, the posting, and everything else that you've done to help me get here.

Work not submitted for assessment

During my PhD I contributed to a number of published works which do not appear in this thesis for assessment. They are listed here for completeness:

- Cornish, S.B., Johnson, H., **Mallett, R.D.C.**, Dorr, J., Kostov, Y., Richards, A.E. Rise and fall of ice production in the Arctic Ocean's ice factories. Accepted in Nature Communications.

- Stroeve, J., Nandan, V., Willatt, R., Dadic, R., Rostosky, P., Gallagher, M., **Mallett, R.D.C** ... & Schneebeli, M. (2022). Rain on snow (ROS) understudied in sea ice remote sensing: a multi-sensor analysis of ROS during MOSAiC (Multidisciplinary drifting Observatory for the Study of Arctic Climate). The Cryosphere, 16(10), 4223-4250.

- Rabe, B., Heuzé, C., Regnery, J., ... **Mallett, R.D.C.** ... Zhu, J. (2022). Overview of the MOSAiC expedition: Physical oceanography. Elementa: Science of the Anthropocene, 10(1).

- **Mallett, R.D.C.**, Stroeve, J.C., Cornish, S.B., Crawford, A.D., Lukovich, J. V., Serreze, M.C., Barrett, A.P., Meier, W.N., Heorton, H.D.B.S., & Tsamados, M. (2021). Record winter winds in 2020/21 drove exceptional Arctic sea ice transport. Communications Earth & Environment, 2(1), 1-6.

- **Mallett, R.D.C.** (2021). Snow structure with the snow crystal card. Nature Reviews Earth & Environment, 2(3), 165-165.

- Stroeve, J., Liston, G. E., Buzzard, S., Zhou, L., **Mallett, R.D.C.**, Barrett, A., ... & Stewart, J. S. (2020). A Lagrangian Snow-Evolution System for Sea

Ice Applications (SnowModel-LG): Part II-Analyses. Journal of Geophysical Research: Oceans, e2019JC015900.

- Stroeve, J., Nandan, V., Willatt, R., Tonboe, R., Hendricks, S., Ricker, R., Mead, J., **Mallett, R.D.C.** ... and Tsamados, M. 2020. Surface-Based Ku- and Ka-band Polarimetric Radar for Sea Ice Studies. The Cryosphere, 14(12), 4405-4426

Contents

1 Introduction **15**

1.1 Climate change in the Arctic Ocean 15

1.2 Sea Ice Thickness 23

1.2.1 Importance 23

1.2.2 Satellite Monitoring 24

1.3 Snow on sea ice 25

1.3.1 Snow and estimates of sea ice thickness from satellite-mounted radar-altimeters 26

1.3.2 Snow as a thermal insulator 29

1.3.3 Light attenuation by the snow cover 29

1.4 Observational requirements for snow and sea ice thickness 30

1.5 Soviet North Pole drifting stations 31

1.5.1 Snow depth and other measurements for Chapters 4 & 5 . . 31

1.5.2 The Warren Climatology 32

2 Conventional assumptions involving the speed of radar waves in snow introduce systematic underestimates to sea ice thickness and seasonal growth rate estimates **35**

2.1 Introduction 36

2.2 Different Treatments of the Radar Propagation Correction 37

2.3 Impact of Seasonal Snow Density Evolution on the Radar Wave Propagation Correction 42

2.4 Discussion 46

2.4.1 Different Fixed Densities 46
2.4.2 Comparison to Radar Freeboards 46
2.4.3 Incomplete Radar Wave Penetration of the Snowpack 48
2.4.4 Snow Depth Decline Since W99 Collection 48
2.4.5 Broader Implications 49
2.4.6 Summary 50

3 Faster decline and higher variability in the sea ice thickness of the marginal Arctic seas when accounting for dynamic snow cover 52

3.1 Introduction 52
3.1.1 The Role of Snow in Radar-Altimetry Derived Sea Ice Thickness Retrievals 53
3.2 Data Description 55
3.2.1 Regional Mask 55
3.2.2 Radar Freeboard Data 55
3.2.3 The Warren Climatology (W99) 57
3.2.4 The modified Warren Climatology (mW99) 59
3.2.5 Ice Type Data 59
3.2.6 SnowModel-LG 60
3.2.7 NASA Eulerian Snow on Sea Ice Model (NESOSIM) 61
3.3 Methods 62
3.3.1 Contributions to thickness determination from snow and radar freeboard data 62
3.3.2 Assessing Snow Trends and Variability at a point 63
3.3.3 Assessing Regional Interannual Variability 64
3.3.4 Assessing Regional Temporal Trends 66
3.4 Results 67
3.4.1 Comparison of point-trends and point-variability 67
3.4.2 Realistic SWE Interannual Variability Enhances Regional SIT Interannual Variability 70
3.4.3 New and faster thickness declines in the marginal seas . . . 76

3.4.4 Changes to the sea ice thickness distribution and seasonal growth . . . 80
3.5 Discussion . . . 80
3.5.1 Sensitivity of Findings to Choice of Snow Product . . . 80
3.5.2 Study Limitations . . . 83
3.5.3 Inter-Mission Bias between Envisat and CryoSat-2 . . . 83
3.5.4 The Impact of Enhanced Variability from SnowModel-LG . 85
3.5.5 The Impact of New and Steeper Trends in Mean Sea Ice Thickness . . . 86
3.5.6 The interannual relationship between radar freeboard and snow depth . . . 88
3.6 Summary . . . 89

4 A simple model for the sub-kilometre snow depth distribution derived from transect data 90

4.1 Introduction . . . 90
4.1.1 Snow transects from Soviet drifting stations . . . 92
4.2 Method . . . 95
4.2.1 Choice of Skew Normal Distribution . . . 98
4.3 Results . . . 99
4.3.1 Cross-validation . . . 99
4.3.2 Evaluation against MOSAiC Measurements . . . 101
4.3.3 Evaluation against SHEBA Measurements . . . 105
4.4 Discussion . . . 110
4.4.1 Negative Snow Depths . . . 110
4.4.2 Potential for Application to First Year Ice . . . 110
4.4.3 Application to point-measurements of snow depth . . . 114
4.4.4 Length Scales . . . 115
4.4.5 Relevance in a changing Arctic Ocean and other limitations 118
4.5 Summary . . . 119

5 Comparing the characteristics of NP station snow melt and ablation to satellite radiometry and modelling 120

5.1 Introduction 120

5.1.1 What triggers snow melt onset and subsequent ablation? . . 121

5.1.2 The importance of melt onset and ablation 123

5.1.3 Determining melt onset and ablation timing from space . . . 124

5.1.4 Modelling melt onset and snow ablation 126

5.2 Data 128

5.2.1 NP Data 128

5.2.2 Satellite radiometry derived melt onset products 129

5.2.3 Parcel-wise SnowModel-LG Data 129

5.3 Methods 131

5.3.1 Generating station-wise melt onset timing from satellite products 131

5.3.2 Defining the timing of in-situ snow ablation 132

5.3.3 Comparing timing and speed of in-situ snow ablation at NP stations to SnowModel-LG 134

5.3.4 Comparing satellite melt onset products to SnowModel-LG output 135

5.3.5 Mean meteorological conditions before, during and after snow ablation 137

5.4 Results 138

5.4.1 Comparison with satellite-derived melt onset products . . . 138

5.4.2 Characteristics of snow ablation at NP stations 143

5.4.3 Comparing snow ablation at NP stations with SnowModel-LG 145

5.4.4 Comparing Melt Onset in SnowModel-LG with Satellite Products 148

5.4.5 Mean meteorological conditions in the melt onset period . . 151

5.5 Discussion 155

5.5.1 Satellite melt onset products at NP stations 155

5.5.2 Comparison of Snow Ablation at NP Stations with SnowModel-LG Parcels 157
5.5.3 Representation of snow melt onset timing in SnowModel-LG compared to satellite products 159
5.5.4 Changes in ensemble-average snow and meteorological conditions surrounding snow ablation 161
5.5.5 Future Research Directions 162
5.6 Summary 164

6 Thesis Summary and Future Directions 167
6.1 The ESA Sea Ice Challenge 167
6.2 Satellite Radar Altimetry 168
6.2.1 Radar Penetration of Snow on Sea Ice 169
6.2.2 Increasing Hostility of the Arctic Ocean to Radar Altimetry 169
6.3 The Sub-Kilometre Scale Snow Depth Distribution 170
6.3.1 Satellite Altimetry 171
6.3.2 Snow Distribution Sensitivity to Meteorological Forcing . . 172
6.4 Melt Onset Timing and Altimetry 173
6.5 Future Satellite Altimetry Missions 175
6.6 Future Field Campaigns 177
6.6.1 Antarctica 177
6.6.2 The Arctic 179

Supplementary Material 179
Supplement to Chapter 1 180
Supplement to Chapter 2 183
Supplement to Chapter 3 189
Supplement to Chapter 4 208
Supplement to Chapter 5 216
Supplement to Chapter 6 228
Colophon 229

Chapter 1

Introduction

1.1 Climate change in the Arctic Ocean

The Arctic is currently warming at over three times the global average rate (Rantanen et al., 2022). The rapid heating of the region is related to rapid declines in sea ice areal coverage (Stroeve and Notz, 2018), sea ice age (Tschudi et al., 2020), and sea ice thickness (Kwok, 2018). These changes have local and global impacts on both natural and human systems (e.g. Post et al., 2013; Vihma, 2014; Meier et al., 2014; Steiner et al., 2019). Some of these sea ice changes are shown in Fig. 1.1. Proxy-based reconstructions of Arctic sea ice extent indicate that the present decline is unprecedented in the last 1460 years (Kinnard et al., 2011).

Even with radical global action to reduce the emission of greenhouse gasses, these environmental changes are unlikely to stop within the next quarter-century (IPCC, 2021, Fig. 8). In fact, almost all models indicate the Arctic Ocean will become practically ice free before the year 2050 (Notz and SIMIP Community, 2020; Docquier and Koenigk, 2021). Ongoing sea ice retreat will drive further rapid change in the physical, ecological and human systems of the Arctic and the planet (e.g. Singarayer et al., 2006; Bhatt et al., 2014; Wei et al., 2020; England et al., 2020; Lannuzel et al., 2020). To illustrate the impacts of sea ice retreat, I will now summarise its key role in some key earth and human systems.

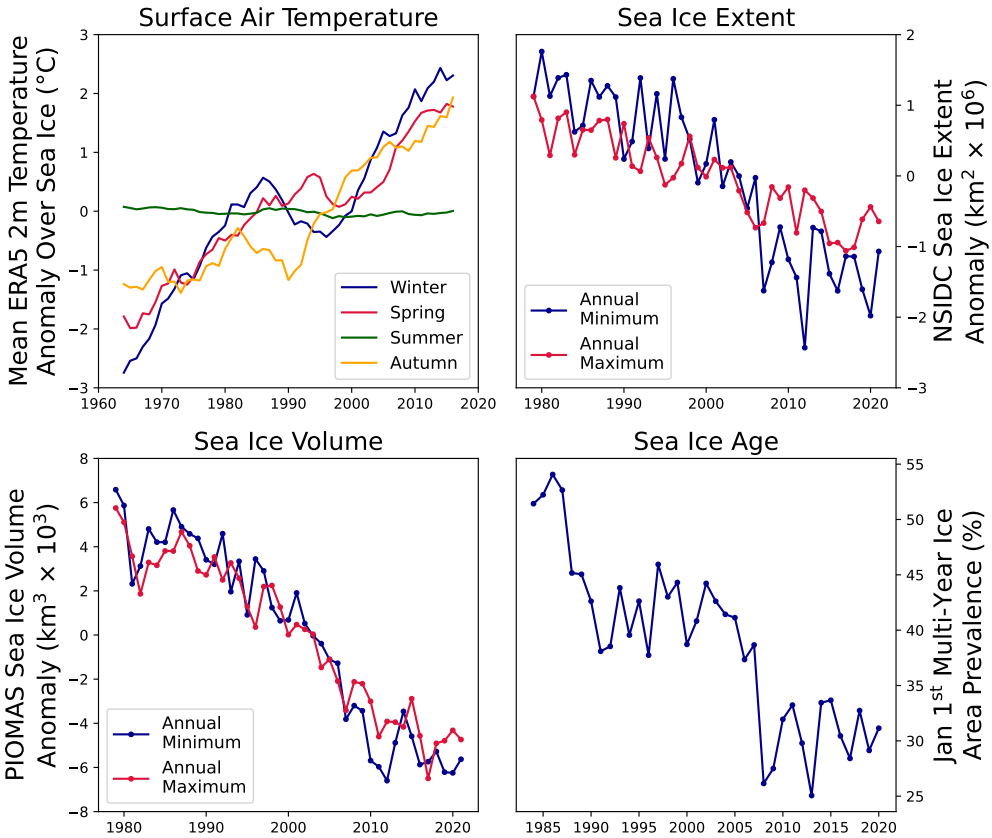

Figure 1.1: The evolution of four sea ice related quantities in the late 20th and early 21st century. Sea ice extent, volume and age have decreased, while surface air temperatures have increased in winter, spring and autumn. Air temperature data were downloaded from the ERA5 atmospheric reanalysis (Hersbach et al., 2020), sea ice extent data were downloaded from the National Snow and Ice Data Center Sea Ice Index (Fetterer et al., 2010), sea ice volume data are taken from the PIOMAS sea ice reanalysis product (Zhang and Rothrock, 2003), and sea ice age data are taken from the National Snow and Ice Data Center age product (Tschudi et al., 2020). Technical details on the construction of this plot (e.g. regridding and averaging procedures) is given in the supplement (Sect. S1)

Sea Ice Loss and Arctic Amplification

Sea ice loss contributes to, and is forced by, recent observed rises in the Arctic's surface air temperature. This entanglement leads to outsized warming relative to the global average, known as *Arctic Amplification*. One way that sea ice amplifies increases in surface air temperatures is through the *ice-albedo feedback*. Sea ice and its overlying snow are highly optically reflective (Perovich et al., 2002; Perovich and Polashenski, 2012), such that the majority of incident sunlight is reflected rather than absorbed. As sea ice retreats and open water is exposed, incident sunlight at the surface is less reflected and more absorbed (Pistone et al., 2014), heating the surface layer of the ocean. The additional heat stored in this layer acts to melt nearby ice (Kashiwase et al., 2017), and delay freeze-up in the following Autumn (Stroeve et al., 2014).

While a reduction in the surface albedo from sea ice retreat is often the focus of discussions around Arctic amplification, several other key mechanisms exist, some of which may potentially be more consequential than the albedo effect (Previdi et al., 2021). This is clear from the fact that the ice-albedo feedback is most active in summer (when insolation is largest), whereas Arctic amplification is largest in winter and smallest in summer (Chung et al., 2021). For example, changes in the vertical temperature profile of the lower atmosphere, and a relatively lower Planck feedback[1] in polar regions drive amplification of comparable magnitudes to the ice-albedo feedback (Goosse et al., 2018). The combined result of these feedbacks is that areas that have experienced consistent sea ice retreat see particularly high amplification. For example, surface temperatures around Svalbard and Novaya Zemlya have experienced trends (1979 - 2021) of 0.125°C per year (Rantanen et al., 2022), warming more in a decade than the Earth has warmed on average since the pre-industrial era.

[1]The *Planck Feedback* emerges from the more powerful thermal radiation of a warmer body. As the Earth's surface warms, its outgoing thermal radiation to space increases non-linearly relative to the warming. Globally this results in a negative feedback on surface warming, however this feedback is weaker at the poles because absolute temperatures are lower. A weaker negative Planck feedback in the Arctic results in Arctic amplification.

Other Physical Changes Resulting from Sea Ice Loss

As sea ice has thinned (Kwok, 2018), it has become more dynamic (Rampal et al., 2009; Kwok et al., 2013), with impacts on ocean gyre circulation (Petty et al., 2016; Armitage et al., 2020). These impacts on Beaufort Gyre circulation are particularly important, as they affect the freshwater balance and ocean heat partitioning of the Arctic Ocean (Timmermans and Toole, 2022).

Sea ice decline is also driving changes in the cloud cover of the Arctic Ocean. While the role of increasing cloud cover in Arctic amplification remains unclear (He et al., 2019; Sledd and L'Ecuyer, 2021), it is clear that areas that have experienced sea ice retreat become increasingly cloudy. Liu et al. (2012) found that a 1% decrease in sea ice concentration leads to a 0.36% - 0.47% increase in cloud cover. This is mostly driven by increases in moisture availability (Abe et al., 2016); the role of sea ice retreat on the availability of cloud condensation nuclei is complex and relatively unconstrained (Browse et al., 2014).

In the Eastern/European Arctic, sea ice retreat has been linked to the process of Atlantification (Barton et al., 2018). This process involves warmer "Atlantic" water penetrating into the surface layer of the Arctic Ocean, which inhibits sea ice growth (Asbjornsen et al., 2020). Reductions in sea ice export through the Fram Strait have potentially altered the surface oceanography of the Greenland Sea, which in turn intensifies Atlantification of the Fram Strait region (Wang et al., 2020).

The increasing ocean-atmosphere moisture flux resulting from sea ice decline has also been linked to more frequent and more extreme precipitation over nearby land. For example, retreat of sea ice from the Barents sea contributed to extreme snowfall in Northern Europe in 2021 (Bailey et al., 2021), and sea ice extent east of Greenland has been shown to control extreme precipitation in Svalbard (Müller et al., 2022). Kopec et al. (2016) investigated the fraction of total Arctic precipitation that originated as Arctic evaporation ('Arctic Sourced Moisture'; ASM). The authors found that the ASM fraction increased by around 15% per 100,000 square kilometers of ice lost. These changing precipitation patterns have biological and human impacts (e.g Forbes et al., 2016) that will be discussed in the next section.

Sea ice acts as a semi-permeable cap on gas transport (Parmentier et al., 2013; Vancoppenolle et al., 2013). Its retreat therefore affects the underlying ocean's role as a potential net sink of atmospheric carbon (MacGilchrist et al., 2014) and the ocean acidificiation that results. Increasing exposure of the ocean surface to the atmosphere has combined with meltwater-driven changes in the seawater chemistry to position the Arctic Ocean as the most rapidly acidifying ocean basin on Earth (Qi et al., 2022).

Finally, sea ice retreat is changing the momentum flux from the atmosphere to the ocean. For example, longer open water seasons have made large waves in the Beaufort and Chukchi seas more common, with the potential to impact the remaining ice pack at its edge (Thomson et al., 2016). Sea ice retreat also drives increased wind energy input to the surface ocean (Rainville et al., 2011). The vertical mixing that results may weaken upper-ocean stratification, increasing the heat flux to the ice when and where it is present (Ivanov et al., 2016).

Sea Ice Loss and Arctic Ecology

The Arctic Ocean is partially shaded by its sea ice cover in summer, with profound effects on the spatial distribution of photosynthesising primary producers and the ecological webs that they support (Andersen, 1989; Nicolaus et al., 2012a; Ji et al., 2013; Ardyna et al., 2020). Declining sea ice may increase the primary productivity of the Arctic ocean through increased light availability, making *pelagic* (floating) primary producers beneficiaries of the transition (Arrigo and van Dijken, 2015). However, a number of *sympagic* species are endemic to sea ice itself (Hop et al., 2000), and may not be able to adapt to a diminishing and potentially disappearing ice habitat in summer (Mundy and Meiners, 2021).

Sea ice also provides a critical ecosystem service in sustaining polar cod, *Boreogadus saida*. This is a *keystone species* which links the primary production above to higher-level consumers such as birds and seals (Bradstreet et al., 1986). Polar cod depend on sea ice to rest and avoid predators (Gradinger and Bluhm, 2004), and use it to feed while in their larval and juvenile stages (Craig et al., 1982). Sea ice decline may therefore stress this key link in the Arctic Ocean food chain.

Sea ice also directly provides ecosystem services for larger animals such as marine mammals (Kovacs et al., 2011) and birds (Karnovsky and Gavrilo, 2016). For instance, it moderates the hunting behaviours of narwhals and polar bears (Pagano and Williams, 2021) and provides a denning venue for ringed seals (Hamilton et al., 2017). As for birds, the timing of sea ice break up is becoming asynchronous with the development and migratory cycles of birds. Gaston et al. (2009) documented poorer growth rates in thick-billed murres in response to earlier ice breakup, as they hatch after the peak in prey has passed. Fort et al. (2013) documented the importance of the sea ice edge position for the migration of little auks, and indicated the resulting threat to the species from sea ice decline.

Biological impacts are not just limited to the ocean environment: sea ice loss can have indirect impacts on terrestrial ecosystems through atmospheric pathways. For example, unusually low winter sea ice conditions in the Barents and Kara seas during 2006 and 2013 caused rain on snow events which led to mass mortality of reindeer on the Yamal Peninsula (Forbes et al., 2016). Sea ice loss was also implicated by Statham et al. (2015) in the redistribution of terrestrial caribou herds, which in turn stressed the local, hunting-orientated Inuit food system.

Regional, Human Systems

As alluded to above, sea ice decline directly impacts those who live in the Arctic, and particularly those who use it. It is used by Arctic residents as a platform for transport (Kapsch et al., 2010; Aporta, 2009), fishing (Steiner et al., 2019) and hunting (Huntington et al., 2016), and is part of the region's cultural heritage (Aporta, 2010).

Taverniers (2010) documented changes in a small West-Greenland community after a period of retreating sea ice; changes included substituting on-ice dog-sled travel with motorboat travel, a pivot to fishing as opposed to hunting, increasing dependence on imported food (due to reduced seal catches), and reduced making of seal-skin clothes. Hunters caught fewer migratory birds due to the absence of a previously persistent polynya, and the local schoolteacher observed that traditional skills such as hunting, fishing and travelling were no longer being passed on due to

lack of access to the sea ice.

Sea ice decline is also impacting Arctic communities that are vulnerable to waves from storms and coastal erosion (Overeem et al., 2011; Barnhart et al., 2014). This is because sea ice loss expands both the fetch over which waves build, and the length of the open water season for which waves can act on a coastline (Barnhart et al., 2015; Casas-Prat and Wang, 2020). One striking case study of this is the town of Shishmaref (Alaska, USA), which is in the process of being relocated due to rapid coastal erosion linked to sea ice decline (Major et al., 2021). Coastal permafrost change has also influenced investment and decision making in the coastal town of Nome (Alaska, USA). Residents have observed degradation of key infrastructure: roads have become undulating, utilities have failed, and buildings have subsided (Birchall and Bonnett, 2020).

Global, Natural Systems

The Arctic sea ice also influences hemispheric and global environmental systems. As well as cooling the planet via its high albedo as described above, the sea ice also affects midlatitude weather. While its role in the variability of the jet stream remains contested (Cohen et al., 2020; Overland et al., 2021), studies have shown that sea ice behaviour drives weather phenomena at low latitudes by several other means (England et al., 2020, and references therein). For instance, sea ice loss has been associated with a weakening of the Atlantic Meridional Overturning Circulation (Sévellec et al., 2017; Liu et al., 2019). Ocean dynamics drive several tropical responses to sea ice loss including intensification of the intertropical convergence zone and the Hadley circulation (Wang et al., 2018; Chemke et al., 2019).

It is also the case that sea-ice loss drives Arctic amplification (Sect. 1.1), which in turn drives local changes in the Arctic which can individually have a global reach. For instance, Arctic amplification is increasing (and will continue to increase) the contribution of Greenlandic ice-sheet melting to global sea level rise (Fyke et al., 2014). Permafrost decay due to amplified temperatures and sea ice loss is also a source of methane (Shakhova et al., 2015), thus increasing global greenhouse gas concentrations.

Global, Human Systems

The Arctic sea ice forms a physical barrier to conventional shipping, and blocks attractive routes for international trade (Cressey, 2007; Zhang et al., 2019; Tseng et al., 2020). This necessitates the use of ice-strengthened vessels in winter if goods are to be shipped via either the North-East or North-West passages, which allow direct travel between the North Atlantic and the North Pacific. However, the rapid thinning of sea ice in the North-East passage in recent years has allowed for a string of 'break-through' winter transits by conventional vessels (Kubny, 2021). Research in this thesis (Chapter 3) sheds light on the rate at which sea ice in this key passage is thinning. Delayed freeze-up and earlier ice-retreat, combined with the general retreat of the September ice edge from the Siberian coast over the last few decades has also facilitated more conventional, open-water shipping voyages in summer. Sea ice conditions in the Northern Sea Route (part of the North-East passage) have taken on new importance in 2022 due to the Russia-Ukraine conflict. Increasing dependence of Russian gas exports on Chinese demand (in light of Western sanctions) has enhanced Russian reliance of the Northern Sea Route, which houses several liquid petrolium gas (LPG) terminals (Odgaard, 2022).

While changes in the conventional routes (North-East and North-West passages) are underway (Stewart et al., 2013), the prospect also looms of more direct journeys directly across the pole in the second half of the 21st Century (Melia et al., 2016; Cariou et al., 2019). As well as being a potential highway for international trade, the Arctic Ocean is also a venue in itself for the extraction of natural resources (Kontorovich et al., 2017). As the sea ice retreats, the potential for extraction of fish and precious metals is being assessed (Lasserre and Têtu, 2017; Petrick et al., 2017).

As the Arctic increases in its economic and geopolitical value with ice retreat, a growing body of literature now addresses resurgent political conflict and militarisation in the Arctic after three decades of post-cold-war de-escalation (e.g. Oxford Analytica, 2015; Wilson, 2015; Gricius, 2021). As a barrier between Russia and NATO countries during the conflict in Ukraine, the Arctic has become a venue for increasing military tensions in 2022 (Odgaard, 2022). De-escalating these tensions

is particularly difficult at present, given Russia's chairmanship of the Arctic Council in the 2021-2023 period (Sergunin, 2022).

1.2 Sea Ice Thickness

Having just emphasised the important role of sea ice across scales in both human and earth systems, I will now introduce discuss the nature and importance of *sea ice thickness* (SIT) in particular.

During autumn, open water areas freeze, forming new ice that can then grow thermodynamically by 1.5 to 2.5 m over a winter season. Further deformation and thermodynamic ice growth can lead to thicknesses in excess of 5 m. The rate of seasonal ice growth is discussed in Chapter 2. Today, the Arctic is undergoing a period of profound transformation, with the thickness of the floating sea ice cover in decline (e.g. Kwok, 2018). The rate and nature of this decline in the marginal Arctic seas is discussed in Chapter 3. Reductions in sea ice thickness are driven by a variety of factors including later freeze-ups, earlier melt onsets and increased winter air temperatures (Graham et al., 2017; Stroeve et al., 2018).

1.2.1 Importance

As well as being a sensitive indicator of climate change, winter SIT also functions as a prognostic variable in the polar climate system, affecting the amount and distribution of sea ice that will survive the summer melt season. Accurate knowledge of SIT is particularly important where data are assimilated into forecasting systems and other complex models, which often exhibit sensitive dependence on initial conditions (Chevallier and Salas-Mélia, 2012; Day et al., 2014; Blockley et al., 2018; Schröder et al., 2019).

The importance of SIT in forecasting and modelling stems from its key role in partially decoupling the ocean and atmosphere systems. Thicker sea ice is more thermally insulating and limits heat transfer from the ocean to the atmosphere in winter and consequent thermodynamic growth (Petty et al., 2018a). As mentioned previously, SIT also exerts control on sea ice dynamics and rheology (Vella and Wettlaufer, 2008; Rampal et al., 2009; Kwok et al., 2013). The thickness of sea ice

during snow accumulation also dictates whether the sea ice surface drops below the waterline, potentially increasing sea ice growth through the formation of snow-ice (Rösel et al., 2018).

The impact of the end-of-winter SIT distribution persists into the melt season, with thick sea ice decreasing the transmission of solar radiation to the surface ocean and reducing the potential for in- and under-ice primary productivity (Mundy et al., 2005; Katlein et al., 2015; Stroeve et al., 2021).

As well as being a key parameter for the processes described above, the value of sea ice thickness can be multiplied by the sea ice area to produce the sea ice volume, one of the most sensitive indicators of Arctic climate change (Schweiger et al., 2019).

1.2.2 Satellite Monitoring

While continuous and consistent monitoring of Pan-Arctic SIT has not been achieved on a multi-decadal timescale, the long-term decline in sea ice thickness mentioned above has been suggested using a combination of different techniques (Kwok, 2018; Stroeve and Notz, 2018). Satellite altimeters using both radar and lidar have provided a valuable record of changing sea ice thickness, but have often been limited for various reasons. Some have been limited spatially by their orbital inclination (e.g. the European Remote Sensing (ERS) satellites, Envisat, AltiKa and Sentinel radar altimeters have operated up to only 81.5°N), and others in temporal coverage (e.g. ICESat was operated in 'campaign mode' rather than providing continuous coverage). Two satellite altimeters currently offer continuous and meaningful Pan-Arctic monitoring of the Arctic sea ice: the ICESat-2 and CryoSat-2 altimeters. ICESat-2 has been in operation since September 2018 and so far has documented four winters of sea ice thickness (Kwok et al., 2020b). While products from CryoSat-2 have traditionally only been available for the cold season (October - April), a year-round sea ice thickness product has recently been developed (Landy et al., 2022).

Although the launch of the CryoSat-2 radar altimeter (henceforth CS2) in 2010 allowed significant advances in understanding the spatial distribution and interannual variability of Pan-Arctic SIT (Laxon et al., 2013), a statistically significant decreasing

trend within the CS2 observational period has not been detected for the Arctic as a whole. The lack of certainty regarding any trend in SIT is in part due to the various uncertainties associated with SIT retrieval from radar altimetry (Ricker et al., 2014; Zygmuntowska et al., 2014). Major contributors to these uncertainties are the relatively large footprint of a radar pulse when compared to laser altimetry, the variable density of sea ice (Jutila et al., 2022), retracking of radar returns from rough sea ice (Landy et al., 2020), and the need for an *a priori* snow depth and density distribution (Kern et al., 2015). This poses a challenge to the identification of statistically significant trends among uncertainty-induced noise; this challenge was highlighted by the IPCC's most recent assessment report (Fox-Kemper et al., 2021, see quote below).

1.3 Snow on sea ice

The role of sea ice as a moderator of ocean-atmosphere interaction is itself often influenced by its snow cover (e.g. Sturm and Massom, 2016). In fact, many of the key properties often ascribed to the sea ice cover (high albedo, thermal insulation) are in fact more intrinsic to its snowpack than the underlying ice.

Furthermore, snow blocks direct satellite observation of the ice cover. The sea ice itself must generally either be studied with snow-penetrating electromagnetic frequencies from the microwave spectrum, or by inferring ice properties from the properties of the overlying snow. Given snow's key role in Arctic Ocean climate and in remote sensing of the underlying ice, it is therefore unfortunate that the snow cover itself is poorly monitored. The 2019 IPCC Special Report on the Ocean and Cryosphere in a Changing Climate identified snow on sea ice as a *key knowledge gap and uncertainty* (Meredith et al., 2019), stating:

> "Snow depth on sea ice is essentially unmeasured"

Furthermore, Working Group 1's contribution to the IPCC's sixth assessment report (Fox-Kemper et al., 2021) attributed the *low confidence* in sea ice thickness change since 2011 to:

"snow-induced uncertainties in the retrieval algorithms, the shortness of the record, and the small identified trend"

I will now introduce some key aspects of the Arctic Ocean snow cover which are most relevant to this thesis:

- Snow and radar estimates of sea ice thickness
- Snow as a thermal insulator
- Snow reflection and attenuation of light

The above list underplays the diversity of areas in which snow properties are important. For instance, this thesis will not discuss the role of the Arctic Ocean snow cover in:

- providing a habitat for mammals (e.g. seals, polar bears) and micro-organisms (e.g. Kovacs et al., 2011; Maccario et al., 2019)
- pressing the underlying ice below the waterline, generating *negative freeboards* and snow-ice (e.g. Rösel et al., 2018)
- moderating the transport of gasses into and out of the ice (e.g. Nomura et al., 2010)
- preconditioning for the formation melt-ponds (e.g. Petrich et al., 2012)
- reducing the ability of icebreaking ships to mount and fracture floes (e.g. Huang et al., 2019)

1.3.1 Snow and estimates of sea ice thickness from satellite-mounted radar-altimeters

The full impact of snow on radar-altimetry-derived estimates of sea ice thickness is worthy of its own lengthy and detailed review paper. A summary is given here, with a more detailed and quantitative treatment developed through Chapters 2 & 3. However this treatment is confined to the conventional paradigm of total radar-wave penetration of overlying snow.

Satellite altimeters release short pulses of coherent electromagnetic radiation and measure the timing of their return. The round-trip return time of the pulse is a measure of the range of the target. At wavelengths in the *Ku-band* (around 13 GHz), detected backscatter is conventionally assumed to have scattered from the snow-ice interface, having penetrated the snowpack.

However, snow properties are also known to impact the penetration characteristics of radar waves. That is to say, different snowpacks can diferentially admit radar waves of the same frequency. The penetration assumptions described in the previous paragraph are therefore not universally true. For Ku-band waves (the topic of Chapters 2 & 3), in-situ, airborne and satellite-based evidence indicates that snow-stratigraphy, snow-temperature, and the presence of saline snow all affect the depth distribution over which which backscattered radar waves return (Willatt et al., 2010, 2011; Ricker et al., 2015; Armitage and Ridout, 2015; Nandan et al., 2017; King et al., 2018). Limited penetration is a key obstacle to successful retrieval of sea ice thickness from Ku-band radar-altimeters such as that mounted on the CryoSat-2 satellite.

The presence of snow also weighs down the ice cover when it is floating in hydrostatic equilibrium. A heavier overlying snow cover will press the ice downwards, affecting the *ice freeboard*. This is relevant to sea ice thickness retrievals, as the conventional approach relies on the conversion of an ice-freeboard observation to an ice-thickness estimate through invoking Archimedes' principle. A full description of this process is given in Chapter 3. Here I summarise the general situation in the Arctic: snow generally has a density of between 100 to 500 kg/m^3. At these densities, it depresses the ice surface by between 0.1 and 0.5 cm per cm of accumulated snow. Because of this effect, the weight of overlying snow must be accounted for when inferring sea ice thickness from an ice-freeboard measurement.

Finally, snow slows the propagation of electromagnetic waves such as those emitted and detected by Ku-band altimeters. This increases the round-trip time for radar-pulses, even if the distance travelled in real space remains the same. Without correcting for this effect, waves backscattered from the snow-ice interface would be

interpreted as being scattered from too far away. This slowing down gives rise to the difference between the *radar range* and the *true range* of a satellite radar altimeter. This effect is the subject of Chapter 2, which explores the delay-time based on snow density and depth data derived from observations at Soviet drifting stations (Warren et al., 1999). Chapter 3 of this thesis explores the climatological nature of the data set derived from the stations, and the impact of the data on sea ice thickness retrievals by comparison to the output from a recently developed model.

The effects of snow loading described above (freeboard depression and propagation delay) mean that underestimation of the snow loading results introduces an overestimating bias on the derived sea ice thickness. In Chapter 3 (Eq. 3.3) I will show that for a given radar retrieval:

$$\frac{\partial(SIT)}{\partial m_s} = \frac{\rho_w}{\rho_w - \rho_i} \times 1.81 \times 10^{-3} \tag{1.1}$$

Where SIT represents sea ice thickness (in metres), m_s the snow loading in millimetres of snow water equivalent, ρ_w the density of seawater, and ρ_i the density of seawater. The above equation implies that for every centimetre of snow (at a typical density of 300 kgm^{-3}), an extra 4.5 centimetres of sea ice thickness is inferred (at a typical sea ice density of 900 kgm^{-3}).

It is important to note that several other large uncertainties exist when estimating sea ice thickness; for instance, sea ice density remains poorly constrained (e.g. Jutila et al., 2022) and the interpretation of radar waveforms remains highly uncertain (e.g. Landy et al., 2020). As such, it is not possible to categorically state that when snow loading is underestimated then the resulting sea ice is underestimated. Because other biases may be compensating, improved representation of snow in some cases may lead to less accurate sea ice thickness retrievals. As such, I opt to phrase snow loading uncertainty in the language of ‘introducing’ an over/underestimating bias in resulting estimates, rather than as ‘leading to’, ‘producing’ or ‘generating’ some bias.

1.3.2 Snow as a thermal insulator

Snow is a mixture of ice and air, and therefore acts like a thermally insulating blanket on the sea ice. The difference between snow and ice in this regard is significant: the thermal conductivity of snow is generally between 0.1 and 0.4 $Wm^{-1}K^{-1}$ (Calonne et al., 2011). This is an order of magnitude below sea ice, which generally has a thermal conductivity between 2 and 2.3 $Wm^{-1}K^{-1}$ (Pringle et al., 2007). This disparity allows the deposition and ablation of snow to control the thickness of ice underneath where that ice is thin enough to be sensitive (Maykut et al., 1971; Ledley, 1991; Lecomte et al., 2013; Holland et al., 2021). Thinner snow produces greater thermodynamic sea ice growth in winter, as it allows more latent heat form freezing to be transported away from the base of the sea ice to the atmosphere. However, the power of this control is significantly diminished when sea ice becomes thick: 3 metre ice has approximately the same total (not specific) conductivity as a 30 centimetre snow cover, and would therefore be considerably less sensitive to the snow's insulating effect.

The moderating power of snow on sea ice growth is true at both the large scale, but also the local scale. Snow is redistributed by wind into dunes and bedforms (e.g. Moon et al., 2019), and can accumulate in drifts near ice topography such as ridges (Liston et al., 2018). Heat is able to flow more easily through thin patches in the snow, making the sub-kilometre scale distribution of snow depth relevant to calculations of heat flux and ice growth (Sturm et al., 2002b). This distribution is the topic of Chapter 4 of this thesis.

1.3.3 Light attenuation by the snow cover

Fresh snow is often described as the most optically reflective natural material on earth (e.g. Webster et al., 2018). With an albedo of $\sim$0.85, dry snow also has a high albedo relative to the bare ice surface ($\sim$ 0.55 - 0.65 Perovich and Polashenski, 2012). Despite the above, light can penetrate snow to a depth of several tens centimetres (Dumont and Gascoin, 2016), although the exact functional form of the attenuation remains challenging to model from first principles (Libois et al., 2013). This is because in the optical portion of the electromagnetic spectrum, snow has an

extremely high scattering power relative to its ability to absorb (Kokhanovsky, 2022). As such, a small fraction of incident photons in the visible portion of the spectrum can penetrate deep into snow through multiple scattering events.

It is therefore the case that when light is incident on a snow cover with a depth distribution, it is not the *mean depth* of the snow, but instead the areal prevalence of *optically thin* snow that determines light transmission to the ice surface. As such, the distribution of snow depth is a critical determinant of in-ice light availability (Abraham et al., 2015). As above, this distribution of snow depths is the topic of Chapter 4 of this thesis.

Furthermore, the timing with which the snow melts affects the timing with which in- and under-ice primary producers are supplied with light. This timing is spatially variable in a given year, and interannually-variable at a given point (e.g. Markus et al., 2009; Bliss and Anderson, 2018). For instance, Galindo et al. (2014) documented how earlier snow melt in 2011 (relative to 2010) in the Canadian Archipelago drove more light penetration of the ice surface. This precipitated an earlier algal bloom, but also accelerated the subsequent detachment of the algal mat at the ice base. The timing and nature of snow melt onset is the topic of Chapter 5 of this thesis.

1.4 Observational requirements for snow and sea ice thickness

Having stressed the importance of snow and sea ice thickness, I will now introduce the observational requirements for these variables specified by the Global Climate Observing System (WMO, 2022a), a body of the World Meteorological Organisation. The situation has recently changed, with the addition in 2022 of three new variables under the singular 'Essential Climate Variable' category of sea ice:

- concentration
- extent
- thickness

- drift
- surface temperature*
- surface albedo*
- overlying snow depth*

Where asterisks (*) indicate variables new in 2022, in addition to the variables defined in 2018. The relationship between the sea ice ECV, and its constituent variables (listed above) is discussed by Lavergne et al. (2022).

The sea ice thickness constituent variable has the following observational requirements as a minimum threshold: 50 km horizontal resolution, on a monthly basis in wintertime, to a two-sigma measurement uncertainty of 0.25 m.

For overlying snow depth, the threshold observational requirements are: a 50 km horizontal resolution, on a monthly basis in wintertime, with a two-sigma measurement uncertainty of 0.1 m (WMO, 2022b).

1.5 Soviet North Pole drifting stations

Between 1937 and 1991 the Soviet Union operated a series of research installations on drifting Arctic sea ice; these were termed *North Pole* or *NP* stations. The program was restarted by the Russian Federation in 2003, although data from this era are not publicly available. During their operational periods, the crews collected a wide range of meteorological observations, alongside snow depth and density measurements.

1.5.1 Snow depth and other measurements for Chapters 4 & 5

The relevant measurements analysed in Chapters 4 & 5 are described in the chapters themselves (Sects 4.1.1 & 5.2), and as such are only summarised here:

- Daily measurements of the mean snow depth a three stakes demarking the corners of a 25 m square, recorded to the nearest cm.
- Snow depths were also measured every 10 or 20 days at 10 m intervals along transects of either 500 or 1000 m in length.

- Incident and reflected shortwave radiation was measured by in-situ broadband radiometers.
- 3- or 6-hourly observations of 2-metre air temperature, relative humidity, low-cloud coverage and total-cloud coverage.

1.5.2 The Warren Climatology

The snow depth measurements itemized above were combined into monthly climatological distributions by Warren et al. (1999, henceforth 'W99'). Transect-based measurements were used in preference to stake-based measurements for two reasons: one is that the spatial sampling statistics are improved; the second is that the transects were less influenced by the nearby station in terms of albedo reductions from combustion and wind-drifting of snow. The locations at which the constituent snow depth transects were made are displayed in Fig. 1.2a. The performance of these fits in representing the input data are shown in Fig. 1.2b. The distributions themselves feature prominently in Chapters 2 & 3, and are displayed here in Fig. 1.3.

Examination of these distributions indicates that there is an element of *overfitting* present: while the transect data that produce the fits match well (Fig. 1.2b), there are large areas of negative snow depths in some winter months in the Barents Sea. The values are also too high in some areas of sea ice coverage (such as Baffin and Hudson Bays), precluding the climatology's realistic use in those areas. For completeness I reproduce the W99 fits for snow water equivalent in Supplementary Fig. S1, and the fits for snow density produced by dividing the SWE by the depth in Supplementary Fig. S2.

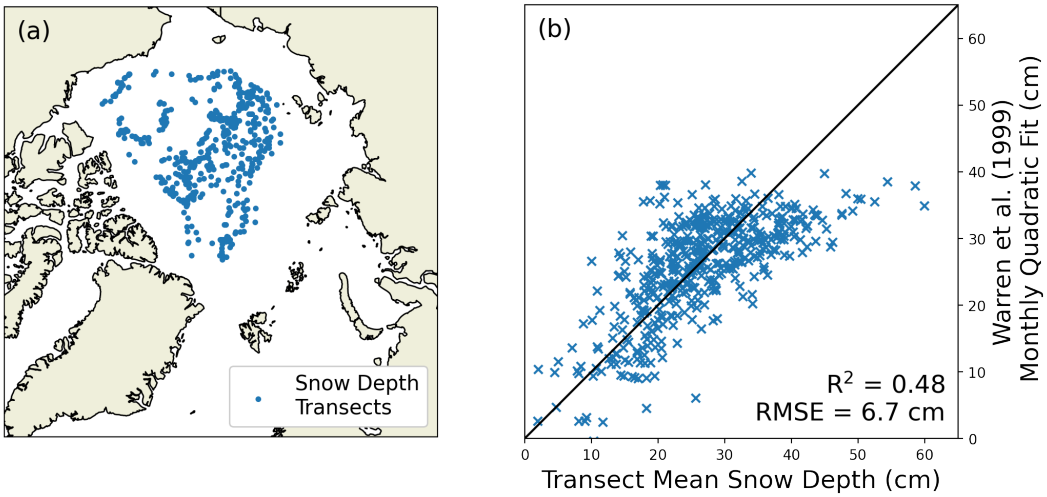

Figure 1.2: (a) the positions of the snow depth transects contributing to the W99 snow depth climatology. (b) The W99 monthly quadratic fits evaluated against the in-situ measurements from which the fits were generated.

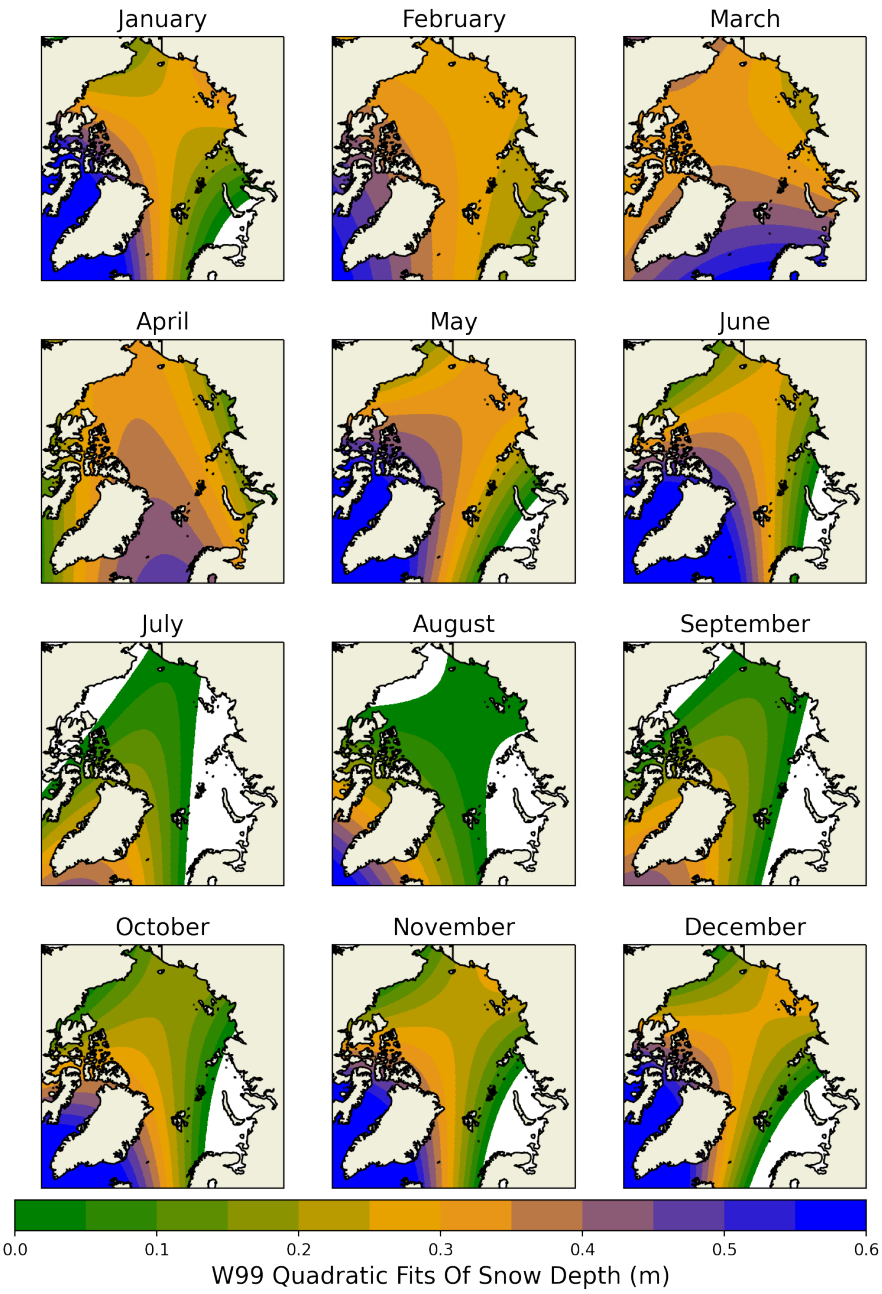

Figure 1.3: Monthly evolution of the quadratic fits of snow depth given by the Warren Climatology (W99). White colored areas indicate regions where the quadratic fits generate negative values for snow depth.

Chapter 2

Conventional assumptions involving the speed of radar waves in snow introduce systematic underestimates to sea ice thickness and seasonal growth rate estimates

The contents of this chapter are drawn from the following publication:

Mallett, R.D.C., Lawrence, I.R., Stroeve, J.C., Landy, J.C., & Tsamados, M. (2020). Brief communication: Conventional assumptions involving the speed of radar waves in snow introduce systematic underestimates to sea ice thickness and seasonal growth rate estimates. The Cryosphere, 14(1), 251-260.

However the original publication only assessed data up to summer 2018. The figures and statistics in this chapter have been updated to include data up to summer 2021.

.

2.1 Introduction

As described in Chapter 1, sea ice thickness is a key control on the strength of the decoupling between the Arctic Ocean and the Arctic atmosphere. It has been observed through various methods including upward-looking sonar from submarines, ice mass-balance buoys, electromagnetic induction sounding and satellite laser and radar altimetry (e.g. Schweiger, 2017; Kwok, 2018). The CryoSat-2 mission has played a leading role over the last decade, providing radar ranging observations from which the sea ice thickness may be derived (Wingham et al., 2006; Laxon et al., 2013; Tilling et al., 2018; Landy et al., 2022).

Ku-band radar altimeters such as CryoSat-2 and Sentinel-3 do not directly measure sea ice freeboard, but instead measure 'radar freeboard' through a time-of-flight calculation. The radar freeboard is the difference in radar ranging between the snow-ice interface and the local, instantaneous sea level (assuming perfect radar wave penetration through the snowpack). Since the radar wave speed is reduced in snow, a priori knowledge of the snow depth and density is required to convert the radar freeboard to the true ice freeboard. Following the freeboard calculation, sea ice thickness can then be estimated through the assumption of hydrostatic equilibrium (e.g. Laxon et al., 2003). This again requires a priori knowledge of snow depth and density to account for freeboard reduction due to the weight of overlying snow. The impact of correcting for the weight of overlying snow on sea ice thickness is of comparable magnitude to the correction for slower wave propagation in snow (Supplementary Material Sect. S2).

An important consideration in the conversion of radar freeboard (F_r) to ice freeboard (F_i) and in turn ice thickness is therefore the time delay due to slower radar pulse propagation in snow (Kwok, 2014). In this study we highlight two different approaches to the calculation of this time delay used in published literature. Correct handling of this time delay has a significant impact on the retrieval of sea ice thickness and volume from radar altimetry, as we show here. This is particularly the case as snow settles and densifies over the winter season.

We further investigate the impact of assuming a fixed snow density throughout

winter when calculating this time delay. At present, three groups operationally produce publicly available sea ice thickness products from CryoSat-2. Only one of these (the Alfred Wegener Institute; AWI) factors monthly evolution of snow density into their correction for slower radar wave propagation in snow, despite often including an evolving density in their calculation of the floe's hydrostatic equilibrium. AWI did not do this until 2020, at which point it was incorporated in response to the paper associated with this chapter (Hendricks and Ricker, 2020). The impact of this assumption is assessed and found to introduce underestimates of the rate of winter thermodynamic sea ice growth, with October-April growth currently being underestimated by over 10 cm over multiyear ice.

2.2 Different Treatments of the Radar Propagation Correction

The correction to the radar range to account for slower radar wave propagation in snow, $\delta h = F_i - F_r$, is often expressed as the product of snow depth, Z, and some function of wave velocity in snow, $f(c_s)$ (e.g. Tilling et al., 2018; Kwok, 2014) such that:

$$\delta h = Z \times f(c_s) \tag{2.1}$$

We now present a short derivation of $f(c_s)$ and thus δh through consideration of the extra time taken, δt, for a radar wave to travel a distance Z through a specified snow depth rather than through free space. The time delay induced by the snow layer is expressed:

$$\delta t = t_{snow} - t_{vacuum} \tag{2.2}$$

$$\delta t = Z/c_s - Z/c \tag{2.3}$$

$$\delta t = Z(1/c_s - 1/c) \tag{2.4}$$

Where c_s the wave speed in snow, and c is the radar wave speed in free space

(2.998 x 10^8 ms^{-1}). To convert this time delay (δt) into a path difference (δh), one multiplies by the speed of the wave in free space:

$$\delta h = \delta t \times c = Z(c/c_s - 1) \tag{2.5}$$

Some works (Tilling et al., 2018; Kwok and Markus, 2018; Kwok and Kacimi, 2018) have used this formulation to correct the radar range for the slower wave propagation speed through snow. Other works have used an alternative form of Eq. (2.5), generated by multiplying δt in Eq. (2.4) by the wave speed in snow (Kwok, 2014; Kurtz et al., 2014; Kwok and Cunningham, 2015; Ricker et al., 2015; Armitage and Ridout, 2015; Hendricks and Ricker, 2019; Landy et al., 2017; Xia and Xie, 2018):

$$\delta h = Z_r(1 - c_s/c) \tag{2.6}$$

For Eq. (2.6) to be true, Z_r must be regarded as:

$$Z_r = Z(c/c_s) \tag{2.7}$$

However, Z_r is conventionally interpreted as the real snow depth (Z) and δh is therefore erroneously reduced by a factor of c_s/c. When Eq. (2.7) is incorporated into Eq. (2.6), δh is redefined in terms of Z and becomes Eq. (2.5).

Conventional interpretation of Z_r as the real snow depth therefore leads to a bias in the freeboard (B_f) where:

$$B_f = Z \times \frac{(c - c_s)^2}{c \times c_s} \tag{2.8}$$

Bias in the freeboard then propagates into estimates of sea ice thickness by a multiplicative factor of $\rho_w/(\rho_w - \rho_i)$, where ρ_w represents the density of seawater and ρ_i represents the density of sea ice. Because first year ice (FYI) is generally denser than multiyear ice (MYI Jutila et al., 2022), a fixed snow thickness will introduce a greater bias on the thickness of first year ice. However, typical biases

introduced by this treatment over FYI are generally expected to be lower due to reduced snow accumulation. The bias introduced to sea ice thickness retrievals (B_{SIT}) due to conventional, erroneous use of Eq. (2.6) is therefore:

$$B_{SIT} = Z \times \frac{(c - c_s)^2}{c \times c_s} \times \frac{\rho_w}{\rho_w - \rho_i} \tag{2.9}$$

Equation (2.9) illustrates that the bias grows linearly with snow depth. In addition to this, B_{SIT} is also dependent on the speed of the radar wave in snow, which is itself a function of snow density. Several empirical relationships have been proposed for the relationship between snow density and radar wave speed, however the most commonly used three (Hallikainen et al., 1982; Tiuri et al., 1984; Ulaby et al., 1986) deviate negligibly from each other in the typical density range for snow observed on Arctic sea ice (Fig. S3). In this investigation, we use the relationship from Ulaby et al. (1986):

$$c_s = c(1 + 0.51\rho_s)^{-1.5} \tag{2.10}$$

As snow density increases, c_s decreases and B_{SIT} increases. This positive relationship between $f(c_s)$ and bulk snow density is shown in Fig. (2.1a). Because both snow depth and snow density generally increase throughout the season as snow accumulates, compacts and settles, any δh generated through incorrect expression of $f(c_s)$ becomes increasingly underestimated.

Furthermore, B_{SIT} increases even as a fixed snow water equivalent densifies and shrinks in volume. This is because B_{SIT} scales more rapidly with increasing snow density than it reduces with decreasing snow depth. The increase in bias with snow density for constant snow water equivalent (SWE) is illustrated in Fig. (2.1b).

Since B_{SIT} is explicitly a function of snow depth and implicitly a function of snow density via Eq. (2.10), its spatial mapping requires the use of an Arctic snow distribution. Here we use snow depths and densities from Warren et al. (1999) (henceforth 'W99') to illustrate these underestimates. To be consistent with current data products that rely on W99 for their snow depth distribution, we halve snow

depths over first-year ice as per Laxon et al. (2013) and only consider the Central Arctic basin (see Fig. S4) where W99 is considered most reliable (Kwok and Cunningham, 2015). Data on sea ice type and extent were taken from the sea ice type product of the EUMETSAT Ocean and Sea Ice Satellite Application Facility (OSISAF; Aaboe et al., 2016).

We find that where sea ice thicknesses are calculated using W99 snow depths and densities in the Central Arctic, thickness underestimates introduced by erroneous interpretation of Eq. (2.6) increase throughout the winter to values exceeding 15 cm in April over multi-year ice (Fig. 2.1c). This is equivalent to the result of a 3 - 4 cm underestimation in snow depth (see Eq. 2.1). Over FYI the mean bias increases from 4.2 cm in October to 9.8 cm in April (compared to 6.4 cm and 13.6 cm for MYI). In April, 28% of MYI has a bias exceeding 15 cm, and 7% exceeds 16 cm. These values are relative to a typical ice thickness in the same region of $\sim$1.6 m in October increasing to $\sim$2.7 m by April.

How does this bias impact sea ice thickness products currently available to the science community? Most commonly-used products do not correct for slower wave speed using the W99 density distributions in time or space, but instead use a reference density to calculate a fixed value for $f(c_s)$ in Eq. (2.1). This value is fixed not only across the Arctic basin, but throughout the winter. In version 2.2 of the CryoSat-2 sea ice thickness product from the Alfred Wegener Institute (AWI; Hendricks and Ricker, 2019), $f(c_s)$ is taken as $(1 - c_s/c)$ as in Eq. (2.6). Citing the reference spring snow density given by Kwok (2014) of 350 kg m^{-3}, they generate a fixed δh of $0.22Z$.

On the other hand, the Centre for Polar Observation and Modelling (CPOM) takes $f(c_s)$ to be $(c/c_s - 1)$ (Eq. (5); Tilling et al., 2018). However, the CPOM product uses a lower reference density of 300 kg m^{-3} (taken from Kwok et al. (2011)), generating a reference δh of $0.25Z$. AWI's use of a higher reference density mitigates the difference introduced by their erroneous interpretation of Eq. (2.6). Were AWI to use a similar reference density to CPOM's 300 kg m^{-3} with Eq. (2.6), their reference δh would be $0.19Z$, contrasting starkly with CPOM's $0.25Z$.

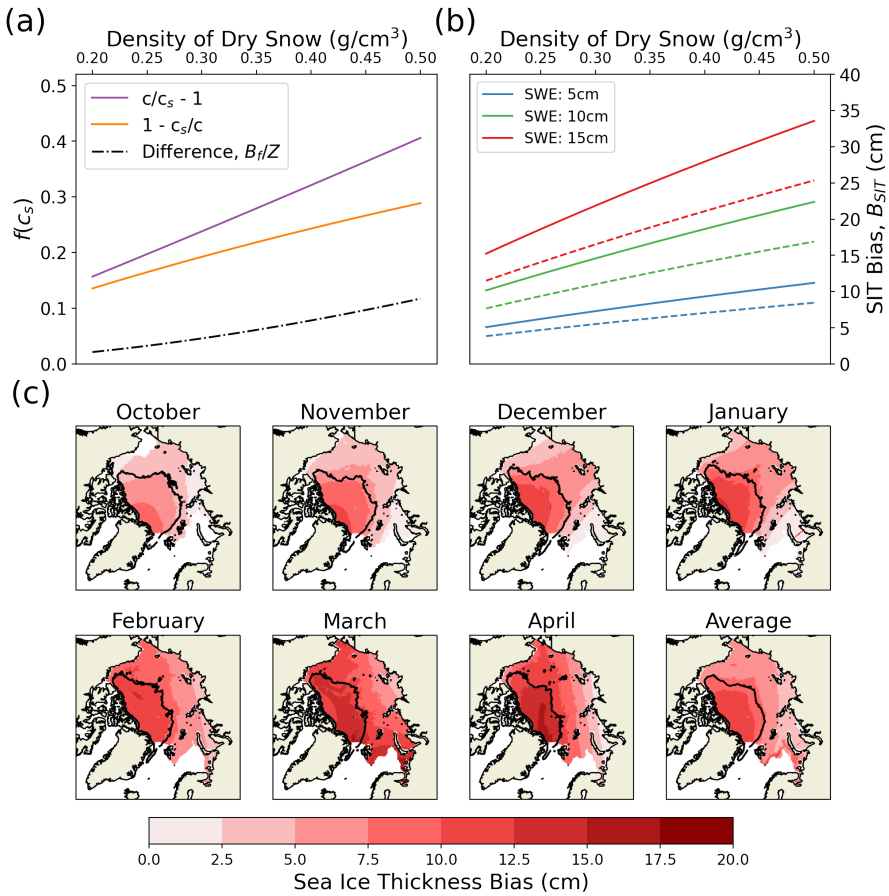

Figure 2.1: (a) Difference between conventional use of Eq. (2.6) and Eq. (2.5) as a function of snow density. This bias increases with snow density, ultimately exceeding a factor of 0.1 of the snow depth for dense snow. (b) Sea ice thickness bias for a fixed mass of snow increases as it densifies and contracts with time. Solid lines indicate bias for first year ice, dashed lines for multiyear ice assuming fixed densities of 916.7 and 882 kg m^{-3} respectively. (c) Monthly thickness bias introduced by conventional and erroneous use of Eq. (2.6) when calculated using W99 density and depth distributions. Pixels are only displayed where sea ice type is known in all years 2010-2018. Black line indicates region where multiyear ice is present in over 50% of years. Monthly averages derived from years 2010-2018.

The decision to use a fixed snow density for the wave-speed propagation correction throughout the winter introduces biases of its own with regard to the rate of thermodynamic growth; this is discussed in the next section.

2.3 Impact of Seasonal Snow Density Evolution on the Radar Wave Propagation Correction

Despite recent developments in pan-Arctic scale snow density modelling (Petty et al., 2018b), the Arctic snow density distribution remains poorly constrained in time and space. Because of this, representative values for pan-Arctic average snow density are often combined with the snow depth distributions from W99 to calculate the radar wave propagation correction (Kurtz et al., 2014; Hendricks and Ricker, 2019; Tilling et al., 2018).

This constant value contrasts with the ubiquitous inclusion of density evolution in the adjustment to an ice floe's hydrostatic equilibrium due to the weight of overlying snow. It is important to note here that snow densification does not increase the snow loading on sea ice in an absolute sense, since it does not represent the physical addition of snow to the system. Instead, it represents additional loading for snow of a given depth, as dictated by a snow product such as W99. A density evolution curve was derived from W99 by Kwok and Cunningham (2008) and implemented in sea ice thickness estimates derived from ICESat and CryoSat-2 (Kwok et al., 2009; Kwok and Cunningham, 2015). It is notable that Kwok and Cunningham (2015) include density evolution in both their calculation of the propagation correction and the adjustment to hydrostatic equilibrium.

To investigate the impact of an evolving snow density on the propagation correction, we calculated the propagation correction over Arctic sea ice by two methods: The control method used a fixed reference density in the wave speed correction (i.e. 300 kg m^{-3}) as done by CPOM and AWI. The other method incorporated a rate of snow densification obtained from W99 in the Central Arctic Basin.

The control method used the parameters employed by Tilling et al. (2018) producing a radar wave speed in snow of 2.4×10^{8} m s^{-1} corresponding to a reference

density of 300 kg m^{-3} when converted using Eq. (2.10). As discussed in Sect. 2.2, estimates of absolute sea ice thickness are sensitive to the choice of reference snow density. However, the estimated rate of thermodynamic growth (the focus of this section) is more responsive to the density's time derivative, which for a fixed value ($\rho_s = 300$ kg m^{-3}) is zero. As such, our results with respect to growth rate are applicable to different reference densities such as those used by AWI (350 kg m^{-3}) and the NASA Goddard Space Flight Center (320 kg m^{-3}; Kurtz et al., 2014).

For the 'evolving' method, we calculated a representative winter (Oct-Apr) densification rate using the average densification rate of snow over the Arctic Ocean given by W99. This was found to be approximately +6.50 ($\pm$ 0.8) kg m^{-3} per month. The October starting density was taken as the spatial average of the W99 October density field over the same region - this choice served to minimise sea ice thickness differences at the start of the growth season and better enable comparison of growth rate. Snow density in the 'evolving' method can therefore be written as:

$$\rho_s = 6.50t + 274.51 \tag{2.11}$$

Where t represents the number of months since October.

The W99 snow density evolution of five Arctic regions were also examined and found to be similar to the basin-wide rate, with the exception of the Laptev Sea which shows only a small (but positive) seasonal densification rate (Fig. S5). As in Sect. 2.2, we halved the W99 snow depths over FYI and only analysed the Central Arctic basin where W99 is considered most reliable. One consideration here is that the W99 rates are based on density observations over MYI, and the densification rate here may not be the same as FYI environments. In particular, depth hoar formation is potentially more aggressive in MYI environments: King et al. (2020) indicate that faceted and depth hoar grains over MYI have lower density.

When the evolving density shown in Eq. (2.11) was included in our calculation of the radar wave propagation correction, we found sea ice thickness to grow on average by an extra 10.1 cm between October and April over MYI. This corresponds to an extra 1.7 cm per month when compared to a fixed $f(c_s)$ of 0.25Z. Density evo-

lution caused FYI to grow an extra 6.4 cm over the same time period, corresponding to an extra 1.1 cm per month.

Given the poor state of knowledge concerning the current distribution of pan-Arctic snow densities and the difficulty in collecting in-situ data, we cannot conclude whether this increased growth should correspond to higher-than-previous thicknesses at the end of winter or lower-than-previous thicknesses at the start of winter. Put another way, in this section we show a systematic bias in the thermodynamic growth rate rather than absolute ice thickness values.

Having illustrated the effect of snow densification on the radar wave propagation correction, we now justify its inclusion.

While the absolute values for regional mean densities have conceivably changed since the data were collected for W99, it remains almost certain that snow density still increases over winter for the majority of the Arctic basin as documented in W99. Furthermore, the rate of snow densification shown in W99 is likely now underestimated, with field observations indicating densification rates of >20 kg m^{-3} per month on FYI (Langlois et al., 2007) and FYI now occupying significantly more of the Arctic basin than in the 1954-91 period over which W99 was compiled (Stroeve and Notz, 2018). While significant uncertainty in the true densification rate exists, effectively setting the rate to zero for the radar wave propagation correction introduces a systematic bias in sea ice thickness calculations.

Finally, commonly used products (e.g. Tilling et al., 2018; Hendricks and Ricker, 2019) have included a seasonally evolving snow density in the 'snow loading correction' (for change in the hydrostatic equilibrium of the floe due to the weight of snow cover), which features a very similar sensitivity to uncertainty in snow density (Fig. S6). The latest product of the Alfred Wegener Institute (v2.3 Hendricks and Ricker, 2020) was changed in response to the manuscript associated with this chapter, such that it reflects the treatment given here.

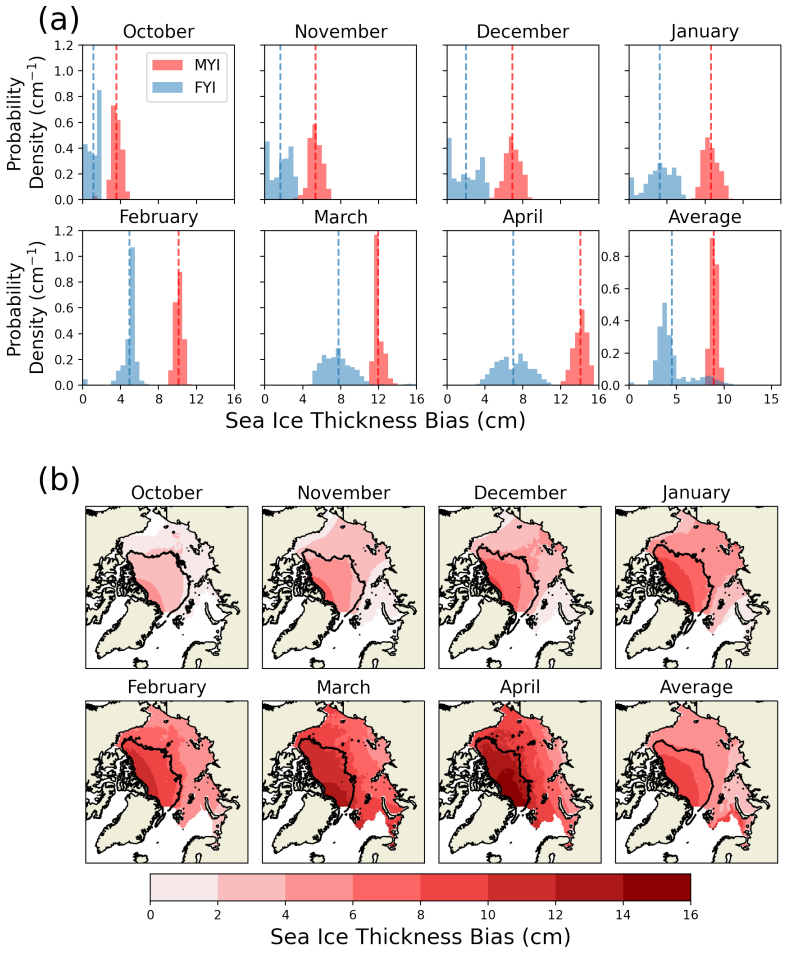

Figure 2.2: Monthly biases in sea ice thickness due to the effect of ignoring snow densification in calculating propagation correction (a) Spatially averaged histograms indicating the area of ice subjected to a given bias. Data separated into pixels that feature MYI for that month in more/less than 50% of years 2010-2018. Pixels that typically feature MYI experience greater bias in all months, largely due to halved W99 snow depths over FYI. (b) Sea ice thickness bias introduced by use of a static snow density in the calculation of the propagation correction. Pixels are only displayed where sea ice type is known in all years 2010-2018, so bias is not displayed in some areas of ambiguous ice type. Black line indicates region where MYI is present in over 50% of years. These values are typically 3-8% of the resulting sea ice thickness.

2.4 Discussion

2.4.1 Different Fixed Densities

To further explore this issue, we calculated the expected difference between sea ice thickness estimates from CPOM and AWI introduced by their usage of $\delta h = 0.25Z$ and $\delta h = 0.22Z$ respectively. Since the difference in δh is partially due to different choices of a representative snow density, resulting sea ice thickness differences cannot be seen as bias from a true value until Arctic snow densities are better constrained. This variation is superimposed on the bias introduced by fixed snow densities discussed above. We find that CPOM's higher value for $f(c_s)$ produces a higher mean MYI thickness of 5 cm in November, growing to 7 cm by April. 16% of MYI exhibited a difference of > 8 cm. For FYI, the mean difference is 2.8 cm in November and grows to 4.7 cm by April (Fig. S7).

2.4.2 Comparison to Radar Freeboards

To investigate these biases further, we compare them by converting pan-Arctic CryoSat-2 radar freeboard retrievals from late 2010 to early 2018 (processed under the assumption of a lognormal ice roughness distribution (Landy et al., 2019)) to estimates of sea ice freeboard using:

1. Equation (2.5) versus Eq. (2.6) (with conventional, erroneous interpretation) using the depth and density fits from W99

2. A monthly evolving density versus the fixed density used in Hendricks and Ricker (2019), both with spatially constant density across the Arctic basin

We find that the bias introduced by the erroneous interpretation of Eq. (2.6) remains relatively constant as a fraction of the sea ice freeboard at around 6% (despite increasing in an absolute sense) (Fig. 2.3a).

We find that the bias introduced by the assumption of a non-evolving snow density (in calculation of the propagation correction) grows throughout the season relative to the sea ice freeboard and in an absolute sense. The bias grows from 2.3% to 6% of the ice freeboard (Fig. 2.3b), indicating that the growth rate is underestimated when a fixed density is assumed.

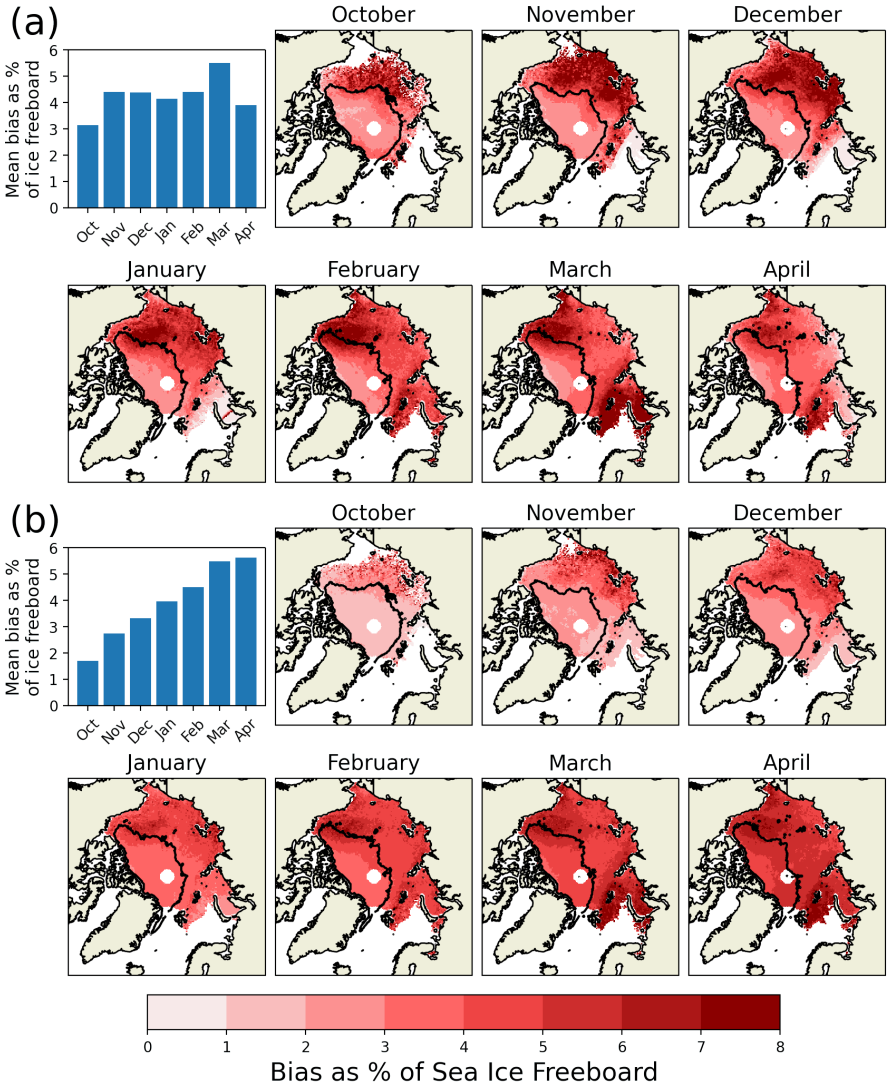

Figure 2.3: Percentage bias in sea ice freeboard. The bias induced by two effects was compared to the radar freeboards proccessed using the assumptions of Landy et al. (2019). (a) Percentage bias introduced by the use of Eq. (2.5) vs Eq. (2.6) when combined with the W99 fits for depth and density. As a fraction of the growing ice freeboard, biases remain relatively constant, indicating they grow at the same rate. (b) Percentage bias introduced by an evolving snow density derived from W99 data. This bias increases as a fraction of the ice freeboard from 2.3% to >6%, indicating that thermodynamic growth rates are underestimated.

2.4.3 Incomplete Radar Wave Penetration of the Snowpack

The biases introduced in this analysis are derived based on the common assumption that Ku-band radar waves penetrate the entire snowpack. However, in-situ studies of Antarctic snow on sea ice indicate that snow with significant morphological features can scatter the radar above the snow-ice interface (Willatt et al., 2010). Airborne investigations during the CryoVEx and N-ICE2015 campaigns also revealed elevated dominant scattering horizons (Willatt et al., 2011; King et al., 2018). Furthermore, snow salinity has also been shown to elevate the dominant scattering horizon from the snow-ice interface. Nandan et al. (2017) found the horizon to be elevated by 7 cm based on FYI data from the Canadian Arctic.

Radar wave scattering from a horizon above the ice-snow interface introduces an overestimating bias on sea ice freeboard and thickness. The size of this bias is potentially larger than those discussed above, and may be dominant in determining the sign of the overall bias. If this is the case and sea ice thickness is overestimated overall, fixing the underestimating biases discussed in this analysis would shift estimates further away from the true value. As such, while improving the realism of the retrieval algorithm, the results may not become more accurate.

2.4.4 Snow Depth Decline Since W99 Collection

The climatology assembled by Warren et al. (1999) was collected from drifting ice stations largely over MYI in the period 1954-91. Since then the average age of MYI has declined and freeze-ups have become increasingly delayed (Stroeve and Notz, 2018). This has had the effect of decreasing snow depth over MYI in the Western Arctic (Webster et al., 2014); it is unclear how snow depths have changed in the Eastern Arctic. While W99 has been modified to better apply over FYI using comparatively recent Operation Ice Bridge data (e.g. Laxon et al., 2013; Webster et al., 2014), this has not been similarly carried out for MYI snow depths in this analysis or other publicly available products. As such, the snow depths conventionally used for thickness retrievals are likely overestimates over MYI and this introduces an overestimating bias on freeboard and sea ice thickness. This would add to the effect described in Sect. 2.4.3, where fixing underestimating biases may

not make the overall estimate closer to the truth. In response to the issues associated with the W99 climatology, I explore the alternative use of a model-based snow depth in Chapter 3, finding it has strong implications for the calculation of sea ice thickness trends and variability.

Furthermore, lower snow depths and/or incomplete radar wave penetration of the snowpack would decrease the magnitude of the biases described here (as Eq. (2.8) and Eq. (2.9) both scale linearly with snow depth).

2.4.5 Broader Implications

Sea ice thickness is closely tied to sea ice volume, a sensitive indicator of climate change but also a quantity of major interest for the modelling community. The thickness underestimates highlighted in Sect. 2.2 have some impact on total sea ice volume, although this is well within the currently large uncertainty bounds. Nonetheless, we argue that these uncertainty bounds have been systematically biased through conventional use of Eq. (2.6) in some products.

In addition, the fact that these biases increase over winter means the seasonal growth rate is also biased through conventional use of Eq. (2.6). While the rate of winter sea ice growth is still uncertain and interanually variable, the use of a fixed, seasonally-constant value for the snow density will bias growth rates low.

Accurate characterisation of thermodynamic growth is important to a variety of systems. A higher growth-rate will impact the surface salinity balance as more freshwater than previously estimated is locked up in sea-ice during thermodynamic growth and then ejected to the mixed-layer when ice melts in summer. The rate of sea ice growth is an important variable in the characterization of the negative conductive feedback (thin ice thickens faster: Stroeve et al., 2018; Petty et al., 2018a). Finally, end of winter sea ice thickness moderates subsequent light transmittance through the ice, impacting under-ice ecosystems and related geochemical processes (Nicolaus et al., 2012b).

Sea ice thickness products featuring the misinterpretations of Eq. (2.6) have fed several forecast and reanalysis models (e.g. Xia and Xie, 2018). Thickness products featuring a constant-density assumption built into the propagation correction are

near-ubiquitous (with the exception of Kwok and Cunningham (2015)) and have also fed forecast and reanalysis models (e.g. Yaremchuk et al., 2019; Blockley et al., 2018). While these biases may be small compared to the effects of partial radar wave penetration into the snowpack, they are simply remediable. We suggest this is done before further work is undertaken to estimate the extent of and incorporate the effects of partial radar wave penetration into the snow cover.

2.4.6 Summary

We investigated two conventional methods for correcting radar altimetry derived sea ice freeboard retrievals for slower radar wave propagation in snow. We found that a commonly used treatment (conventional use of of Eq. (2.6)) for this correction introduces an initial and seasonally-increasing underestimating bias on sea ice thickness from October through to April. While most commonly-used products then transform this bias (where present) by choosing a fixed snow density, we find underestimation of April sea ice thickness to exceed 15 cm over some multiyear ice when this treatment is applied in conjunction with the snow density climatology from Warren et al. (1999).

We also investigated the impact of assuming a seasonally-fixed snow density on the radar wave propagation correction. While uncertainties in the absolute value of Arctic snow density preclude any conclusion about whether sea ice thickness is being under- or overestimated in this respect, this treatment is found to introduce an underestimating bias on the thermodynamic growth rate of multiyear ice of $\sim$1.7 cm per month leading to a $\sim$10.1 cm bias over the October-April period.

While these biases on sea ice thickness (Sect. 2.2) and growth rate (Sections 2.2 & 2.3) retrievals are small compared to the total uncertainty, they are systematic and easily addressed. While remaining unaddressed, they propagate into derived products and model projections, calibrations and reanalyses (Sect. 2.4.5).

Since the publication of the manuscript associated with this chapter, the Alfred Wegener Institute's sea ice thickness retrieval algorithm has been changed to reflect this work. Specifically, Section 2.6.1 of Hendricks and Ricker (2020, "Fall 2020 Update") includes the changes:

"Updated computation of wave speed correction in the snow layer following Mallett et al., 2020"

and

"Used hemisphere-wide snow density values following Mallett et al., 2020"

Chapter 3

Faster decline and higher variability in the sea ice thickness of the marginal Arctic seas when accounting for dynamic snow cover

The contents of this chapter are drawn from the following publication:

Mallett, R.D.C., Stroeve, J.C., Tsamados, M., Landy, J.C., Willatt, R., Nandan, V., & Liston, G.E. (2021). Faster decline and higher variability in the sea ice thickness of the marginal Arctic seas when accounting for dynamic snow cover. The Cryosphere, 15(5), 2429-2450.

However the original paper only assessed data up to summer 2018. The figures and statistics in this chapter have been updated to include data up to summer 2021.

3.1 Introduction

Chapter 1 introduced the key role of sea ice as a moderator of moisture, heat and momentum between the Arctic Ocean and the Arctic atmosphere. The role of sea ice thickness as a key variable in this moderation was then summarised. The Chapter

also introduced the key role of the snow cover in radar-based estimates of sea ice thickness.

Chapter 2 presented the results of a study on the delay to radar-wave propagation by the snow cover. Specifically, two different formulas for this delay were discussed, along with their relative impacts on resulting sea ice thickness estimates. The role of including seasonal snow density evolution in the calculation of this delay was estimated. This was done using the climatological data used in most sea ice thickness products for calculation of floe hydrostatic equilibrium. This climatology is from 'the Warren climatology' (W99 Warren et al., 1999).

In this chapter, we present the results of a broader investigation into the role of snow cover on sea ice thickness retrievals. In particular, I introduce a way of combining the effect of wave-propagation delay with the role of snow in the hydrostatic equilibrium of the floe; this allows different snow products to be simply compared. Specifically, I go on to compare the snow climatology used in Chapter 2 (W99; derived from NP drifting stations) to results from a newly developed snow model.

3.1.1 The Role of Snow in Radar-Altimetry Derived Sea Ice Thickness Retrievals

The impact of snow-depth uncertainty on SIT retrievals was recently included by the IPCC in a list of 'Key Knowledge Gaps and Uncertainties' (Meredith et al., 2019). More specifically, Bunzel et al. (2018) found snow to have a strong influence on the interannual variability of SIT and consequent detection of thickness trends. In this Chapter we investigate the impact of a new, Pan-Arctic snow depth and density data set (SnowModel-LG; Liston et al., 2020; Stroeve et al., 2020a) on trends and variability in regional $\overline{SIT}$ when used in place of the traditional, climatological data set (Warren et al., 1999, Used in Chapter 2). We show that traditional calculations of $\overline{SIT}$ omit significant interannual variability due to their reliance on a snow climatology, and we quantify this omission. We also show that sea ice is likely thinning at a faster rate in some marginal seas than previously thought, because the snow water equivalent on the sea ice is declining too.

We now quantify the combined role of snow cover in conventional sea ice thickness estimation (in terms of hydrostatic equilibrium and wave propagation delay), before revealing and explaining the effects of previously unincorporated trends and variability.

As mentioned in Chapters 1 & 2, the Ku-band radar waves emitted from CryoSat-2 are generally assumed in mainstream SIT products to scatter from the snow/sea-ice interface (Kurtz et al., 2014; Tilling et al., 2018; Hendricks and Ricker, 2019; Landy et al., 2020). The difference in radar ranging (derived from time-of-flight) between areas of open water and areas of sea ice is known as the 'radar freeboard', f_r. The height of the sea ice surface above the waterline is referred to as the sea ice freeboard, f_i. This is extracted from the radar freeboard through (a) assuming that the primary scattering horizon corresponds to the sea ice surface, and (b) accounting for the slower radar wave propagation through the snow cover above the sea ice surface (Armitage and Ridout, 2015; Mallett et al., 2020). The sea ice freeboard can then be converted to sea ice thickness by considering the floe's hydrostatic equilibrium given the sea ice density and weight of overlying snow. In the simplified case of bare sea ice, we would calculate:

$$SIT_{bare} = f_r \frac{\rho_w}{\rho_w - \rho_i} \tag{3.1}$$

Where ρ_w is the density of seawater and ρ_i the density of sea ice. In order to adjust the above equation for the presence of overlying snow, the twin effects of the snow's weight and the snow's delaying influence on radar pulse propagation must be taken into account. These three influences on SIT (the radar freeboard measurement, the pulse propagation delay and the freeboard depression from snow weight) can therefore be expressed as three terms (see supplementary information) in the following way:

$$SIT = h_r \frac{\rho_w}{\rho_w - \rho_i} + h_s \frac{\rho_w}{\rho_w - \rho_i} \left[\frac{c}{c_s} - 1 \right] + h_s \frac{\rho_s}{\rho_w - \rho_i} \tag{3.2}$$

In this chapter we introduce a simple method for combining the second and

third terms of the above equation into a single term that is proportional to the snow water equivalent (Sect. 3.3.1). This helps to easily separate the influences of snow data and radar freeboard measurements on the determination of sea ice thickness. Specifically, we compare the impact of two snow products on regional trends and variability in sea ice thickness. These products are the snow climatology given by Warren et al. (1999) and the output of SnowModel-LG (Liston et al., 2020; Stroeve et al., 2020a).

3.2 Data Description

3.2.1 Regional Mask

We define seven regions of the Arctic Basin using the mask from Stroeve et al. (2014) which is gridded onto a 25 km resolution EASE grid (Brodzik et al., 2012, Fig. 3.1). We define the 'marginal seas' of the Arctic Basin as the color coded areas of Fig. (3.1) excluding the Central Arctic. All constituent regions of the 'marginal seas' grouping lie within the coverage of Envisat barring a negligible portion of the Laptev Sea.

3.2.2 Radar Freeboard Data

To examine the impact of snow products on Enivsat/CryoSat-2 thickness retrievals, we used radar freeboard data from the ESA Sea Ice Climate Change Initiative (Hendricks et al., 2018). These data are available from October in the winter of 2002/03 until April in the winter of 2016/17. This product was chosen for two main reasons: (a) it provides a consistent record for both the Envisat and CS2 missions (Paul et al., 2018), and (b) it is publicly available for download. CS2 carries a delay-Doppler altimeter that significantly enhances along-track resolution by creating a synthetic aperture. For this reason as well as its higher latitudinal limit, we used CS2 radar freeboard measurements over Envisat during the period when the missions overlapped (November 2010 - March 2012). To create a radar freeboard product that is consistent between the Envisat and CS2 missions, Envisat returns are retracked using a variable threshold retracking algorithm. This variable threshold is calculated from the strength of the surface backscatter and the width of the leading edge of the

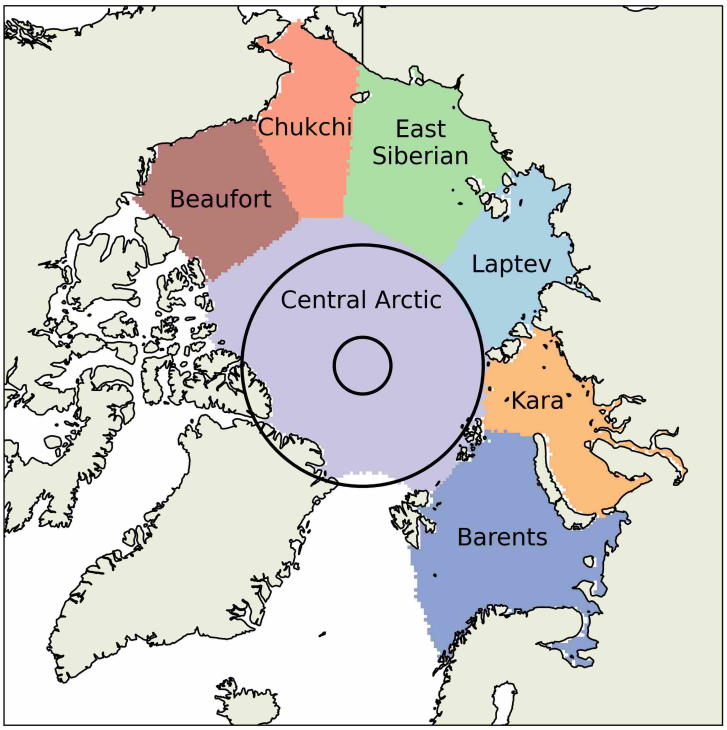

Figure 3.1: The definitions of the marginal Arctic seas used in this chapter, from Stroeve et al. (2014). Two black, concentric circles indicate the latitudinal limits of the CryoSat-2 (inner circle; 88°N) and Envisat (outer circle; 82.5°N) missions.

return waveform such that the inter-mission bias is minimised (Paul et al., 2018). The results are comprehensively analysed in the Product Validation & Intercomparison Report (Kern et al., 2018). One key finding of this report is that while Envisat radar freeboards are calculated so as to match CS2 freeboards during the period of overlap over the whole Arctic basin, there are biases over ice types. In particular, Envisat ice freeboards (not radar freeboards) are biased 2-3 cm low (relative to CS2) in areas dominated by multi-year ice (MYI), and 2-3 cm high in areas dominated by first-year ice (FYI). We discuss the implications of these biases in Sect. 3.5.3.

While the ESA CCI data are only available from the CCI website until the winter of 2016/17, the CryoSat-2 radar freeboards in this data are identical to the CS2 radar freeboard product of the Alfred Wegener Institute (Hendricks and Ricker, 2019, this was manually confirmed). We were therefore able to extend our radar freeboard timeseries through the winter of 2020/21, which is when our snow data from SnowModel-LG (see below) ended.

All radar freeboard data used in this study are supplied on a 25 km EASE grid (Brodzik et al., 2012), the same as that of SnowModel-LG.

3.2.3 The Warren Climatology (W99)

The most commonly used radar-altimetry SIT products use algorithms developed by the Centre for Polar Observation and Modelling, the Alfred Wegener Institute and the NASA Goddard Space Flight Centre (Tilling et al., 2018; Hendricks and Ricker, 2019; Kurtz et al., 2014). Another commonly used but not publicly available product is from the NASA Jet Propulsion Laboratory (Kwok and Cunningham, 2015). All four groups utilize modified forms of the snow climatology assembled by Warren et al. (1999) from the observations of Soviet drifting stations between 1954 and 1991 (henceforth referred to as W99).

While the consistent use of W99 for sea ice thickness calculation is convenient for intercomparison of products (e.g. Sallila et al., 2019; Landy et al., 2020), the data have a number of drawbacks. This work is centered around two key issues with the use of W99 for SIT retrieval: inadequate representation of interannual variability and trends.

The Warren Climatology includes quadratic fits for every month of snow water equivalent and snow depth. We projected these fits over the 361×361 EASE grid (for combination with our radar freeboard data and comparison with SnowModel-LG) to create SWE and depth distributions across the Arctic basin as defined in Sect. (3.2.1).

3.2.3.1 Drifting Station Coverage Illustration

At this point it is instructive to briefly illustrate the coverage of the drifting stations from which W99 was compiled. We analysed position and snow depth data from the twenty-eight drifting stations that contributed to W99 (Fig. 3.2a). It is clear that the vast majority of these operated in the Central Arctic or in the East Siberian Sea, with very little sampling done in most other marginal seas. But while these tracks illustrate the movements of the drifting stations, it is important to note that the stations were not always collecting snow data which would contribute to the W99

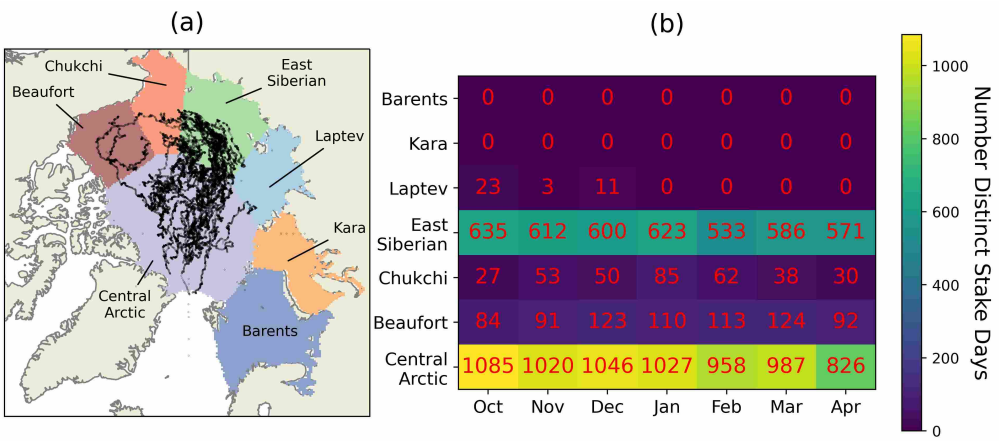

Figure 3.2: (a) tracks of Soviet drifting stations 3 - 31. (b) Number of days in each region in each month that snow stake measurements were taken.

climatology. To assess the spatial distribution of snow sampling, we cross-referenced the position data with days on which the drifting stations recorded the snow depth at their measuring stakes. We then calculated the number of 'measurement-days' in each region-month combination (Fig. 3.2b). We note that when two drifting stations were operating at the same day, we count this as two distinct days (as they were rarely so close together so as to collect redundant data).

This reveals that no snow measurements were taken in the Barents and Kara Seas, and none in the Laptev Sea for four of the seven winter months. While 'snow-line' transect data also contributed to W99 (and indeed was used in preference to stake data where possible), we find that snow-line data was overwhelmingly collected on days where stake-data was also collected. As stated in Chapter 1, the transect-based measurements were used in preference to stake-based measurements due to improved spatial sampling statistics and because of the potential influence of the nearby station on the stake measurements.

Figure 3.2 illustrates that the quadratic fits of W99 are not obviously appropriate for use in several of the marginals seas. However we note that a number of authors have still used the climatology for sea ice thickness retrievals in these regions, often in the course of sea ice volume calculations (e.g. Laxon et al., 2003, 2013; Tilling et al., 2015, 2018; Kwok, 2018; Li et al., 2020a; Belter et al., 2020; Li et al., 2020b). We therefore consider these regions in this chapter, but with the understanding that

mW99 is potentially not representative of the snow conditions.

3.2.4 The modified Warren Climatology (mW99)

The W99 climatology is by definition invariant from year to year, and was implemented in this way by Laxon et al. (2003) and Giles et al. (2008a) to estimate sea ice thickness using ERS 1 & 2. When implemented like this, the amount of snow on sea ice exhibits no interannual variability.

The implementation of W99 was then modified by Laxon et al. (2013) based on the results of Operation IceBridge flights which showed approximately halved snow depth over first year ice (Kurtz and Farrell, 2011). This implementation, known as 'mW99', consists of halving snow depths over first year ice with snow density kept constant. Because the areal fraction and spatial distribution of FYI changes from year to year, this modification introduces a small degree of interannual variability into the contribution of snow data to sea ice thickness. We investigate this in Sect. (3.4.1.1).

The mW99 halving scheme is fairly crude. And more generally, the W99 climatology is now fairly old, predating the observed, precipitous decline in sea ice extent. This chapter explores a more sophisticated snow product produced by a recently developed model (SnowModel-LG; Sect. 3.2.6)

3.2.5 Ice Type Data

Sea ice type data are required to modify W99 and create mW99. One popular product for this (e.g. Tilling et al., 2018; Hendricks and Ricker, 2019) is an operational product from the EUMETSAT Ocean and Sea Ice Satellite Application Facility (OSI SAF, www.osi-saf.org). However, these data begin in March 2005. This is after our study begins (in October 2002).

A similar product exists, published by the Copernicus Climate Data Store (CDS, www.cds.climate.copernicus.eu; Aaboe, 2020). This product's underlying algorithm is adopted from the OSI SAF processing chain, but has been modified to produce a consistent record compatible with reanalysis. Furthermore, the CDS product only assimilates information from 'passive' satellite radiometers, whereas the OSI

SAF operational product assimilates additional data from 'active' scatterometers. Despite these differences, a brief comparison of the products reveals a high degree of similarity.

It would be possible to use the CDS product prior to the beginning of the OSISAF product in 2005, but this approach raises issues surrounding the continuity of the products across the 2005 transition. Since our investigation focusses on trends and variability, we prioritise a consistent record and opt to use the CDS ice type product for the entirety of our study.

Both ice type products occasionally include pixels of ambiguously classified ice. We implemented a very simple interpolation strategy to classify these points while creating our mW99 data, although they are rarely present in winter within the regions analysed in this chapter. Where the ambiguous pixels are generally surrounded by a given ice type then they are classified as the surrounding type. In the case where the ambiguous classification is on the boundary between the two types, the snow depth was not divided by two.

3.2.6 SnowModel-LG

To investigate the impact of variability and trends in snow cover on regional sea ice thickness we use the results of SnowModel-LG (Liston et al., 2020; Stroeve et al., 2020a). SnowModel-LG is a Lagrangian model for snow accumulation over sea ice; the model is capable of assimilating meteorological data from different atmospheric reanalyses (see below) and combines them with sea ice motion vectors to generate pan-Arctic snow depth and density distributions. The sea ice motion vectors used were from the Polar Pathfinder dataset at weekly time resolution (Tschudi et al., 2020). SnowModel-LG exhibits more significant interannual variability than mW99 in its output because it reflects year to year variations in weather and sea ice dynamics.

SnowModel-LG includes a relatively advanced degree of physics in its modelling of winter snow accumulation. The model creates and merges layers based on precipitation and snowpack metamorphism. The effects of sublimation, depth-hoar formation and wind-packing are included. However, the effects of snow loss to leads by wind and extra snow accumulation due to sea ice roughness are not included. Fur-

thermore, the heat flux to the snow is not sensitive to the thickness of the underlying sea ice. Instead, the lower boundary condition for the snow temperature is locked at -1.0°C (Liston et al., 2020, Appendix F).

SnowModel-LG creates a snow distribution based on reanalysis data, and the accuracy of these snow data are unlikely to exceed the accuracy of the input. There is significant spread in the representation of the actual distribution of relevant meteorological parameters by atmospheric reanalyses (Boisvert et al., 2018; Barrett et al., 2020). The results of SnowModel-LG therefore depend on the reanalysis data set used. However, the data product used has been tuned to match Operation Ice Bridge derived snow depths during spring time, and snow depth differences between the reanalysis products were found to be less than 5 cm (Stroeve et al., 2020a). Tuning parameters for the precipitation forcing were developed for each individual atmospheric reanalysis product, and calculated for each year. The average for all the years for each product was then taken (producing two average values), and applied to the model to generate the two outputs analysed here (One output for each reanalysis data set Liston et al., 2020, Sect. 2.5 for more details).

We note that the vast majority of Operation Ice Bridge flights were over the Beaufort Sea and the Greenlandic side of the Central Arctic, which is generally covered by multiyear ice. It is therefore conceivable that the scaling factors would be different if FYI were better sampled by OIB. The time-averaged regional differences between SnowModel-LG runs forced by ERA5 and MERRA2 reanalysis data are shown in Fig. (S3). The SnowModel-LG data used in this study are generated from the average of SnowModel-LG runs forced by the two reanalysis products. The SnowModel-LG data are provided on the same 25 km EASE grid as the ESA-CCI radar freeboards described above at daily time resolution. We averaged this daily product to produce monthly gridded data for combination with the monthly radar freeboard data.

3.2.7 NASA Eulerian Snow on Sea Ice Model (NESOSIM)

To support and broaden the impact of our findings, we repeat our analyses with NESOSIM data from 2002-2021 (Petty et al., 2018b). NESOSIM data are released

on a 100×100 km grid which was interpolated to the 25×25km EASE grid of the SnowModel-LG and radar freeboard data. NESOSIM runs in a Eulerian framework and like SnowModel-LG can assimilate precipitation data from a variety of reanalyses data. In contrast with SnowModel-LG's multi-layered scheme, NESOSIM uses a two-layer snow scheme to represent depth-hoar and wind-packed layers. To define these layers, it assimilates surface winds and temperature profiles from reanalysis. Wind-blown snow loss is parameterised to leads using daily sea ice concentration fields (Comiso, 2000, updated 2017).

In this study we use data from a NESOSIM run initialised on the 15th August for each year. The initial depth was produced by a 'near-surface air-temperature-based scaling of the August W99 snow depth climatology'. This is a linear scaling based on the duration of the preceeding summer melt season. Snow density was initialised using the August snow-line observations of Soviet NP drifting stations 25, 26, 30 and 31. Data from the most recent publicly available drifting stations were chosen to maximise their relevance in a changing climate.

3.3 Methods

3.3.1 Contributions to thickness determination from snow and radar freeboard data

We now identify that the height correction due to slower radar pulse propagation in snow scales in almost direct proportion to the total mass of penetrated snow (m_s; Fig. S1). As such, it can be easily combined with the change to the floe's hydrostatic equilibrium from snow loading (also linearly dependent on m_s) to make one transformation to modify Eq. (3.2) such that:

$$SIT = f_r \frac{\rho_w}{\rho_w - \rho_i} + m_s \frac{\rho_w}{\rho_w - \rho_i} \times 1.81 \times 10^{-3} \tag{3.3}$$

Physically, the first term of Eq. (3.3) corresponds to the SIT were the sea ice known to have no snow cover. The second term is the additional sea ice thickness that is inferred from knowledge of the overlying snow cover. SIT has been

decomposed into linearly independent contributions from radar-freeboard data and snow data. This allows the contributions of the two data components to SIT to be assessed independently. A derivation of the 1.81×10^{-3} coefficient is available in the supplementary material.

We highlight here that our expression in Eq. (3.3) of the contribution of snow data to SIT determination solely in terms of snow mass is technically convenient for using W99 to estimate sea ice thickness, as quadratic fits of density (unlike depth and snow water equivalent) are not publicly available for all months. This has led to the required density values often being set to a constant value or 'backed out' by dividing the published SWE distributions by the depth distributions.

Eq. (3.3) and its factor of 1.81×10^{-3} allow the simple expression of the theoretical change to the radar freeboard under rapid snow accumulation or removal. Making f_r the subject of the equation and assuming SIT constant we find:

$$\frac{\partial f_r}{\partial m_s} = -1.81 \times 10^{-3} \quad m/kgm^{-2}) \tag{3.4}$$

We stress that the above equation assumes total radar penetration of overlying snow, an assumption discussed in Sect. (3.5.3.1). As well as allowing independent analysis of the radar and snow data contributions to SIT at a point, the linearly independent nature of Eq. (3.3) in terms of f_r and m_s allows for a simple calculation of the average SIT in a region ($\overline{SIT}$) as:

$$\overline{SIT} = \overline{RF} + \overline{Snow} \tag{3.5}$$

Where $\overline{RF}$ and $\overline{Snow}$ represent the spatial averages of the first and second terms of Eq. (3.3).

3.3.2 Assessing Snow Trends and Variability at a point

In Sect. (3.4.1) we briefly compare the statistics for trends and variability at drifting stations published in Warren et al. (1999) with those introduced by mW99 and SnowModel-LG at a given point. We carry out this analysis to establish that the mW99 variability and trends at a given point (chosen as pixels on a 25x25 km EASE grid) are considerably smaller than those observed at drifting stations.

The monthly interannual variability (IAV) values published in Warren et al. (1999) are calculated as the standard deviation of the snow depths at drifting stations when compared to the climatology at the position of the stations. The IAV values at a point-like drifting station in a region will therefore naturally be higher than the IAV of the region's spatial-mean. As such, to compare IAV values from point-like drifting stations to mW99, we calculate the IAV at individual ice-covered points on a 25×25 km equal-area grid (Brodzik et al., 2012). These are all positive values, which we then average for comparison with the drifting stations. By regionally averaging the IAV values of many points rather than calculating the IAV of regional averages, we replicate the statistics of the point-like drifting stations.

However, the main part of this chapter does not focus on trends and variability at a point (as measured by drifting stations), but instead investigates trends and variability in $\overline{Snow}$ and $\overline{SIT}$ at the regional scale (Sections 3.4.2 & 3.4.3). This variability is significantly lower than the typical variability at a point, as many local anomalies from climatology within a region are averaged out in the calculation of single, area-mean values which form a timeseries for each region.

3.3.3 Assessing Regional Interannual Variability

Sect. (3.4.2) of this chapter focuses on the interannual variability in regional $\overline{SIT}$ which (treating $\overline{RF}$ and $\overline{Snow}$ as random, dependent variables) can be expressed thus:

$$\sigma^2_{\overline{SIT}} = \sigma^2_{\overline{RF}} + \sigma^2_{\overline{Snow}} + 2\,\mathrm{Cov}(\overline{RF}, \overline{Snow}) \tag{3.6}$$

Where the final term represents the covariance between spatially averaged radar freeboard and snow contributions. This covariance term can be expressed as $2r \times \sigma_{\overline{Snow}} \times \sigma_{\overline{RF}}$, where r is the dimensionless correlation-coefficient between the variables and ranges between -1 and 1. To further explain this term, if years of high $\overline{RF}$ are correlated with high $\overline{Snow}$, then the covariance term will be high and interannual variability in $\overline{SIT}$ will be amplified. If mean snow depths are anti-correlated with mean radar freeboard across the years, interannual variability in $\overline{SIT}$ will be reduced.

$\overline{SIT}$, $\overline{RF}$ & $\overline{Snow}$ were calculated where any valid grid points existed on the 25x25 km EASE grid. Because of this, no average values were computed in the Kara Sea in October 2009 or 2012. Furthermore, no October values were generally available in the Barents Sea after 2008 (with the exception of 2011 and 2014). The impact of this on our resulting analysis is clearly visible in the top left panel of Fig. (3.10). We do not exclude the Barents Sea in October from our analysis because of the low number of valid points, but we do highlight the undersampling issue here. We continue to consider it because we do not find statistically significant declining trends with the data we have, so essentially we are reporting a null result. Our calculations of interannual variability in this month is inherently adjusted for the small sample size, but we nonetheless urge caution in interpretation of the values. The number of grid points available for averaging in each region in each month are shown in Fig. (S2).

The three terms on the right hand side of Eq. (3.6) correspond to the three unique terms of the covariance matrix of the two terms of Eq. (3.5). The main-diagonal elements of this 2×2 matrix correspond to the variance of the snow contribution and the radar freeboard contribution to sea ice thickness, terms one and two of Eq. (3.6). The off-diagonal elements are identical and sum to form the third term of Eq. (3.6).

We calculated this matrix for each region in each month to investigate the sources of regional interannual variability in $\overline{SIT}$ for the time period under consideration (2002-2021). The Central Arctic region is not sufficiently well observed by the Envisat radar altimeter (see Fig. 3.1), so the covariance matrix for the region was only calculated for the CS2 period (2010-2018).

In some cases a natural degree of covariance is introduced between the regional $\overline{Snow}$ and $\overline{RF}$ timeseries because they both display a decreasing trend. This 'false-variance' would not be present were the system in a steady state. As such, we detrended the regional timeseries prior to calculation of the covariance matrix. We found that doing this significantly decreased the value of the covariance term in Eq. (3.6) .

We consider the relative contributions of these three terms to $\sigma^2_{\overline{SIT}}$ in calculations

involving mW99 and SnowModel-LG (Sect. 3.4.2). In light of these results, we then re-assess the statistical significance of regional trends in $\overline{SIT}$ using SnowModel-LG.

Detection of temporal trends in $\overline{SIT}$ is critically dependent on accurate characterisation of $\sigma^2_{\overline{SIT}}$. This is because conventional tests for trend exploit the known probability of a system with no trend generating the data at hand through variability alone (Chandler and Scott, 2011, p. 61). In this chapter we argue that the $\sigma^2_{\overline{Snow}}$ term of Eq. (3.6) has been systematically underestimated through the use of a quasi-climatological snow data set (mW99). As an alternative to this we use the results of SnowModel-LG, a snow accumulation model that incorporates interannual changes in precipitation amount, freeze-up timing and sea ice distribution.

3.3.4 Assessing Regional Temporal Trends

In Sect (3.4.3) we examine temporal trends in regional $\overline{SIT}$ for each month of the growth-season (October - April), and decompose the results by sea ice type. It is stressed that these regional trends are each the trend of a single timeseries of spatially averaged thickness values, rather than the average of many trends in sea ice thickness at various pixels in a region. Regional trends were deemed statistically significant if they passed a two-tailed hypothesis test with p-value less than 0.05, with a null hypothesis of no trend. Trends were calculated for regional $\overline{SIT}$ over the Envisat-CS2 period (2002-2021) for all regions apart from the Central Arctic for which only CS2 data were available. We assess the relationship of these trends in $\overline{SIT}$ to trends in $\overline{RF}$ and $\overline{Snow}$ (Fig S19).

In Sect. (3.4.1.2) we show that basin-wide average snow depth and SWE is decreasing in SnowModel-LG in most months, but only in October for mW99. We point out here that (under the paradigm of total radar wave penetration of snow on sea ice) under-accounting for potential reductions in SWE may partially mask a decline in sea ice thickness, as reductions in radar freeboards are partially compensated by reductions in snow depths. From Eq. (3.5):

$$\frac{\partial(\overline{SIT})}{\partial t} = \frac{\partial(\overline{RF})}{\partial t} + \frac{\partial(\overline{Snow})}{\partial t} \tag{3.7}$$

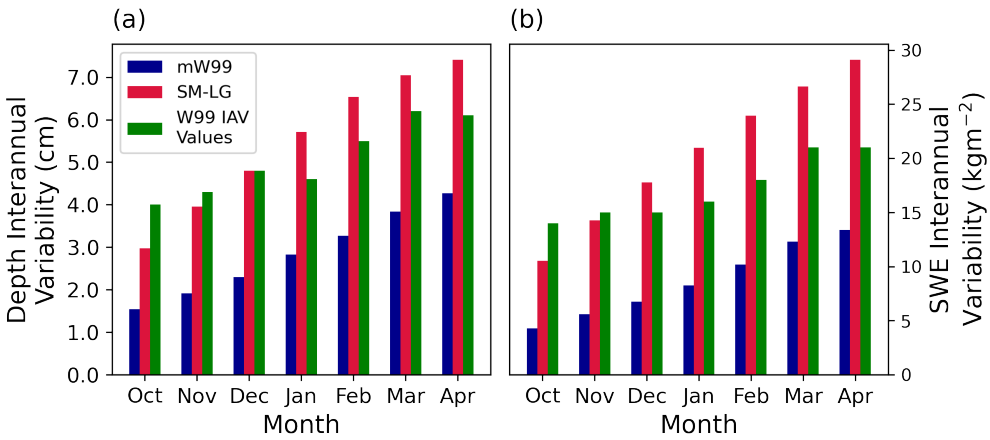

Figure 3.3: Interannual variability (2002-2021) in snow depth from mW99 and SnowModel-LG compared to the values given in Table 1 of Warren et al. (1999).

3.4 Results

3.4.1 Comparison of point-trends and point-variability

3.4.1.1 Low interannual variability in mW99 compared to drifting stations and SnowModel-LG

How does the variability in mW99 and SnowModel-LG at a given point compare to the values recorded at Soviet drifting stations published by Warren et al. (1999)? These values for interannual variability are not currently used in sea ice thickness retrievals (although they do contribute to uncertainty estimates in the ESA-CCI sea ice thickness product). Nonetheless, they offer a benchmark against which to evaluate the variability induced by mW99 at a given location.

Using the method described in Sect. 3.3.2 we find that the snow variability at a point from mW99 (Fig. 3.3, blue bars) is on average about 50% of the values recorded at the drifting stations (Fig. 3.3, green bars). By comparison, SnowModel-LG snow depth variability at a given point is significantly higher, ranging from ∼75% of the drifting station values in October to ∼115% by the end of winter.

We present this analysis of the point-like snow variability to illustrate that mW99 does not introduce enough variability at a given point to match that observed at drifting stations from year to year. Furthermore, the variability that does exist is confined to a distinct band of the Arctic Ocean (Fig. 3.4). This band represents

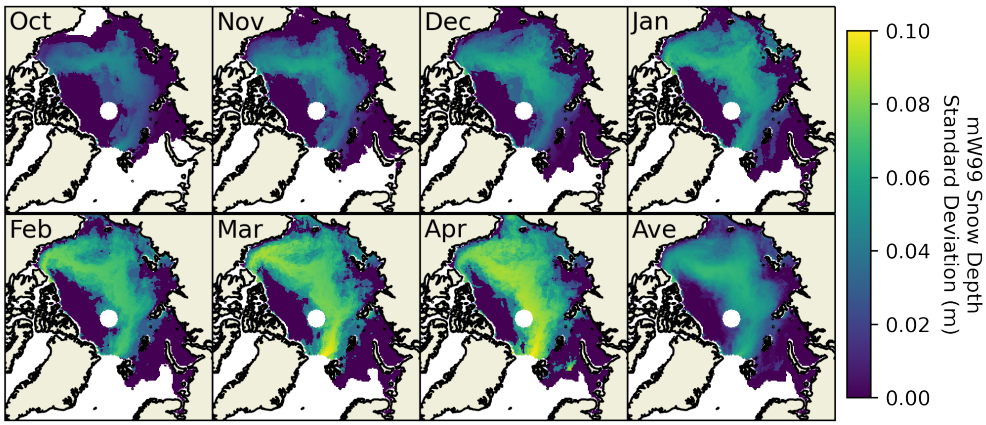

Figure 3.4: mW99 snow depth variability at each EASE grid point over the 2002-2021 period. This is calculated by generating a timeseries of snow depth at each point and then calculating the standard deviation of that timeseries. High variability is displayed in a band where sea ice type typically fluctuates from year to year. IAV is zero in areas that do not exhibit sea ice type variability, introducing unphysically low variability in SIT.

areas where the sea ice type is not typically either FYI or MYI. Instead it is either switching between the two, or it is an area where FYI has replaced MYI during the period of analysis. In areas where sea ice type is temporally unchanging, snow variability is not present. This has implications at the regional scale as marginal seas with a consistent sea ice type experience unrealistically low $\sigma_{\overline{Snow}}$ in the mW99 scheme.

3.4.1.2 Lack of Temporal Trends in mW99 compared to SnowModel-LG and in-situ data

Weak trends exist at some points in the mW99 Arctic snow distribution due to the shifting distribution and abundance of first year ice in the Arctic. In this section we briefly address their size, sign and veracity, leaving regional analysis until Sect. (3.4.2).

Values for SWE and depth trends measured by individual drifting stations are given in W99, but the values are not statistically significant for any of the winter months, and as such are not displayed here. We instead compare the point-trends at all color coded regions of Fig. 3.1 from mW99 and SnowModel-LG (Fig. 3.5).

We find that when we average the point-trends at a basin-wide scale, we find a

positive, statistically significant trend (at the 5% level) for mW99 snow depth for the month of October (+0.11 cm/yr; Fig. 3.5). This increasing trend in snow depth is in part due to the diminishing area of October FYI relative to that of MYI (Fig. S11), and in part due to the retreat of the October sea ice into the Central Arctic where W99 exhibits higher snow depths and SWE. The increasing October areal dominance of MYI is in part driven by delayed Arctic freeze-up (Markus et al., 2009; Stroeve et al., 2014). That is to say, the sea ice cover is becoming increasingly dominated by MYI in October. The area of sea ice over which the W99 climatology is halved in October is therefore shrinking, and basin-wide mean snow depths in mW99 are increasing. Trends in sea ice type fraction for each winter month are displayed in Fig. (S4), and monthly timeseries for mW99 SWE are displayed in Fig. (SS12). When this analysis was originally performed in (Mallett et al., 2021) (from 2003-2018), no months of Fig. 3.5 showed statistically significant negative declines; however, updating the analysis to include 2018-2021 shows that the months of January and February are statistically significant. The months of November, December, March and April remain non-significant at the 5% level.

Unlike mW99, SnowModel-LG exhibits statistically significant, negative point-trends for the later five of the seven winter months (when averaged at a basin-wide scale). We identify two processes as responsible for this decreasing trend: the MYI area is shrinking, so a smaller sea ice area is present during during the high snowfall months of September and October (Boisvert et al., 2018); also freeze-up commences later, so a lower FYI area is available in these months and more precipitation falls directly into the ocean. Webster et al. (2014) observed a -0.29cm/yr trend in Western Arctic spring snow depths using both airborne and *in situ* sources. This airborne contributions to this statistic included data over both sea ice types, and the in-situ contributions included data from individual NP drifting stations as well as drifting buoys. The statistic compares well with the behaviour of SnowModel-LG (-0.20 cm/yr in March and April), but is considerably beyond the trends in W99 and mW99.

What might the effects of this decline be on SIT at regional scales and larger? In terms of Eq. (3.7), models and observations indicate that $\partial(\overline{Snow})/\partial t$ is negative

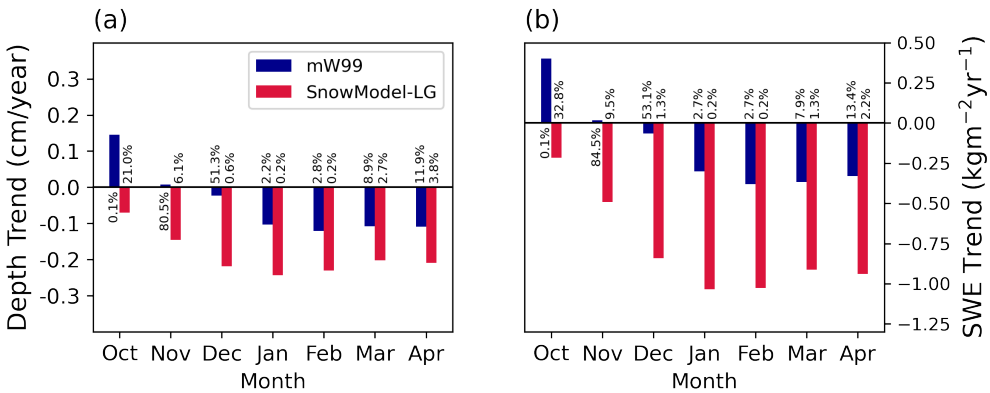

Figure 3.5: Basin-wide spatial average of point-like trends in (a) snow depth and (b) SWE, from mW99 and SnowModel-LG. Calculated for the Envisat-CS2 period (2002-2021). Significance values (in %) are given at the base of each bar. Only October trends for mW99 are significant at the 5% level, whereas significant negative trends exist in SnowModel-LG for December - April.

on long timescales (Webster et al., 2014; Warren et al., 1999; Stroeve et al., 2020a). However, the use of mW99 sets $\partial(\overline{Snow})/\partial t$ close to zero, and to a positive value in October. This has the effect of biasing $\partial(\overline{SIT})/\partial t$ high (and towards zero). Section 3.4.3 examines the effect of using SWE data with a more realistic decline on regional $\overline{SIT}$ trends; this is mediated by the effects of higher interannual variability, which is examined in Sect. (3.4.2).

3.4.2 Realistic SWE Interannual Variability Enhances Regional SIT Interannual Variability

Having illustrated the deficiency of point-trends and point-variability in mW99, we now move on to the impact of snow data on SIT at the regional scale.

We calculate the interannual variability of detrended timeseries of the snow contribution to the thickness determination ($\overline{Snow}$) from mW99 and SnowModel-LG. We display some of these results in Fig. (3.6). We did this for every winter month (Oct-Apr) and for each region defined in Fig. (1). SnowModel-LG data produce more variable timeseries of $\overline{Snow}$ (i.e. higher values of $\sigma^2_{\overline{Snow}}$; c.f. Eq. 3.6). This is the case for all months, in all regions. For snow in the Kara Sea, mW99 introduces almost four times less interannual variability into $\overline{SIT}$ via $\overline{Snow}$ than SnowModel-LG in the April timeseries. This analysis is further broken down by sea ice type in Figs

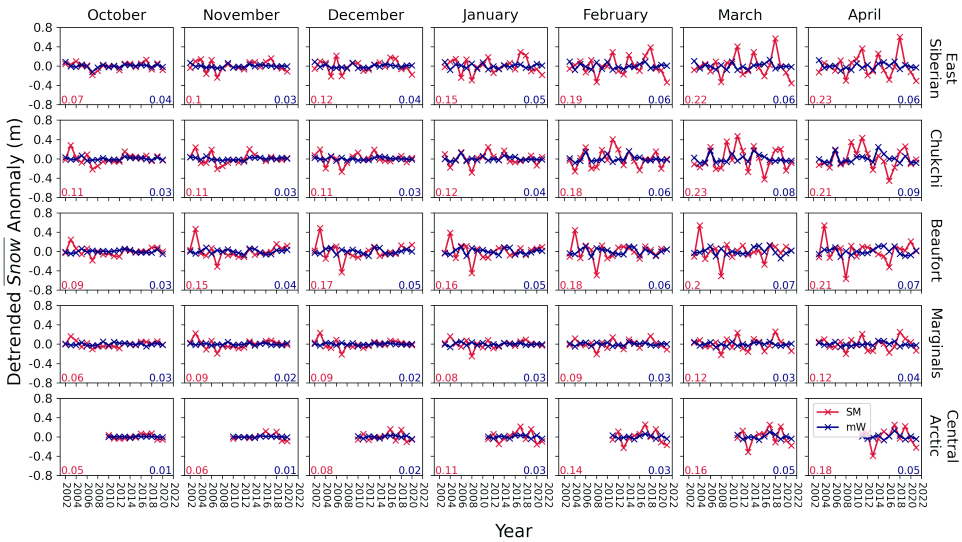

Figure 3.6: Detrended timeseries of spatially averaged snow contributions to sea ice thickness ($\overline{Snow}$) by region from W99 (blue) and SnowModel-LG (red). Standard deviation values are displayed for SnowModel-LG (lower left, red), and mW99 (lower right, blue). All regions are plotted in Supplementary Fig. (S6)

S7 and S8.

Having shown that SnowModel-LG's contribution to $\overline{SIT}$ is more variable than mW99, how does this increased variability propagate into sea ice thickness variability itself ($\sigma^2_{\overline{SIT}}$)? To answer this question, we must examine the way in which the snow contribution to SIT combines with data from satellite radar freeboard measurements. Having calculated the $\sigma^2_{\overline{Snow}}$ term of Eq. 3.6 (displayed in Fig. 3.6), we now turn to the $2\,\mathrm{Cov}(\overline{RF},\overline{Snow})$ term. To assess this we calculate the magnitude and statistical significance of correlations between the detrended $\overline{RF}$ and $\overline{Snow}$ contributions to $\overline{SIT}$ in individual years, regions and months.

To do this we calculated a monthly timeseries of $\overline{RF}$ and $\overline{Snow}$ for each region over the time-period 2002-2021 (with the Central Arctic being 2010-2018). Because we considered eight regions and seven months, this led to to 56 pairs of timeseries for $\overline{RF}$ and $\overline{Snow}$. We then detrended each of them. We then calculated the correlation between each of the pairs of detrended timeseries. We note here that the correlation between the timeseries is dependent on their relative position to a linear regression. These correlation statistics are thus independent of the absolute magnitude of the values, their units, or any linear scaling of the axes. We therefore choose to present

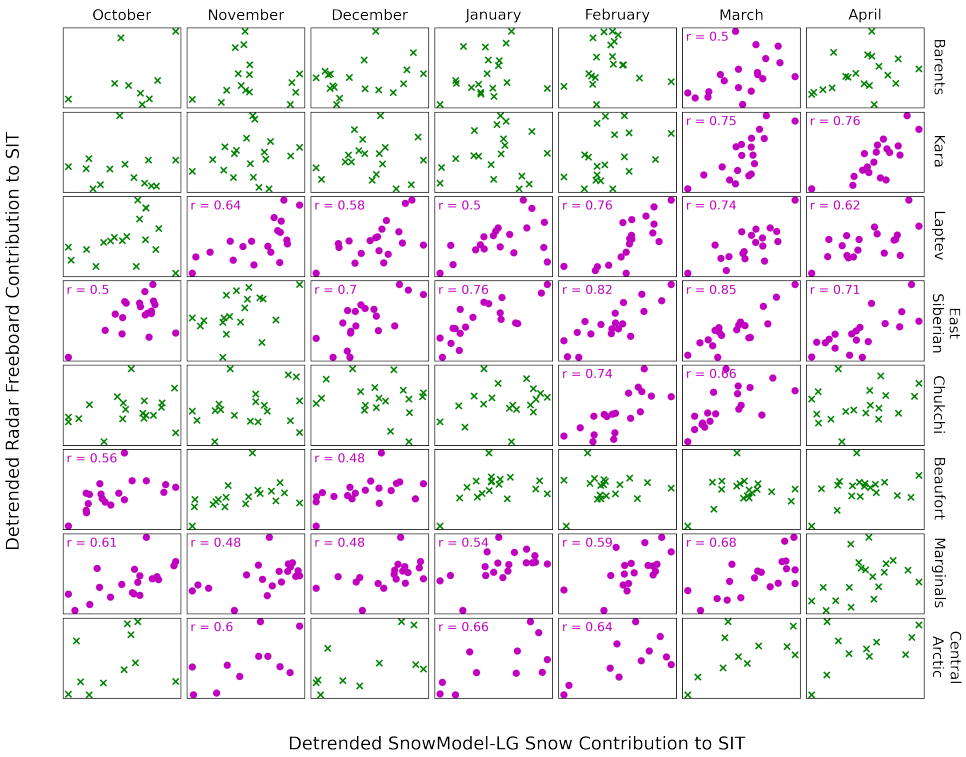

Figure 3.7: Covariability of contributions to sea ice thickness from radar freeboard and SnowModel-LG derived snow components over all sea ice types. Plots are colored with magenta when a a statistically significant correlation is present between the contributions (p¿0.95). Analogous plots are displayed for the FYI and MYI components of the regions in Figs S9 & S10.

the correlations in Fig. (3.7) without axes and scaled to the rectangular panels, so as to best show the relative positions of the points without extraneous numerical information.

We find statistically significant correlations between $\overline{Snow}$ and $\overline{RF}$ to generally range between 0.5 - 0.85 (Fig. 3.7). All statistically significant correlations were positive ones, and this was also the case when individual sea ice types were considered for each region. When all sea ice types were considered, the Laptev and East Siberian seas exhibited statistically significant correlations ($p < 0.05$) in five and six of the seven growth-season months respectively. The Barents Sea, the Beaufort Sea, and the Central Arctic exhibited one, two, and three months of correlation respectively. When analysed as a single, large region, the 'Marginal Seas' area exhibits correlations in six of the seven months analysed, with the strength of these

broadly correlations increasing over the season.

We continued this analysis by breaking down the regions by sea ice type. The area of the Central Arctic sea ice covered with first year ice exhibits relatively strong correlations (0.75 - 0.89) from December - March (Fig. S9). The Laptev sea's first year ice (which is the dominant ice type) exhibits correlations for six of the seven winter months. This figure is five for the East Siberian.

When considering correlations over multi-year ice (MYI), the 'Marginal Seas' grouping exhibits correlations in six of the seven winter months (Fig. S10). The MYI cover of the Central Arctic exhibited no correlations. We note that this analysis is relatively sensitive to the detrending process. When performed without detrending, statistically significant correlations are noticeably more common. This is because $\overline{Snow}$ and $\overline{RF}$ are both in decline in several areas, which introduces an inherent correlation from the trend.

Having identified and quantified regions and months of significant covariance between $\overline{Snow}$ and $\overline{RF}$ (Fig. 3.7), we are in a position to fully answer the question of how the increased variability of SnowModel-LG over mW99 (shown in Fig. 3.6) ultimately impacts $\sigma^2_{\overline{SIT}}$. We plot the three contributing components to $\sigma^2_{\overline{SIT}}$ for each region in each winter month (Fig. 3.8). We note that in the case of negative covariability between $\overline{Snow}$ and $\overline{RF}$, it is possible for $\sigma^2_{\overline{Snow}} + \sigma^2_{\overline{RF}}$ to be larger than $\sigma^2_{\overline{SIT}}$. This is the case for one month of the winter in each of the Kara, Barents and Chukchi Seas. This is not problematic because $\sigma^2_{\overline{Snow}} + \sigma^2_{\overline{RF}}$ does not represent a real quantity when the variables are not independent.

In the marginal seas $\sigma^2_{\overline{Snow}}$ overtakes $\sigma^2_{\overline{RF}}$ to become the main constituent of $\sigma^2_{\overline{SIT}}$ by end of the growth season (Fig. 3.8). This is particularly driven by the behaviour of the Beaufort, Kara and East Siberian Seas, where this relationship is clearly visible. In the Central Arctic $\sigma^2_{\overline{RF}}$ narrowly remains the dominant component of $\sigma^2_{\overline{SIT}}$, throughout the cold season although $\sigma^2_{\overline{Snow}}$ plays an increasing role as the season progresses.

Covariance between $\overline{RF}$ and $\overline{Snow}$ makes relatively constant contributions to $\sigma^2_{\overline{SIT}}$ of the 'marginal seas' grouping in comparison to the other two components,

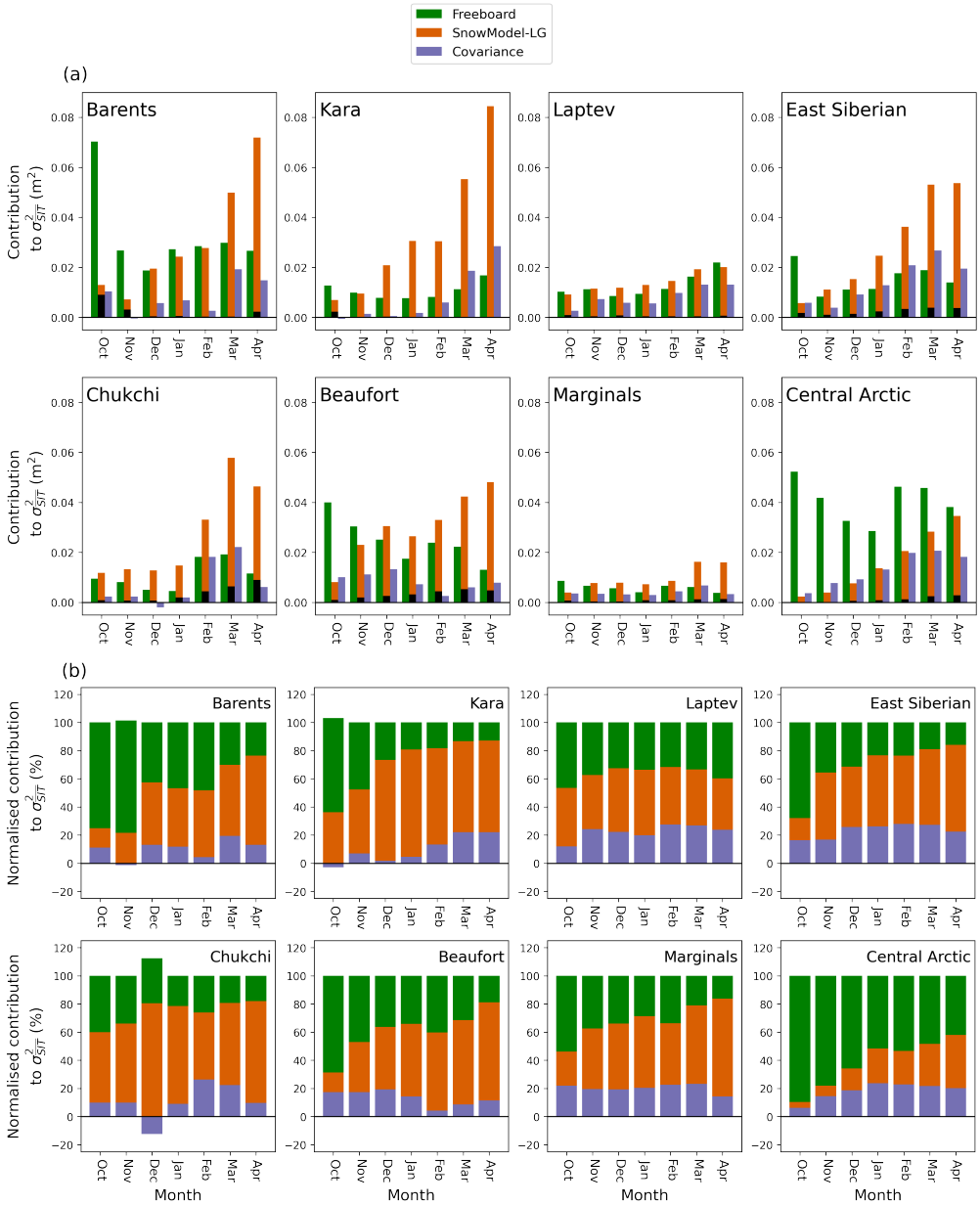

Figure 3.8: Constituent parts of $\sigma^2_{\overline{SIT}}$ of different regions. Bars represent the variance (σ^2) of $\overline{RF}$ and $\overline{Snow}$ and the covariance between the two. (a) illustrates the absolute variance contributions (b) illustrates their relative contributions. The variance of $\overline{Snow}$ in mW99 is indicated in panel (a) by a superimposed black bar. Snow contributes significantly more variability in the late winter than radar freeboard in most of the marginal seas.

but analysis of this grouping conceals more significant variation at the scale of the individual group members. The covariability term of Eq. (3.6) makes a larger contribution than radar freeboard variability itself at times, for example in the Kara and East Siberian seas at the end-of-winter, and for the Chukchi Sea in February and March. For the Central Arctic, the covariability term generally makes less of a contribution to total SIT variability than radar freeboard or snow variability individually, and is negative in the first two months of winter.

Finally, we directly compare the variability of $\overline{SIT}$ itself, when calculated using SnowModel-LG and mW99. We conduct this exercise in both absolute terms (Fig. 3.9a) and as a fraction of the regional mean thickness (Fig. 3.9b).

Calculation of regional SIT with SnowModel-LG reveals higher variability in all marginal seas of the Arctic basin in all months. When the marginal seas are analysed as a contiguous entity, the mean standard deviation is 0.08 m with mW99 and 0.15 m with SnowModel-LG. This represents an increase in $\overline{SIT}$ variability of 91%. For the Central Arctic this figure is considerably smaller, at 41%. When the individual marginal seas are considered, the largest increase was the Kara Sea (147%) and the smallest was the Beaufort Sea (52%).

One key aspect of interannual variability is how it compares to typical values. When IAV is expressed as a percentage of the regional mean thickness, the Barents Sea exhibits the largest increase when calculated with SnowModel-LG: the standard deviation (as a percentage of mean thickness) increases from 15% to 25%. When variability is viewed in this way, the increase in the Central Arctic is small (9.2% to 12.9%). Variability as a fraction of mean thickness is also highest in the Barents Sea when calculated with SnowModel-LG - whereas with mW99 this designation would go to the Beaufort Sea. When analysed as one area, variability (as a fraction of mean thickness) in the marginal seas transitions from being 6.8% of the mean thickness to 13.8% when calculated with SnowModel-LG.

We also note that MYI exhibits more thickness variability than FYI (both absolutely and relative to the sea ice type's mean thickness) in all the marginal seas (Fig. S11). For the marginal seas as a single group, MYI is roughly twice as variable

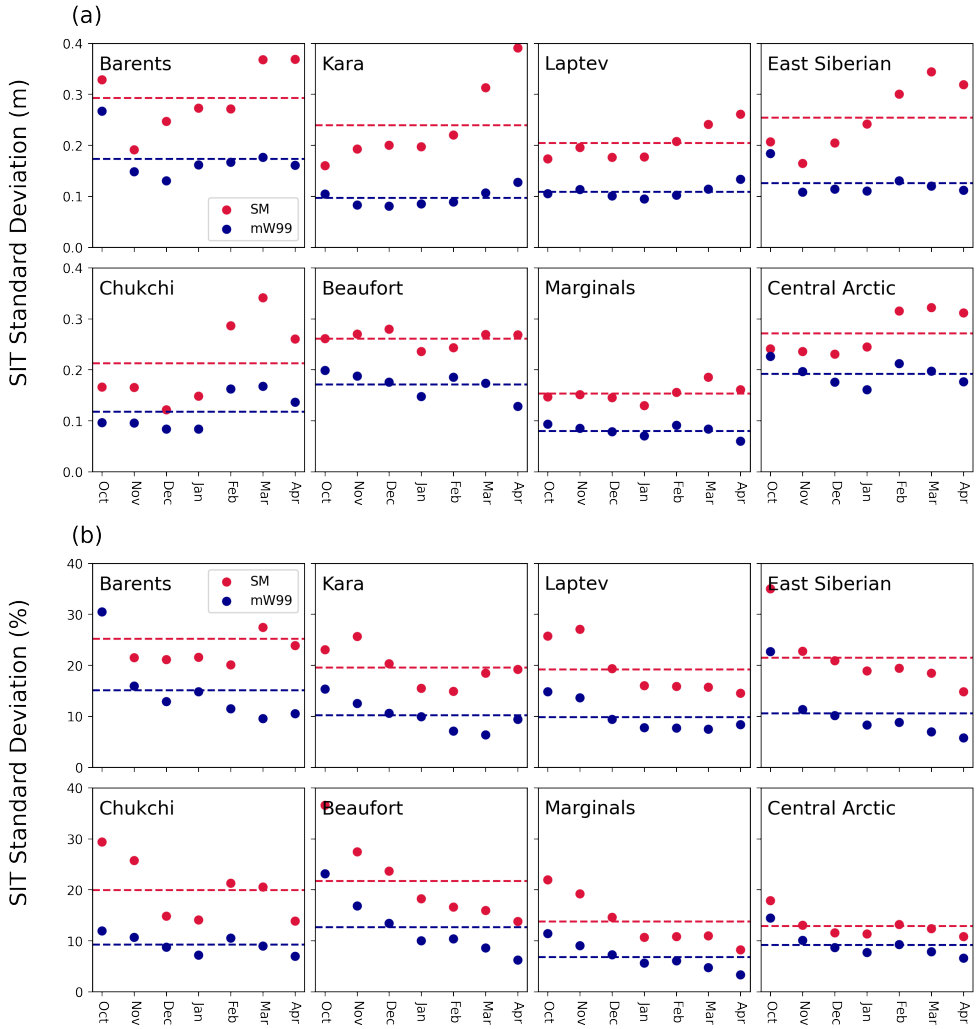

Figure 3.9: Standard deviation in sea ice thickness over the period 2002 - 2021 except for the Central Arctic: 2010-2021 (a) calculated in absolute terms (b) calculated as a percentage of the regional mean thickness over the period. Mean growth-season values shown with dashed lines. The individual detrended regional timeseries from which this figure is synthesised are available in Fig. (S12).

in absolute terms. This is not the case in the Central Arctic, where the thickness variability of the individual sea ice types is highly similar (with FYI IAV slightly larger when calculated relative to regional mean thickness).

3.4.3 New and faster thickness declines in the marginal seas

As well as exhibiting higher interannual variability than mW99, SnowModel-LG $\overline{Snow}$ values decline over time in most regions due to decreasing SWE values year-on-year. Here we examine the aggregate contribution of a more variable but declining

$\overline{Snow}$ timeseries in determining the magnitude and significance of trends in $\overline{SIT}$.

We first assess regions where $\overline{SIT}$ was already in statistically significant decline when calculated with mW99. This is the case for all months in the Laptev and Kara seas, and four of seven months in the Chukchi and Barents sea. The rate of decline in these regions grew significantly when calculated with SnowModel-LG data (Fig. 3.10; green panels). Relative to the decline-rate calculated with mW99, this represents average increases of 62% in the Laptev sea, 81% in the Kara Sea, and 102% in the Barents Sea. The largest increase in an already statistically-significant decline was in the Chukchi Sea in April, where the decline-rate increased by a factor of 2.1. When analysed as an aggregated area and with mW99, the total 'Marginal Seas' area exhibits a statistically significant negative trend in November, December, January and April. The East Siberian Sea is the only region to have a month of decline when calculated with mW99 but not with SnowModel-LG.

We now turn our attention to new trends that stem from the use of SnowModel-LG over mW99 (Fig. 3.10; red panels). Our analysis reveals a new, statistically significant $\overline{SIT}$ decline in the Chukchi Sea in April (taking the number of months with a decline in SIT to six). The analysis of the 2002-2018 period in Mallett et al. (2021) showed that the aggregated Marginal Seas region exhibited two new months of statistically significant declining $\overline{SIT}$ in October and February, taking the total number of declining months from four to six. However the updated analysis (to 2021) for this chapter indicates that statistically significant declining trends are now present in all months for either mW99 or SnowModel-LG for the Marginal Seas aggregated grouping. No months in any individual region exhibited a statistically significant increasing trend in $\overline{SIT}$ (with either snow data set).

The Central Arctic region exhibited a statistically significant thickening October trend with both snow data sets (10 cm/yr and 9 cm/yr with SnowModel-LG and mW99) in the 2002-2018 period. However with our updated analysis (2002-2021), the Central Arctic now exhibits no statistically significant trend in any month.

We also analyse these regional declines as a percentage of the regional mean sea ice thickness in the observational period (2002-2021). We observe the average

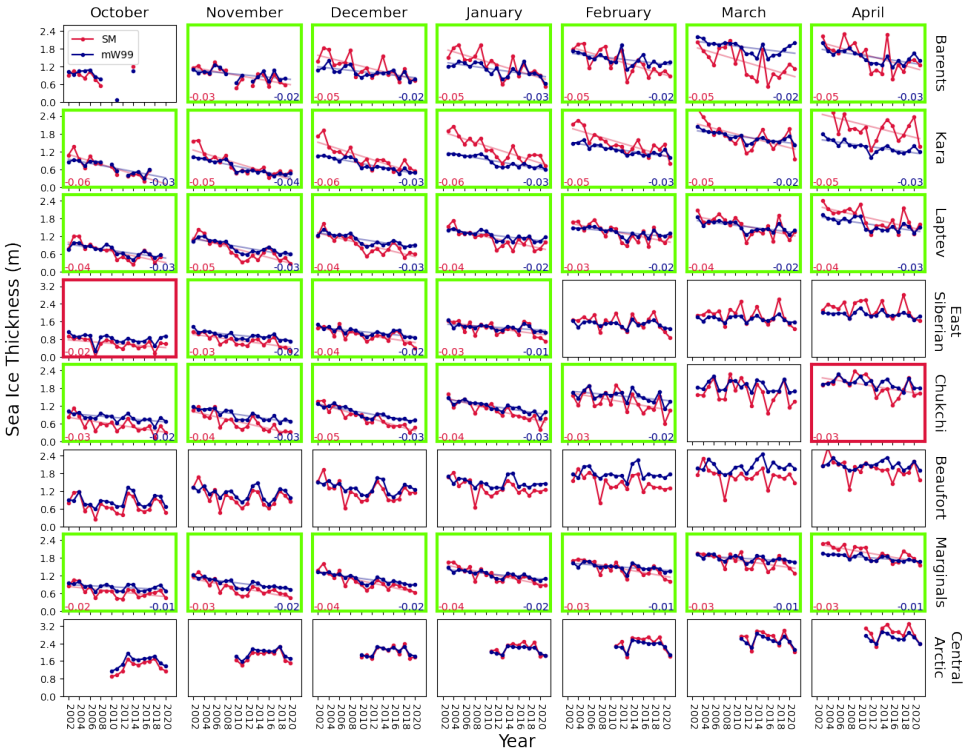

Figure 3.10: Regional $\overline{SIT}$ timeseries calculated using mW99 and SnowModel-LG. Note different y-axis scale for Central Arctic and East Siberian Sea. Panels featuring a statistically significant trend in sea ice thickness when calculated both mW99 & SnowModel-LG framed with green. Red frames indicate where trend is only significant when calculated with SnowModel-LG. Where trends are statistically significant, trend lines are superimposed.

growth-season thinning to increase from 18% per decade to 38% per decade in the Barents Sea, 35% to 49% per decade in the Kara Sea, and 23% to 40% per decade in the Laptev Sea when using SnowModel-LG instead of mW99. Six of the seven growth-season months in the Chukchi Sea exhibit a decline with SnowModel-LG of (on average) 43% per decade. This is much more than that of the five significant months observable with mW99 (24% per decade). We find the Marginal Seas (when considered as a contiguous, aggregated group) to be losing, on average, 28% of its mean thickness per decade in each winter month when SIT is calculated using SnowModel-LG (as opposed to mW99, for which the figure is 13%).

We further analyse these declining trends by sea ice type. This reveals the aggregate trends in the marginal seas to be broadly driven by thickness decline in FYI rather than MYI. We note that the FYI sea ice cover in the Kara and Laptev seas

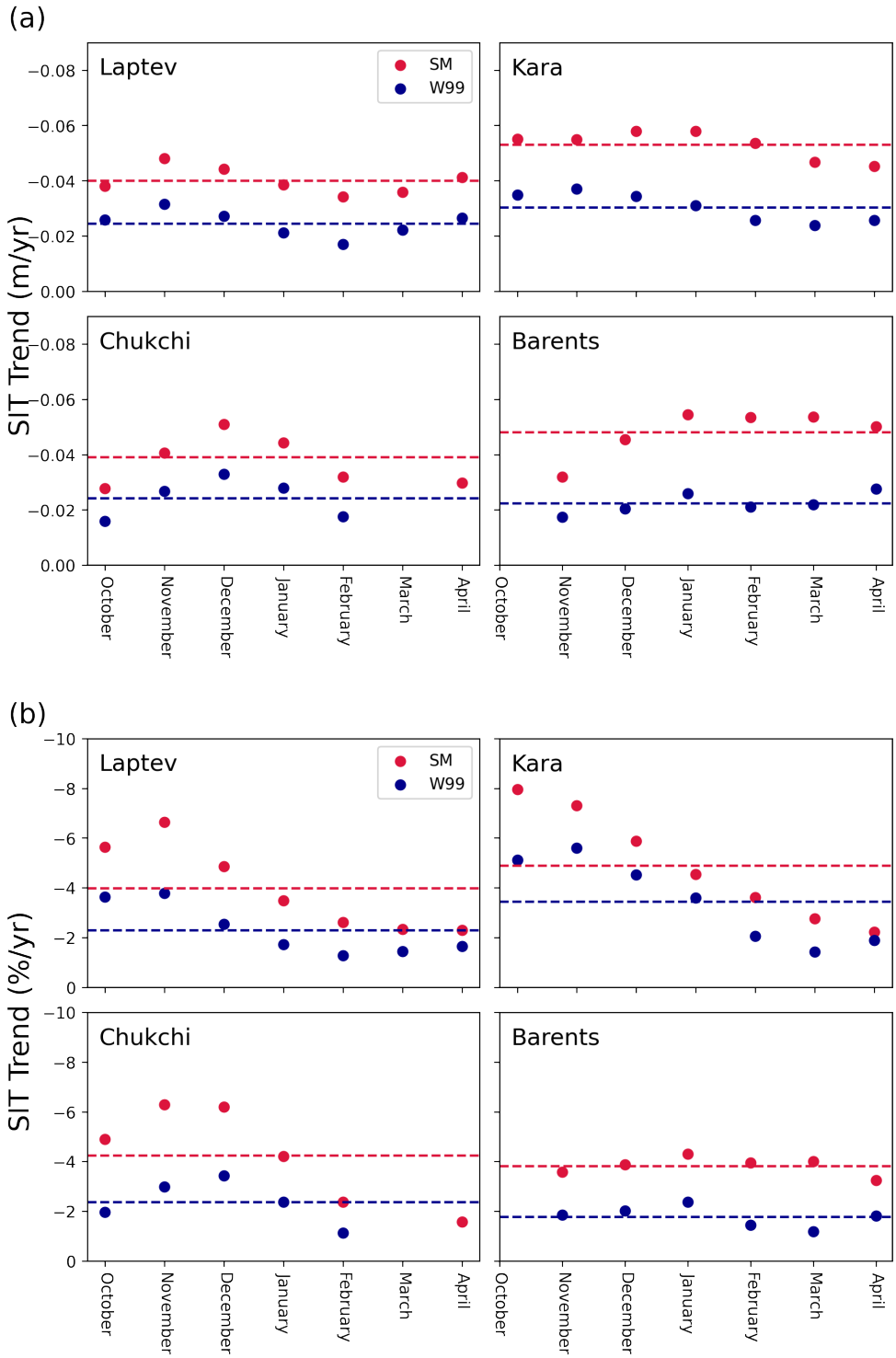

Figure 3.11: Sea ice thickness trends in the four marginal seas that exhibited robust trends in several winter months in the period 2002-2021. Average winter trend (calculated only from statistically significant months) from each snow product shown with dashed lines. Data points are only shown where a statistically significant trend is present for that month and for the relevant snow data.

is in statistically significant decline with either snow product in all months. The FYI cover in the Barents Sea is also in decline for six of the seven winter months when calculated with SnowModel-LG. We find that (when analysed with SnowModel-LG) if any month in a specific marginal sea is in 'all types' decline, its first year ice is also statistically significantly declining.

3.4.4 Changes to the sea ice thickness distribution and seasonal growth

We now consider differences in the spatial sea ice thickness distribution introduced by a snow product with IAV. Because mW99 has low spatial variability in its SWE fields (the quadratic fits are relatively flat), it produces a more sharply peaked and narrow SIT distribution with lower probabilities of thinner or thicker sea ice in the months January - April. The SIT distribution also exhibits some degree of bimodality due to the halving scheme. This bimodality is to a large degree represented in the SnowModel-LG histograms - an encouraging result (Fig. S13).

The regional, seasonal growth rate is also similar when comparing calculations with SnowModel-LG and mW99 (Fig. S14). These rates were calculated over the period 2002-2021 with the exception of the Central Arctic which was restricted to the period 2010-2021. Among the most salient differences are the much smoother seasonal evolution of snow cover in the Barents Sea from SnowModel-LG and the decline in SWE from March to April in the Kara, Laptev and Beaufort seas with mW99 (compared to a continued increase with SnowModel-LG). In the East Siberian and Laptev seas there is clearly a slightly lower seasonal growth rate when calculated with mW99; this is also true to a lesser extent in the Chukchi Sea.

3.5 Discussion

3.5.1 Sensitivity of Findings to Choice of Snow Product

3.5.1.1 Choice of Climatology - Combining AMSR2 with mW99

The most recent sea ice thickness product from the Alfred Wegener Institute (Hendricks and Ricker, 2019) makes use of a new snow climatology, generated by the

merging of W99 with snow depth data derived from the AMSR2 passive microwave record. This is then applied with a halving scheme based on sea ice type in a similar way to mW99 (but with the AMSR2 component not halved). This likely improves the absolute accuracy of snow depths (and thus sea ice thickness), but does not resolve the issues discussed in this chapter involving trends and variability. The modified AMSR2/W99 climatology functions in a very similar way to mW99 - a weak IAV is introduced in areas of interannually fluctuating sea ice type. Any trends will be the result of trends in the relative dominance of sea ice type. This was discussed in Sect. 3.4.1.2 and illustrated in Fig. (S4).

3.5.1.2 Choice of Reanalysis Forcing for SnowModel-LG

Barrett et al. (2020) reviewed precipitation data from various reanalysis products over the Arctic Ocean using records from the Soviet drifting stations, and found the magnitude of interannual variability to be similar. They further broke these data down to the regional scale using the same regional definitions in this chapter, and found that this similarity persisted. Boisvert et al. (2018) conducted a similar analysis with drifting ice mass balance buoys, and found the interannual variability of the data sets to also be similar (although the authors found larger discrepancies in magnitude). These differences in magnitude however cannot be physical (as there is only one Arctic), and Cabaj et al. (2020) were able to bring precipitation estimates into better alignment using CloudSat data with a scaling approach. However this scaling approach preserved the interannual variability of the data sets, which Barrett et al. (2020) and Boisvert et al. (2018) found to be in comparatively good agreement. To investigate how this variability propagates into $\overline{Snow}$ variability, we calculate $\overline{Snow}$ timeseries from SnowModel-LG runs forced by both MERRA-2 and ERA-5 data and find their variability to be very similar (Fig. S15).

With regard to trends, we find that the two different reanalysis forcings generally introduce minimal differences in the SIT trends (Fig. S16). We do however find that small differences in SWE cause the $\overline{Snow}$ contribution of the MERRA-2 SnowModel-LG run to exhibit statistically signficant ($p<0.05$) decline in regions and months where the ERA-5 run does not (with only a small change to the p-value). Analysis of

the absolute $\overline{Snow}$ timeseries reveals them to be otherwise similar (Fig. S17).

We take these clear similarities as evidence that our findings are in principle robust to the choice of atmospheric reanalysis.

3.5.1.3 Choice of Model - Comparison with NESOSIM

Some uncertainty is introduced into the spatial distribution of snow in a given year by SnowModel-LG snow parameterisations and simplifications, such as the lack of snow loss to leads. We therefore repeat our analyses with 2002-2015 data from the NASA Eulerian Snow On Sea Ice Model (NESOSIM; Petty et al., 2018b).

We find that doing this increases the relative importance of snow variability to sea ice thickness variability (Fig. S18). We also observe that the NESOSIM calculations are considerably more similar to those done with SnowModel-LG than with mW99. NESOSIM replicates the increasingly dominant $\sigma^2_{\overline{Snow}}$ contribution to $\sigma^2_{\overline{SIT}}$ over the winter in the Marginal seas, and also replicates the higher contribution of $\sigma^2_{\overline{RF}}$ in the Central Arctic compared to both the individual and aggregated marginal seas. Striking resemblances are seen for the Kara Sea and the East Siberian Sea. Furthermore, the negative covariances for November in the Barents Sea and December in the Chukchi are replicated (albeit with significantly greater magnitude in the Barents Sea). NESOSIM also replicates the negative covariances in October and November in the Central Arctic, but also introduces negative covariance in December (unlike SnowModel-LG).

Because the NESOSIM data is only publicly available from 2002-2015, any underlying trends in the SIT timeseries are more challenging to detect because of the shorter observational period (by comparison to regions where all relevant data is available from 2002-2021). On the other hand, the calculated interannual variability is not reduced by the shorter timeseries, further obscuring any potential underlying trends. But despite these differences, both snow data sets produce statistically significant decline in all months in the Laptev Sea. NESOSIM reproduces six of the seven months of decline in the Kara Sea shown by SnowModel-LG, and three of the five in the Marginal Seas.

Further inspection of the individual data points across all regions and months

reveals good agreement in regional SIT when calculated with either SnowModel-LG or NESOSIM - we take this as evidence that our findings concerning trends and variability over the longer 2002-2021 period are robust to the choice of reanalysis-accumulation model.

3.5.2 Study Limitations

3.5.2.1 Statistical Treatment

We have assumed in calculating single figures for variances that the interannual variability of the systems at hand is time-stationary. It is unclear whether this is the case, as the timeseries are limited in length and time-resolution and thus offer limited scope to test for stationarity. Furthermore we only tested for linear trends, when trends may in fact be non-linear. However, a visual inspection of Fig. (3.10) implies that this approximation is adequate on a qualitative level. Our trend tests also were two-tailed, with the null hypothesis that there was no trend. We could have formulated an alternate test where our null hypothesis was that the trend was positive. This would have given a higher number of statistically significant instances of negative trends, but we deemed this inappropriate as one of the regions (the Central Arctic) does exhibit significant positive trends with the two-tailed test.

3.5.3 Inter-Mission Bias between Envisat and CryoSat-2

An extensive validation exercise for the merged products indicated that although Envisat radar freeboards match well with CS2 freeboards in the Arctic overall, some biases do exist over specific ice types (Kern et al., 2018). In particular, analysis of the inter-mission overlap period indicates that Envisat freeboards were biased low (relative to CS2) in areas dominated by MYI, and high in areas dominated by FYI.

We first make the point that this will have a relatively minimal effect on our findings regarding interannual variability, as $\overline{Snow}$ is unaffected by this and $\sigma^2_{\overline{RF}}$ is likely relatively independent of the absolute magnitude of $\overline{RF}$.

With regard to trends, if Envisat radar freeboards (and thus $\overline{RF}$) are in fact biased high over FYI between 2002-2010 (relative to CS2), then the total trend in many regions dominated by FYI could potentially be smaller than calculated in this

chapter.

We do however add that our findings regarding the impact of declining $\overline{Snow}$ is unaffected by any inter-mission bias in $\overline{RF}$. Because the trend in $\overline{SIT}$ is determined by both $\overline{Snow}$ & $\overline{RF}$, the trend in $\overline{SIT}$ will always be more negative when calculated with downward trending data for $\overline{Snow}$.

3.5.3.1 The Effects of Incomplete Radar Penetration of the Snowpack

This investigation has been carried out within the paradigm of total Ku-band radar wave penetration of the snow cover (as suggested by Beaven et al. (1995)), however some in situ investigations have cast doubt on this. The issue was highlighted in an Antarctic context by Giles et al. (2008b) for ERS radar freeboards, and it was shown subsequently that significant morphological features in the snowpack (e.g. depth hoar, wet snow or crusts) enhanced radar scattering from within the snowpack (Willatt et al., 2010). For the Arctic, Willatt et al. (2011) found that airborne Ku-band radar backscatter in the Bay of Bothnia was returned from nearer the snow-ice than snow-air interface in only 25% of cases when the temperature was close to freezing, the figure increasing to 80% at lower temperatures. Nandan et al. (2017) observed that the presence of brine in the base of the snowpack can raise the scattering horizon by several centimeters. However, these investigations were often (but not exclusively) carried out at the end of the winter season or in the Sub-Arctic, when warmer temperatures may have increased the snow's brine volume fraction and diurnal forcing can drive rapid snow metamorphism. Both of these factors will be less prevalent in the colder months of winter. This analysis is therefore carried out using the imperfect historical assumption present in publicly available sea ice products (that of total penetration).

What would the effects of incomplete penetration of the snowpack be on our findings? As the height of the primary radar scattering horizon rises through the snow, the altimeter operation transitions from that of a radar altimeter to that of a lidar altimeter. Knowledge of overlying snow contributes positively to the inference of SIT in the case of a radar altimeter (i.e. the coefficient of m_s term of Eq. 3.3 is

positive). However, the influence of overlying snow on lidar-based SIT estimates is negative (i.e. the presence of more snow for a given measured radar freeboard implies less underlying sea ice). As the scattering horizon rises through the snowpack, the SIT contribution of snow therefore decreases, reaches zero (in the top half of the snowpack, the exact location depending on snow density) and proceeds to negative values. The result of potential incomplete penetration for our study is that the magnitude of the reported trend and variance underestimations is diminished. Were our investigation based on a similarly long timeseries of lidar freeboards combined with a snow climatology, one of our conclusions would be that diminishing snow cover is leading to *overestimation* of rates of decline in the marginal seas.

We finally note the potentially confounding influence of negative freeboard in regions such as the Atlantic sector of the Central Arctic region and the Barents Sea. In the case of high snowfall and low sea ice thickness, the sea ice surface can be depressed to the waterline or below. Beyond this point Eq. (5) no longer functions. The prevalence of negative freeboards has been studied by Rösel et al. (2018) and Merkouriadi et al. (2020), but has yet to be incorporated into any radar-altimetry based sea ice thickness retrievals. This situation can be driven by storm tracks entering the Arctic from the Atlantic (but also the Bering Strait). These intrusions of warm air can also drive snow grain metamorphism, which may well affect radar penetration through the snowpack.

3.5.4 The Impact of Enhanced Variability from SnowModel-LG

When used instead of mW99, SnowModel-LG data increases the interannual variability of $\overline{SIT}$ in the marginal seas by more than 50%. The main way that this occurs is though increasing $\sigma^2_{\overline{Snow}}$ values (Fig. 3.6). The second and less significant way that $\sigma^2_{\overline{SIT}}$ is increased is through some positive correlations between $\overline{Snow}$ and $\overline{RF}$ values for individual months in some regions (Fig. 3.7). Because the two timeseries are positively correlated in some cases, $\sigma^2_{\overline{SIT}}$ is increased; for the Marginal Seas region this covariance term makes up around 15-20% of $\sigma^2_{\overline{SIT}}$ (Fig. 3.8).

While values for interannual variability are given in W99, it was previously impossible to apply those values to either a given year or to fulfil Eq. (3.6). SnowModel-

LG offers similar variability to the SWE statistics given in W99 (Fig. 3.3), and can generate a yearly timeseries of values. Furthermore it can be combined with radar freeboard data to generate all terms of Eq. (3.6) for a direct calculation of $\sigma^2_{\overline{SIT}}$.

Comparing our IAV values to the literature is challenging due to differences in the area over which other authors have calculated IAV values. Haas (2004) investigated the interannual variability of an area within the Transpolar Drift in the Central Arctic and Northern Barents Sea, and found a 0.73 m standard deviation. This is considerably higher than the values determined in this study, although this data was collected by electromagnetic sounding in late summer over a ten year period that does not overlap with this analysis. Laxon et al. (2003) defined a 'region of coverage', which essentially consisted of the marginal seas considered in this analysis with the addition of some areas of the Canadian Archipelago and the Greenland sea. The authors found a variability of 0.24 m using W99 in this region of coverage over an eight year timescale. Unlike Haas (2004), this value is lower than our findings using either mW99 or SnowModel-LG. Similar to Haas (2004), the time period is considerably shorter and the geographical area is not identical. Finally, Rothrock et al. (2008) found interannual variability in SIT to be 0.46 m over a twenty-five year period (1975-2000), using submarine records from a variety of Arctic regions. It is likely that the values in these studies differ due to the unequal spatial extent over which the IAV was calculated; averaging over a larger area reduces the IAV due to the averaging out of local anomalies.

3.5.5 The Impact of New and Steeper Trends in Mean Sea Ice Thickness

The replacement of multiyear ice with first year ice has been documented to be reducing Arctic-mean SWE on sea ice in spring (Webster et al., 2014). However, progressively later freeze-ups in the Arctic are also likely driving a reduction in mean SWE in the early cold-season. This is because sea ice covers a relatively smaller area in the high precipitation months of September and October. When the sea ice area then expands with the progression of the growth-season, the newer sea ice has not been exposed to this snowfall. This mechanism is not accounted for in mW99, and

as such snow depths do not decrease at a statistically significant level in any month.

In this study we have assessed how these negative trends in $\overline{Snow}$ propagate through into trends in $\overline{SIT}$. In every area where a statistically significant decline in radar freeboards is observed, a statistically significant decline in SnowModel-LG SWE is also observed (Fig. S19). In addition to this, SnowModel-LG also exhibits $\overline{Snow}$ decline in other months in the Beaufort and Barents Sea. As such, reductions in $\overline{Snow}$ usually act in concert with observed reductions in $\overline{RF}$, amplifying decline in $\overline{SIT}$. This relationship is illustrated by the fact that several months in several regions do not exhibit either a statistically significant decline in $\overline{RF}$ or $\overline{Snow}$ (Fig. S19), but despite this they do exhibit decline in $\overline{SIT}$ (Fig. 3.10). We note here that this 'co-decline' in $\overline{Snow}$ and $\overline{RF}$ is separate to the covariability presented in Sect. 3.4.2 and Fig. 3.7, as that was calculated from detrended data.

Because SnowModel-LG data feature a steeper decline in $\overline{Snow}$ than mW99, a steeper decline is observed in the $\overline{SIT}$ of several regions. However, SnowModel-LG $\overline{Snow}$ contribution to $\overline{SIT}$ also exhibits significantly more variability, which acts to reduce statistical significance of $\overline{SIT}$ trends. Despite this compensating effect, the statistical significance of trends in $\overline{SIT}$ were generally greater than those calculated using mW99. Furthermore, statistically significant trends emerged in new months and new regions.

Kwok and Rothrock (2009) analysed 42 years of submarine records and the five year ICESat record. However, it is challenging to draw comparison with our results, as trends were gleaned from submarine track crossings and by comparing the thickness difference between the period of submarine observation and that of ICESat observations. Difficulty in comparison is further compounded by differences in regional designation and the area of the submarine data release (which is generally confined to the Central Arctic region where the radar altimetry timeseries is at best limited to the CryoSat-2 era). This is also the case for the updated analysis of Kwok (2018), who seasonally adjusted mean thickness values to match crossover points in submarine tracks in time and space.

Our findings of enhanced interannual variability and steeper decline have im-

plications for Arctic stakeholders and the deployment of human infrastructure. The marginal seas are heavily used for the shipping of goods along the Northern Sea Route in summer (Eguíluz et al., 2016) and provide the setting for potential extraction of natural resources (Petrick et al., 2017). Furthermore, the season during which vessels may traverse the Northern Sea Route is lengthening. Higher variability in sea ice thickness may pose a challenge to the planning of this seasonal travel, particularly with regard to the need for ice-strengthened escorts for conventional vessels (Melia et al., 2017; Cariou et al., 2019). The enhancement of declining trends where they exist is perhaps of benefit these industries.

3.5.6 The interannual relationship between radar freeboard and snow depth

We finally consider the physical mechanisms behind positive or non-significant correlations between $\overline{Snow}$ and $\overline{RF}$ displayed in Fig. (3.7). Assuming total radar penetration of the snow cover, as snow accumulates on sea ice it should lower the local radar freeboard by a distance on the order of half its accumulated height (Eq. 3.4). This lowering is a result of physical depression of the sea ice surface and an increase in the radar ranging due to slower radar wave propagation in snow (in approximately a 60:40 ratio). Over short time scales (days to weeks), this would result in a negative correlation between local snow depth and local radar freeboard. This corresponds to a negative covariability term in Eq. (5) and is represented by purple bars in Fig. (3.8). Negative values are generally not seen, with the exception of October and November in the Central Arctic, November in the Barents Sea and December in the Chukchi and Kara seas. Furthermore, snow is a highly insulating material and its accumulation limits sea ice thermodynamic growth. This would also bring about a negative correlation between snow depth and radar freeboard, lagged over a period of weeks.

The lack of negative correlations between $\overline{RF}$ and $\overline{Snow}$ from year to year is likely indicative of the timescale of our analysis. If present, the negative correlation implied by Eq. (3.4) and the mechanisms above must only be present on shorter timescales (e.g. days). So what drives the positive correlations between $\overline{RF}$ and

$\overline{Snow}$ where they exist? One driver over FYI is likely sea ice age. Sea ice formed at the beginning of the season has a longer time to (a) grow thicker, and (b) accumulate snow. Both variables are therefore likely controlled by regional freeze-up timing, explaining the correlation. The combined evolution of $\overline{Snow}$ and $\overline{RF}$ anomalies as a function of regional freeze-up timings is likely to be the subject of future study. The relationship between MYI radar freeboards and accumulated SWE may also form an avenue for further study.

3.6 Summary

In this chapter we used a novel approximation for the slowing of radar waves in snow to decompose the conventional method for estimating sea ice thickness into two contributions: one originating from radar freeboard data (from satellite altimeters), the other from snow data of varying provenance.

This allowed a regional assessment of the conventional impact of snow on variability and trends in sea ice thickness. We then used a new snow data set (from SnowModel-LG) with a more realistic magnitude of interannual variability and trends to calculate the regional sea ice thickness timeseries.

We found that interannual variability in average sea ice thickness ($\sigma^2_{\overline{SIT}}$) of the marginal seas was increased by more than 50% by accounting for variability in the snow cover. On a seasonal timescale we find that variability in the snow cover makes an increasing contribution to the total variability of inferred sea ice thickness, increasing from around 20% in October to more than 70% in April.

We also observed that the trends in SnowModel-LG data propagated through to the SIT timeseries, amplifying decline in regions where it was already significant, and introducing significant decline where it did not previously exist. This occurred in spite of the compensating effect of enhanced interannual variability.

Chapter 4

A simple model for the sub-kilometre snow depth distribution derived from transect data

This chapter is based on the following publication:

Mallett, R.D.C., Stroeve, J.C., Tsamados, M., Willatt, R., Newman, T., Nandan, V., Landy, J.C., Itkin, P., Oggier, M., Jaggi, M. and Perovich, D.K. (2022). Sub-kilometre scale distribution of snow depth on Arctic sea ice from Soviet drifting stations. Journal of Glaciology, 1-13

4.1 Introduction

This importance of snow on sea ice was introduced in Chapter 1, and its key role in altimetry was explored in Chapters 2 & 3. This role in particular has driven the development of a range of modelling and remote sensing approaches to accurately characterise the snow cover (see Zhou et al., 2021, for intercomparison of several products). Satellite remote sensing approaches (e.g. Rostosky et al., 2018; Lawrence et al., 2018) are generally limited by their low (multi-kilometre) spatial resolution, which has the effect of averaging out kilometre and sub-kilometre scale variability.

Modelling approaches (e.g. Petty et al., 2018b; Liston et al., 2020; Stroeve et al., 2020a) have similar limitations, with grid resolutions not falling below tens of kilometres. This in part reflects the coarse spatial resolution of standard atmospheric reanalysis and sea ice drift products.

This lower-bound on spatial resolution is a significant barrier to scientific progress, as the effects of snow on fluxes and sea ice thickness retrievals cannot be characterised solely by the mean snow depth in a grid-cell of a traditional data product (Iacozza and Barber, 1999). To account for the observed variability of snow depth on scales below a grid-cell (e.g. Farrell et al., 2012), a *sub-grid* scale snow depth distribution must be employed (see Petty et al., 2020; Glissenaar et al., 2021, for impacts on sea ice thickness retrievals). For instance, the amount of shortwave solar radiation incident on the ice surface in a multi-kilometre grid cell is sensitive to the fractional coverage of snow that is *optically thin* ($<\sim 0.15$ m for dry snow; Warren, 2019). This area cannot be straightforwardly gleaned from modelling or satellite observations of the mean snow depth in the grid cell (Stroeve et al., 2021).

In the example above, the area of optically thin snow within a larger area of snow with given mean depth will be primarily dictated by wind redistribution (Moon et al., 2019). Snow is dynamically transported through wind suspension and saltation and is eroded and deposited heterogeneously around any ice topography such as ridges and hummocks (Sturm et al., 2002a; Chung et al., 2011). Furthermore, turbulence-induced features such as sastrugi introduce depth variability even on level ice (Eicken et al., 1994; Massom et al., 1997). The probability of snow transport and redistribution is dependent on its bulk and microstructural properties such as density and bond-radius (Filhol and Sturm, 2015). The combination of these factors makes deterministic modelling of snow redistribution a major challenge when the local ice topography is not known to a high level of detail (e.g. Liston et al., 2018), which is generally the case on sea ice. Because of this limitation on deterministic modelling, in this chapter we instead aim to derive a statistical model for the snow depth distribution. The model is trained on the large number of snow depth measurements taken at Soviet drifting stations, and requires only the mean snow depth to generate

a distribution.

4.1.1 Snow transects from Soviet drifting stations

We analyse the results of snow depth transects performed at Soviet North Pole (NP) drifting stations between 1955 and 1991 (Figures 4.1 & 4.2). These were crewed stations that drifted year-round in the Arctic Ocean while measuring a range of atmospheric, oceanographic and cryospheric parameters on what was generally multi-year sea ice. In particular we examine 33539 snow depth measurements from 499 transects from NP stations 5 - 31. Snow transects did not begin until NP 5, and the NP program was halted in 1991. While it was restarted in 2003, these data are not publicly available.

Snow depths were measured every 10 m along a line of either 500 or 1000 m in length when snow depth was at least 0.05 m and more than 50% of the surrounding area was snow covered based on a qualitative assessment. 166 transects were around 500 m long and 333 were around 1000 m long, with transects prior to 1974 generally being 500 m long (Fig. 4.2b). The vast majority of transects were of the exact length specified above, however around 6% of transects were slightly shorter by around 10%: it is unclear why this was the case, however the operational challenges of Arctic research (e.g. ice dynamics, polar bears, severe weather) may explain this. The direction of the line was chosen randomly but did deviate where hummocks were present, and was at least 500 m from the station at its closest point. We note that this deviation around hummocks may introduce a bias in the snow depth measurements to sample more level ice with thinner snow. Where successive transects were taken at the same station, each was offset by 3 m from the previous line. This was do avoid the disturbance of snow caused by walking along the snow line (Warren et al., 1999).

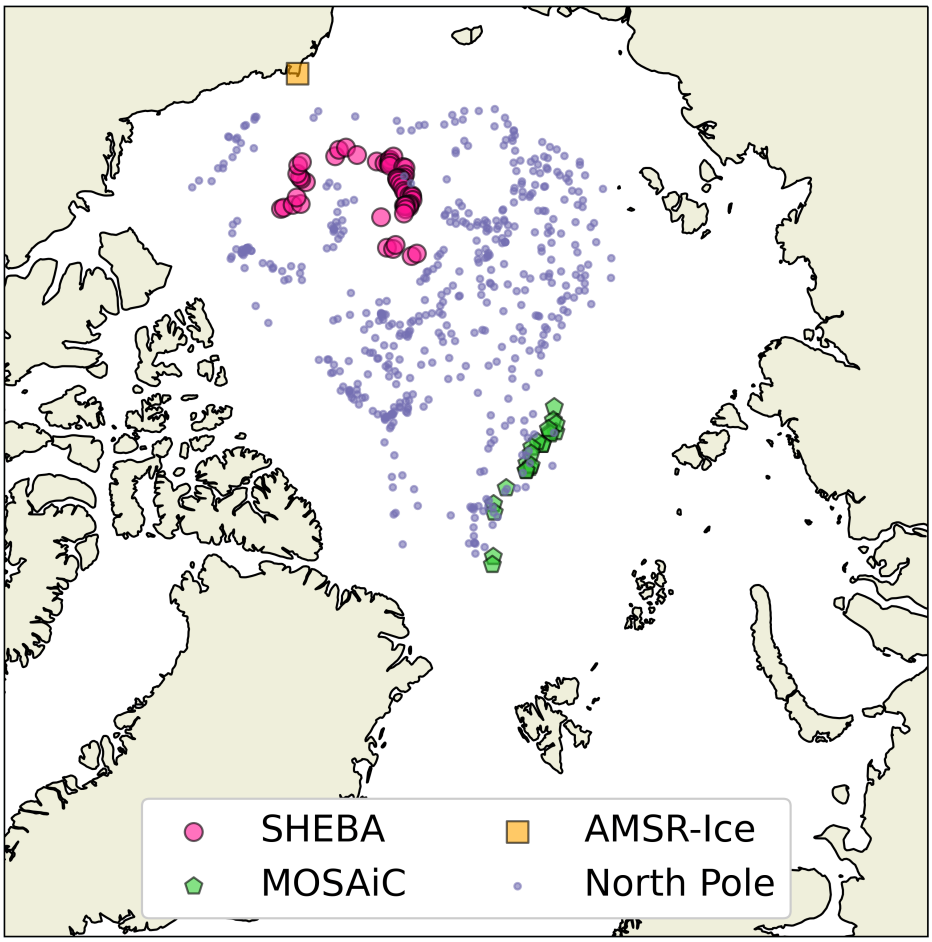

Figure 4.1: Map indicating the locations of snow transects used in this study. Small purple dots indicate locations of transects taken at Soviet North Pole drifting stations. Pink circles and green pentagons indicate transects taken on the SHEBA and MOSAiC expeditions respectively. Orange square indicates the locations of the AMSR-Ice transects, which would not be individually well-resolved on the map.

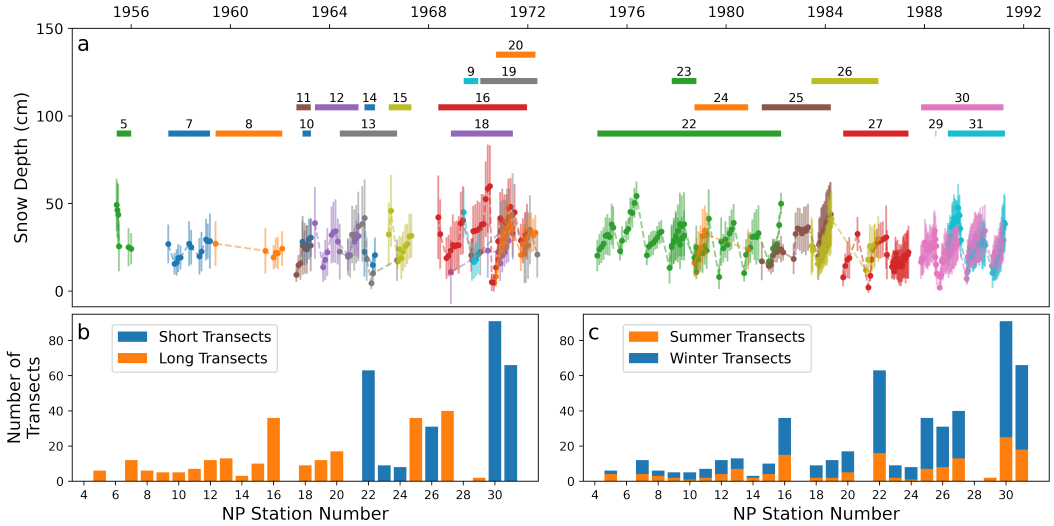

Figure 4.2: (a) Operational periods of the Soviet 'North Pole' (NP) stations contributing to this study. Bars at top indicate the time period between the first and last snow depth transect of the station. Solid circles indicate mean snow depth of transects, with vertical bars indicating one standard deviation in snow depth (b) The number of transects measured by each station, broken down by transect length (500m vs. 1000m). (c) Number of transects measured by each station broken down by summer (May-Sep) and winter (Oct-Apr).

4.2 Method

We now present a method for transforming an estimate of mean snow depth (from remote sensing or modelling) into a distribution of snow depths. We first characterise the linear relationship between the standard deviation of snow depths measured along a transect and the mean of that transect (Fig. 4.3a). This ratio is known as the coefficient of variation (CV; Brown, 1998). When a linear regression is performed (and forced through the origin), the root-mean-square of the residuals is 0.032 m, meaning that the standard deviation of the transect depths can be predicted with this standard-error where the mean is known. For every 1 m increase in the mean snow depth, we find the standard deviation of the snow depths to increase by 0.417 m.

$$\sigma_D = 0.417 \times \overline{D} \tag{4.1}$$

where σ_D is the standard deviation of snow depth in a transect, and $\overline{D}$ the mean depth of the transect. In the above equation 0.417 represents the coefficient of variation. This was calculated using all depth 33,539 depth measurements in all seasons, and the relationship is strongest June - August and weakest December - March (Fig. S28). All NP station snow depth measurements are then converted into depth-anomalies from their respective transect means. We then divide all measurements by the standard deviation of their respective transects. These anomalies can then be plotted as one distribution (Fig. 4.3b). To this distribution we fit a skew normal curve.

Our skew normal distribution function is defined following O'Hagan and Leonard (1976) and Azzalini and Capitanio (1999) such that:

$$f(a,\xi,\omega,\sigma_D) = \frac{1}{\omega\sqrt{2\pi}}\left(1+\mathrm{erf}\left(\frac{ax}{\sqrt{2}}\right)\right)e^{-\frac{x^2}{2}} \quad \text{where} \quad x = \frac{\sigma_D - \xi}{\omega} \tag{4.2}$$

with a being the skewness parameter, ξ being a location parameter, ω being a scaling parameter, and erf being the error function. Through fitting a skew normal curve using the technique of maximum likelihood estimation (Richards, 1961), we

find the best-fit values of the three parameters to be a = 2.54, ξ = -1.11, ω = 1.50.

We repeat this process for the winter and summer seasons individually (October-April, May-September). While coefficient of variation is slightly larger in summer (Fig. 4.3c), the shape of the summer probability distribution does not depart greatly from the winter distribution (Fig. 4.3d). This seasonal difference in the coefficient of variation is relatively small compared to the uncertainty and residuals in the regression, and as such we opt for a singular analysis, considering all transects from all months. Here we point out that in summer a measurement bias is introduced in the form of a 'surface scattering layer' (e.g. Polashenski et al., 2012), which forms at the snow-ice interface and can be penetrated by a probe despite being formed of ice rather than snow. Because this would theoretically increase the mean but not the standard deviation of depth measurements along a transect, it would introduce a low-bias on the CV in summer. In reality, we see the summer CV being larger than in winter.

A full breakdown of Fig. 4.3 by the four meteorological seasons is given in Supplementary figures S28 & S29. The coefficient of variation appears appropriate for all four seasons (Fig. S28), although it is slightly too high in September/October/November, and slightly too low in March/April/May (relative to the annual mean in Fig. 4.3a). It is noticable also that the correlation between a transect's mean depth and its standard deviation is stronger in the six months of June - November (compared to December - May). This is contrast to the fit of the skew-normal distributions in the individual seasons (Fig. S29), where the six month December - May matches the annual mean better than June - November. In particular, the September/October/November distribution is more skewed than the 'Full Year' distribution, and the skew-normal fit appears to not be entirely appropriate for March/April/May data.

The above method allows the standard deviation of the snow depth to be estimated from the mean snow depth (Fig. 4.3a). When both of these quantities are known, a statistical model for the snow depth distribution may be calculated using the skewed normal curve shown in Fig. 4.3b.

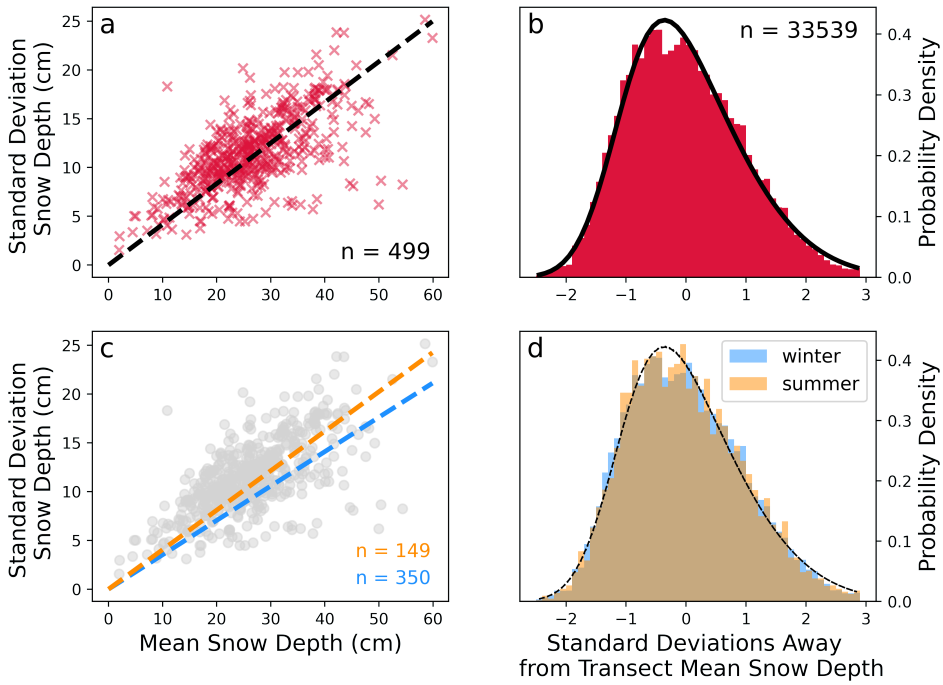

Figure 4.3: **(a)** Relationship between a transect's mean snow depth and the standard deviation. The slope of the regression (forced through the origin) is 0.417, the root-mean-squared-residual is 0.032 m, and the Pearson correlation coefficient (r value) is 0.66. A visualisation of the point density of this panel is given in Supplementary Fig. S27. **(b)** The probability density of a snow depth being measured such that it is a given number of standard deviations from the mean of the transect. The empirical distribution is given in red from drifting station data and a skew normal curve is fitted in black. **(c)** Same as a, but with individual regressions for winter and summer transects. **(d)** same as b, but with individual probability density distributions for winter and summer transects. The two seasonal skew normal fits (black) are visually indistinguishable.

For instance, if the mean snow depth is assumed to be 0.5 metres, then the standard deviation of the snow depth distribution is estimated using Eq. 4.1 such that $\sigma_D = 0.209$ m $\pm$ 0.032 m. Transforming the x coordinates of the distribution in Fig. 4.3b from units of standard deviations to units of snow depth (using the coefficient of variation), it can be inferred (for example) that the probability of randomly sampled snow of depth less than 0.3 m is 17%, and the chance of sampling snow deeper than 1 metre deep is 1.8%.

For calculations of light flux through thin snow, it may be found that for snow with a mean depth of 0.5 m, the probability of snow depth being less than 0.15 m is 2.3%. In contrast, this probability for snow with a mean depth of 0.25 m is 16.6%.

4.2.1 Choice of Skew Normal Distribution

Several authors have characterised terrestrial snow depth distributions with other curves than the skew normal, such as log-normal (Donald et al., 1995; Pomeroy et al., 1998; Marchand and Killingtveit, 2004) or gamma distributions (Skaugen, 2007; Egli et al., 2012). Luce and Tarboton (2004) and Kuchment and Gelfan (1996) applied both, with the latter finding the log-normal distribution to provide a superior fit. However, this comparison was over a significantly larger area (basin-scale rather than sub-kilometre). In contrast, Skaugen and Melvold (2019) and Gisnas et al. (2016) observed that the gamma distribution offered an improved fit over a log-normal fit.

We find that the skew normal curve provides a marginally better fit to the data than both the log-normal and gamma distributions (Fig. 4.4). We first characterise the goodness of fit of these distributions using the one-sample Kolmogorov-Smirnov test. The test statistics for all three distributions result in extremely small p-values, indicating that none of the distributions fully capture the observed data. However, the test statistic is largest for the gamma and smallest for the skew normal distribution, with the p-value being smallest for the gamma distribution, and largest for the skew normal distribution. This indicates that the skew normal distribution is the best of the three fits to the data, and the gamma the worst. For completeness, we also calculate the RMSE of the observations against the best-fit of all three distributions in bins of 0.1 standard deviations of snow depth. We again find that the skew normal curve performs best, and the gamma distribution worst (Fig. 4.4b). We note that that the improved performance of the log-normal fit over the gamma distribution is not a contradiction of previous work with the opposite findings (e.g. Skaugen and Melvold, 2019; Gisnas et al., 2016), as these studies concerned terrestrial environments where meteorological forcing, surface topography and snow properties are different.

All three of the above distributions have the same number of fitting parameters. Because of the superior goodness-of-fit, we therefore use the skew normal distribution in this chapter. However, we also provide the best-fit parameters for the log-normal and gamma distributions in the supplementary material.

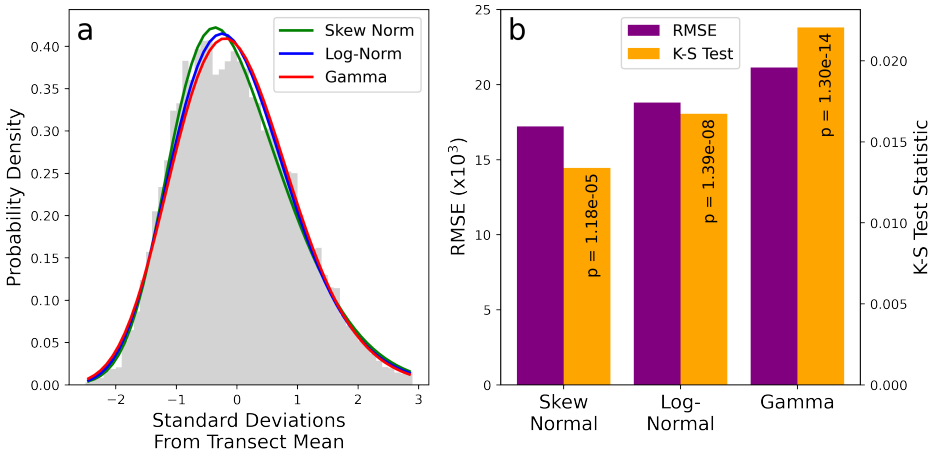

Figure 4.4: (a) The best-fit curves of the skew normal, log-normal and gamma distributions. The log-normal and gamma distributions have historically been fitted to terrestrial snow depth distributions, however we find that the skew normal distribution provides a superior fit to our data. (b) The RMSE and one-sample Kolmogorov-Smirnov test statistics. Both metrics for goodness of fit indicate that skew normal has the best fit, and gamma the worst. The quantities of Probability Density, RMSE and the K-S Test statistic have the same units as the number of standard deviations, which is unitless.

4.3 Results

4.3.1 Cross-validation

We now evaluate the consistency of our snow depth distribution model with a leave-one-out-cross-validation (LOOCV) approach (Stone, 1978). To do this we select a single transect and recalculate the skewed-normal curve using the remaining 498 transects. We then assess the goodness-of-fit of the curve against the selected transect. This is performed iteratively for each transect such that 499 goodness-of-fit statistics are generated. We calculate the goodness-of-fit using the root-mean-square error (RMSE) for the fitted probability distribution and that of the transect, using ten equal-width depth bins that span from 0 m to the maximum depth measured.

This cross-validation exercise allows for the estimation of model skill as a function of different variables, such as the transect's length, its mean depth and the month in which it was performed (Fig. 4.5a - c). We also investigate whether the snow depth distribution of a transect can be better predicted with the NP Station based model presented here (the 'NP model') when its corresponding station has

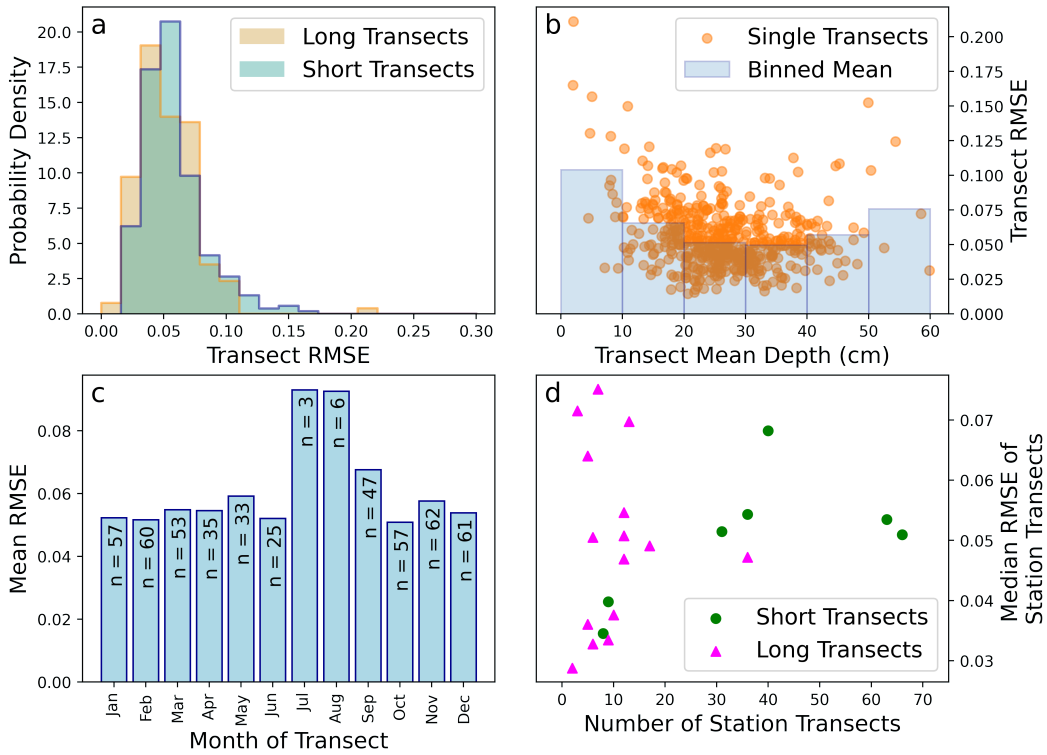

Figure 4.5: (a) Histograms of the RMSE for long transects (1km) and short transects (500m) separately. (b) RMSE of the NP distribution against observed transects shown as a function of transect mean depth. (c) NP distribution RMSE as a function of month. 'n' indicates the number of transects contributing to the model from that month (d) Mean RMSE of all transects at a given station, shown as a function of the number of transects at that station. RMSE values are unitless as they represent the error in a probability distribution.

contributed many other transects to the distribution (Fig. 4.5d).

We first show that the NP model's skill is very similar when applied to both long and short NP transects (Fig. 4.5a). The mean RMSE for long and short transects is 0.053 and 0.057 respectively (a difference of 7%). This similarity is to be expected, with the difference likely reflecting the more incomplete sampling of the local snow depth distribution by a shorter transect. We also show that the skill of the NP distribution is relatively independent of the depth of the transect. The skill of the model is maximal for snow distributions with means in the range of 0.2 - 0.4 m. Transects where the model exhibited lowest skill had very shallow depths (<0.1 m). In this category the model's skill is halved relative to the 0.2 - 0.4 m range (which represents 69% of all transects). This mean-depth dependent skill reflects the relative

representation of transects that contribute to the NP model: the model performs best when predicting transects similar to those on which it was trained (Fig. 4.3a).

The model's skill is relatively insensitive to the month of the year with the exception of July and August (Fig. 4.5c). In these two summer months its skill is diminished with the RMSE being on average 67% higher in these two months by comparison to the average of the other months. Again, this is ostensibly a reflection of the low contributions of these months to the total number of transects: July and August contribute three and six transects to the NP model respectively, whereas the other months on average each contribute 49 transects. Low skill in these months is also likely a reflection of the snow depths being lowest, which is also associated with low skill (see Fig. 4.5b). It is also noticeable that the deepest snow conditions also exhibit low skill.

We finally address the potential lack of independence between successive transects at the same station. Our LOOCV approach assumes that by not training the model with the transect being validated against, the validation transect is independent. But the potential exists that information about the validation transect enters the model through previous and subsequent transects at the same station that are included. If successive transects are strongly related, we would expect stations that contribute more transects to the model to have their transects perform better in the LOOCV exercise. Application of the non-parametric Spearman's Rank test for correlation reveals no statistically significant relationship ($p<0.05$) between the number of transects contributed by a station to the model and the mean or median RMSE of its transects in the LOOCV exercise (Fig. 4.5d). This supports the premise that LOOCV is an appropriate tool with which to evaluate the skill of the NP model.

4.3.2 Evaluation against MOSAiC Measurements

We compare our regression and fitted curve (Fig. 4.3a, b) against the snow surveys taken on the MOSAiC expedition using a magnaprobe (Figs 4.6, 4.7 Itkin et al., 2021). To do this we select snow suveys of the "Northern Transect" (Nicolaus et al., 2022), which predominantly consisted of second-year ice.

We first note that the NP-based coefficient of variation (CV) is lower than

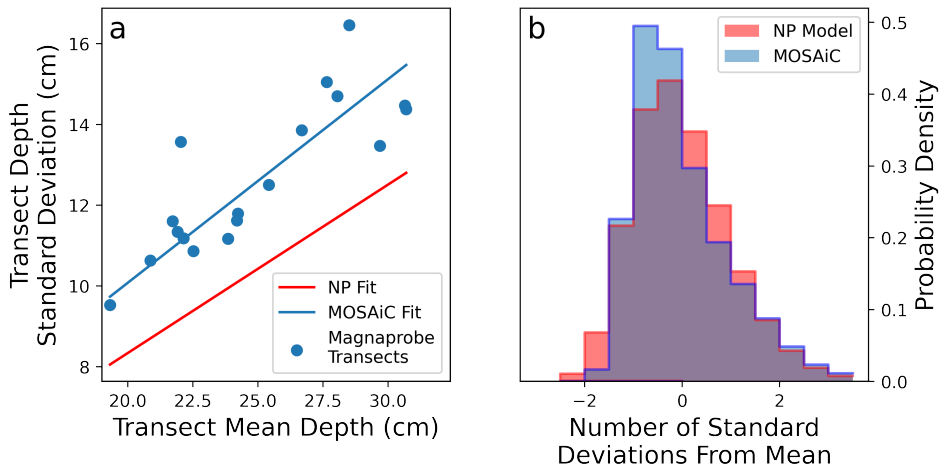

Figure 4.6: (a) Snow depth variability for a given mean depth was larger on the MOSAiC transects than on average for the NP stations. Regression for NP station data shown in red, MOSAiC transects in blue. (b) Because the depth variability is lower in the NP model, the probability distribution in standard deviation space is wider (as the standard deviations themselves are smaller).

that observed on the MOSAiC transects (Fig. 4.6a). The effect of this is that the width of the modelled depth distribution is too high in standard-deviation space (Fig. 4.6b), i.e. the NP model distribution is insufficiently 'peaked'. Symptoms of this are underestimation of the two modal bins (relative to the MOSAiC data), and overestimation of the low tail probabilities. This extra width can be understood because the standard deviations are themselves smaller.

Despite this bias, the NP model generally provides a good fit to the individual MOSAiC transects (Fig. 4.7). The skewness parameter of the NP model ($a = 2.54$) is smaller than when a skew normal fit is applied to the MOSAiC transects ($a = 6.4$). This results in the modal depth bin often being overestimated by the NP model (Fig. 4.7). For clarity, the skewness parameter (a) of the skew normal distribution is different to the commonly calculated *sample skewness* (γ), although both quantities consistently have the same sign. We calculate and report the sample skewness for the NP data and all evaluation data in Supplementary Figure S30.

A corollary to this underestimation of skewness by the NP model is that that where the modal bin is overestimated by the model, the probability (or fractional coverage) of the depth bin is underestimated. This can be seen (for example) in the

panel of Fig. 4.7 corresponding to January 30th. The skewness parameter of data in this panel is 13.7, higher than that of the NP model. This results in the model's modal depth bin being one too high (0.2 - 0.25 m vs 0.15 - 0.20 m), and the probability of the modal bin being 3.5% too low. However, we recognise that the binning process involved in this comparison places a lower resolution limit on any comparison of modal values. As such, we also compare the modal value of the NP model with that of a skew normal curve fitted to each magnaprobe transect (Supplementary Fig. S31). We find that, similarly to Fig. 4.7, the modal depth of the NP model is higher by comparison to the mode of the skew normal curve of best fit to the observations. This discrepancy grows over the winter from 0.027 m at the start of October to 0.095 m by the end of February. We stress that although a precise number can be determined for the difference in the mode of the NP model and the observationally-derived curves, the curve-fitting process to the magnaprobe observations does not necessarily fully capture the underlying data, particularly with regard to the position of the modal value.

The fractional coverage of shallow snow is a key parameter for energy flux modelling, so is now given specific consideration. We find the NP model underestimates the coverage of thin snow (<0.10 m) in early winter (end of October - mid December) with respect to MOSAiC observations. The observed coverage is 6.1%, and the NP model produces a coverage of 4.3%. After mid December the model begins to overestimate the thin snow coverage. On average it was observed to be 1.5%, and modelled to be 2.1%, an overestimate by 0.6 percentage points. With regard to heat fluxes, an overestimation of the thin snow coverage would lead to an overestimate of the heat flux from the ice to the atmosphere (and accompanying overestimation of sea ice growth rate).

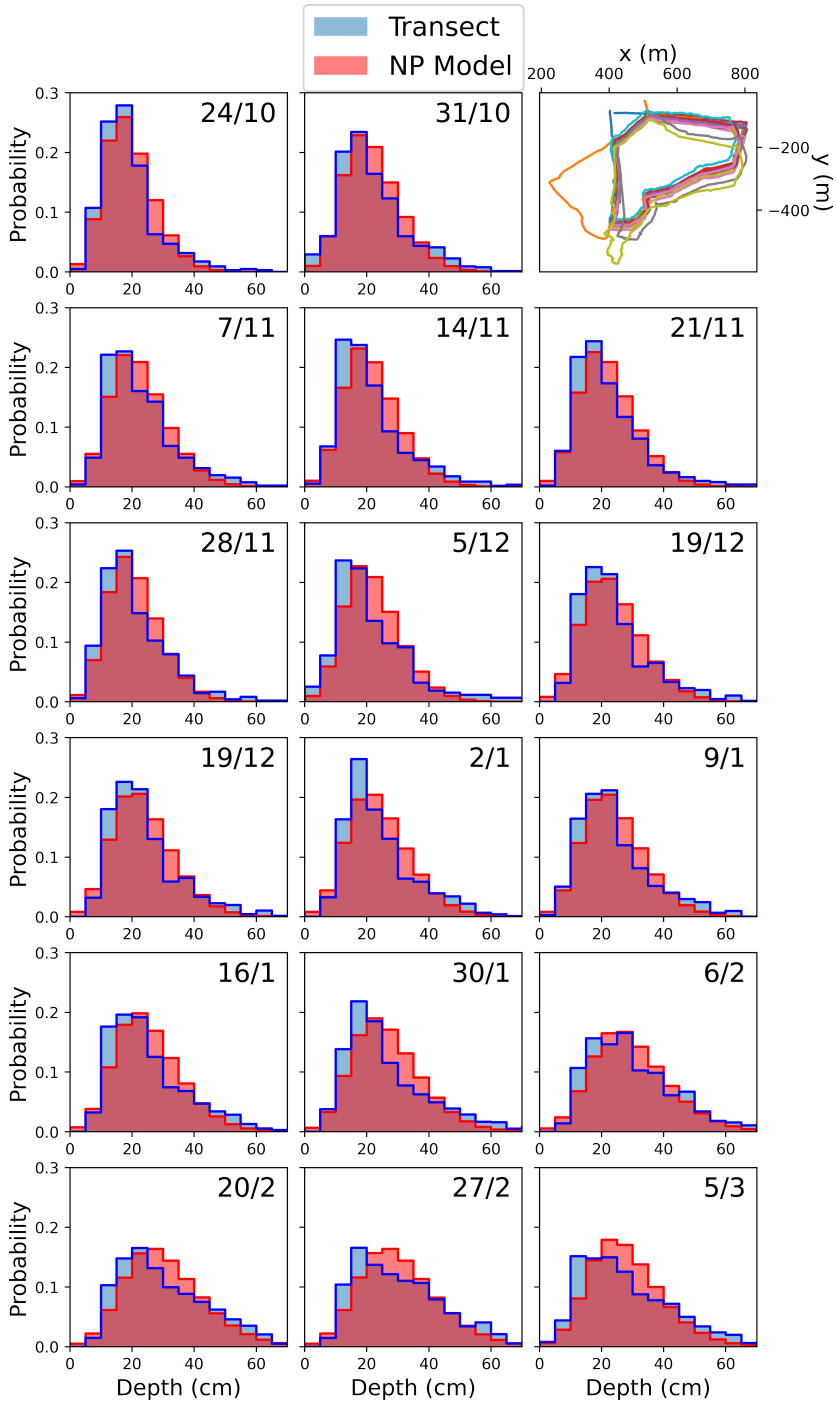

Figure 4.7: Winter evolution of the snow depth distribution on the MOSAiC Northern Transect (blue histograms, 0.05 m bins). The modelled depth distribution described in this chapter shown in red. Top right: plots of the fourteen transects contributing to the MOSAiC evaluation exercise, with panel coordinates being the relative coordinates of the floe with the research vessel Polarstern at the origin orientated upwards).

4.3.3 Evaluation against SHEBA Measurements

We now evaluate our model using snow depth transect data from the Surface Heat Budget of the Arctic (SHEBA) expedition (Uttal et al., 2002; Sturm et al., 2002a). Snow transects were taken over a variety of ice types during the SHEBA expedition, and here we opt to compare our model to transects taken in the 'Atlanta' and 'Tuktoyaktuk' (henceforth 'Tuk') areas which were dominated by multi-year ice (for best comparison with the NP data). These areas were described using ice-class codes, and were indicated as 2-3 and 4 respectively. Class 2 indicates 'Refrozen melt ponds', 3 'Hummocky', and 4 'Deformed' (Sturm et al., 2002a). Snow depths were initially measured with a marked ski-pole, with a prototype magnaprobe being used later. While the NP-model provides a good fit to the Atlanta transects, it is less appropriate for Tuk transects (where the RMSE is on average doubled compared to Atlanta).

4.3.3.1 Atlanta Transects

We find the coefficient of variation to be very similar between the SHEBA and NP transects (Fig. 4.8a). Removing transects from the high-melting month of July from the SHEBA data marginally improves this agreement, but not greatly relative to the uncertainty in the regressions. We note that no transects were taken in the Atlanta region in August.

Unlike the coefficient of variation, the agreement of the snow depth distribution is clearly improved by removing July transects from the SHEBA distribution (Fig. 4.8b). We attribute this to strong alteration of the snow depth distribution by melt ponds in this month, which developed at the site in the second half of June (Webster et al., 2015). Outside of this period the snow depth distribution is primarily dictated by wind redistribution, but within the period it is dictated by the production of liquid water at the surface of the snow, consequent runoff and potential melt pond formation.

The poor performance of our model in July and its association with intense snow melting is shown in Fig. 4.8c. After strong melting (decreasing snow depth) in June, the snow depth distribution begins to diverge from the NP model during the

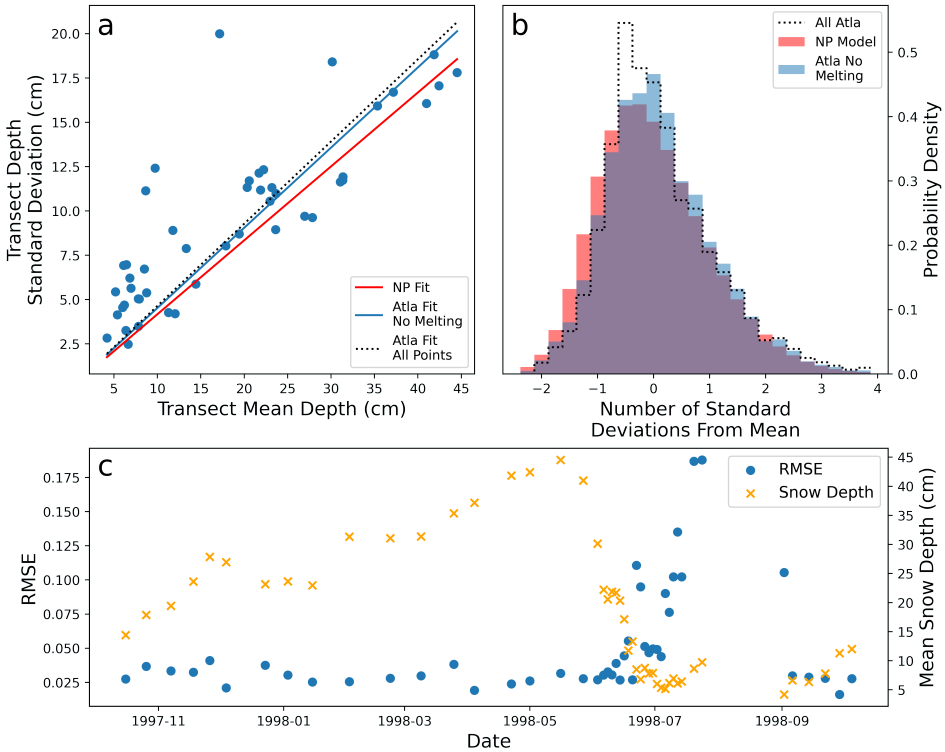

Figure 4.8: (a) Relationship between the mean snow depth and standard deviation of the snow depth on SHEBA 'Atlanta' transects (blue scatter). Linear regressions through the points are shown both including and excluding data points from July and August (blue solid and black dotted lines respectively). Linear regression from all NP transects shown by red line. (b) The snow depth distribution on the SHEBA 'Atlanta' transect excluding July and August (blue) and from NP stations (red). The SHEBA fit from all transects including July and August shown by black dotted line. (c) Time evolution of the error in this chapter's model (blue scatter). RMSE is higher during July and August than in other months, which coincides with melted snow (depth in orange scatter).

transition from June to July, and increases throughout July.

4.3.3.2 Tuk Transects

The NP model performs considerably less well when applied to Tuk transects (Fig. 4.9). Unlike Atlanta, the standard deviation of snow depth on Tuk transects is significantly underestimated by the NP regression. Furthermore, the skew-parameter of the NP model ($a = 2.54$) is less than half that of a skew normal curve fitted to the Tuk transects ($a = 6.27$). The corresponding value for Atlanta is 2.9.

It is striking that the mismatch in the skewness parameter for the Tuk transects is slightly smaller than the MOSAiC transects, but the model-observations mismatch is

much larger. Furthermore it is notable that although the skewness of the Tuk transects is larger than the NP model, the NP model still does a good job of predicting the modal depth bin. We would expect the modal bin to correspond to snow depth that is too deep where the skewness is underestimated (see Fig. 4.7). These features are explained by the fact that a skew normal curve cannot be easily fitted to the Tuk transects in standard deviation space (Fig. 4.10).

To illustrate, we display the transect data alongside the best possible skew normal fit (not involving the NP data) to the data. The agreement is good for the Atlanta and MOSAiC data sets, but noticeably less good for the Tuk data (Fig. 4.10). This indicates that unlike the MOSAiC northern transects and the SHEBA Atlanta transects, the SHEBA Tuk transects do not display a skew normal distribution of snow depths.

We attribute the deviation of the Tuk data from the skew normal distribution to the highly deformed nature of the ice relative to that seen at Atlanta and the MOSAiC northern transects, and at most of the NP stations. Firstly we point out that over strongly deformed ice the wind dynamics may cause snow to be distributed differently. Secondly we raise the fact that NP transects deviated around highly deformed ice such as that dominating the Tuk transects. There is a related sampling bias for the MOSAiC Northern transect, because the transect layout was chosen such that a snowmobile could drive around it.

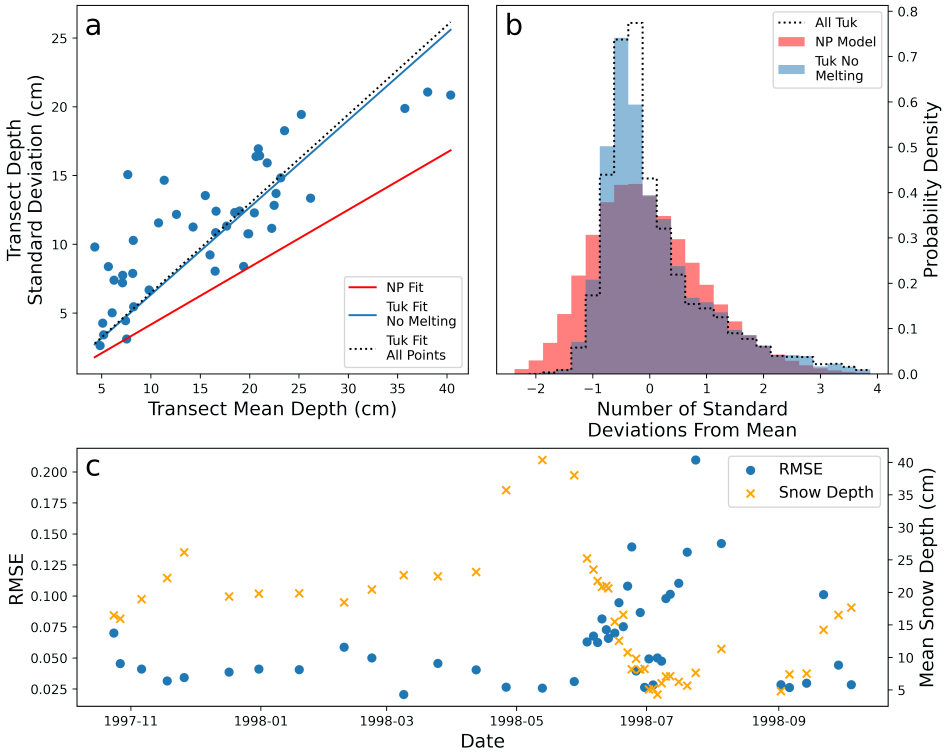

Figure 4.9: (a) Relationship between the mean snow depth and standard deviation of the snow depth on SHEBA 'Tuk' transects (blue scatter). Linear regressions through the points are shown both including and excluding data points from July and August (blue solid and black dotted lines respectively). Linear regression from all NP transects shown by red line. (b) The snow depth distribution on the SHEBA 'Tuk' transect excluding July and August (blue) and from NP stations (red). The SHEBA fit from all transects including July and August shown by black dotted line. (c) Time evolution of the error in this chapter's model (blue scatter). RMSE is significantly higher during July and August than in other months, which coincides with melted snow (depth in orange scatter).

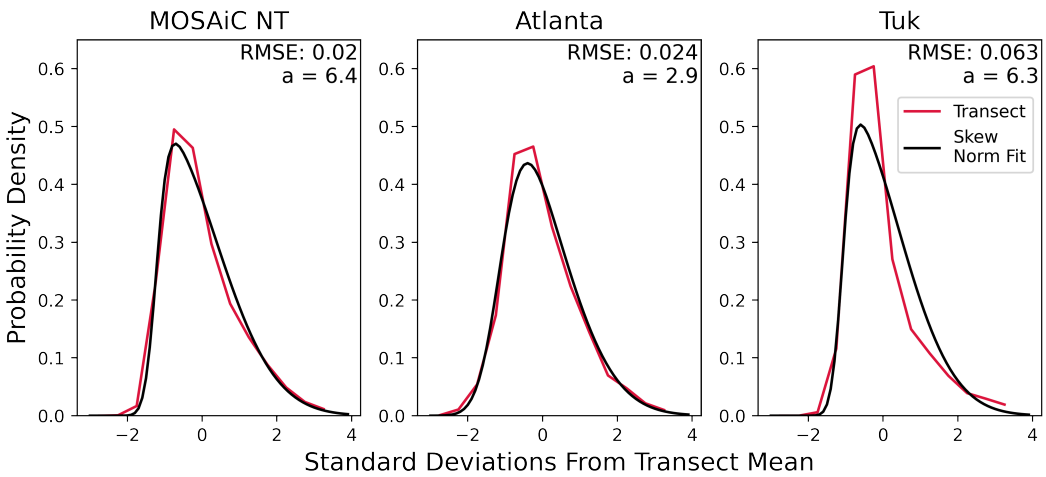

Figure 4.10: Distribution of relative depth anomalies for the three evaluation data sets used in this chapter (red). Distributions were generated with a bin width of 0.5 standard deviations. skew normal distributions are fitted to each and show variable agreement (black).

4.4 Discussion

4.4.1 Negative Snow Depths

The use of a skewed normal distribution results in a small fraction of negative snow depths. The total fraction is relatively constant at 0.1% in the 0 - 0.50 m range of mean snow depths. Above this range, it transitions to a linear decline with increasing mean snow depth, dropping below 0.075% for snow depths larger than 2 m (Supplementary Fig. S32).

Because the fraction of negative snow depths does not exceed 0.1%, we treat it as negligible in our analysis. However, if this distribution were implemented in a snow-conserving model it would be necessary to modify the low-tail of the distribution. This could be done by merging the distribution with an exponential curve at low values, or by truncating it at zero and redistributing the coverage so that the area under the probability distribution is unity. In the redistribution case, it would be possible to either scale the whole curve by a small amount, or instead preferentially add the 'lost' coverage to the low-end of the distribution. We stress however that the effect of this would be extremely small (and not noticeable in the analysis of this chapter), and so is only necessary for applications where snow must be precisely conserved. For completeness we point out that when a log-normal distribution is fitted to the data in Fig. 4.3a (instead of a skew normal), the fraction of negative snow depths is a similar function of the mean depth as in the skew normal case, but around 100 times smaller in magnitude.

4.4.2 Potential for Application to First Year Ice

No multi-station data similar to the NP transects exist for first year ice (FYI). This is in part because first year ice cannot be drifted on for long before experiencing a melt season, but also because FYI is thinner and more liable to break up, making crewed research installations difficult to establish. Because of these difficulties, it is natural to wonder whether the NP snow depth distribution can be applied to FYI and with what uncertainty. To investigate this we apply the NP model to FYI snow depth transects taken on the AMSR-Ice03, AMSR-Ice06 (Sturm et al., 2006) and MOSAiC

field campaigns (Nicolaus et al., 2022). Several of these transects were performed in Elson Lagoon (EL in Fig. 4.11), which consists of level ice. This contrasts with the more deformed ice on the nearby Beaufort sea measured during AMSR-Ice03 (BS in Fig. 4.11). During AMSR-Ice06 a level-ice section in the Chukchi Sea was also surveyed (CS in Fig. 4.11). Finally, during the MOSAiC expedition, successive transects were taken on a refrozen lead (nicknamed the 'runway', described in Stroeve et al. (2020b)), which provides some information about the thin-snow regime on FYI (Fig. 4.11 g, h & i). For the eight transects described above we calculate the RMSE of the NP model when applied based on the mean value, calculated with 0.05 m bins. We also fit a skew normal curve to the transect data and investigate the skewness-parameter (a) to shed light on the mismatch between the NP model and the observations.

We first observe that all eight FYI transects have coefficients of variation (CV) roughly consistent with that observed in the NP stations (Fig. 4.11a), particularly those from AMSR-Ice06. The average difference between the FYI CV values and that of the NP model is 0.74 (a unitless quantity), or around 17% of the CV of the NP model. We display the CV values for all FYI data in Supplementary Figure S33. We also note that the skewness parameter of the AMSR-Ice06 data (a = 1.6 & 2.2) is close to the skewness parameter of the NP-model (a = 2.54). These characteristics lead to the NP model performing better on the AMSR-Ice06 data than the AMSR-Ice03 data. The AMSR-Ice06 survey on Elson Lagoon has the lowest RMSE of all eight FYI transects (0.012) when compared to the NP model - this is related to it having the most closely matching skewness parameter to the NP model.

While all three AMSR-Ice03 transects have very similar mean snow depths to each other ($\sim$0.30 m), the coefficient of variation is lower than for the NP station transects for the Elson Lagoon transects, but higher for the Beaufort Sea (Fig. 4.11a). That is to say, the snow over the deformed first year ice in the Beaufort Sea exhibited considerably more variability than that over the level ice in Elson Lagoon during AMSR-Ice03. In addition to being more variable, the Beaufort Sea transect showed a much higher skewness parameter (a = 5.14) than those on Elson Lagoon (a = 1.02

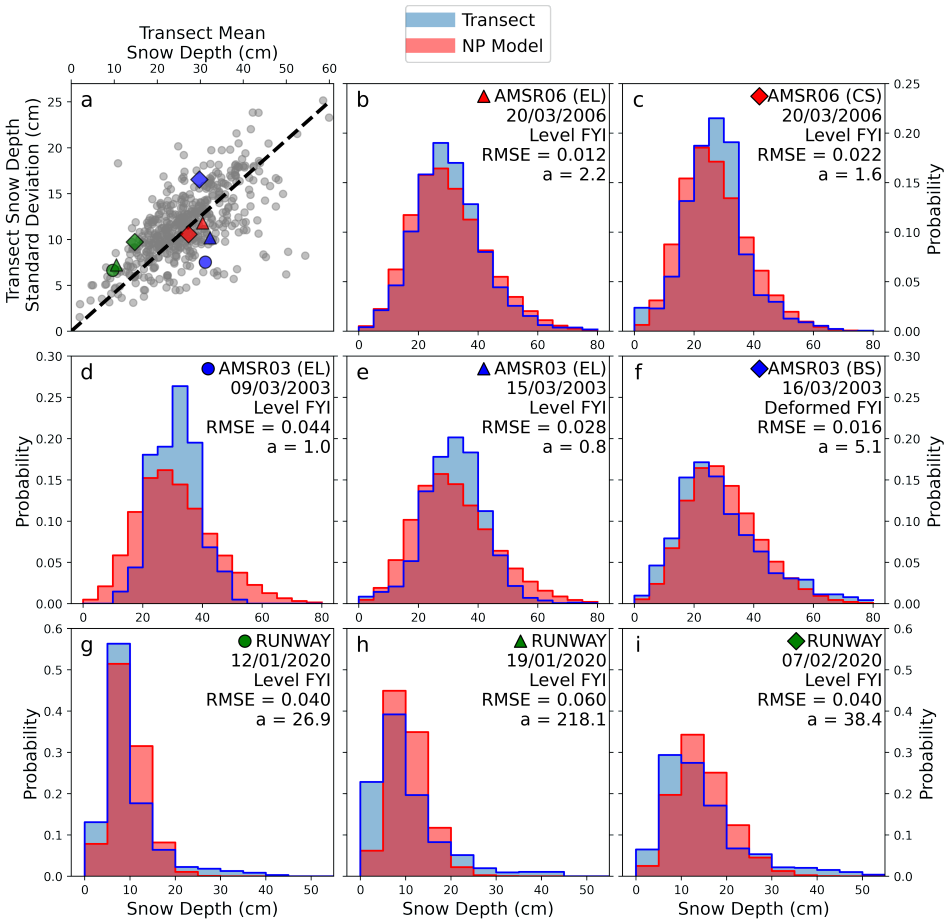

Figure 4.11: Comparison of the NP model with data from first year ice transects taken during the AMSR-Ice 03, AMSR-Ice 06, and MOSAiC field campaigns. Panel (a) shows the ratio of snow depth standard-deviation to transect mean depths (the coefficient of variation, CV) for the FYI transects (large markers) as well as for the NP transects (gray dots). All other panels show the snow depth distribution produced by the NP model (red) against the transects (blue), with 0.05 m wide depth bins for comparative purposes. Panels represent (in order b-i) Elson Lagoon (EL) and level ice on the Chukchi Sea (b & c), two transects on Elson Lagoon one week apart (d & e), a transect on FYI of the Beaufort sea near Elson Lagoon (f). Bottom row (g - i) displays snow transects taken on a refrozen lead during the MOSAiC expedition.

& 0.844). The transect over deformed ice exhibits the lowest RMSE value of the AMSR-Ice03 transects by some margin.

We attribute the low-skewness (symmetry) of the 2003 Elson Lagoon data to a lack of ice topography around which to build up a 'long tail' of drifted, thick snow. Conversely, the highly deformed ice of the Beaufort Sea produces a noticeable long tail of thick snow, such that the probability of finding snow deeper than 0.55 m is underestimated by the NP model (Fig. 4.11f). However, it is striking that the AMSR-Ice06 transects at Elson Lagoon are more weakly governed by this: while the skewness parameters are still lower than for the NP transects, there is a smaller difference. It is possible that this variability is produced by the cumulative effect of wind redistribution, and particularly strong wind events. Investigating the role of strong-wind events on the coefficient of variation and skewness of the snow depth distribution may form the basis for future work.

We now turn to the thin snow cover of the three MOSAiC 'runway' transects (Fig. 4.11 g, h & i). We first point out that a skew normal curve cannot be easily fitted to these data (Supplementary Fig. S34; similar to the situation with the SHEBA 'Tuk' transects above). This indicates that the NP model will not be a good fit, even before it is applied. Because of this feature, the skewness-parameter values listed in the panels of Fig. 4.11 should not be assumed to properly capture the underlying transect data. When the NP model is applied and compared, it exhibits a high RMSE relative to the other FYI transects. As well as being related to the poor approximation with a skew normal curve, this performance is also linked to the three 'runway' transects having the highest error in the coefficient of variation (Fig. 4.11a) by comparison to the NP transects. One key physical difference between the runway transects and the other FYI surveys is the low average snow depth. However, other contextual differences exist: for example the transects were performed in a geographically distinct region with potentially different snowfall and wind conditions. It is also the case that an ice floe in free drift (such as the 'runway' environment) will experience a turning force from wind- and ocean-drag (e.g. Debernard, 2003). This may result in a different snow depth distribution than for snow on ice that is locked in place with

respect to the wind direction such as that of the AMSR-Ice campaigns. This feature of landfast ice marks out the AMSR-Ice campaign from the rest, and may limit its relevance for comparison. In future, it is possible that a model such as SnowDunes (Liston et al., 2018) could be used to investigate the size and nature of this effect.

Because of the differences in the age of the snow (and the ice topography over level ice), there is no a priori reason that the NP-model for the snow depth distribution derived in this chapter should be applicable to FYI, and indeed our model works relatively poorly when simulating the 'symmetrical' snow depth distributions at Elson Lagoon in 2003, and the thin snow on the MOSAiC runway.

However in the instance where the ice was deformed (Fig. 4.11f) the model performs relatively well. Perhaps counterintuitively given the 2003 results, the NP model also performed well in 2006 over both level ice transects. The RMSE of the NP Model when applied to the Beaufort Sea transect was 0.016, which is in fact lower than the corresponding values for the MOSAiC Northern Transects (Fig. 4.7), which ranged from 0.019 - 0.031. By this metric the performance of the model over FYI in 2006 was also better (lower RMSE, 0.012) and comparable (similar RMSE, 0.022).

In summary, we have shown that the NP model is capable of performing well over deformed FYI, and even over level ice in the case of 2006 (where 'well' is defined with reference to its performance over MYI at MOSAiC). But despite this capability, it also clearly performs poorly in the case of thin snow (at MOSAiC runway, where we observed that the measurements could not be well-represented by any skew normal distribution), and also in the case of highly symmetrical (low-skew) snow distributions over FYI (Elson Lagoon in 2003).

4.4.3 Application to point-measurements of snow depth

There are several drifting, autonomous platforms in existence that record the snow depth at a single point, such as snow buoys and ice mass balance buoys (Nicolaus et al., 2021). If the buoy is deployed at random, it is most likely to sample the modal snow depth. In reality these instruments are often not deployed at random, and a conscious choice is made to sample what is perceived to be the modal depth.

However, for applications such as laser and radar altimetry retrievals of sea ice thickness, the mean snow depth is the quantity required for characterising the floe's hydrostatic equilibrium (e.g. Mallett et al., 2021). We now present a simple method of relating these point measurements to the mean snow depth of the surrounding area.

If the mean snow depth ($\overline{D}$) is related linearly to the standard deviation (σ_D, Fig. 4.3a, Eq. 4.1) by the coefficient of variation (CV), and we observe the modal snow depth to be X standard deviations below the mean (Fig. 4.3b), then we can relate the modal depth to the mean depth as follows:

$$\sigma_D = CV \times \overline{D} \quad \& \quad \overline{D} = D_{mode} + X\sigma_D \tag{4.3}$$

$$\overline{D} = \frac{D_{mode}}{1-(X \times CV)} \tag{4.4}$$

Using the NP data from Fig. (4.3) we now calculate that $X = 0.35$. The CV was found earlier (Eq. 4.1) to be 0.417. We therefore calculate that the mean snow depth is 17% larger than the modal depth. Where singular drifting instruments are assumed to retrieve the modal snow depth in their environment, we recommend this correction for estimation of the mean.

4.4.4 Length Scales

The NP station transects were performed over distances of 500 - 1000 m, and this characterises the length scale on which our distribution is relevant. If the same transects were theoretically performed over just a few centimetres, the coefficient of variation (Fig. 4.3a) would be lower, and the distribution about the mean would likely be different. The distribution would be sensitive to the small-scale roughness of the snow surface, rather than larger scale features like sastrugi and snow drifts around ice topography. If the transects were performed (again, theoretically) over thousands of kilometres then the snow distribution would again be different, and more representative of synoptic variability in snowfall and ice type. As such we stress that the distribution of snow depths has been characterised at the *sub-kilometre*

length scale (on the order of hundreds of metres).

We also investigate the sensitivity of our analysis to the spatial sampling interval of the transects, which was 10 m for the NP stations. In particular, we consider the possibility that adjacent (and near-adjacent) snow depth measurements on a given transect may be correlated (Moon et al., 2019), and the impact that this might have on our main results. To do this we perform an autocorrelation analysis for each of the 499 transects, testing the correlation of a spatially-lagged series against the original set of measurements. We find that for a lag of one measurement (10 m), 26% of transects show a statistically significant autocorrelation ($p<0.05$). To put this another way, we detect that adjacent points are correlated in 26% of transects. This fraction drops by roughly half at a lag of 2 measurements (20 m, 12%), and half again for a lag of 3 (30 m, 7%; Fig. 4.12a). We performed our test for correlation at the 5% level (i.e. significance at $p<0.05$), and as such would predict one in twenty transects to exhibit a correlation even in the case where all snow depth measurements were sampled randomly from a normal distribution. As such, we see the fraction of statistically significant transects tend to this level at higher lag values (Fig. 4.12a). We also analyse the strength of positive autocorrelations where they are statistically significant. The typical strength (r value) of these statistically significant correlations is broadly similar (0.364, 0.315 & 0.31 respectively for lag = 1, 2 &3; Fig. 4.12b).

The effect of adjacent points being correlated on our main analysis can be obviated by only analysing every other transect measurement. To remove the effect of autocorrelation for a lag of two samples, we can perform our analysis again but only consider every third measurement, etc. The results of this exercise on the main results are displayed in Fig. 4.12 c & d (c.f. Fig. 4.3 a & b). The coefficient of variation (Fig. 4.12 c) is essentially unchanged by only analysing every second or third measurement from the transects, and this is also true for the calculated skew normal distribution (Fig. 4.12 d). To stretch this approach, we also display the results of taking every fifth and tenth sample from transects.When comparing a 10 m sampling interval to a 100 m sampling interval, the coefficient of variation decreases from 0.416 to 0.361, and the skewness parameter decreases from 2.54 to

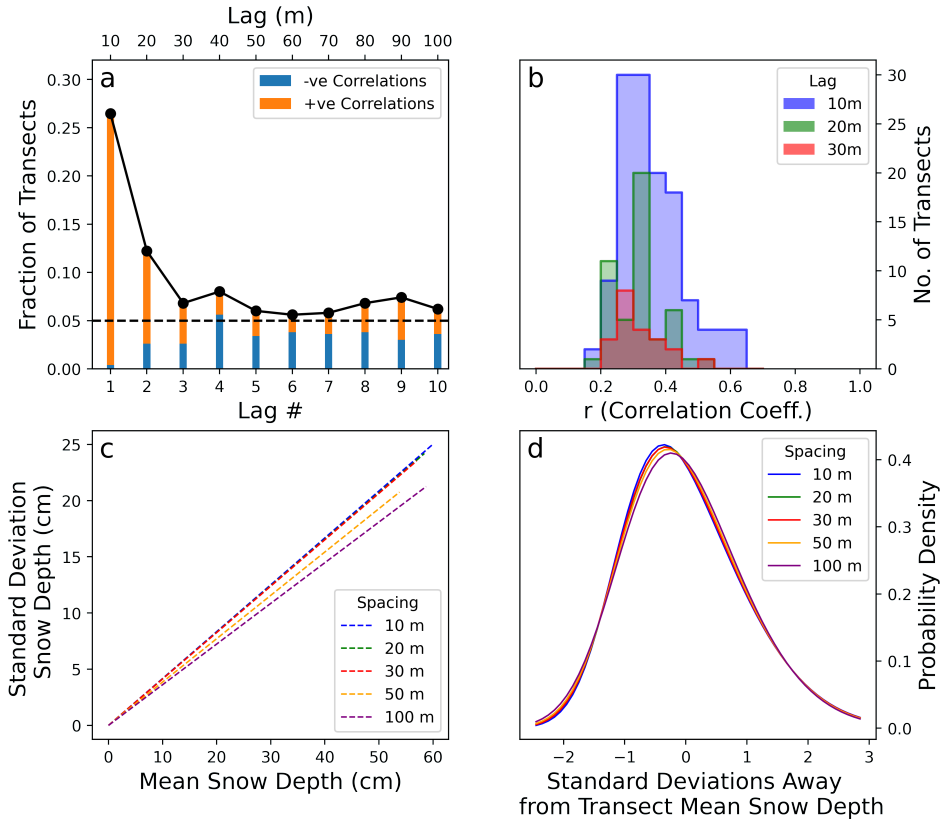

Figure 4.12: (a) Fraction of transects with a statistically significant autocorrelation at various lags. 26% of transects exhibit correlated adjacent measurements at lag = 1. (b) The distribution of Pearson r correlation coefficients for various lags, where correlations are statistically significant. The mean strength of the statistically significant correlations decreases slowly as the lag increases. (c) Impact of undersampling the transect by taking every second, third, fifth and tenth measurement on coefficient of variation, and (d) the probability density distribution in standard deviation space. The impact of this sampling is small for the double-spacing and triple-spacing, indicating that the correlation of adjacent points in 28% of transects has a negligible impact on the main results in this chapter.

1.84. Extrapolating from this trend, magnaprobe samples used in the validation data sets which have a very low sampling interval of 1 m may therefore have a high-skew and high coefficient of variation bias relative to transects from NP stations. However, the corresponding analysis for these data sets is significantly more complex as, unlike the NP transects, the samples were generally neither regularly spaced nor taken along a straight line.

For completeness we also investigate a common statistic for correlation between adjacent measurements: the *autocorrelation length* (Supplementary Fig. S35). This is calculated for a transect by, as above, calculating the correlation of lagged transects with the original transect at increasing lags. The *correlation length* is then defined as the lag at which the correlation drops to a value of 1/e. Because only a minority (28%) of transects have statistically significant correlations for adjacent points (Lag = 1 sample, 10m), the correlation lengths for the transects are generally below 10 m. Because of the coarse spatial resolution of the measurements, we must interpolate to get the correlation length, and this was done linearly. When calculating in this way, we find the modal correlation length of the transects to be 6.8 m (Supp. Fig. S35 b), although this would be highly sensitive to the interpolation method. 9.4% of transects had a correlation length of 10 m or greater.

4.4.5 Relevance in a changing Arctic Ocean and other limitations

The potential for application of the NP-model to first year ice was discussed above, and it was found that while the NP model was capable of performing well over FYI, it performed poorly when simulating the distribution of thin snow, and overestimated the skew in some cases. Here we point out that the Arctic Ocean is becoming increasingly dominated by first year ice, so arguably the relevance of this MYI-trained model is in slow decline.

There may also be spatial limitations on applicability. The NP drifting stations generally operated in the Central Arctic Ocean (Fig. 4.1) rather than in the marginal regions such as the Kara, Beaufort and Barents Seas (Warren et al., 1999). However, these areas are generally dominated by first year ice, so this geographic constraint is

less strict that the ice-type one described above.

The average age of multi-year ice is in decline, with the coverage of ice aged five years or more shrinking from 28% to 1.9% between 1984 and 2018 (Stroeve and Notz, 2018). The mean thickness of sea ice is also in decline (Kwok, 2018). Because we produce our statistical model using drifting station data from 1955 - 1991, it likely reflects snow conditions on ice older and thicker than that which currently exists in the Arctic. We note however that our model does still display good skill with respect to the MOSAiC transects, which were generally performed on ice that had only experienced one melt season, making it the youngest form of multiyear ice.

4.5 Summary

In this chapter we have developed a generic snow depth distribution for multi-year ice that can be fully characterised by the mean snow depth. This allows it to be superimposed onto estimates of mean snow depth from satellites and models for the purposes of flux modelling and altimetry studies.

We performed a cross-validation exercise and found the model's skill to be highest in winter, and lowest during the summer months of intense melt and sparse measurements. We then evaluated the distribution against snow depth transects from the MOSAiC, SHEBA and AMSR-Ice field campaigns. These analyses revealed that the model generally overestimated the variability in snow depths for the MOSAiC campaign, but the fit parameters were otherwise broadly appropriate. On the smoother multiyear ice of the SHEBA campaign the model performed well, but the model performed poorly on transects executed over highly deformed ice. This was related to the fact that the snow depth distribution in this area was not well approximated by the skewed normal distribution used in the NP model. Application of the distribution to eight transects conducted over first year ice shows that while the NP-model was capable of performing well (over deformed FYI and in two cases over level ice), it performed poorly when simulating thin snow on a refrozen lead in the Central Arctic, and also when simulating a highly symmetrical snow distribution over level ice.

Chapter 5

Comparing the characteristics of NP station snow melt and ablation to satellite radiometry and modelling

5.1 Introduction

As polar night ends in the Arctic, the sun exerts an increasing influence on the sea ice surface. Surface air temperatures rise as the sun shifts higher in the sky, until the snow surface reaches its melting point. When snow reaches this point, further input of solar energy produces liquid water within the snowpack. This water accumulates in the snow until gravity allows it to drain out, in a transition from the pendular to the funicular drainage regime (e.g. Denoth, 1982). Upon drainage, water can pool at the bottom of the snowpack to form melt ponds, depending on the underlying ice properties such as roughness and thickness distribution (e.g. Webster et al., 2022). Where melt ponds are not present, the snow in most parts of the Arctic Ocean melts almost entirely back to a 'surface scattering layer' on the ice (Smith et al., 2022b), with an associated drop in albedo (Langleben, 1969; Perovich et al., 2002). This melting (or *ablation*) is associated with rapid reductions in snow depths (Iacozza and Barber, 2001; Kwok et al., 2020a). These reductions in snow depth represent *snow ablation*, which can occur well after melt onset.

Snow can also thin without melting; this can happen locally via wind redistribu-

tion (Leonard and Maksym, 2011), and on larger spatial scales through compaction under its own weight (Sturm and Holmgren, 1998), by wind-action (Sommer et al., 2018), or by sublimation/evaporation (Hurley, 1954; Déry and Yau, 2002).

The timing of Arctic Ocean snow melt onset is spatially variable in a given year, and varies interannually at the same place. Several satellite-based melt onset detection algorithms have been developed to chart this variability (Anderson, 1987; Winebrenner and West, 1994; Drobot and Anderson, 2000; Markus et al., 2009; Howell et al., 2019). Figure 5.1a illustrates a climatology of the snow melt onset timing from one such product. Melt onset generally occurs later at higher latitudes, with the latest melt onset occurring in a small patch on the West-Russian side of the North pole that generally remains frozen for more than 180 days of the year. Several studies have used these products to investigate a climate-change driven shift to earlier melt onset in some parts of the Arctic Ocean (e.g. Stroeve et al., 2006; Markus et al., 2009; Stroeve et al., 2014), and the pattern of spatial trends is visualised in Fig. 5.1b.

Satellite determination of Arctic snow melt onset timing over sea ice is a particular challenge relative to the nearby terrestrial-ice environment of the Greenland ice sheet for several reasons. The main challenge in the sea ice environment is the dynamic opening of leads due to ice divergence. This exposes liquid water with a similar microwave emission signal to the emergence of liquid water in the snowpack - a unique challenge to the sea ice environment. As well as posing a challenge to satellite observations, the opening of leads can also drive sudden changes in temperature and humidity, that may actually drive sudden and ephemeral melt onset, or initiate a more permanent shift (e.g. Vivier et al., 2016).

5.1.1 What triggers snow melt onset and subsequent ablation?

Variability in the timing of melt onset on large scales is linked to synoptic weather and large scale atmospheric circulation patterns. Crawford et al. (2018) showed that melt onset timing in the Siberian marginal seas is controlled in part by the timing of terrestrial snow retreat in the West Siberian Plain. This mechanism operates by controlling the amount of atmospheric moisture that is advected into and out of the Arctic, which moderates the downwelling longwave radiation (See also Mortin et al.,

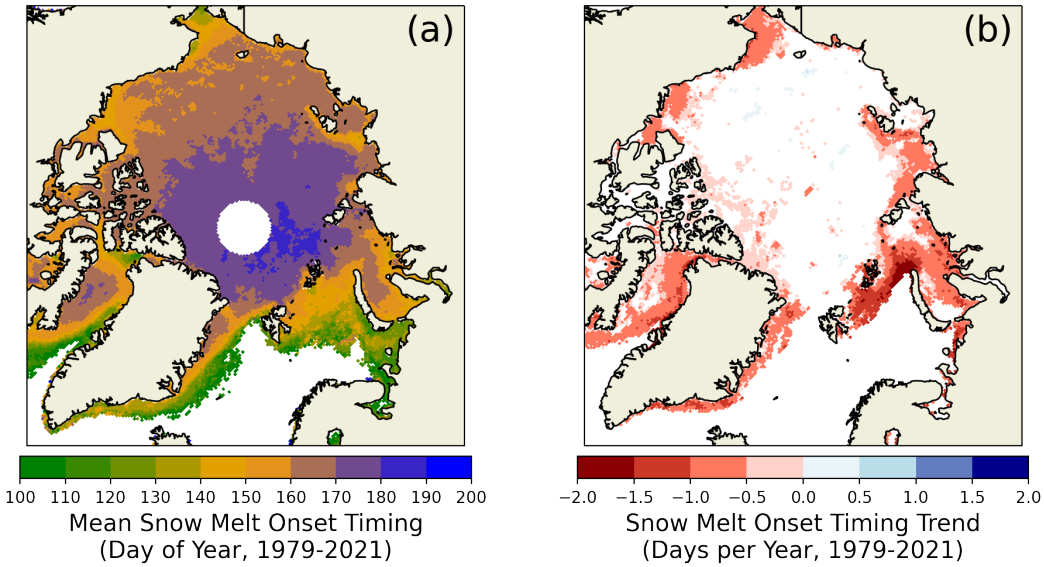

Figure 5.1: (a) A climatology of melt onset timing based on the product of Markus et al. (2009). Colors show the mean day-of-year on which snow melt onset was observed. (b) Trends in Arctic Ocean snow melt onset timing based on the same product. Trends are only visualised where r-value correlations are statistically significant ($p<0.05$). Trends are generally localised to the marginal and sub-Arctic seas.

2016). Horvath et al. (2021) showed that earlier melt onset in the Arctic Ocean was associated with a dipole pattern of sea level pressure which funnelled atmospheric moisture into the Arctic Ocean from the Bering/Chukchi region.

On local scales, melt onset is mostly controlled by the radiative balance of the snow and the surface air temperature. To explore the relationship between surface air temperature and melt onset timing, several studies have made use of surface air temperature data sets. In the period of overlap between NP station operation and the satellite era, this has often been using the International Arctic Buoy Programme / Polar Exchange at the Sea Surface (IABP/POLES) data set (Martin and Munoz, 1997). For instance Belchansky et al. (2004b) and Rigor et al. (2000) took a 14-day running average of the IABP/POLES temperatures and showed that the timing with which they rose above a threshold was closely related to melt onset timing from remote-sensing products.

In addition to air temperature, Dou et al. (2019) emphasised the sometimes critical nature of spring rain on snow events in lowering the snowpack's albedo and

warming it via latent heat release near Utkiagvik, Alaska. Along these lines, drizzle contributed to melt onset at the SHEBA expedition (Persson, 2012), and a rain event also drove the first occurance of melt in the Hudson Bay campaign documented by Ehn et al. (2006). Analysis of satellite-derived melt onset the East Siberian and Laptev seas by Marcovecchio et al. (2022) indicated that early melting years had above average precipitation (in atmospheric reanalysis) before and after the first melt event.

5.1.2 The importance of melt onset and ablation

The timing of snow melt onset is an indicator of climate change in the Arctic Ocean (e.g. Stroeve et al., 2006; Stroeve and Notz, 2018). Markus et al. (2009) identified trends towards consistently earlier melt onset in all Arctic Ocean regions in the period 1979 - 2009, with these trends strongest in the marginal seas of the Arctic Ocean. This earlier melt onset mirrors increasing delays in the timing of autumn freeze-up; the result of these two factors is a significant lengthening of the Arctic Ocean melt season (Stroeve et al., 2014).

As well as being an indicator of changes in the Arctic system, the timing of melt onset drives and moderates several environmental processes. The snow ablation associated with melt onset leads to increased light flux to in- and under-ice primary producers, however this also coincides with a flushing of algae from in-ice channels (Galindo et al., 2014). A reduction in snow albedo is associated with snow melt onset even prior to melt ponding (Langleben, 1969; Vérin et al., 2022), and this helps advance the subsequent melt (Curry et al., 1995). Total transformation from dry snow to ice and melt ponds can be associated with reductions in albedo from 0.8 to less than 0.5 (Langleben, 1966; Perovich et al., 2003).

As mentioned above, the timing of melt onset also impacts the length of the melt season, which in turn controls the cumulative longwave and shortwave energy absorbed by the surface (whether that be ice or ocean, Stroeve et al., 2014). Earlier insolation of the sea surface is relevant to the subsequent growth season and timing of sea ice advance, as the heat energy is stored either in the ocean's mixed layer where it must be lost prior to freeze up, or in a slightly lower near-surface temperature

maximum, where it can slow subsequent growth (Timmermans, 2015). Perovich et al. (2011) noted that the seasonal evolution of sea-ice albedo and the resulting summer solar heating of the ice–ocean system is more sensitive to the date of melt onset than the date of fall freeze-up.

Melt onset also poses a challenge to the determination of sea ice thickness by radar altimeters. The conventional, underpinning assumption of Ku-band radar altimetry is that emitted radar waves penetrate the overlying snow pack and backscatter from the snow/ice interface (Mallett et al., 2021, and references therein). However, the occurrence of melt onset precludes this - wet snow is known to be both highly scattering and highly absorbing in the gigahertz frequency range (Ulaby and Long, 2014, p142-145). The timing of melt onset therefore represents the seasonal end of the period of possible radar-derived estimates of sea ice thickness under the conventional assumption of full radar penetration (See Tilling et al., 2018, p1209 for impacts). However, this does raise the possibility of characterising melt onset timing with radar altimeters themselves, something that was briefly explored by Dawson et al. (2022).

5.1.3 Determining melt onset and ablation timing from space

Some of the earliest observations of the seasonal melt onset from space were made by observing changes in its microwave emissions (see Carsey, 1984, for characterisation with the Electrically Scanning Microwave Radiometer). The first dedicated application of radiometry to the timing of Arctic melt onset was by Anderson (1987), who compared the brightness temperatures measured by different channels of the scanning multichannel microwave radiometer (SMMR). This was based on SMMR observations of Antarctic sea ice by Comiso et al. (1984), who remarked upon the signature of surface melt present in the vertically polarised 18 and 37 GHz channels.

Because of the time-span of the SMMR observations, the passive microwave record is the longest pan-Arctic record of melt onset timing (1979 - present). While substantial work has been put into melt onset characterisation using active methods (e.g. Winebrenner and West, 1994; Howell et al., 2019), active-sensor records generally suffer from larger ‘pole holes’ due to the reduced orbital inclination and field of

view of active-radar systems as opposed to contemporary radiometers. For instance, the ERS satellite had a latitudinal limit of 81.5°. That is not to say that the passive-microwave record is without flaws: the SMMR pole hole extends north of 87.5°, and the Arctic was scanned every other day due to power constraints. Furthermore, the replacement of the SMMR with the special sensor microwave/imager (SSM/I) and the special sensor microwave imager/ sounder (SSMI/S) also brought a shift in the central frequency of a relevant channel from 18 to 19 GHz, introducing uncertainty into the record. But despite these drawbacks, the radiometry-based record of melt onset timing is best placed to provide a useful record of long-term environmental change. The record of satellite-mounted radiometers is set to continue with the Copernicus Imaging Microwave Radiometer (CIMR; Kilic et al., 2018), which recently advanced to the status of 'High Priority Candidate Mission' for construction and launch by the European Space Agency.

Several studies have sought to evaluate the performance of satellite-derived melt onset products using surface air temperature data sets, however this approach has a number of uncertainties and biases. For example, Winebrenner and West (1994) and Smith (1998) compared their melt onset products with the NCEP atmospheric reanalysis, which has a documented warm bias (Batrak and Müller, 2019). Later work (Belchansky et al., 2004a; Rigor et al., 2000) used the IABP/POLES data set (Martin and Munoz, 1997), which was introduced previously in the context of exploring the impact of surface air temperatures on melt onset timings. This has its own uncertainties involving the gridding and interpolation procedures required to make the product. It was pointed out by Stroeve et al. (2006) that surface air temperature products such as IABP/POLES cannot capture small scale features of melt timings, due to being interpolated over large distances. For example, Belchansky et al. (2004b) used a 12-hourly, 100 km resolution product, which was then downsampled to 24-hourly and upsampled to 25 km through averaging and linear interpolation. Drobot and Anderson (2001) used the same data but gridded by 1° latitude and longitude to evaluate the development of the AHRA melt onset product.

To address the above challenges to effective evaluation, in this chapter I specifi-

cally investigate melt onset and ablation by using *in-situ, Lagrangian* measurements of air temperature and snow depth, where no gridding or spatial interpolation is necessary. This allows a more precise evaluation of the relationship between satellite products, meteorological forcing, and snow geophysical evolution.

By comparison to melt onset timing, the timing of snow ablation has been considerably less studied from space, with the most relevant work being Kwok et al. (2020a). The retrievals of ablation rates and timings by Kwok et al. are hindered by the necessary use of the sea ice thickness reanalysis data set by Zhang and Rothrock (2003), and the low repeat-rate of the IceSat-2 orbital cycle. Kwok et al. compare their ablation rates to a single drifting station in a single year (NP 22, 1979). This more comprehensive treatment of the NP snow ablation record will provide therefore useful for comparative purposes.

5.1.4 Modelling melt onset and snow ablation

Dedicated modelling investigations of pan-Arctic Ocean melt onset timing is a relatively new field, despite the fact that melt onset timing has been shown to be a useful diagnostic for the validity of sea ice simulations (Smith et al., 2020). Smith et al. (2022a) used a satellite simulator to model brightness temperatures from a melting snowpack and test the skill of a model (CESM2; Danabasoglu et al., 2020) in simulating the observed melt onset timings.

Cheng et al. (2006) performed a one-dimensional model sensitivity analysis, and found that melt onset timing in the Central Arctic Ocean depended strongly on incorporating a large number of layers in the model run and inclusion of a time-evolving surface albedo. However, this model-evaluation exercise was confined to only one Lagrangian coordinate, as the model was compared to snow pit results from a drifting ice camp. Hanesiak et al. (1999) found that hourly forcing of a snow model had a considerable impact on the timing of snow ablation when compared to daily average forcing (making melt onset earlier and more realistic). This change was driven by higher shortwave radiative fluxes from higher-resolution inputs. They also found that snow ablation, while occurring sooner, progressed more gradually and realistically under hourly forcing.

In this chapter I examine results from the recently developed model SnowModel-LG (Liston et al., 2020; Stroeve et al., 2020a, henceforth SM-LG), which also featured in Chapter 2. Understanding the snow melt characteristics of SM-LG is important to two research avenues: the creation of a year-round sea ice thickness product from satellite-mounted radar altimeters, and charting the evolution of year-round in- and under-ice light intensity. The former is already underway (Dawson et al., 2022; Landy et al., 2022), and the latter is a likely prospect in the near future.

I now illustrate the importance of accurate modelling of snow melt and ablation timing to radar altimetry, before turning to light attenuation. The summer sea ice freeboard product by Dawson et al. (2022) was evaluated around the 200th day-of-year, when there is essentially no snow cover on the ice. However, to produce a sea ice thickness product earlier in the summer, the snow loading must be accounted for. Given the snow loading can change by several centimetres per day during snow ablation, it is important to accurately model this aspect of the seasonal cycle. As discussed above, there is also a shift to relative radar-opacity with the onset of melt, due to the high dielectric permittivity of liquid water relative to ice and air. While this transition can arguably be derived from satellites, the timing of the snow becoming radar-opaque must appropriately lead the timing of snow ablation by melting if radar estimates of sea ice thickness are to be consistent across melt onset and ablation period.

Stroeve et al. (2021) used the output of SM-LG to model the evolution of light intensity under sea ice in the ice-growth months. The authors limited their analysis to the growth period due to uncertainty in summer sea ice thickness determination. This uncertainty stems partially from uncertain ice density and in part due to the radar penetration issues discussed above. However, with the advent of a year-round sea ice thickness product (Landy et al., 2022), year-round, pan-Arctic in- and under-ice light intensity modelling is an increasingly viable prospect. To do this, SM-LG's timing of snow wetting and ablation (and its uncertainty) must be understood, so as to realistically reflect the timing of the light-intensity increase.

5.2 Data

5.2.1 NP Data

In this chapter I consider melt onset and snow ablation from the perspective of daily snow depth measurements at stakes. For each station, these were recorded at a site around 100 m from the nearest building, with three stakes situated at the corners of a 25 m square area. The mean depth at all three stakes was taken, and recorded to the nearest centimetre.

I contextualise the timing of snow melt onset and ablation with reference to the surface air temperature. The following information on the measurement techniques was supplied with the data: near-surface air temperatures were recorded in a shelter to protect them from insolation (similar to a Stevenson's screen). Thermometers were mounted 2 metres above the ice surface. Until NP-21 mercury thermometers were used for temperatures above 30°C, and alcohol thermometers were used for those below. Beginning at NP-21 stations began to use copper-wire resistance thermometers which recorded data electronically. The mercury thermometers had a scale spacing of 0.2°C, with a nominal measurement error of 0.3°C. The scale spacing of the alcohol thermometers was 0.5°C, with a nominal measurement error of 0.5°C in the temperature range in which they were used. The copper-wire thermometers had an uncertainty of 0.2°C.

To investigate the geophysical variables that drive and respond to melt onset, I analyse data on low cloudiness and snow albedo. Low cloudiness was recorded in tenths corresponding to the total amount of sky covered. Low cloud was defined where clouds had a base at a height of <2000 m height (Leningrad, 1969), measured using optical-drum ceilometers. I calculate snow albedo from daily radiometer measurements of the broadband, shortwave global radiation and reflected radiation. However, it is unclear whether these measurements were taken synchronously from the same patch of snow. I therefore describe these data as 'derived albedo'. A longer description of the radiometry setup at NP stations is given by Marshunova and Mishin (1994). There is also the question of whether these data are representative of the snow cover at the floe-scale after melt onset, given the highly spatially variable albedo of

melt-ponded ice. As such, the derived values should be treated with caution.

5.2.2 Satellite radiometry derived melt onset products

I consider two commonly used data sets for the timing of melt onset: the Advanced Horizontal Range Algorithm (AHRA) developed by Drobot et al. (2001; data span 1979 - 2017), and the Continuous Melt Onset (CMO) developed by Markus et al., (2009; data span 1979 - 2021). These data were downloaded as part of a combined data set (Steele et al., 2019) which is provided on a 25 km polar stereographic grid. When regional averages were calculated, the variable size of the grid-cells was accounted for.

Both data sets are subject to the limited orbital inclinations of radiometer-carrying satellite missions in the late 20th century. Satellite radiometers only covered an area up to 84.5°N between 1979 - 1987, 87.2°N between 1987 - 2007, and 89.18°N from 2007 to the present (Peng et al., 2018).

It is important to consider that the AHRA algorithm was designed to detect the first appearance of liquid water in snow, whereas the CMO algorithm was designed to detect the onset of *continuous melt*. As such, the products should not be expected to precicely agree when the snow melt is initially ephemeral. However the two products can still be evaluated against the same meteorological variables such as air temperature and albedo, with the understanding that closer agreement with the evaluation data does not necessarily mean one product is 'more accurate' than the other.

5.2.3 Parcel-wise SnowModel-LG Data

I use the in-situ observations from NP stations to evaluate the performance of SnowModel-LG (SM-LG). To do so, I analysed the track-wise (Lagrangian) parcels produced by a model run driven by the ERA5 atmospheric reanalysis product (Hersbach et al., 2020). Snow depth and density data from these parcels were gridded to form the publicly available product (Liston et al., 2021). The track-wise data were received in a private communication. Because the model requires ice motion vectors to run, it can only produce data from 1980 onwards. SM-LG produces around 55,000

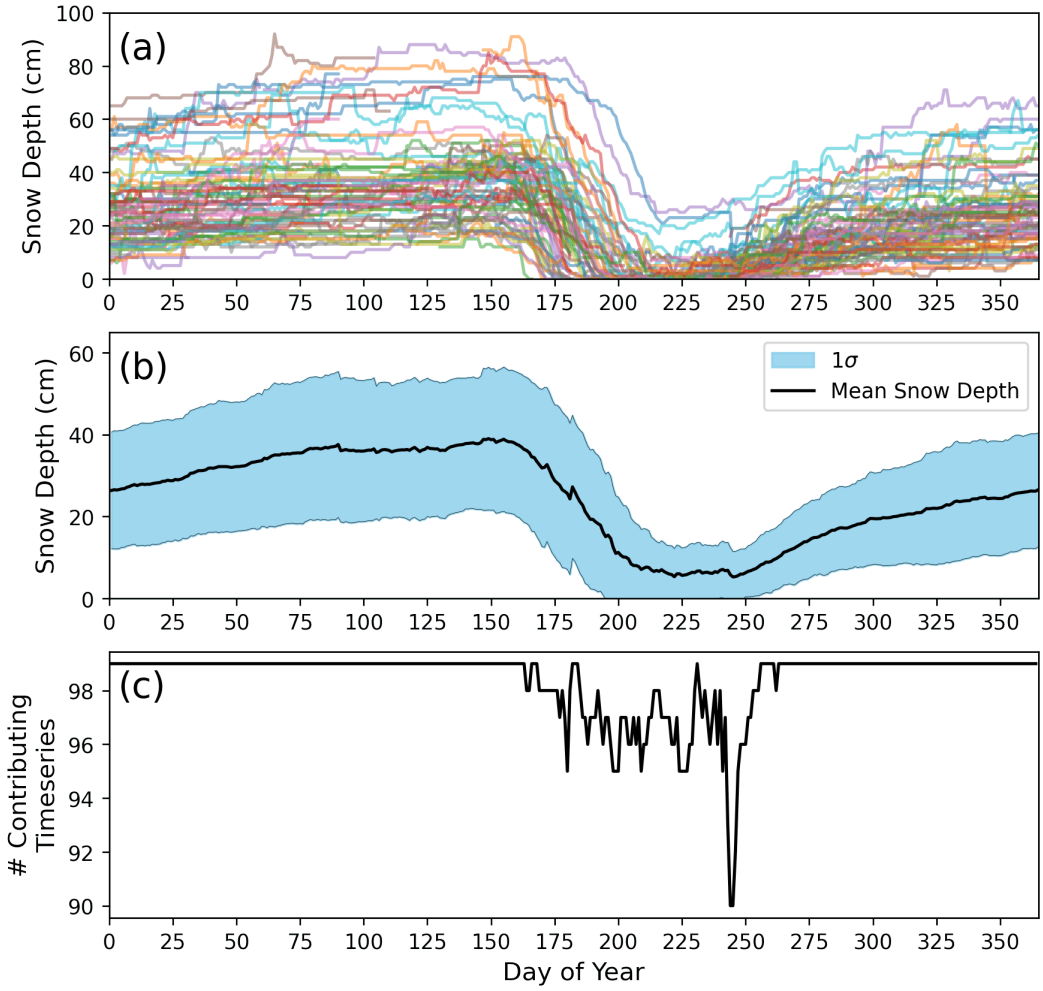

Figure 5.2: **(a)** Timeseries of three-stake-averages of snow depth to the nearest centimetre over the seasonal cycle at NP stations. **(b)** Mean seasonal cycle of all three-stake-average timeseries where data were available. Data were not collected once the ice at stakes began to ablate. Where measurements were stopped, data no longer were considered for the averaging. This is the cause of the sharp uptick around day-of-year 182, and the sudden drop around day 244. **(c)** The number of snow depth timeseries contributing to the mean and 1σ limits of panel b. Sudden drops or jumps in the number can drive spurious variability in the visualisation of the mean seasonal cycle.

tracks per year; for each of these tracks I processed the daily output of snow surface (skin) temperature, snow depth, snow density, total daily melting, and basal runoff. I also similarly processed the 2 m temperature data, which was a model forcing but was output trackwise for analysis.

Basal runoff is determined as follows: liquid water is made available at the snow surface by liquid precipitation or melting, and then percolates down due to gravity. It freezes during this journey depending on the modelled, layerwise cold content. It does not freeze in layers with density above a maximum value of 550kgm^{-3}. Upon reaching the base of the modelled snowpack, it 'drains' out of the snow and is considered runoff (Liston et al., 2020, Appendix C7).

5.3 Methods

In this chapter I address the following four questions:

- To what extent does the timing of in-situ snow ablation reflect the timing of satellite-derived melt onset?
- How well does SnowModel-LG represent the timing and speed of snow ablation at NP stations, and can the causes of differences be identified?
- How well does SnowModel-LG represent the timing of melt onset in satellite-derived products?
- How does the weather and snow albedo at NP stations drive and respond to melt onset and snow ablation?

5.3.1 Generating station-wise melt onset timing from satellite products

I generate a satellite-based estimate for the day-of-year on which each station experiences snow melt onset. To do this, I consider the full track of a given NP station and how it moves along it with time. As the station moves along this trajectory, it moves through a series of grid-cells corresponding to the two satellite melt onset products described in Sect. 5.2.2. I identify the satellite melt onset date as the date

in the first grid-cell that the station moves through that is either experiencing or has experienced melt onset on that day. This method means that as well as disagreeing in time, the satellite products can also disagree in space (Supp. Fig. S36). That is to say that the satellite products identify melt onset for the same station as happening in different locations, as well as on different days of the year (a feature of the station itself drifting).

5.3.2 Defining the timing of in-situ snow ablation

To analyse the timing and speed of snow ablation at NP stations it is necessary to establish an objective definition of the timings themselves. To do this, I calculate the maximum spring snow depth for a given NP station in a given year, and define the *reference snow ablation timing* as when the snow depth drops past a threshold-fraction of that value. This timing is distinct from the melt-onset timing, which represents the timing with which liquid water first starts to appear within the snow. The snow ablation timing is instead based on the timeseries of snow depth, and is designed for comparison with other snow depth timeseries such as those produced by SnowModel-LG. An analogous comparison of melt onset timing between the NP stations and SnowModel-LG is not available, as snow liquid water content timeseries are not available from either data source.

I iterated through a series of percentage-threshold values to determine the most suitable one to apply to all timeseries. For each candidate threshold (e.g. 40%) I calculated the snow ablation timing based on the candidate threshold and plotted all snow depth timeseries relative to their reference ablation timing. For example, I show these in grey for a threshold of 40% in Fig. 5.3a. I then calculated the daily ensemble average of all timeseries - this is shown in red in Fig. 5.3a. I then calculated the gradient of that ensemble average - the gradients for all tested thresholds are shown in Fig. 5.3b.

It is clear that the peak ablation rate of the ensemble average (in cm/day) comes between the day that the threshold is exceeded and the day prior. This is taken as evidence that 'dropping below a threshold-fraction of spring maximum' is an appropriate method, because the timing that the threshold is exceeded is a reasonable

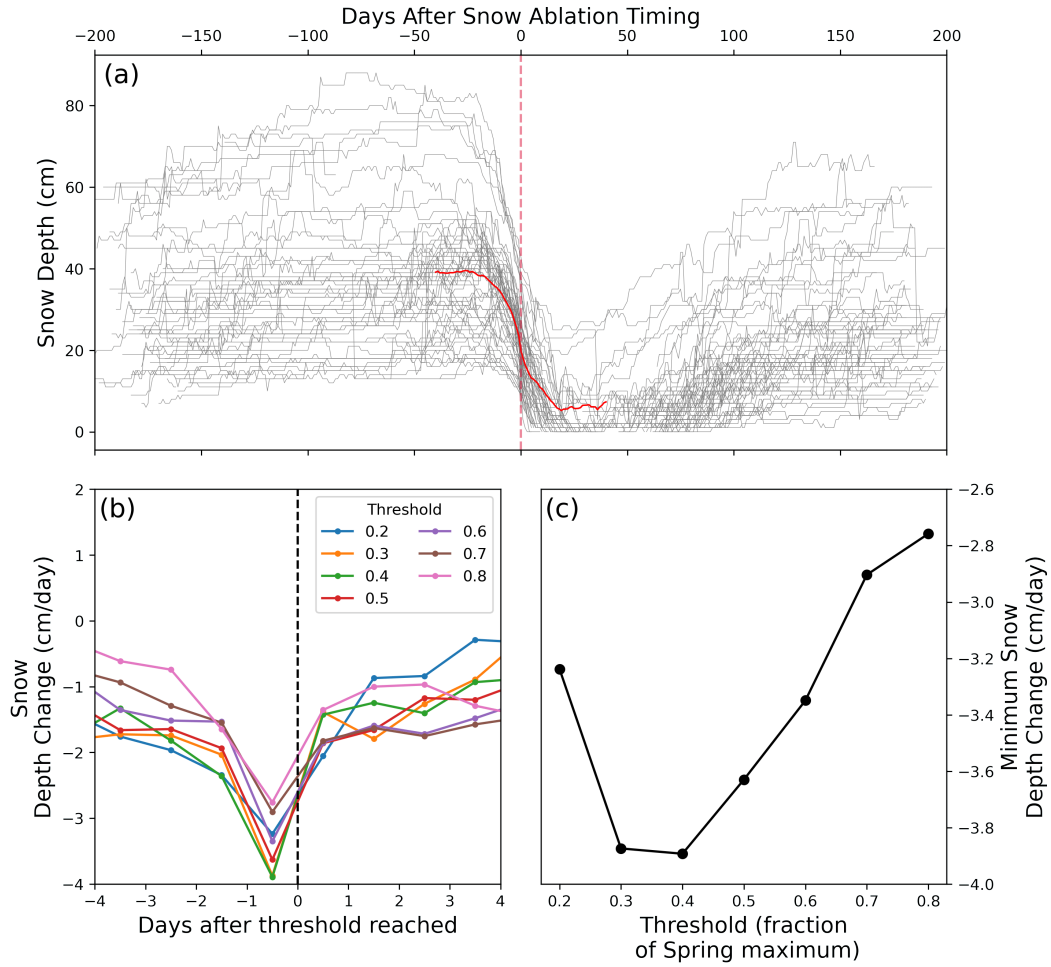

Figure 5.3: (a) Timeseries of snow depth arranged such that x = 0 is the date on which the snow depth drops below 40% of its spring maximum value. The 40% figure is the result of the sensitivity analysis illustrated in the lower panels. Red line indicates the ensemble average of all the timeseries. Compare with panel *a* of Fig. 5.2. (b) Gradient of the ensemble average of the timeseries (red line in upper panel) for different threshold values. (c) The minimum value of each timeseries in panel (b). The threshold that produces the steepest gradient (lowest value in panel b) is 0.4. This is the criterion on which the 40% threshold of spring maximum snow depth was selected.

approximation of the timing of the ensemble-average's *peak snow ablation*.

I select the threshold that minimises the peak ablation rate of the ensemble average. That is to say, I select a threshold that delivers the lowest minimum value in Fig. 5.3b & Fig 5.3c - this corresponds to the largest magnitude of change in snow depth. This figure is 0.4, or 40% of the spring maximum value. When this value is chosen, the lowest gradient of the red line in Fig. 5.3a is -3.8 cm/day. The 40%

threshold defines the reference day of ablation for all timeseries for the rest of this manuscript. Because each timeseries has a different spring-maximum snow depth, each therefore has a different *absolute* threshold (e.g. 23 cm, 31 cm etc.) which, when crossed, forms the reference day of ablation.

It is worth considering that the rate of snow depth reduction captures both physical phase change (of ice into water), but also densification that arises from changes in the microstructural bond-geometries and strengths. It is therefore not safe to assume that, say, a 20 cm snow depth reduction represents the melting of SWE equal to 20 cm of snow at the density prior to melt. Instead, it is likely that a smaller amount of SWE has melted, and some densification has also occurred.

5.3.3 Comparing timing and speed of in-situ snow ablation at NP stations to SnowModel-LG

I sought to compare the snow depth evolution at NP stations to those of closely corresponding SM-LG parcels. To find the most comparable Lagrangian parcels, I searched all tracks for each year to identify the nearest one on the 100th day of the year. This date was chosen as it is prior to melt onset and snow ablation at all stations. These were, on average, 8 km away (see Fig. S38 for the distribution). However, while the drift-tracks of the stations and the model-parcels matched in a broad sense, the NP stations generally drifted slightly further in the time until August 1st (when my analysis ended; Fig. S39).

To make a quantitative comparison between the timing of snow ablation at paired SM-LG parcels and NP stations, I applied the same thresholding method to the SM-LG parcel. The spring maximum of the SM-LG parcel's snow depth timeseries was found. The day on which the snow depth subsequently dropped below 40% of that value was then found, and compared to the corresponding value at the paired NP station.

As well as timing, I investigate the speed of melt onset at NP stations and for SM-LG parcels (for comparison with Kwok et al., 2020a). To do this, I generate the reference day of snow ablation as above. I then take a three or five-day window centred on that timing, and perform a linear regression through the snow depths in

that window. A sensitivity analysis indicated that the window-width does not have a significant effect on the calculated ablation speeds.

To investigate the causes of observed differences in snow ablation timing in SM-LG and in-situ, I compare the timeseries of surface air temperatures in the SM-LG forcing to those measured in-situ. Here I analyse input and output of the model when forced by the ERA5 atmospheric reanalysis (Hersbach et al., 2020), although I note that other model runs have been done driven by the MERRA2 atmospheric reanalysis.

5.3.4 Comparing satellite melt onset products to SnowModel-LG output

While it does not directly relate to snow observations from NP stations, I also investigated how melt onset in SM-LG compares to satellite products of melt onset. In Sect. 5.4.3 I compare the timing of snow ablation in SM-LG with the timing of snow ablation measured in-situ at nearby stations. However, due to the differences between the timing of melt onset (snow reaching melting point) and the timing of actual snow ablation (snow depth decreasing), it would not make sense to compare the timing of the '40% the prior maximum depth' method used in Sect 5.4.3 to the passive-microwave satellite products described in Sect. 5.4.1, even with a fixed offset.

To provide a more meaningful comparison between SM-LG and passive-microwave-based products, I diagnose when liquid water appears in SM-LG parcels. To do this, I analysed two variables: the daily snow melt (in cm of snow water equivalent) and the skin temperature of each SM-LG parcel in each year. The daily snow melt diagnostic is similar to that used by Nicolaus et al. (2006) with the SNTHERM model (Jordan, 1991). Once I identified that a parcel had experienced melt onset, this was marked in a database. This resulted in a list of position/date pairs, with one pair corresponding to each Lagrangian track that was present at melt onset. The dates were then gridded onto the same polar stereographic grid as the satellite melt onset product for comparison using both a drop-in-the-bucket method (e.g. Dinnat and Brucker, 2017) and an inverse-distance weighting method (following Liston

et al., 2020). I first defined the date of snow melt onset in an SM-LG parcel as when the snow melt first exceeded 5 mm per day. This threshold was settled on after a sensitivity analysis: if the threshold is too high, parcels do not necessarily reach it, and some areas do not experience melt onset. There seems to be a fairly small penalty for setting it too low. Lower thresholds generally result in earlier melt onset (the threshold is exceeded earlier), which increases the bias of SM-LG relative to the satellite product. However,the representation of interannual variability is slightly improved. I elected to focus my evaluation of SM-LG on its representation of interannual variability (i.e. does the model capture anomalously late- and early-melting years in a 25 $\times$ 25 km pixel or region), and so I set a low threshold of 5 mm/day. Further details concerning the sensitivity analysis can be found in Supplementary Fig. S37.

When capturing a SM-LG parcel's melt onset characteristics from the perspective of the skin temperature, I set a temperature threshold of -0.1 °C, and marked melt onset as the first day that threshold was exceeded. Because the snow in SM-LG melts at 0°C, it is not practically possible to set this value as a threshold. The skin temperature diagnostic contains an implicit assumption that the snow is melted first from the top, and sub-surface melting (e.g. Koh and Jordan, 1995) is not a significant influence on the timing of melt onset in the model. The choice of threshold value also reflects the fact that snow salinity is not included in SM-LG, so all snow melts at 0°C and not below.

I carried out my analysis both at the 25 $\times$ 25 km pixel scale, and on the regional scale. For the pixel scale, I compared the coverage of statistically significant correlations between the different diagnostics, and the average strength of those correlations. For the regional analysis, I split the Arctic Ocean up into six marginal seas and the Central Arctic using the definitions of Meier et al. (2007, see Chapters 2 & 3). For each year and each region I generated a timeseries of the area-mean melt onset timing in the satellite product and the three model-based diagnostics described previously.

In my comparisons, the surface air temperature-based diagnostic of melt onset

timing acts as a control. If the two model-derived diagnostics (snow melt and skin temperature) outperform the surface air temperature based diagnostic, then SM-LG is assumed to show skill in representing the timing of melt onset. If the air temperature based diagnostic outperforms the model-based ones, then SM-LG is assumed to not be meaningfully representing the extra effects of radiative balance and snow physical properties on melt onset timings.

5.3.5 Mean meteorological conditions before, during and after snow ablation

I analysed several meteorological variables over the period of melt onset and snow ablation. Specifically, I sought to extract the statistical behaviour of the variables from the relatively noisy individual timeseries by synchronising the records with respect to the reference snow ablation timing. The most rigorous way to do this was to use the quantitative estimate of snow ablation timing described previously - i.e. the day on which the snow depth falls below 40% of its spring-maximum value. It is important to stress that this is indeed a *statistical* delineation, and there is no specific geophysical interpretation of the threshold.

After synchronising the snow and meteorological timeseries, I created ensemble means of the derived albedo, surface air temperature, specific humidity and low cloudiness. I also analysed the relative humidity, total cloudiness, sea level pressure and wind speed in a similar fashion; plots of these variables are available in the supplement but analysis is not carried out in the main text. The shortwave radiometry measurements necessary for calculation of derived albedo were only available from NP 17 (1965) onwards, and as such there are fewer contributing timeseries to the ensemble than for the meteorological variables.

I note that a similar analysis of albedo evolution was performed in Perovich et al. (2002, Fig. 13), however the novelty of this analysis is that the timeseries are shifted such that snow ablation is synchronised in each record. By removing the inter-station variability in snow ablation timing from the analysis, the specific relationship between albedo, meteorology and ablation is made clearer. Futhermore, this shift allows the ensemble-mean timeseries to be meaningfully improved from

the monthly resolution at which it was displayed by Perovich et al. (2002).

5.4 Results

5.4.1 Comparison with satellite-derived melt onset products

Figure 5.4 shows how the satellite-derived melt onset timing compares to the timing of snow ablation observed in-situ. The panels indicate that while the satellite products generally capture the rough timing of snow depth decline (ablation), significant mismatches are sometimes present. This is particularly clear when the satellite-products lag behind the snow ablation (e.g. Fig. 5.4f & i). When the satellite product registers melt onset before the snow ablation, it is possible that liquid water did indeed appear in the snowpack, but the snow then refroze before it could substantially ablate. However,when the satellite registers melt onset *after* the snow depth decline, the product is likely not capturing the local geophysical evolution.

Large discrepancies between the satellite product and observations are more common with the AHRA product of Drobot and Anderson (2001, see lags in panels e & f) than the CMO product of Markus et al. (2009). One particularly visible discrepancy is seen at 1979/NP 22 (panel a), where the CMO product roughly captures the timing of the snow ablation, whereas the AHRA product is triggered a month and a half too early. A similar situation seemingly exists for 1990/NP 30 (panel i), where the CMO product misses the snow ablation, whereas the AHRA product is again very early. Where the AHRA is very early, it is noticeable that the triggering coincides with visible spikes in surface air temperature. However, these spikes are not close to crossing the 0°C air temperature threshold. I further investigate these cases in Sect. 5.5.1.

Turning to the surface air temperature threshold analysis, it is noticeable that while the AHRA and CMO algorithms often produce different results, at least one of them is consistently near to the day-of-year where air temperatures exceed zero degrees for the first time. Only three of the eleven melt onsets in Fig. 5.4 feature the temperature threshold being exceeded more than seven days from both of the two melt onset products. The CMO product is more frequently within seven days

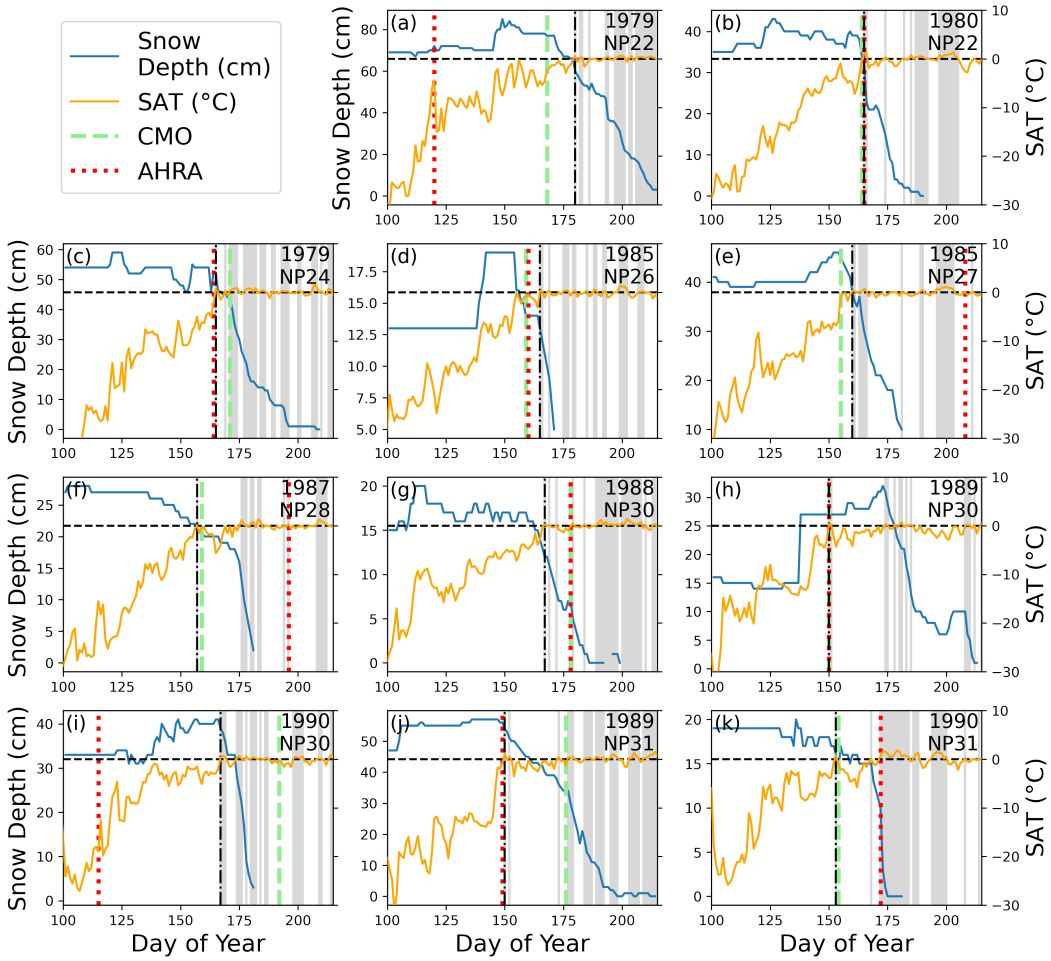

Figure 5.4: Co-evolution of surface air temperature (SAT; orange lines) and snow depth (blue lines) at the eleven NP stations that were both observed by satellite radiometers during the period of melt onset and took daily snow depth observations consistently. Vertical green lines indicate the melt onset timing per the Continuous Melt Onset product of Markus et al. (2009), red lines indicate the timing per the Advanced Horizontal Range Algorithm product first described by Drobot and Anderson (2001). Horizontal black dashed line indicates the 0°C threshold of surface air temperature. Vertical, black dot-dashed line indicates the first day that the surface air temperature exceeds this 0°C threshold. Grey bands indicate periods where the mean daily surface air temperatures was above 0°C

of the temperature threshold being broken (7 of the melt onsets, compared to 5 for AHRA). Furthermore, when the CMO algorithm is not within one week of the temperature threshold, the difference between the two timings is around half that of the corresponding AHRA difference (18.5 days difference vs 38.2 days difference). The overall standard deviation between the CMO product and the temperature threshold method is 12.3 days, compared to 31.1 days for AHRA. From this I infer that the CMO algorithm more closely traces the timing of the 0°C temperature threshold being exceeded (although this should not be interpreted as CMO being 'better' in an absolute sense). The distributions of these timings are displayed as scatter plots in Fig. S40.

It is also instructive to view the triggering of satellite melt onset products alongside the evolution of in-situ derived albedo (Fig. 5.5). There is frequently a dip in albedo that coincides with one or both of the melt onset products being triggered (see AHRA in panel k, both products in panel g, and the CMO product in panel j). It appears that changes in the derived albedo can faithfully indicate modifications of the snow surface by melting. Panel j (NP 31/1989) presents a particularly interesting albedo timeseries: the AHRA product is triggered on day 150 by a 1-day excursion in surface air temperature above zero. The temperature then falls back down below zero for another 23 days, however snow depth consistently declines in that three week period. Why does the snow thin in this time when surface air temperatures are below zero? The albedo timeseries indicates that the snow was fundamentally modified by the day-150 warm event, as its albedo dropped by about 15%. This was associated by a rain event recorded in the meteorological data. Physical modification by rain such that it could absorb more solar radiation is likely a contributing factor to its ablation in the subsequent sub-zero air temperatures, however it may also be symptomatic of more profound changes in the susceptibility of the snow to evaporation or sublimation. On day 175, air temperatures rise again above zero, the CMO algorithm is triggered, and ablation accelerates. This is reflected by another, larger step change in the albedo.

A lack of albedo change as the snow thins is also potentially informative. For

instance at NP 28 in 1987 (panel f), the snow thins consistently before the air temperature rises above 0°C and the CMO algorithm is triggered (on day 160). This 'early' snow thinning is not associated in a change in albedo, which is itself associated with melting. I interpret this as evidence that the snow is thinning without melting, potentially either via wind redistribution or by evaporation/sublimation. When the CMO is subsequently triggered (shortly after a day above 0°C), there is an associated drop in albedo.

A final, striking comparison is between the melt onsets at NP 30 in 1989 (panel h) and NP 22 in 1980 (panel b). The NP 30/1989 melt is the only example where both melt onset algorithms are coincident in time, as well as matching the first day that temperatures exceed 0°C. This is almost the case for NP 22/1980, where the air temperature threshold is exceeded on the same day as AHRA triggering, which both lag the CMO algorithm by one day. It is important to note however that during this period the melt onset products are produced by the SMMR instrument which only had every-other-day sampling, introducing a 1-day margin of error. These two case studies both have good agreement between all three melt onset diagnostics, so I therefore treat the timing as 'high confidence'. Based on the strong agreement, it is interesting that the snow depth at NP 30/1989 does not decrease for another 25 days after the determined day of melt onset. This is in contrast to NP 22/1980, where the depth is already decreasing on the determined day of melt onset and continues to precipitously decline afterwards.

The cause of this difference appears to be the duration for which temperatures remain above zero in the aftermath of melt onset. At NP 30 in 1989, temperatures drop back to around -4°C after the above-freezing excursion. At NP 28, they remain above freezing for three days. These higher temperatures are also associated with higher low and total cloud cover, and higher relative and absolute humidity in both the five- and ten-day period after the respective melt onsets (Supp. Fig. S41). NP 30/1989 illustrates an instance where 'continuous melt onset' is not necessarily strictly continuous at a given site - refreezing and further snow accumulation is possible (See 'Phase II' of Vérin et al., 2022, for a similar case).

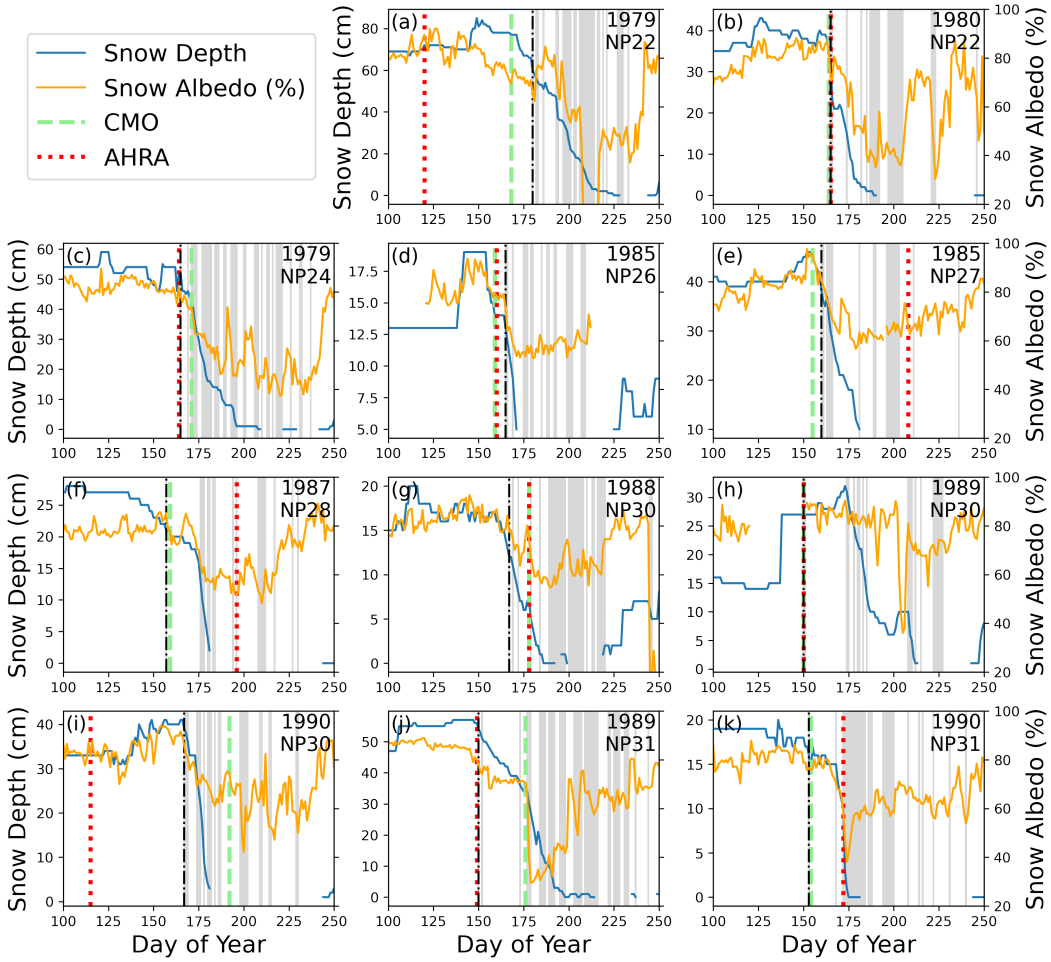

Figure 5.5: Co-evolution of derived albedo (orange lines, %) and snow depth (blue lines, cm) at the eleven NP stations that were both observed by satellite radiometers during the period of melt onset and took daily snow depth observations consistently. Vertical green lines indicate the melt onset timing per the Continuous Melt Onset product of Markus et al. (2009), red lines indicate the timing per the Advanced Horizontal Range Algorithm product first described by Drobot and Anderson (2001). Vertical, black dot-dashed line indicates the first day that the mean daily surface air temperature exceeds 0°C. Grey bands indicate periods where the mean daily surface air temperatures was above 0°C

It should also be considered that the seemingly early melt onset diagnosed by both satellite products at NP 30/1989 is accompanied by a mixed phase precipitation event, which may have modified the snow surface in a way that triggered satellite-based products without actually representing melt onset (Supp. Fig. S42). On the other hand, the melt onset similarly recorded by both diagnostics in 1980 at NP 22 coincides with the first rain event of the season, and is likely caused by it (See Persson et al., 2002; Ehn et al., 2006; Dou et al., 2019). The first appearance of liquid precipitation is also roughly coincident with melt onset at NP 24 in 1979 and NP 31 in 1989 (panels c & j). In both cases, these rain events trigger the AHRA product, but not the CMO.

5.4.2 Characteristics of snow ablation at NP stations

Figure 5.6 shows the distributions and relationships between snow ablation, the prior maximum snow depth, and the speed of ablation at NP stations. The mean ablation rate at the stations around their respective reference ablation days was -2.17 cm/day (when calculated with a five-day window), with a standard deviation of 1 cm/day. When recalculated with a three-day window, it was -2.34 cm/day (with a standard deviation of 1.2 cm/day). The mean day of crossing the 40% threshold was day-of-year 180, with a standard deviation of 11 days.

A statistically significant correlation ($r = 0.38$, $p = 0.009$) was observed between the spring maximum depth and the subsequent time at which the snow depth dropped below 40% of that depth. No statistically significant relationship was observed between the timing of ablation and the ablation rate, or the ablation rate and the prior spring's maximum snow depth.

I also performed an analysis of surface air temperature, to search for a link between higher air temperatures and ablation rate (in the five day window centred on the reference ablation day). Although r-values were consistently negative, none of them were statistically significant. This test was done using various values of window-length.

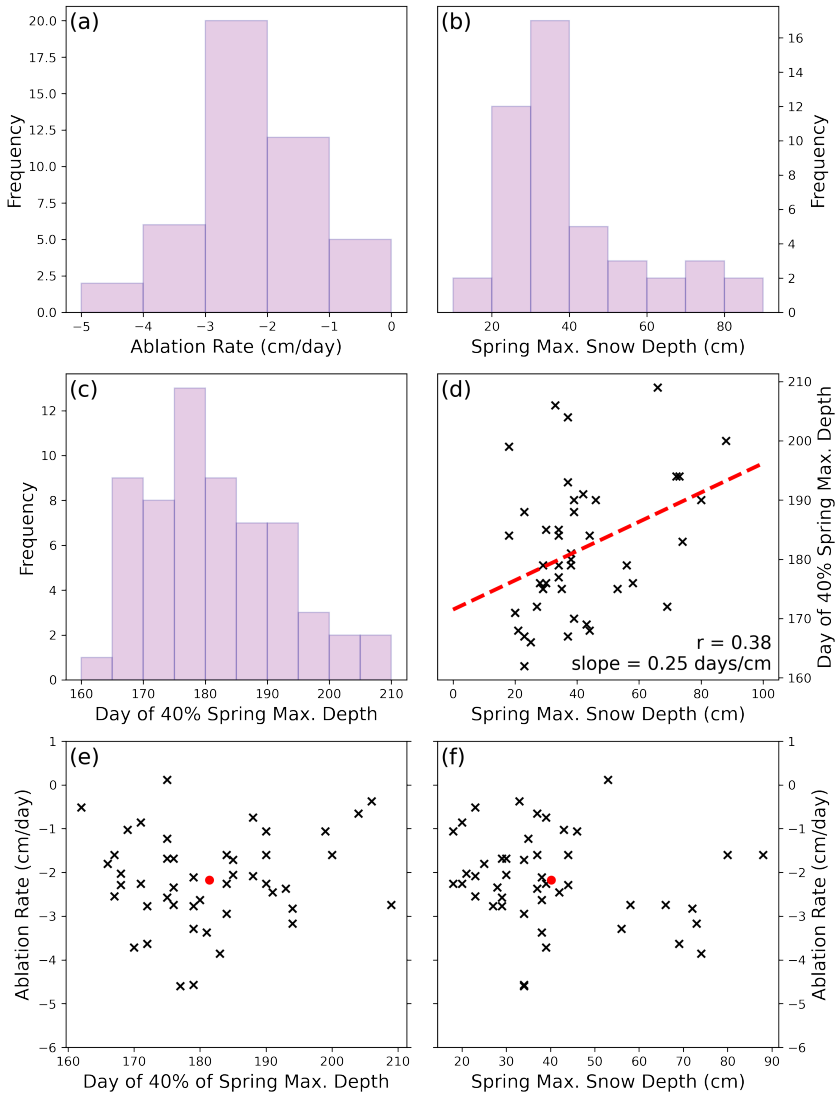

Figure 5.6: (a) Distributions of ablation rate (calculated with a five-day window) on the day that the 40% threshold is crossed. (b) Distribution of prior spring-maximum snow depth prior to ablation. (c) Distribution of timings for when NP station depth crosses 40% of max-value threshold. (d) Relationship between the prior-maximum snow depth and the day on which the snow depth is reduced to below 40% of the value. Red dashed line indicates a regression line through the data (e) Relationship between ablation rate (cm/day at time of dropping below 40% threshold) and the timing of the threshold being exceeded. Later ablation is not obviously associated with faster ablation. (f) Relationship between ablation rate and prior maximum snow depth. Deeper snow does not obviously melt faster. Red markers indicate the centroids of the distributions.

5.4.3 Comparing snow ablation at NP stations with SnowModel-LG

I display the co-evolution of snow depth at the fourteen SM-LG tracks studied, alongside their corresponding NP stations in Fig. 5.7. There are more comparable series in this analysis than for the comparison with radiometer-derived melt onset timings (14 vs 11), as SM-LG has full coverage up to 90°N. The snow depth timeseries from the model demonstrate a persistent early-bias by comparison to observations. To quantify this bias, the day-of-year on which snow depth declines to below 40% prior-maximum value was calculated for both the model output and observations. On average for the fourteen stations (and their corresponding tracks), this threshold was crossed 8.4 days earlier in the model than observed in-situ (Fig. 5.8a).

The literature (Sect. 5.1.1) and Figure 5.4 indicate that the surface air temperature (specifically the 0°C threshold) is a strong driver of melt onset: it is therefore the first line of investigation for bias in SM-LG. In Fig. 5.8b I show that the timing with which the 0°C threshold is exceeded is generally earlier in the reanalysis that drives SM-LG than as measured at the NP stations. In fact on average it is 8.9 days earlier, which is a very similar figure to the 8.4 day SM-LG early bias in snow ablation timing.

Could this 8.9 day-early temperature bias explain the 8.4 day snow ablation bias? It would seem not; Fig. 5.8c shows the relationship between the temperature-threshold and snow-ablation biases for individual stations. There is no clear relationship between a SM-LG parcel exceeding the 0°C threshold particularly early in its forcing (relative to its paired NP station), and its snow ablating anomalously earlier. I discuss other potential reasons for this bias in Sect. 5.5.2.

I now turn to the rate of snow ablation in SM-LG, and compare it to the corresponding NP-stations (Fig. 5.8d). Recall that the ablation rate is calculated as the slope of the regression line through snow depth in the the days surrounding the reference date of snow ablation. On average, SM-LG parcels capture the typical rate of snow ablation observed in-situ. However, the NP stations that ablate faster are not

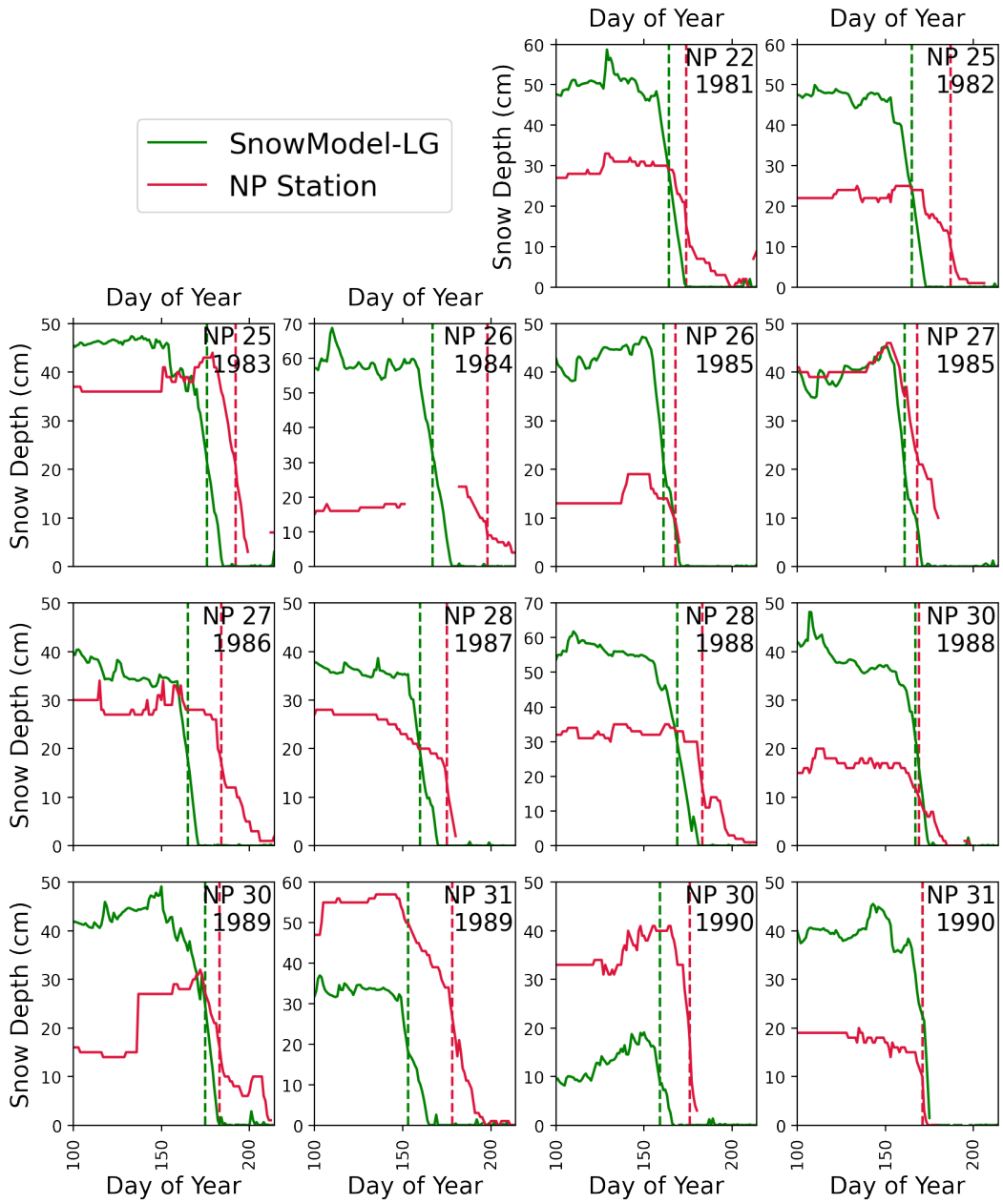

Figure 5.7: Individual comparisons between the timing of snow ablation in SM-LG and nearby NP stations. Solid red lines indicate snow depth observations at stakes, solid green lines indicate modelled snow depth of the nearest SM-LG parcels. Dashed lines indicate the day on which the relevant snow depth drops below 40% of its prior spring maximum value.

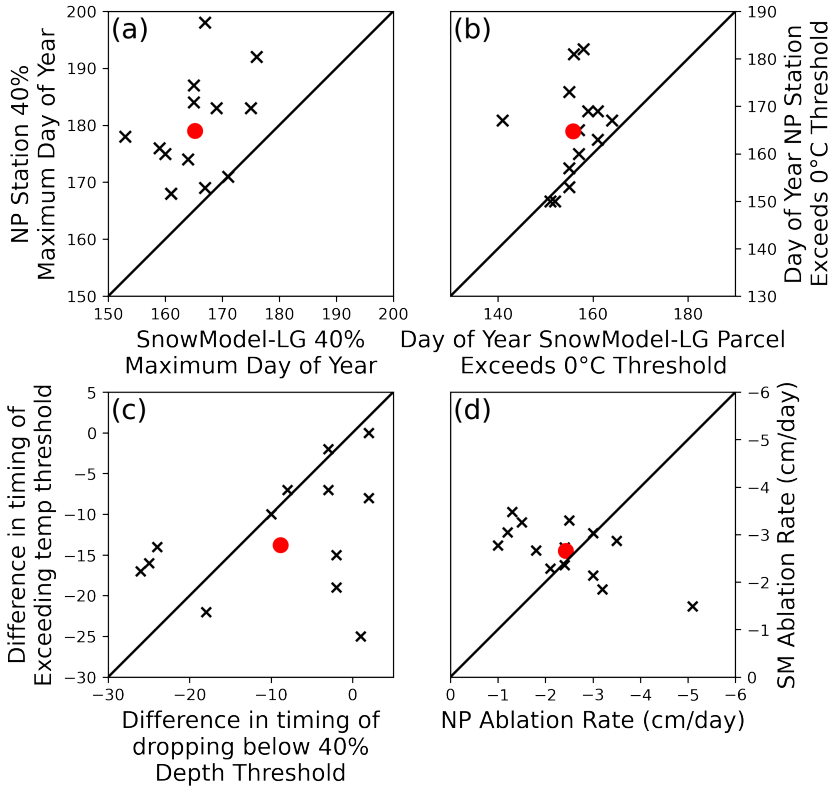

Figure 5.8: (a) Comparison between the timing of snow ablation in SnowModel-LG and nearby NP stations. SnowModel-LG exhibits snow ablation approximately 8.4 days earlier than the corresponding NP stations. (b) Comparison between the timing with which 0°C is reached by the atmospheric reanalysis that forces SnowModel-LG, and by the in-situ thermometers. SnowModel-LG forcing exceeds the threshold earlier than the in-situ measurements by an average of 8.85 days. (c) Relationship between earlier snow ablation in SnowModel-LG and earlier crossing of the 0°C threshold. No clear relationship is visible. (d) Ablation rates at the NP stations and nearby corresponding SnowModel-LG parcels, calculated with a 5-day window centred on the reference day of ablation. Red markers indicate the centroids of the distributions.

paired with fast-ablating SM-LG parcels. In fact, the opposite is the case: there is a statistically significant negative correlation (r=-0.67, p = 0.008) between the speed that an NP station ablates and the speed with which its paired SM-LG station ablates.

The SM-LG parcels considered here generally have less variability in their ablation rates than the NP stations. For example, for the three-day wide window, the standard deviation in the fourteen calculated ablation rates is 1.34 cm/day for the NP stations and 0.716 cm/day for the SM-LG stations. For the five-day window these figures are 1.06 and 0.55 cm per day respectively.

5.4.4 Comparing Melt Onset in SnowModel-LG with Satellite Products

To illustrate my analysis of the 'daily snow melt' quantity in the Lagrangian output of SM-LG, I begin by visualising the data for the same fourteen tracks analysed in the previous section (Fig. 5.9). These data indicate that there is a pulse of melting in the snowpack that coincides with the beginning of the snow ablation. Occasionally (e.g. NP 30 1990), there is a pulse prior to that, while snow is still accumulating. This represents an early and unsustained period of melting, followed by refreezing; this could be seen as corresponding to the *Early Melt Onset* product of Markus et al. (2009).

Turning first to the pixel-scale analysis, all three diagnostics show more widespread correlations with the AHRA melt onset product than they do with the CMO product (Supplementary figures S43 & S44). For the CMO-based comparison, the two SM-LG 'output' diagnostics (snow melt and skin temperature) do not outperform the 'input' diagnostic of ERA5 surface air temperature. As such, the model does not obviously show skill in representing the CMO product at the pixel (25 km) scale. However, for the AHRA comparison, the snow melt diagnostic of melt onset marginally outperforms the air temperature-based diagnostic, and its typical correlation with the AHRA data is higher than any of the CMO based comparisons. SM-LG is therefore understood to show some skill at the pixel scale in representing the AHRA melt onset product.

At the regional scale, the picture is different (Fig. 5.10). For the CMO evaluation, the air temperature still seems to perform better (relative to the skin temperature and snow melt diagnostics) in the individual marginal seas. However, in the Central Arctic region, the aggregated marginal seas area, and the pan-Arctic grouping, the skin temperature consistently performs the best, seemingly due to the larger areas involved. In both the marginal seas aggregation and the pan-Arctic area, the snow melt diagnostic also outperforms the air temperature diagnostic significantly. SM-LG can therefore be understood to show skill at simulating the CMO data on these larger scales (albeit not at the smaller scales of the individual marginal seas).

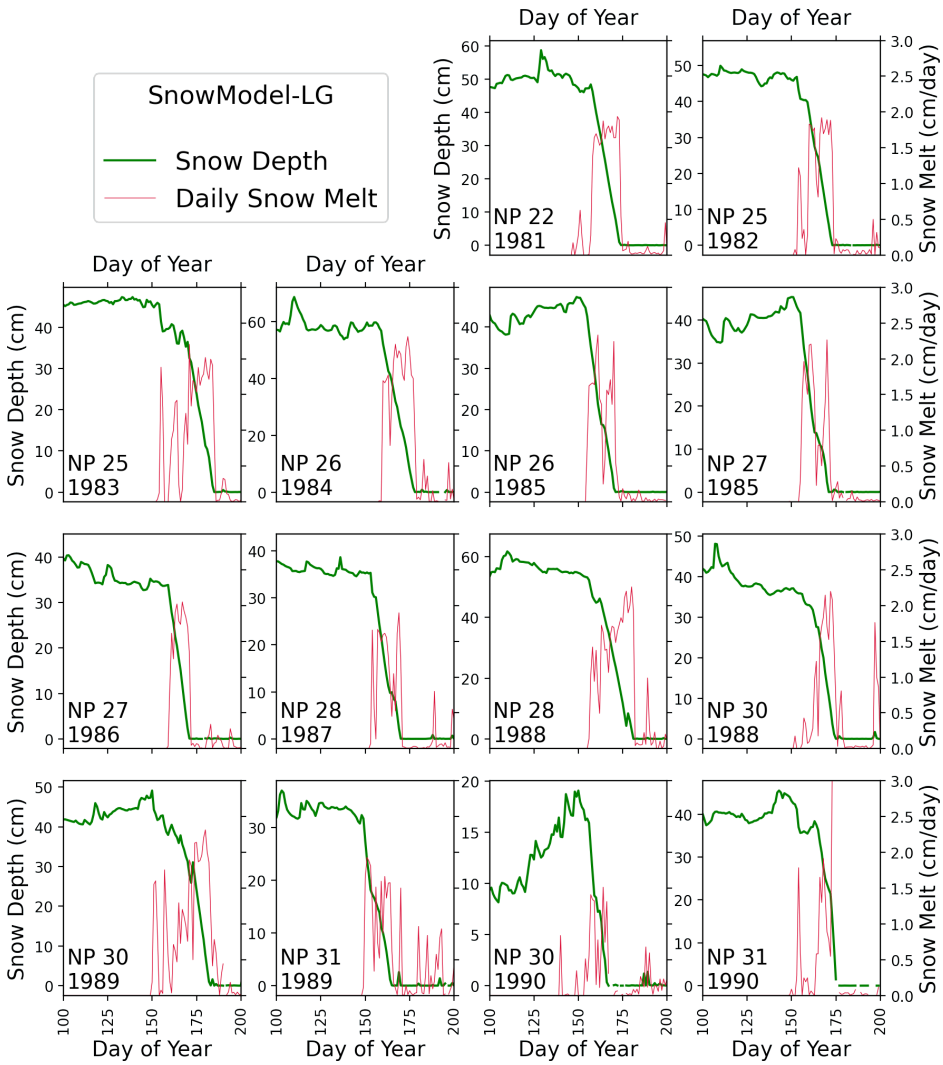

Figure 5.9: Evolution of snow depth and daily snow melt at the 14 SM-LG parcels that were paired with NP stations for comparison. Red lines indicate the snow melt quantity, and show a clear spike that generally coincides with the start of snow ablation.

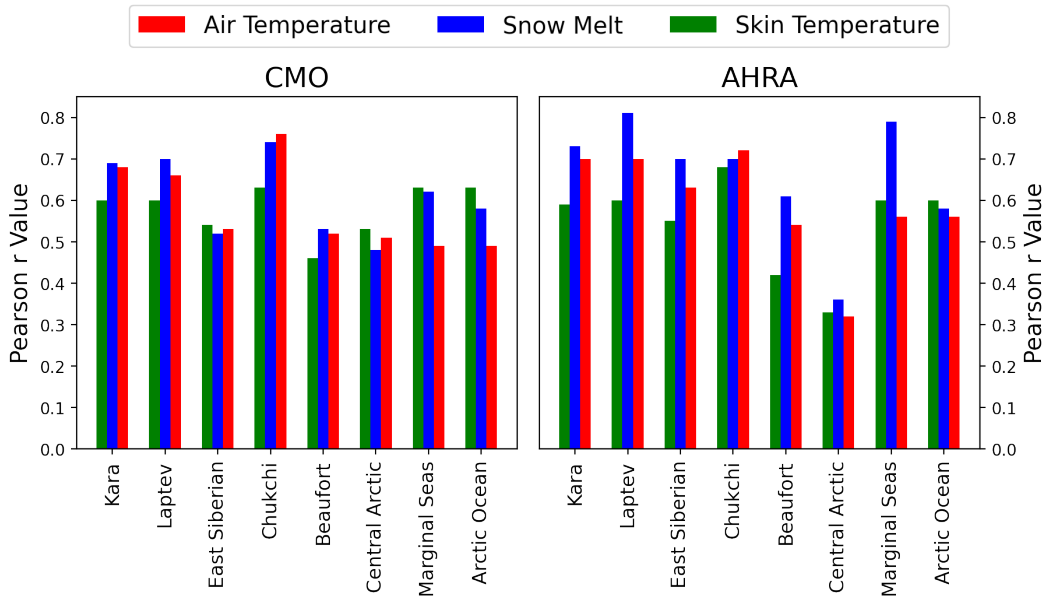

Figure 5.10: Skill of different SM-LG derived diagnostics of melt onset timing, where a diagnostic's skill is defined as representation of regional interannual variability in two radiometry-derived melt onset products. The two products are the continuous melt onset (CMO) product of Markus et al. (2009), and the Advanced Horizontal Range Algorithm product (AHRA) of Drobot and Anderson (2001). Red bars indicate the timing with which daily 2m air temperatures exceed 0°C, blue bars indicate the timing with which snow melt exceeds 5 mm of snow water equivalent per day, and skin temp represents the timing with which the snow surface (skin) temperature exceeds 0°C for the first time.

Unlike the CMO data, the SM-LG snow melt diagnostic appears to show skill even on the regional scale when evaluated against AHRA data. Skill scores of all three diagnostics are noticeably suppressed in the Central Arctic regions relative to the CMO evaluation, where the lowest scores of this evaluation exercise are produced. Conversely, the snow melt diagnostic shows high skill in the aggregated grouping of the 'marginal seas' in the AHRA comparison. The highest score of both regional evaluation exercises is r = 0.81 for the AHRA evaluation in the Laptev Sea. In all but one of the individual marginal seas and all the large areas of the Central Arctic, the aggregated marginal seas, and the pan-Arctic scale, the snow melt diagnostic outperforms the surface air temperature diagnostic. This good performance indicates that SM-LG is realistically representing the physics of the snow radiative balance and the snow's properties in modelling melt onset. This is both on the scale of the individual marginal seas, and the larger, composite areas.

As described previously, once melt onset had been determined for each individual parcel, the parcel-wise data were gridded using both a drop-in-the-bucket method and an inverse-distance weighting. In the former, the date of melt onset for all parcels that experienced melt onset within a 25 km polar-stereographic grid-cell were averaged. In the latter method, a weighted average was performed on the same data, with weights determined by the inverse of the distance of the parcel from the centre of the grid-cell. Implementing the inverse-distance method generally had a small effect in the marginal seas, but did boost the r-value score of the 'snow melt' and the 'skin temperature' methods in the Central Arctic for both satellite data sets by around 0.1.

5.4.5 Mean meteorological conditions in the melt onset period

I now consider the evolution of the ensemble-mean albedo in the period surrounding the reference day of snow ablation. To do this, I plot the evolution of the absolute value and time-derivative (Fig. 5.11b & c). The individual albedo estimates (panel b, grey lines) are fairly constant and tightly grouped in the period between 40 and 25 days before the reference day of ablation. The spread between the timeseries (the standard deviation) then begins to widen before the reference day of ablation. After the reference day of ablation the spread between the lines is noticeably larger: the time-averaged standard deviation after day-zero is more than double the standard deviation before (13% vs 6%).

As well as increasing in spread, the albedo begins to drop off before the reference day of ablation. The steepest drop-off in albedo comes in the seven-day period before peak ablation (when the snow is beginning to ablate; see panel a). The steepest one-day drop-off in the mean albedo timeseries is -3.3%, and occurs between the measurements on the third day and the second day before the reference day of ablation

There is a more noticeable discontinuity across the reference day of snow ablation in the meteorological timeseries (Fig. 5.12) than in the snow albedo. Although there is large spread between the individual timeseries of air temperature, a clear pattern emerges in the ensemble average of the timeseries. In the 20 days leading

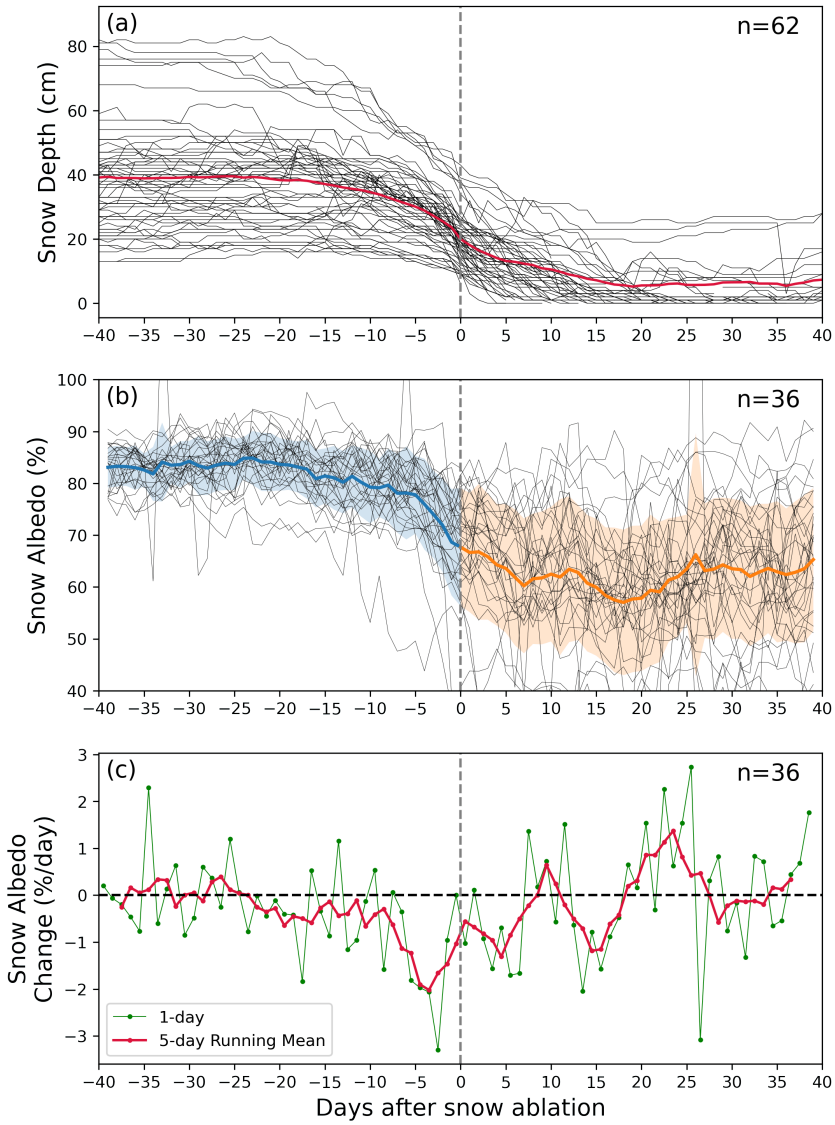

Figure 5.11: Evolution of snow depth and albedo before, during and after snow ablation based on the 40% threshold. Top panel illustrates the snow depth evolution in this period; day-zero is defined as when the snow depth falls below half the maximum value. Middle panel illustrates the evolution of snow albedo - grey lines indicate individual timeseries, blue and orange lines indicates the all-timeseries average before and after day-zero respectively. Shaded regions represent one standard-deviation either side of mean value. Bottom panel shows the gradient of the blue/orange timeseries in the middle panel. Gradient calculated point-to-point (green line), and from a five-day running mean (red line).

up to the reference day of snow ablation, there is a highly linear increase in air temperature towards 0°C. This has the diurnal temperature oscillation superimposed on it. The day prior to the reference day of snow ablation features, on average, above zero temperatures during the warmest part of the day. This is the warmest temperature of the ensemble-mean timeseries. This is clearly relevant to the fact that the peak snow ablation occurs between that day's measurement and the following.

The average temperatures are lower after the day of peak snow ablation, generally not exceeding zero degrees. Unlike before the reference day of snow ablation, where there was a clear trend, there is no trend in daily temperatures afterwards. Another notable feature of the ensemble-mean air temperature timeseries is that the amplitude of the diurnal oscillations is suppressed after snow ablation. To quantify this, I detrended both timeseries shown in Fig. 5.12a by subtracting a multi-day running mean from the values (noting that this had minimal effect on the red timeseries which was essentially detrended already). This acts as a high-pass filter, isolating the diurnal oscillations. I then calculated the standard deviation of the detrended timeseries, and noted that the RMS value for the 'after' timeseries was between 35 and 50% of the 'before' timeseries (Supplementary Fig. S45). This range of values comes from the variable number of days I used for the running mean in the high-pass filter, with wider kernels generally lowering the resulting percentage-value.

There also appear to be contrasting trends in low cloud cover before and after the reference day of snow ablation (Fig. 5.12b). In the 20 days prior to melt onset, the slope of the regression line is -0.05 tenths of cloud cover per day - this results in the reduction of one tenth on average over the period. After the reference day of snow ablation, the slope of the regression line is +0.03 tenths per day. However, to the eye it appears that there is also potentially a step change in the absolute values on the day following the reference day of ablation. The presence of low cloud values *after* the reference day of ablation may in fact be skewing the regression line of the red timeseries to a positive gradient. To put this another way, our break-point at x = 0 for the two regression lines in Fig. 5.12b may not actually be the most physically meaningful one. This is especially the case given the reference day of ablation was

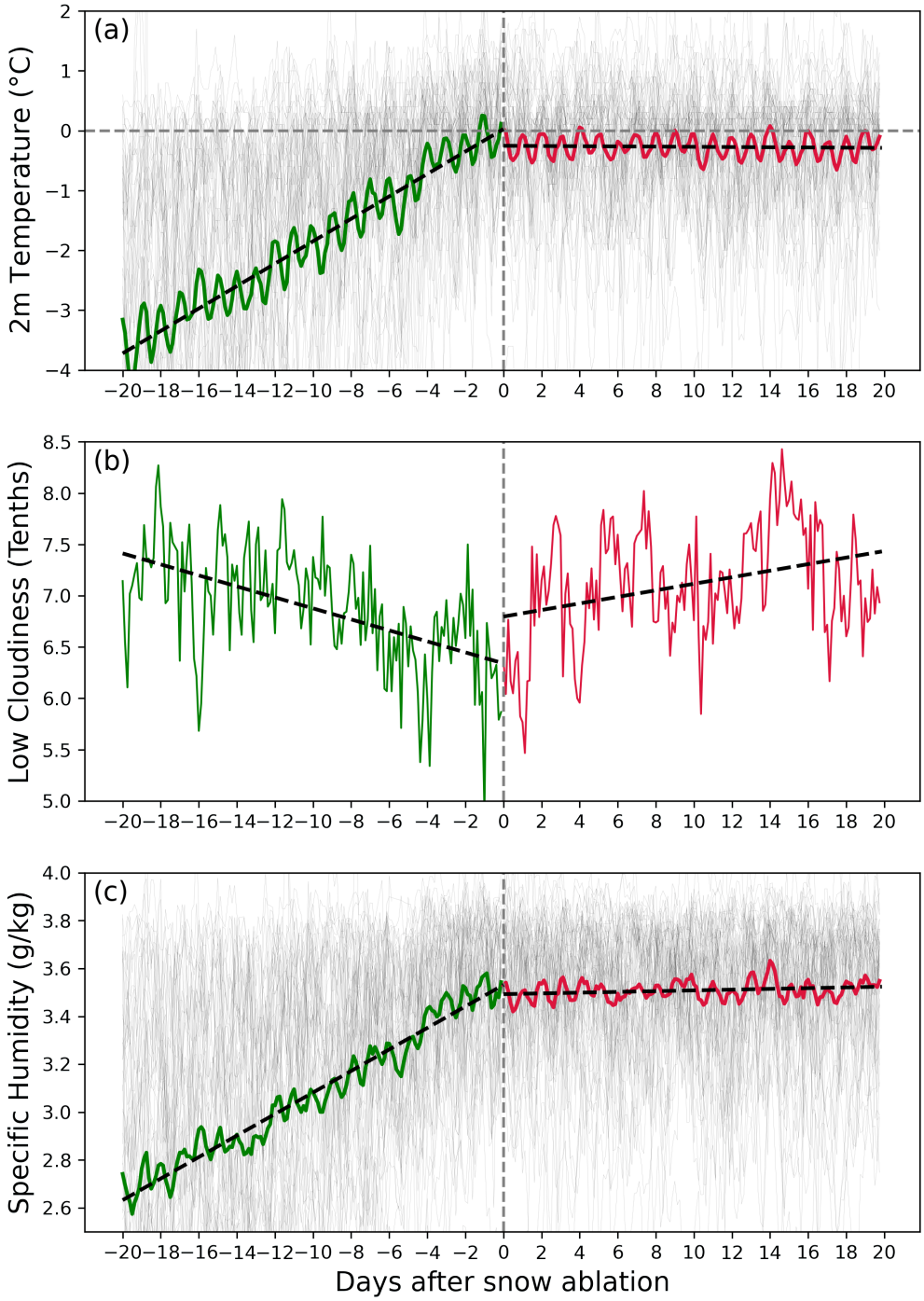

Figure 5.12: Evolution of surface air temperature, low cloud cover and specific humidity before, during and after snow ablation. Day-zero on the x axis represents the timing with which the individual snow depth timeseries (Fig 5.11) fell to less than 40% of their spring maximum value. Green and red lines represent mean values of the timeseries before and after day-zero respectively. Grey tracer-lines represent individual timeseries - these are not meaningfully visible for the low-cloud panel as values tend to oscillate between 0 & 10. Black dashed lines show linear regressions between the before and after timeseries.

statistically defined, and doesn't represent melt onset nor the start or end of snow ablation.

To try to detect the distinction between the potential two regimes, I conducted a break-point analysis following Tomé and Miranda (2004). This involves fitting two regression lines to two different but contiguous parts of the timeseries separated by a *break-point*, and investigating what break-point position results in the best fit of the regression lines. However, unlike Tomé and Miranda I relax the requirement that the regression lines be continuous (i.e. have the same value at the break-point). This allows my analysis to be open to the possibility of a step-change in cloud conditions in response to snow ablation.

The results of the break-point analysis support what was described qualitatively above. The two regression lines fit their respective timeseries best when a break-point is set 36 hours after the point of peak snow ablation. At this point there is a clear minimum in the error-function of the regression lines (Supplementary Fig. S46). This leaves the gradient of the 'before' regression line roughly the same (-0.056 vs -0.053 tenths per day prior), but reduces the gradient of the 'after' regression by an order of magnitude (0.012 vs 0.187 tenths per day prior). For completeness, I also performed the same break-point analysis on the air temperature timeseries. I find that the optimal (error-minimising) break-point is 3 hours after noon on the day of the reference day of snow ablation. I show the results of this break-point analysis in Supplementary Fig. S46. In addition to this, I also display the evolution of the ensemble-mean relative humidity, wind speed, sea level pressure and total cloudiness in Supplementary Fig. S47.

5.5 Discussion

5.5.1 Satellite melt onset products at NP stations

My earlier analysis identified suspicious early triggering of the AHRA algorithm on day-of-year 120 and 115 at NP 22/1979 and NP 30/1990 respectively. Fig. 5.13 provides a view of these incidents in higher time-resolution. For panel a (NP 22/1979), melt onset is detected at the end of a spike in both air temperature and

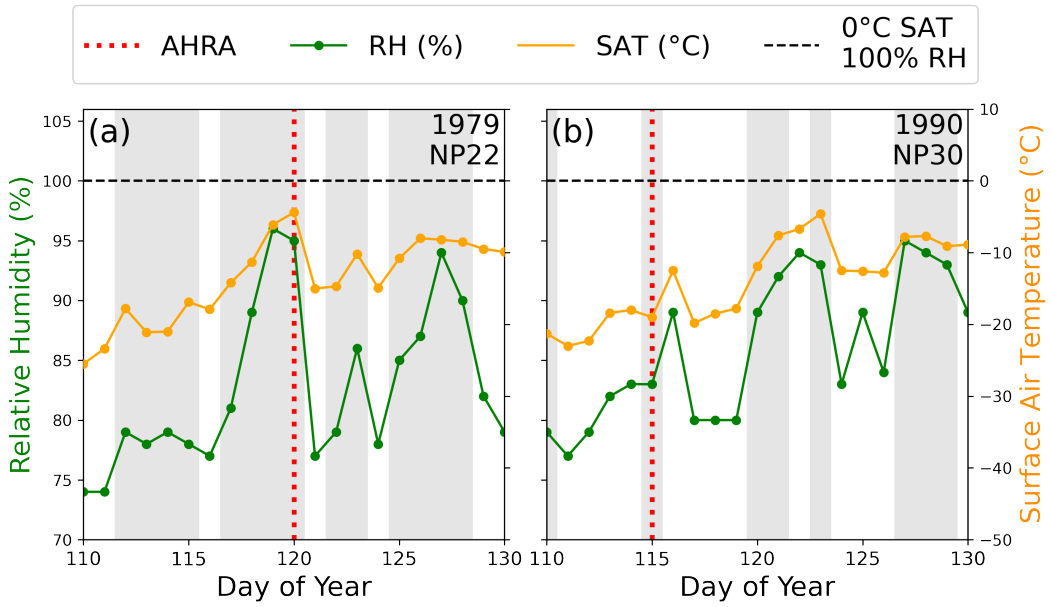

Figure 5.13: Co-evolution of air temperature and relative humidity surrounding the early triggering of the AHRA melt onset algorithm at two NP stations. Grey bands represent periods of high (>5 tenths) low cloud coverage. Black dashed line indicates the 0°C & 100% surface air temperature and relative humidity thresholds. Red dotted line indicates day on which the AHRA algorithm was triggered at each station.

relative humidity. The tendency of the AHRA method to be triggered early was noted by Belchansky et al. (2004a), who specifically discussed the appearance of 'singular melt events in the snowpack that misrepresented onset of the contiguous melt season'. However, it appears that the surface air temperature in neither case was high enough to manifest one of these brief melting events (Fig. 5.13). While a small albedo reduction does take place, albedo generally remains very high and the reduction is well within the weekly variation in frozen periods (Fig. 5.5). However, panel a of Fig. 5.13 does imply that the AHRA algorithm is triggered by some real geophysical signal, since the triggering occurs at a local temperature maximum and a day after a relative humidity maximum. I attribute the early triggering to the opening of a lead, which has been shown to falsely trigger melt onset algorithms such as AHRA (Smith, 1998).

As for panel b (NP 30/1990), the ARHA data feature a visually distinctive swath of early melt onset extending from the North Pole to the Bering Strait (Fig. 5.14).

This swath is not clearly visible in the product of Markus et al. (2009), which was downloaded as part of the same data product from Steele et al. (2019). But does this swath represent a real signal? It is intriguingly also present in all three SM-LG diagnostics of snow melt onset timing (surface air temperature forcing, snow melt and skin temperature). This indicates that it probably does have a physical origin, but likely represents a period of transient melt that does not trigger the 'continuous melt onset' algorithm of Markus et al. (2009).

5.5.2 Comparison of Snow Ablation at NP Stations with SnowModel-LG Parcels

In Sect. 5.4.3 I showed that the ERA5 atmospheric reanalysis typically became warmer, earlier by an amount that seemed consistent with the earlier snow ablation timings. However when considering paired NP stations and SM-LG parcels, parcels that were warmer earlier did not feature correspondingly bigger biases in snow ablation timing. As such, surface air temperature is likely not the primary driving factor of the SM-LG ablation timing bias. Earlier warmth in reanalysis data may in fact reflect another, more relevant variable, such as earlier shifts in downwelling longwave radiation. Unfortunately downwelling longwave radiation was rarely recorded in-situ at drifting stations, so a direct analysis is not possible.

As mentioned in Sect. 5.1.4, Hanesiak et al. (1999) found that the timing of snow melt in a model was sensitive to the time-step of the model forcing due to more intense shortwave forcing. SM-LG is driven by 3-hourly atmospheric reanalysis, begging the question of how melt onset timing would change if the forcing time-step were more frequent. Hanesiak et al. argued that higher time-resolution in forcing resulted *earlier* melt onset, so it seems that increasing the time-resolution of SM-LG is unlikely to reduce the early bias at hand. Running a sensitivity analysis of SM-LG to the forcing time-step may prove insightful in future.

As well as the forcing time-step, the values of the forcings themselves are also uncertain. In this chapter I have focused on the available data produced by the ERA5 atmospheric reanalysis. SM-LG has also been driven by the MERRA-2 atmospheric reanalysis, and a comparison between the model outputs from each forcing data

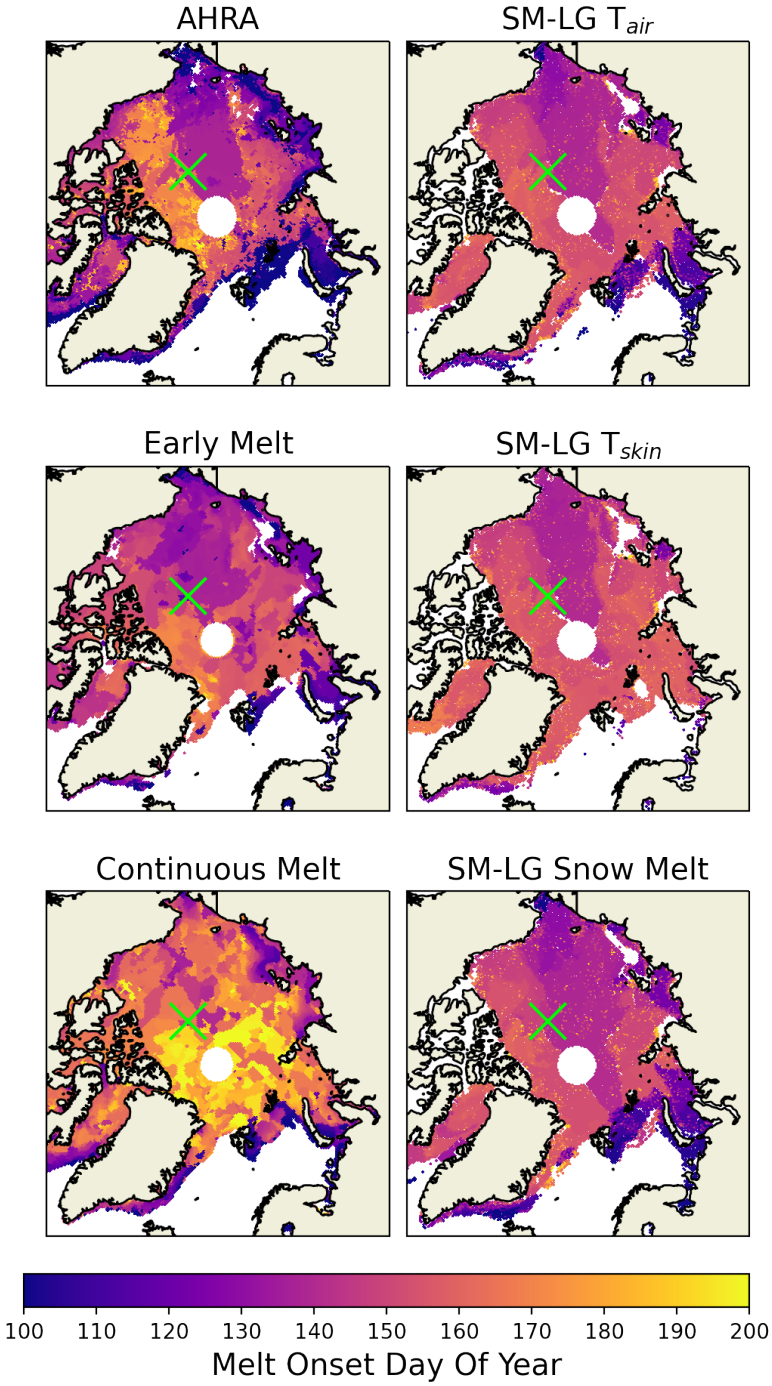

Figure 5.14: Illustration of the 1990 melt onset pattern in both the AHRA (Drobot and Anderson, 2001), Early Melt and CMO (Markus et al., 2009) passive-microwave products, as well as the three SM-LG related melt onset diagnostics. The Early Melt product is generally not discussed in this chapter, however is shown here as it appears it partially reflect the characteristic early streak in SM-LG and AHRA melt onset data. Green marker indicates position of NP 30/1990 when it encounters melt onset per the AHRA product.

set may be instructive as to the impact of the reanalysis uncertainties on modelled melt onset characteristics. However, even if the reanalysis variables were perfectly accurate, there is still uncertainty surrounding how these would translate to forcing of the snow surface. This is because variables such as the snow surface topography are relatively unknown, with knock-on uncertainties on turbulent exchanges of sensible and latent heat. The roughness length for momentum exchange is assumed within the SM-LG meteorology preprocessing to be 10^{-4} m, and conditions of neutral boundary-layer buoyancy are often assumed. Deficiencies in these assumptions may drive inaccuracies in modelled snow ablation timing.

It also possible that higher snow depths in SM-LG parcels compared to their paired NP stations led to their earlier snow ablation. While it is unlikely that the depth will affect the timing of melt onset, it is possible that deeper snowpacks require greater energy input to overcome their liquid water holding capacity and begin significantly reducing in depth due to drainage (Musselman et al., 2017; Colbeck, 1976); this is relevant because reduction in depth is treated synonymously with ablation in this chapter. However, it should be borne in mind that snow depth is just one property of a snowpack; for instance SM-LG may misrepresent the surface albedo of the snow, causing earlier ablation. This was not investigated here as the variable was not available for output. SnowModel-LG might be modified in future to output a larger suite of geophysical variables, which would allow a more precise understanding of its biases.

5.5.3 Representation of snow melt onset timing in SnowModel-LG compared to satellite products

It is unclear what causes the scale dependence of SM-LG's melt onset timing performance when evaluated against radiometry-derived melt onset products. Recall that at smaller scales the model forcing (surface air temperature) performed better relative to the model output diagnostics (snow melt and skin temperature). On large scales, the higher skill of the snow melt diagnostic (a SM-LG output) relative to the air temperature forcing (a SM-LG input) is promising: it indicates that the model is usefully integrating not just information from the surface air temperature, but

also the radiative balance of the snowpack and also the role of the snow conditions themselves. This integration results in improved melt onset timing representation relative to the air temperature alone, at least when evaluated against the AHRA product. At the pixel scale, it is conceivable that the SM-LG performance is poor due to pixel-scale noise in the satellite products themselves, which cannot be replicated by the model.

It is also possible that a sytematic bias exists involving temporal sampling of satellite radiometers. The melt onset products discussed here are generated from gridded products which include the averages of satellite-mounted radiometers on both ascending and descending orbits, thus encapsulating different times of day. However in at some times and places, diurnal forcing is relevant to melt onset timing. An ideal melt onset product would potentially only include data recorded at times of high radiative forcing of the snow.

Considering the marginal seas, what could be the root of the improved SM-LG skill in AHRA relative to CMO? I attribute this to the 'continuous' nature of the CMO algorithm, and my choice of SM-LG diagnostics (in particular the threshold based approach). Because I designed both the snow melt and skin temperature thresholds to be triggered *the first time* that melting and temperature thresholds were exceeded, the resulting timings may not reflect continuous melt, but instead the first instance of melt at a Lagrangian parcel in a given season. This is more similar to the goals of the AHRA algorithm, than the CMO algorithm. In future, the SM-LG diagnostics could require snow melt or skin temperature to remain above a threshold for a certain amount of time to better simulate the CMO product.

In the AHRA evaluation it is noticeable that all diagnostics represent interannual variability in the Central Arctic very poorly; what is it about the Central Arctic that might cause this poor agreement? Firstly, it is striking that because SM-LG does not include the effects of snow salinity, one might expect a worse performance in the marginal seas, where the sea ice is more seasonal and the snowpack is therefore more saline (e.g. Nandan et al., 2017). If this effect is relevant, it appears to be outweighed by other factors. It is also clear that this effect is likely not scale dependent, since

SM-LG performs well in the same evaluation in the aggregated marginal seas, which cover an area comparable to the Central Arctic in size.

One explanatory feature may not be the snow salinity, but the underlying sea ice roughness. It may be that SM-LG better simulates the snow conditions on the more level, first year ice of the marginal seas. This could be due to improved performance in the effects of blowing snow redistribution or turbulent exchanges of heat energy as discussed in Sect. 5.5.2. Improved performance over level ice may allow SM-LG to better capture the timing of melt onset (relative to the air temperature forcing), as it is meaningfully integrating the various relevant snow properties. In the Central Arctic, where ice roughness may diminish SM-LG performance, the modelled snow properties may not be as accurate, and therefore melt onset timing may not be well-represented. However, it is also important to consider that coastal weather stations in Northern Russia may allow hard-to-model reanalysis variables to be better constrained in the marginal seas. This may also lead to better representation of snow properties by SM-LG, and better representation of other forcings in addition to air temperature, such that melt onset is better modelled in the marginal seas. With the above being said, it remains unclear why these mechanisms would diminish the Central Arctic skills so much more in the AHRA evaluation relative to the CMO evaluation.

5.5.4 Changes in ensemble-average snow and meteorological conditions surrounding snow ablation

I first discuss the albedo evolution displayed in Fig. 5.11. The timing of the evolution generally agrees with the two campaigns documented by Vérin et al. (2022), although the NP measurements were not hyperspectral. However, it is noticeable that the mean value post melt onset is higher than Vérin et al. (2022): this is potentially due to the (statistically) thinner snow, or the fact that the underlying ice at NP stations was multi-year. More likely, however, is the differences in the frequency range and sensitivity of the NP-station radiometers, as the albedo of snow is significantly lower at higher wavelengths. These high values after melt onset are also visible in the monthly analysis of Perovich et al. (2002).

Turning to the temperature analysis, there was a clear change in the nature of the timeseries around the reference day of ablation. Prior to the reference day there was a highly linear, increasing trend. Afterwards there was no trend, with daily maxima generally not exceeding 0°C. I interpret this limit as relating to the latent heat of snow and ice melting. As the sun continues to rise in the sky and put more energy into the atmosphere ice system, the energy is used up in changing the phase of the snow and ice. It is therefore not used to raise the temperature of the air; this is why the air temperature increases so linearly before the snow ablation, but remains so flat afterwards. This is also related to why the Arctic Ocean has warmed so much slower in summer compared to the other seasons, particularly where sea ice is present (See Chapter 1, Fig. 1). When energy is put into the atmosphere in winter when temperatures are well below zero, the system is warmed. However, when energy is put into the air in the summer, it goes into melting sea ice. The sea ice therefore 'pegs' the surface temperature near zero degrees, with the energy imbalance due to climate change preferentially acting to melt the sea ice cover rather than warm the lower atmosphere.

The cloud-cover analysis in Fig. 5.12 indicated decreasing cloud coverage in the period leading up to melt onset. This is in contrast to the increasing trends in both absolute and relative humidity in the run up to melt onset (Fig. 5.12c, Fig. S47). While relative humidity increases throughout the 40-day window centered around the reference day of ablation, the absolute humidity (the quantity that controls downwelling longwave) shows a similar trend to the air temperature, increasing to a local maximum before the reference day of ablation, and then plateauing. So it is the case that the cloud retreat causes the incident shortwave forcing to increase faster than would be expected purely due to increasing solar zenith angle, while the absolute humidity is also increasing which is favorable to downwelling longwave radiation.

5.5.5 Future Research Directions

In Sect. 5.4.3 I compared the evolution of SM-LG parcel snow depths with the evolution of nearby, in-situ snow depths at NP stations during the period of snow

melt onset. In future, a comparison could be conducted of snow depth evolution over the full season. This analysis could include the modern snow-buoy data from Nicolaus et al. (2021). Such an analysis could also evaluate the snow density values from SM-LG against snow density measurements taken on the NP snow transects (not shown in this thesis). Such Lagrangian-style evaluations were not performed in the SM-LG evaluation paper of Stroeve et al. (2020a), but would potentially yield significant insight into the performance of the model and accuracy of its forcing.

This study also identified the key role of liquid and mixed-phase precipitation in several of the station melt onsets. In future, this could be the subject of dedicated analysis, perhaps by driving the SNOWPACK model (Wever et al., 2020) across melt onset and comparing runs with and without a small amount of liquid precipitation. This would reveal the impact of liquid precipitation in triggering melt onset relative to control runs. Such a dedicated analysis should also include a more quantitative treatment of the *amount* of rain on snow associated with snow ablation at NP stations. This is non-trivial, as the amount of precipitation recorded does not necessary reflect the amount of actual precipitation due to evaporation-based and wind-driven biases in the NP precipitation gauges (Boisvert et al., 2018, and references therein). More generally, the melt onset detection algorithm of Markus et al. (2009) could potentially be modified to detect rain on snow events, with training based on rain on snow events present in atmospheric reanalysis.

SM-LG showed more skill than reanalysis surface air temperature in reflecting satellite-derived melt onset timings on large spatial scales. This raises the possibility of modelling melt onset timings into the future. SM-LG could potentially be driven into the future with atmospheric forcing and ice motion vectors produced by an earth system model such as CESM2. It would then be possible to investigate the timing of large-scale snow melt onset in the future, based on the SM-LG skin-temperature and daily snow melt outputs.

It would also be instructive to link the parcel-wise output of SM-LG to a radiative transfer model such as the snow microwave radiative transfer model (SMRT; Picard et al., 2018). This would allow direct simulation of the brightness temperatures

that are actually observed by satellite mounted radiometers. This avenue was not considered for this thesis because SM-LG has not yet been configured to output its internally computed snow stratigraphy (a necessary input for SMRT).

5.6 Summary

In this chapter I analysed the evolution of snow depth at NP stations in the period of melt onset, and compared it to two satellite-based products for melt onset timing and the output of a recently developed snow model. While air temperature data from the stations have been used in evaluation of melt onset products before (through assimilation into gridded products such as IABP/POLES and the NCEP atmospheric reanalysis), this was the first time the evolution of snow depth (and the timing of snow ablation) has been used. A Lagrangian analysis of surface air temperature data was also performed, which circumvented gridding and interpolation related uncertainties associated with previous work.

Although the timing of melt onset is not the same as the timing of snow ablation, I was able to find instances where the satellite-products noticeably lagged snow ablation, indicating a lack of skill. It is important to note that the satellite melt onset products do not claim to represent the same quantity, and thus should not be expected to agree with each other: one represents initial melt onset, while the other represents the onset of continuous melt. Qualitative assessment of skill was also performed by comparing the satellite-derived timings to the air temperature and snow albedo timeseries: on average the CMO algorithm of Markus et al. (2009) matched the timing of above-freezing air temperatures more closely than that of Drobot and Anderson (2001). Both satellite-derived melt onset timings and snow-depth-derived ablation timings were associated with drops in derived snow albedo. The above two satellite products were often mismatched with each other. The only two cases where both products matched the timing of the first above-freezing air temperatures was when that timing itself matched the season's first mixed- or liquid-phase precipitation.

I also compared the timing and speed of snow ablation at the NP stations to nearby SM-LG parcels. I found that the timing of snow ablation at NP stations was

around nine days after ablation at their corresponding paired parcels. Investigating the forcing, I found that the surface air temperature went above 0°C around eight days earlier. However, individual variation in the difference between modelled and observed ablation timings did not correlate with individual differences in the timing of the 0°C surface air temperature threshold being exceeded. I also analysed the speed at which the snow ablated, and found SM-LG ablation speeds to be comparable on average with the NP stations. However, individual variability in ablation speed at the NP stations was not reflected in their corresponding SM-LG tracks.

I compared the representation of melt onset in SM-LG with the previously mentioned satellite melt onset products over the 1981-2018 period. I did this by defining melt onset in SM-LG in three ways: a daily snow melt quantity threshold, a snow surface temperature threshold, and (for identifying skill) a surface air temperature threshold. Model skill was defined as the outperformance of the surface air temperature diagnostic by the model-derived snow melt and skin temperature diagnostics. My ability to choose the thresholds allowed me to tune the bias to some extent, so I opted to quantify the skill of each diagnostic in terms of its representation of regional- or pixel-scale interannual variability in melt onset timing. After some sensitivity analysis of my thresholds, I found that the model outputs (skin temperature, daily melt quantity) did not outperform surface air temperature as indicators of either satellite product at the pixel level. This was potentially due to pixel-scale noise in the satellite products themselves. However, the snow melt diagnostic of SM-LG generally outperformed the surface air temperature method when evaluated with the AHRA product at the regional scale and larger, indicating model skill. It was speculated that a more sophisticated diagnostic design in SM-LG would improve its representation of the CMO product. The performance of snow melt as a diagnostic of satellite-derived melt onset timing was found to be sensitive to the parcel regridding technique.

Finally, I investigated ensemble-mean changes in the snow albedo and meteorological conditions before, during and after in-situ observed snow ablation by aligning the relevant timeseries to a consistent reference point of ablation. This

revealed highly linear increase in ensemble-averaged air temperatures up until the reference day of ablation (on which ensemble mean ablation was maximal). After this day, the average air temperature timeseries was flat and rarely exceeded 0°C. This was attributed to the effects of latent heat of melting ice. Ensemble-averaged low cloudiness generally decreased until shortly after the reference day of ablation, after which it showed an increasing trend. This was striking, since on a multi-day timescale both relative and absolute humidity showed fairly monotonic increases up to the reference day of snow ablation: this implies that melt onset is driven by both cloud conditions that are increasingly favorable to shortwave forcing, and water vapor conditions that are favorable to longwave forcing.

Chapter 6

Thesis Summary and Future Directions

In this thesis I have considered snow on Arctic sea ice from different angles, with my investigations all featuring snow observations by Soviet drifting stations in some way. This chapter will begin by reflecting on the context of this thesis in terms of externally set observational requirements and challenges. I will then draw the individual chapters' investigations together, and discuss their relationships to each other. In particular, I will consider the relevance of my investigations to planned future satellite missions and observational campaigns, before discussing the limitations of the data approaches presented here. Finally, I will make recommendations for future fieldwork in both polar regions.

6.1 The ESA Sea Ice Challenge

In 2015 the European Space Agency launched a new *Earth Observation Science Strategy* (ESA, 2015). As part of this, ESA specified five challenges for The Cryosphere, the first of which (C1) is to improve understanding and quantification of:

> "Regional and seasonal distribution of sea-ice mass and the coupling between sea ice, climate, marine ecosystems and biogeochemical cycling in the ocean."

All four research-chapters of this thesis are aligned with this challenge. Chapters 2 & 3 directly address the seasonal cycle of sea ice thickness (and so mass),

and include full regional break-downs. Chapter 4 (on the local-scale snow depth distribution) will help establish the coupling between sea ice and climate (via heat flux), and marine ecosystems (via light flux). This is also true for Chapter 5, which concerns the timing of melt onset: this is vital for fully representing the climate's influence on sea ice in models, and also the timing of light availability for marine ecosystems, with impacts on biogeochemical cycling.

Chapters 2 & 3 also address the user requirements as defined by a recent survey by the ESA Climate Change Intiative (CCI; ESA, 2019). For responses regarding requirements for sea ice thickness:

> "the majority of the respondents required spatial resolution better than 50 km and measurement precision better than 20 cm."

While this thesis does not address the spatial resolution of sea ice thickness retrievals (instead relying on pre-gridded products), the improvements to the treatment of snow in the retrieval-chain will likely result in higher precision of the derived variable.

6.2 Satellite Radar Altimetry

The first two research chapters considered estimates of sea ice thickness from satellite-mounted radar altimeters. Specifically, the role of snow in slowing radar waves was discussed in Chapter 2, and the impact of interannually variable and trending snow loading was assessed in Chapter 3. Taken together, I believe that these chapters represent an advance in the field of satellite retrievals of sea ice thickness from Ku-band altimeters flown on missions such as EnviSat, CryoSat-2 and Sentinel-3. This is relevant in light of Chapter 1 (Sect. 1.4), where I described the status of sea ice thickness as an *Essential Climate Variable*.

I also hope that this work will help the altimetry community extract value from the European Space Agency's upcoming CRISTAL altimetry mission (Kern et al., 2020), which is currently planned for launch in 2027. However, it is important to view the work within this thesis in the context of the remaining, large uncertainties that surround estimates of sea ice thickness from radar altimetry data.

6.2.1 Radar Penetration of Snow on Sea Ice

It is becoming increasingly clear that Ku-band radar waves emitted by altimeters do not consistently return from the sea ice surface. This has been argued by several previous papers (e.g. Willatt et al., 2011; Ricker et al., 2015; Armitage and Ridout, 2015; King et al., 2018), but it is also becoming evident from separate research currently underway at CPOM UCL. This thesis has not grappled with the issue of partial radar penetration of snow, but has simply cited it as a potentially risky assumption. Future studies seeking to refine satellite-based sea ice thickness retrievals (as I have tried to do in Chapters 2 & 3) should engage with this challenge. Part of this engagement will undoubtedly involve modelling the physical properties of snow on sea ice that may cause the unwanted interception of radar waves. The snow and meteorological observations from NP drifting stations may prove useful in guiding and evaluating these modelling exercises.

6.2.2 Increasing Hostility of the Arctic Ocean to Radar Altimetry

The multi-year sea ice of the Arctic Ocean is being replaced with a seasonal, thinner ice cover, which forms and grows in winter, and then is fully melted each summer (Stroeve and Notz, 2018). This more seasonal state is roughly associated with what some have described as the 'New Arctic' (e.g. Petty et al., 2018b), and a process that others have described as 'Antarctification' (Granskog et al., 2019). This new state also represents a departure from the conditions in which the NP station data were gathered, increasingly limiting their usefulness over time. This new Arctic state may be less conducive to Ku-band radar altimetry of sea ice thickness for several reasons:

Firstly, thin sea ice generally has a lower freeboard than thick sea ice. Radar-altimetry of ice with low freeboard has a considerably larger associated uncertainty (Ricker et al., 2017). This is broadly because as the difference in the retracked heights of leads and floes becomes smaller, some uncertainties (e.g. waveform interpretation) remain the same size. As such, the freeboard uncertainty becomes a larger proportion of the freeboard estimate. Evolution of ice freeboard into the future

could be estimated under different emissions scenarios using the publicly available archive of CMIP6 data (see Notz and SIMIP Community, 2020).

The smoother, more seasonal ice may also be more specular, posing additional challenges involving the discrimination of waveforms from leads and floes - however this has not yet been the topic of a dedicated study. Furthermore, the ice in the Arctic Ocean is becoming more dynamic, which is associated with more frequent lead opening (Rampal et al., 2009). While this may bring the benefit of shorter-range interpolation when comparing waveforms from floes with waveforms from nearby leads, it may also lead to more frequent *contamination* of waveforms. Contaminated waveforms, which come from an ambiguous mix of lead and floe surfaces, are currently not analysed in conventional sea ice thickness processing chains. The presence and impacts of potentially more specular and more contaminated ice should be the topic of a future study; it is likely that all data required for this analysis is publicly and readily available.

Finally, the increasingly dominant seasonal ice in the Arctic Ocean is more capable of producing a saline overlying snowpack (e.g. Nandan et al., 2017). The presence of salt and associated liquid water content at temperatures below zero turns radar-scattering in snow from a two-medium problem (ice and air) into a three-medium problem (ice, air and water). This is a notable extra challenge for the Ku-band altimetry community, as the processes controlling upward salt transport in snow are poorly understood. It is also a challenge for those wishing to model radar backscatter with models such as SMRT (Picard et al., 2018), as the three-medium regime has historically been considerably less studied.

6.3 The Sub-Kilometre Scale Snow Depth Distribution

In Chapter 4 I developed a snow depth distribution based on snow depth transects taken at Soviet drifting stations. The underlying motivation for this work was to improve the estimates of ice-air fluxes of heat and light, which are discussed at the end of the relevant chapter. However, there are also applications of the

distribution to altimetry (both laser and radar) and radiometry, which link it directly with the other investigations in this thesis. The snow depth transect data also likely retain unextracted information on the relationship between local scale snow depth distribution and meteorological forcing.

6.3.1 Satellite Altimetry

Topographic roughness is emerging as a key determinant of radar-waveform shape, and must be understood in order to accurately interpret returns from radar-altimeters (Landy et al., 2020). While the role of the snow depth distribution is undoubtedly relevant to this problem of interpretation (particularly at less-penetrating frequencies such as Ka-band), its influence is convolved with the topography of the underlying ice. If thicker snow is coincident with topographically higher ice, the snow surface is rougher than if thick snow is coincident with topographically lower ice (Fig. 6.1).

An obvious next step is to link the thesis chapter on the snow depth distribution (Chapter 3) with the radar altimetry chapters (Chapters 4 & 5). This could be done by combining terrestrial laser scanning (TLS) with precisely geolocated snow depth measurements. TLS generates a 3-dimensional map of the snow surface topography, from which geolocated snow depth measurements can be precisely subtracted to reveal the underlying ice topography. By combining TLS with geolocated snow depth measurements, the relationship of the local snow depth distribution to the underlying ice topography would be revealed, and insight into radar waveform interpretation may be achieved. To do this effectively may require an upgrade in the precision of the GPS unit on the conventional self-measuring snow probes (Sturm and Holmgren, 2018); this might be achieved through the use of differential GPS (DGPS Blackwell, 1985) on landfast ice.

With the relationship between snow depth and ice topography established, a new understanding of topographic roughness could be implemented in radar-altimeter simulators such as that of Landy et al. (2020).

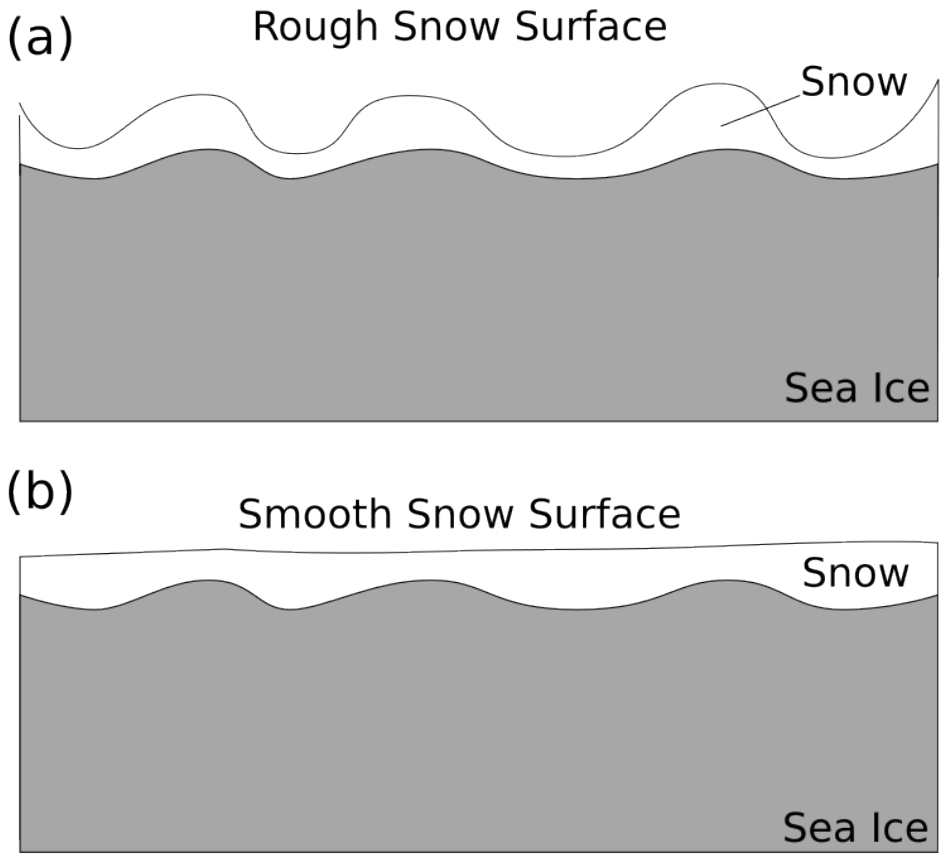

Figure 6.1: Schematic of two theoretical snow surface topographies stemming from different relationships between snow depth and ice surface topography. (a) snow depth is greater where ice topography is higher, creating a topographically rough snow surface. Ice topography is *accentuated* (b) snow depth is greater where ice topography is lower, resulting in a smooth snow surface. Ice topography is *suppressed*.

6.3.2 Snow Distribution Sensitivity to Meteorological Forcing

In Chapter 3 I presented a roughly linear relationship between the mean snow depth of a transect and its standard deviation, with a Pearson r-score of 0.66 (Fig. 4.3). This score indicates that there is considerable spread about the linear regression. Variable roughness of the underlying ice likely explains some of this variation, but the role of meteorological forcing is yet to be fully investigated.

One key meteorological driver may be strong winds, which could act to redistribute the snow and thus change the ratio of standard deviation to mean depth, or the skew of the depth distribution. In Chapter 5 I briefly described the occurrence of early spring mixed- and liquid-precipitation that did not trigger continous melt onset. The

impact of rain on snow in changing, and perhaps *cementing* the sub-kilometer snow depth distribution could be investigated in future. This same is also true for wind-slab formation: if slab-forming events can be identified in the NP meteorological record, their role in fixing the snow-depth distribution might be quantified.

6.4 Melt Onset Timing and Altimetry

In Chapter 5 I investigated the timing of snow ablation at NP stations. I compared these timings with two satellite products for snow melt onset, and also to ablation timings from a recently developed model (SnowModel-LG).

The timing of melt onset and ablation is linked to Chapters 2 & 3 on radar altimetry retrievals of sea ice thickness. As mentioned in Chapter 5, a year-round sea ice thickness product was recently released by Landy et al. (2022). This product uses SnowModel-LG (Liston et al., 2020) data to quantify the impact of snow loading in the conversion of radar freeboard retrievals to sea ice thickness estimates. This makes the comparison between ablation timings at NP stations and SnowModel-LG particularly relevant.

Figure 6.2 shows the evolution of the radar freeboard, snow loading, and derived sea ice thickness in a small 'test region' near the North Pole around the period of melt onset in the new year round product. The coordinates defining this region are given with a map in Figure S48. In several years (2012, 2013, 2014, 2016, 2017, 2020) there is a spike in the radar freeboard around the time of melt onset (as derived using data from Markus et al. (2009)). This spike is likely driven by two phenomena: reduction in the penetrability of the snow as it becomes wet, and subsequent uplift of the ice surface in response to reduced snow loading from snow melt, evaporation and drainage.

In 2011 it is clear that the snow loading (black dotted line) melts too late, in that it occurs after the radiometry-derived melt onset timing (red band). This causes the derived sea ice thickness (green line) to hold unrealistically steady in the face of declining radar freeboards, before rapidly plunging.

In other cases, the modelled snow depth often declines significantly before melt

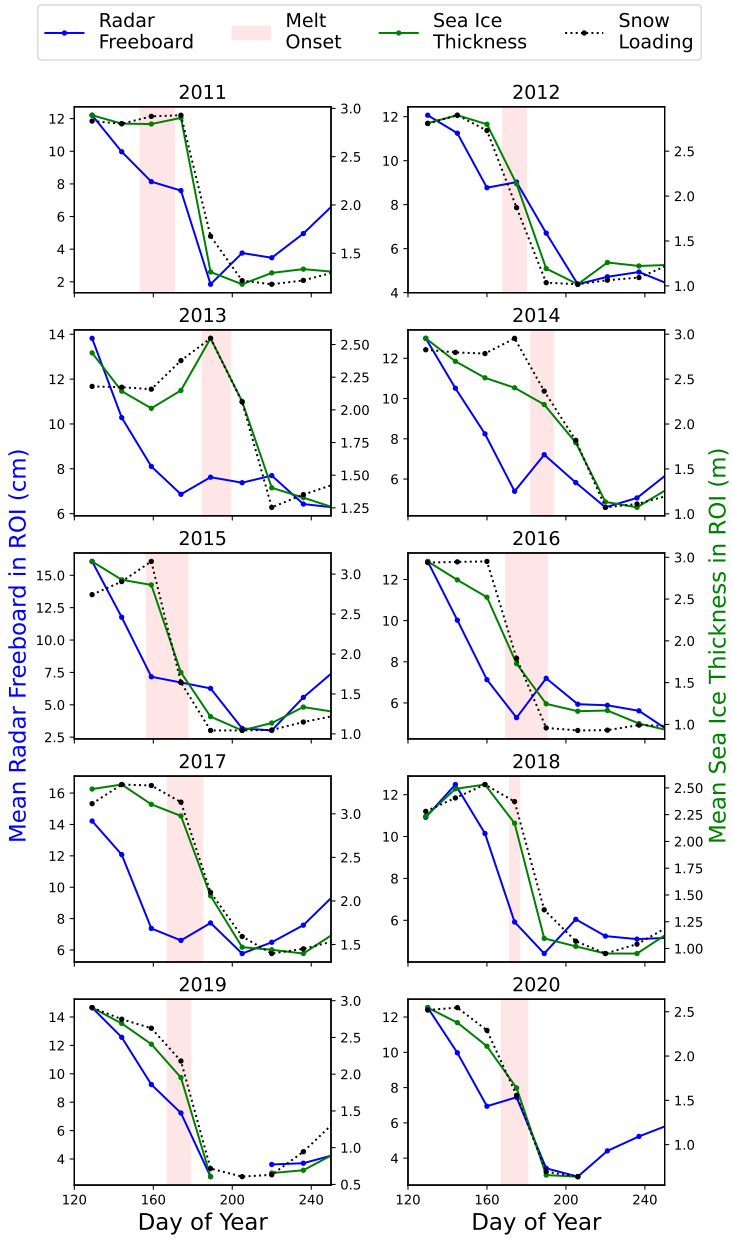

Figure 6.2: Plots of the seasonal evolution of mean radar freeboard, sea ice thickness, and snow loading (from SM-LG) in a region of interest near the North Pole (Supplementary Fig. S48). The timing with which satellite-derived melt onset occurs is marked in red: this represents one standard deviation either side of the mean melt onset timing of grid cells in the region of interest.

onset is detected in the satellite product - this is consistent with the biases I found in Chapter 5. This, in part, contributes to the potentially unrealistic declines in derived sea ice thickness in the weeks before snow melt onset. The work that I have done in this thesis (specifically Sect. 5.4.4) in comparing SnowModel-LG to melt onset products will help refine the product in this period of rapid change.

One final intriguing aspect of Figure 6.2 is that the radar freeboards consistently decline in the weeks before radiometry-derived melt onset. One explanation of this is potentially reduction of the ice freeboard by melting of the ice from below. Another is perhaps a combination of poor radar penetration (meaning the radar freeboard corresponds to the snow surface), and a settling and densification of the snow in the lead up to melt onset. Insights from Chapter 5 into the relationship between melt onset and snow/radar interactions will be the foundation for addressing these questions.

6.5 Future Satellite Altimetry Missions

The European Space Agency plans to launch a 'next generation' altimetry mission dedicated to Earth's cryosphere in late 2027: this is known as the Copernicus Polar Ice and Snow Topography Altimeter (CRISTAL, Kern et al., 2020). It is due to be joined in 2028 by a next-generation radiometer known as the Copernicus Imaging Microwave Radiometer (CIMR, Vanin et al., 2020). Together, these missions will provide future data on sea ice thickness (relevant to Chapters 2 and 3) and on melt onset timing (Chapter 5).

Both CRISTAL and CIMR will likely be used for snow depth determination: for CRISTAL, this will be done by taking the difference in radar-ranging at different frequencies (e.g. Guerreiro et al., 2016), and for CIMR this will be done using the ratio of brightness temperatures at different frequencies and polarisations (e.g. Rostosky et al., 2018). Snow depth determination is an explicit goal of the CRISTAL mission (Kern et al., 2020). Several uncertainty targets are given for the derived snow depths; these result from differing user-group requirements with regard to spatio-temporal resolution. Target uncertainties as low as 0.01, 0.02, and 0.05 m are

listed for horizontal resolutions of between 1 and 10 km (ESA, 2020a; p 68).

The role of snow as characterised in this thesis may prove problematic: the CRISTAL mission requirements document requires a freeboard retrieval accuracy of 0.03 m, and a sea ice thickness retrieval accuracy of 0.15 m. The first potential issue with this is that a 0.03 m accuracy in freeboards would not support 0.15 m accuracy in sea ice thickness, since a freeboard value is multiplied by around a factor of nine in the conversion to sea ice thickness. So even if all aspects of the hydrostatic conversion were known precisely, the target freeboard accuracy would result in a thickness accuracy of around 0.27 m.

The second issue involves the role of snow in the conversion of radar freeboard to true (ice) freeboard, discussed in Chapters 2 & 3. If we assume that Ku-band radar waves penetrate the snowpack fully and we are able to interpret the returned waveforms exactly, then the radar freeboard would differ from the true freeboard by only the mean delay due to slower radar wave propagation in snow. The uncertainty in the correction for slower propagation delay alone could potentially be 0.03 m - the target accuracy of the freeboard retrievals. To illustrate this, a depth-uncertainty of 0.12 m of snow at a typical density of 300 kgm^{-3} (30 kgm^{-2}) would result in an uncertainty in the propagation delay correction of 0.03 m. Any uncertainty regarding penetration or waveform interpretation on top of this would cause the freeboard accuracy target to be missed.

It is noteworthy that the CRISTAL mission will carry a nadir-looking, multi-frequency radiometer for purposes of atmospheric correction (ESA, 2020b; p 36). While the precise channel-frequencies remain uncertain (as there are currently two radiometer designs being considered), it is very likely that the end-design will include channels suitable for snow depth retrieval. This may provide a valuable independent avenue for evaluating CRISTAL dual-frequency snow depth retrievals and informing sea ice thickness retrievals. If this radiometer can be used to also determine ice type and sea ice concentration, CRISTAL's reliance on observations from CIMR will be minimised.

CRISTAL's downward-looking radiometer may also be useful for detecting

melt onset, and the effects of transient melt events on the radar freeboard in the cold-season (October - April). Given the same angular field-of-view, downward looking radiometers have the advantage of having a smaller observed area on the ground relative to the more conventional mounting-angles ($\sim$55°) on missions such like SMMR, SSM/I and CIMR. This smaller observed area will be useful for comparison with the comparatively small footprints of the onboard altimeter.

6.6 Future Field Campaigns

6.6.1 Antarctica

The snow cover and sea ice thickness of Antarctic sea ice remains poorly monitored, in part because fewer field campaigns (like the NP program) have been undertaken there. However, Antarctic sea ice extent has recently been below the long-term average, and reached a record low in 2022 (Turner et al., 2022); this has intensified scientific interest, and has led to the funding and planning of several new field campaigns. These campaigns will investigate the themes of this thesis: the role of snow in radar-based sea ice thickness retrievals, the snow depth distribution, and melt onset characteristics.

Antarctic sea ice campaigns are generally either performed from coastal stations or from ship-based transects. Coastal stations offer the possibility to capture the time-evolution of the snow at a given location. The downside of this type of campaign is that it is challenging to compare the in-situ observations with satellite-based altimeter and radiometer measurements due to issues of land-contamination of the satellite footprint/field of view. Furthermore, sea ice at these sites is often land-fast (particularly when nearby icebergs provide ‘pinning-points’. Landfast ice can have different properties to the pack ice, as floes are less able to reorientate themselves in response to the wind, and weather originating from the landmass may have a strong effect. These issues pose challenges to simple mapping of the science in this thesis to land-adjacent campaigns in Antarctica. Nonetheless, a *overwintering* campaign is planned for 2023 on Adelaide Island in West Antarctica, with a particular focus on the snow cover. This campaign will undoubtedly be influenced by the results in this

thesis. In particular, the decomposition of sea ice thickness retrievals into 'snow' and 'radar freeboard' components (Chapter 3) will influence work performed with an in-situ radar instrument. Snow depth transects will also be performed, and the results compared with the model presented in Chapter 4 (with the caveats concerning the nuances of landfast ice and seasonal ice). Finally, the melt onset characteristics of the snow cover will be observed in the full context of nearby, crewed weather station. The melt onset characteristics of Antarctic snow on sea ice are likely to be different to those described in this thesis for several reasons: the first being that Antarctic sea ice outside of the Weddell and Ross Seas is almost entirely seasonal, leading to the issue of snow salinity described in Chapter 5. However, another key feature of Antarctic sea ice is its low latitude (by comparison to the Arctic, but more so the high-latitude NP stations). This will lead to *stronger* diurnal cycling around the period of melt onset, requiring a higher temporal frequency of in-situ observations.

The alternative to coastal-campaigns in Antarctica is ship-based transects, although very few Langrangian-style drifting campaigns similar to the NP-program have been performed. Notable exceptions to this are the Ice Station Polarstern (ISPOL; Hellmer et al., 2008) and Ice Station Weddell (ISW; Gordon and Schlosser, 1993) campaigns. The dominant mode of ship-based transects do not afford consistent monitoring of the same snow in a way that allows a process-based understanding. Based on the work in this thesis, it is therefore my recommendation that this be undertaken again, in what might be termed a 'Southern MOSAiC' similar to ISPOL and ISW.

Beyond the topic of field campaigns, the snow loading on Antarctic sea ice remains very poorly constrained and this is worthy of comment here. No analogous product to the climatology of Warren et al. (1999) exists (Chapter 2), and models such as SnowModel-LG used in Chapter 3 have not yet been run in Antarctica. This is in large part due to the much higher ratio of snow loading to sea ice thickness in the Southern Hemisphere, which causes snow flooding that is difficult to represent in physical models. It is also the case that the atmospheric reanalysis that is required to drive models like SnowModel-LG is more uncertain due to the paucity of coastal

weather stations and drifting platforms relative to the Arctic. If Southern Ocean sea ice thickness it to be meaningfully retrieved with conventional methods, then hemisphere-specific snow-loading products must be developed.

6.6.2 The Arctic

While the Arctic Ocean is better observed than the Southern Ocean in terms of its snow and sea ice thickness, these variables are nonetheless poorly constrained relative to specifications such as the GCOS Essential Climate Variables (Introduced in Chapter 1; Lavergne et al., 2022). As described in Sections 6.2 & 6.5, advances accompanying the upcoming CRISTAL mission will not resolve the large uncertainties in these variables. Future earth observation missions must therefore be accompanied by future in-situ campaigns, with evaluation campaigns being of particular importance.

The first two chapters of this thesis illustrated the pivotal importance of snow loading in the retrieval of sea ice thickness from radar altimetry. These chapters point to the importance of a rigorous evaluation of the latest generation of Arctic Ocean snow loading products such as SnowModel-LG (Liston et al., 2020) and NESOSIM (Petty et al., 2018b), and the sea ice thickness retrievals that they deliver. This might be done by surface-based campaigns with snow depth probes (e.g. Nicolaus et al., 2022), or with high-resolution radar instruments deployed in airborne campaigns (e.g. Kurtz and Farrell, 2011).

As discussed in Sect. 6.3, the Arctic is becoming dominated by first-year ice, which can have a very different snow depth distribution to the model presented in Chapter 4. First-year ice may also exhibit different behaviour around the period of melt onset (Chapter 5) due to its higher snow salinity. First year ice is also often challenging to conduct fieldwork on as it is generally thinner and more dynamic. Nonetheless, it should be prioritised as a setting for future field research due to its increasing relative presence in the Arctic, and because it is not well represented by historical field campaigns.

Supplement to Chapter 1

S1 Construction of Figure 1.1

Surface air temperature Monthly mean 2-metre air temperature and sea ice concentration was downloaded from the ERA5 atmospheric reanalysis (Hersbach et al., 2020). Air temperature was spatially averaged for each month where the corresponding monthly mean sea ice concentration was larger than 15%. This spatial averaging was weighted to reflect smaller grid cells nearer the poles. The individual months were then averaged into meteorological seasons (e.g. DJF for winter), factoring in different month lengths. Each seasonal timeseries was then plotted as an anomaly from the full-timeseries mean value.

Sea Ice Extent Daily sea ice extent values were downloaded from the Version 3 of the National Snow and Ice Data Center Sea Ice Index (Fetterer et al., 2010). The annual maxima and minima were then identified and plotted.

Sea Ice Volume The daily timeseries of sea ice volume from the Pan-Arctic Ice Ocean Modelling and Assimilation System (PIOMAS; Zhang and Rothrock, 2003). The annual maxima and minima were then identified and plotted.

Sea Ice Age The National Snow and Ice Data Center gridded sea ice age product of Tschudi et al. (2020) was downloaded, and the age distribution in the first week of the year was selected. Grid cells were then classified based on whether they contained only first year ice, or whether they contained ice that had 'survived' at least one summer (multi-year ice). The area of the latter was calculated with a sum based on the area of the grid cells.

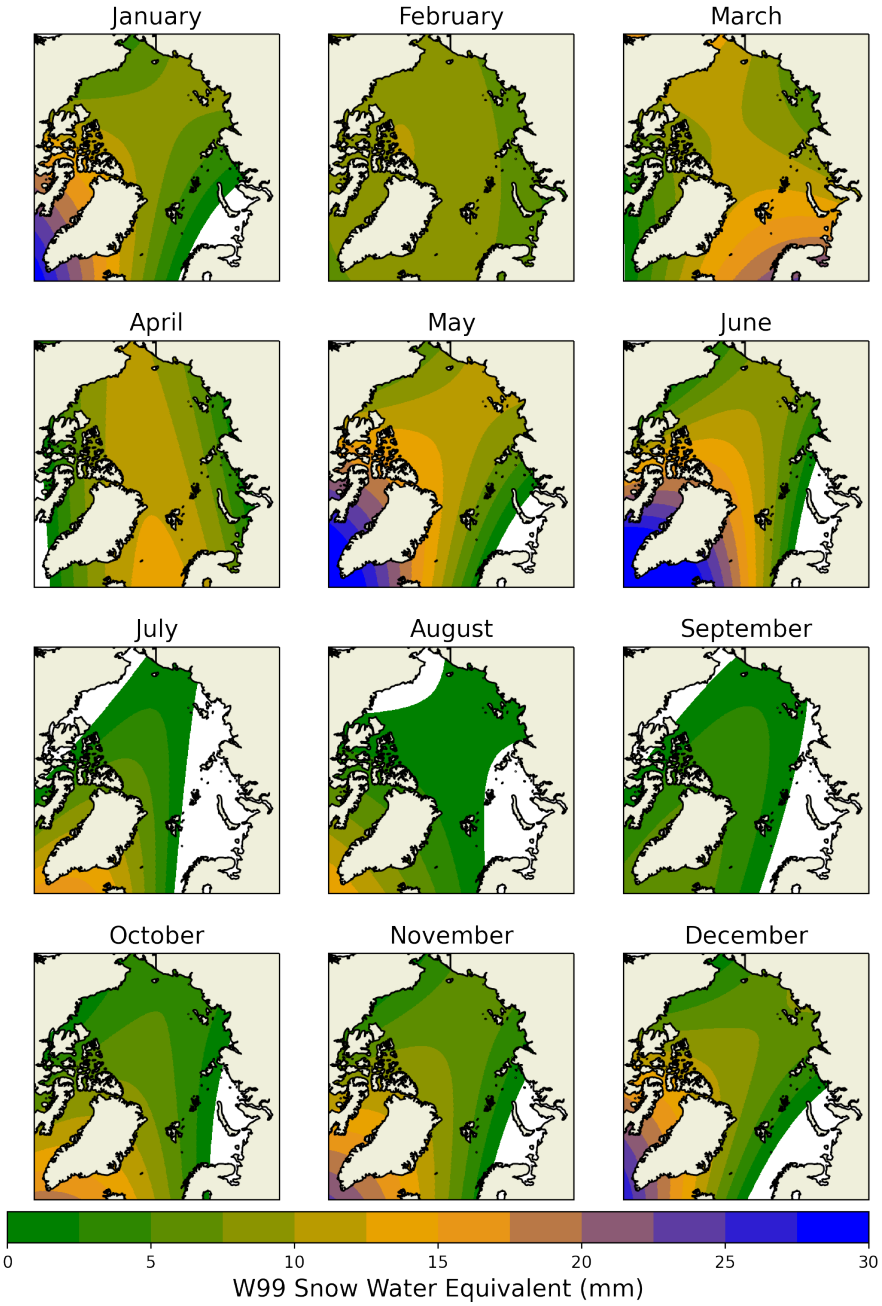

Figure S1: Monthly evolution of Warren Climatology quadratic fits for snow water equivalent. White colored areas indicate regions where the fits generate negative values.

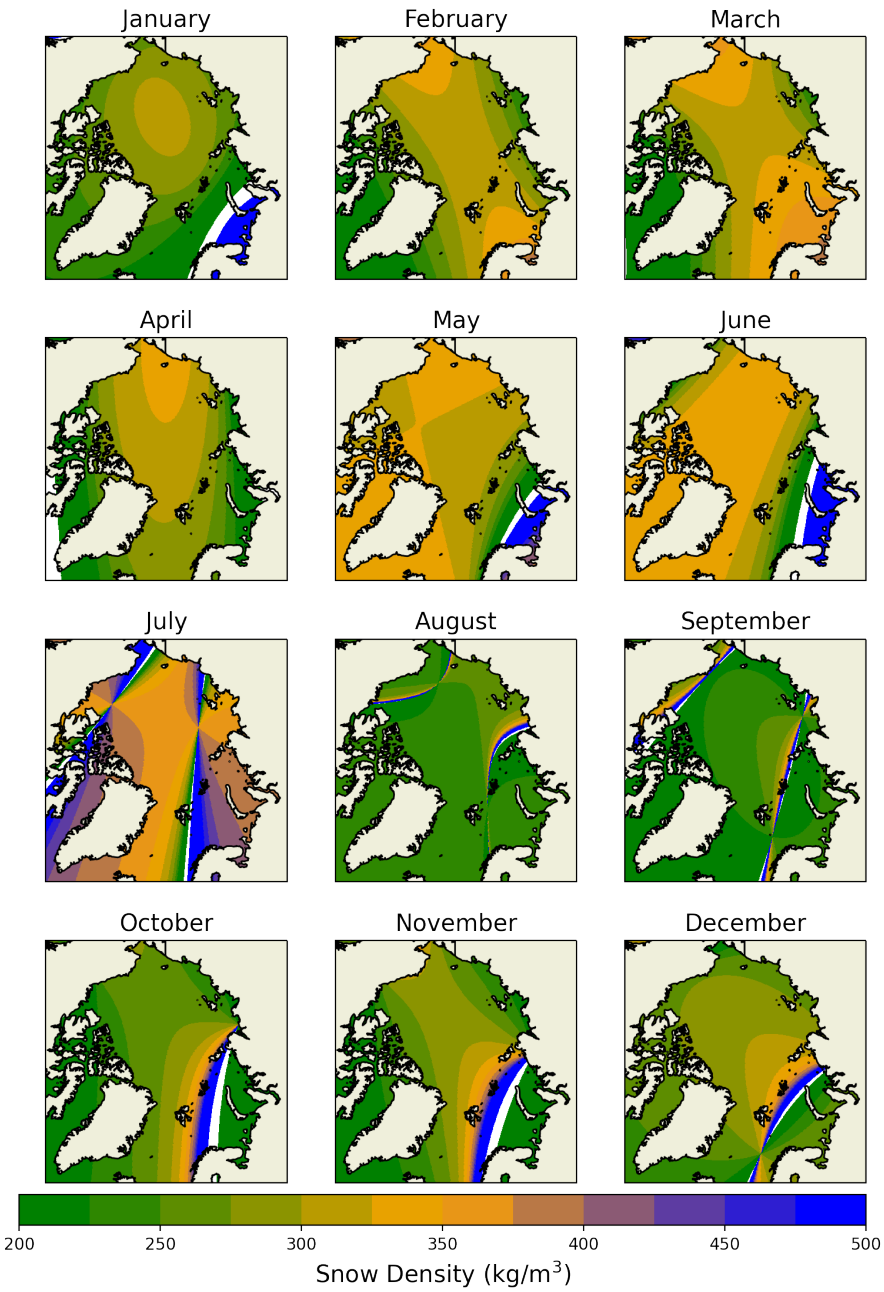

Figure S2: Monthly evolution of Warren Climatology snow density, inferred from dividing the SWE quadratic fits by the depth fits. This is the conventional method used by several altimetry groups.

Supplement to Chapter 2

S2 The Comparable Impacts on SIT of Snow Loading and Slower Radar Wave Propagation in Snow

Ice Freeboard = Radar Freeboard + Propagation Correction(Armitage and Ridout, 2015) (S1)

$$h_i = h_r + h_s(c/c_s - 1) \tag{S2}$$

5 The conversion of a given ice freeboard can be combined with a snow depth to estimate sea ice thickness:

$$SIT = h_i \frac{\rho_w}{\rho_w - \rho_i} + h_s \frac{\rho_s}{\rho_w - \rho_i} \text{(Tilling et al. 2018)} \tag{S3}$$

Substituting Eq. (S2) into Eq. (S3)

$$SIT = h_r \frac{\rho_w}{\rho_w - \rho_i} + h_s \frac{\rho_w}{\rho_w - \rho_i}\left[\frac{c}{c_s} - 1\right] + h_s \frac{\rho_s}{\rho_w - \rho_i} \tag{S4}$$

Sea Ice Thickness = Radar Freeboard Component + Propagation Correction + Snow Loading (S5)

Comparing the relative impacts of the Propagation Correction term and Snow Loading term is relatively simple given they share a common factor of $h_s/(\rho_w - \rho_s)$. The ratio of the two terms is therefore $c/c_s - 1$ to ρ_s/ρ_w. For a typical snow density of 300 kg m^{-3}, this ratio is 0.25 to 0.29. (Using ρ_w = 1023.9 and Ulaby et al. (1986) to relate ρ_s to c_s)

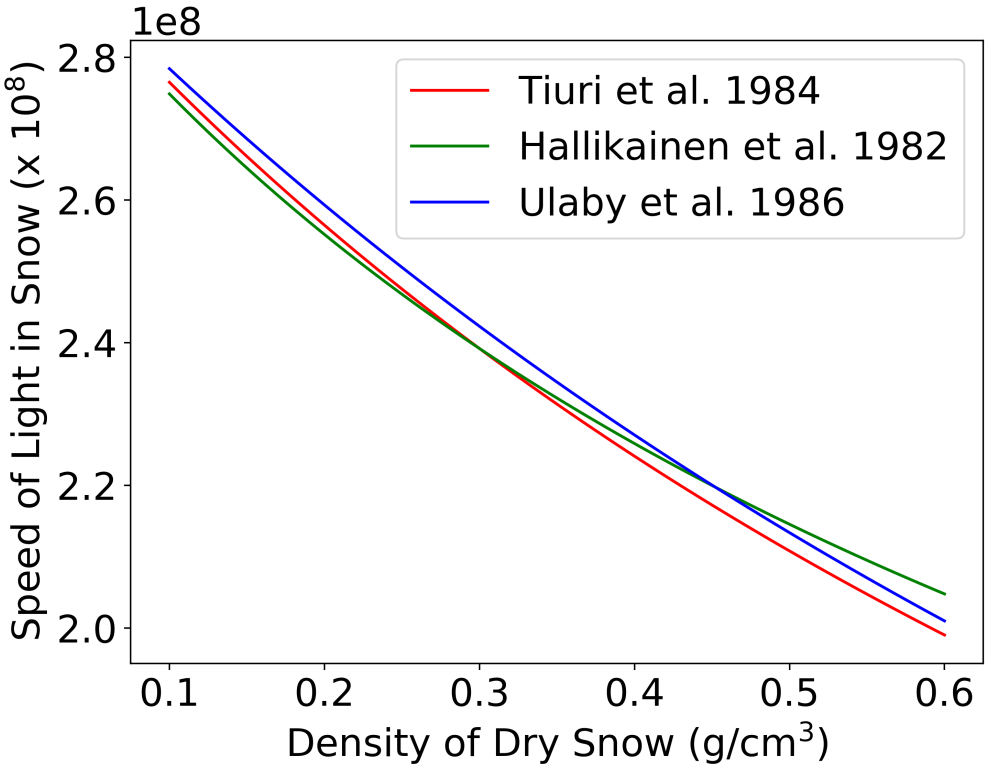

Figure S3: Three commonly used relationships between radar wave speed and snow density Hallikainen et al. (1982); Tiuri et al. (1984); Ulaby et al. (1986).

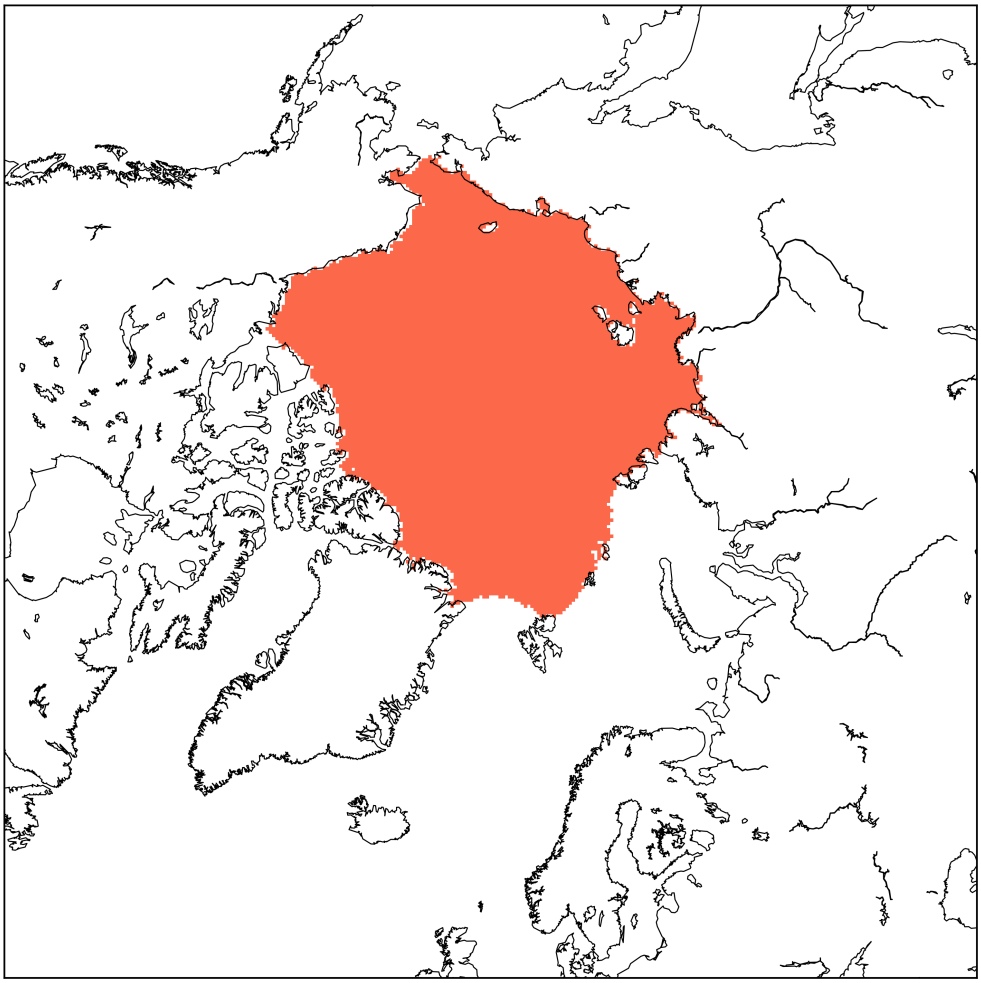

Figure S4: The region over which snow depths published in Warren et al. (1999) are generally considered reliable (Laxon et al. (2013); Kwok and Cunningham (2015)), and over which freeboards are considered in this study.

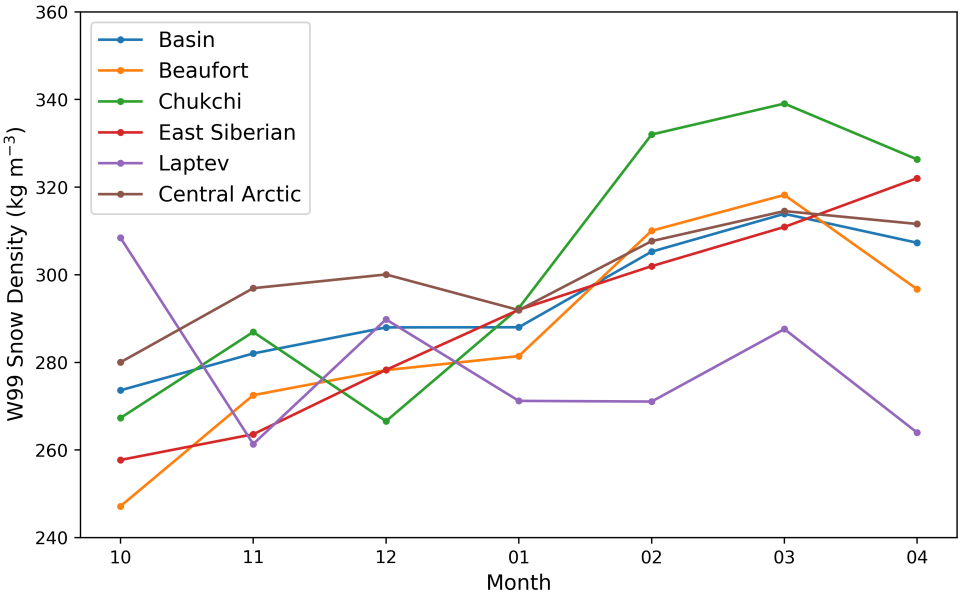

Figure S5: Winter snow densification rates for five regions and the basin-wide average. We defined the 'basin-wide area' as the shaded area in Fig. (S2). We found the basin-wide denisification rate to be roughly representative of its constituent regions apart from the Laptev, which exhibited a small but positive densification.

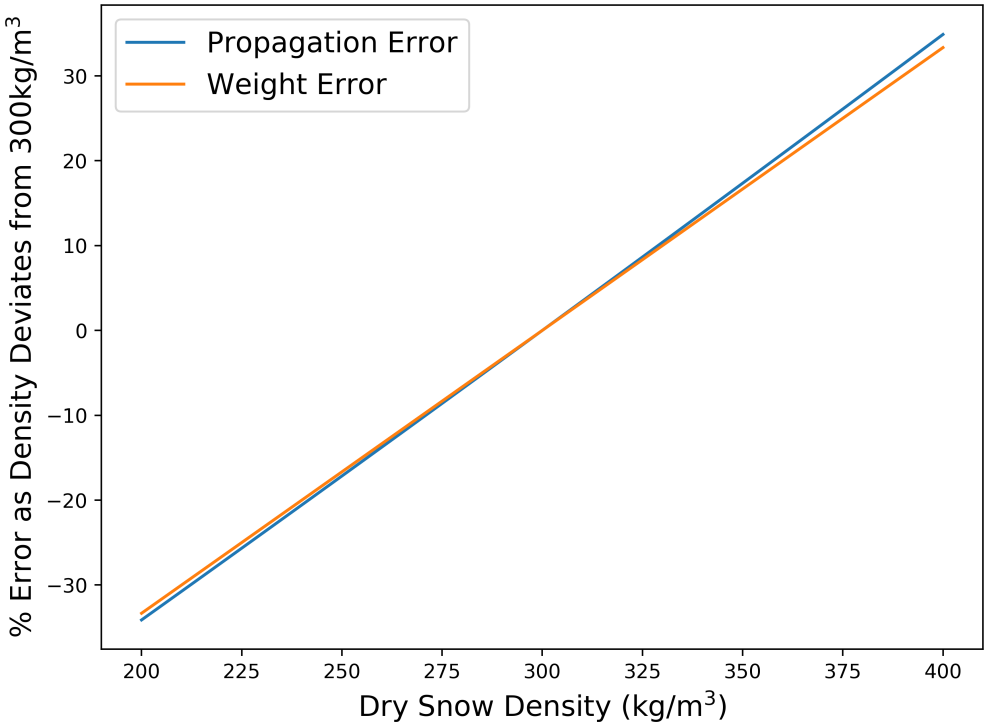

Figure S6: While the functional form and magnitude of expressions for the effect of snow weight and slower radar propagation are different, they have a similar error dependence on snow depth. That is to say, the percentage error introduced to the "weight correction" by snow density uncertainty is the same as that for the "propagation correction".

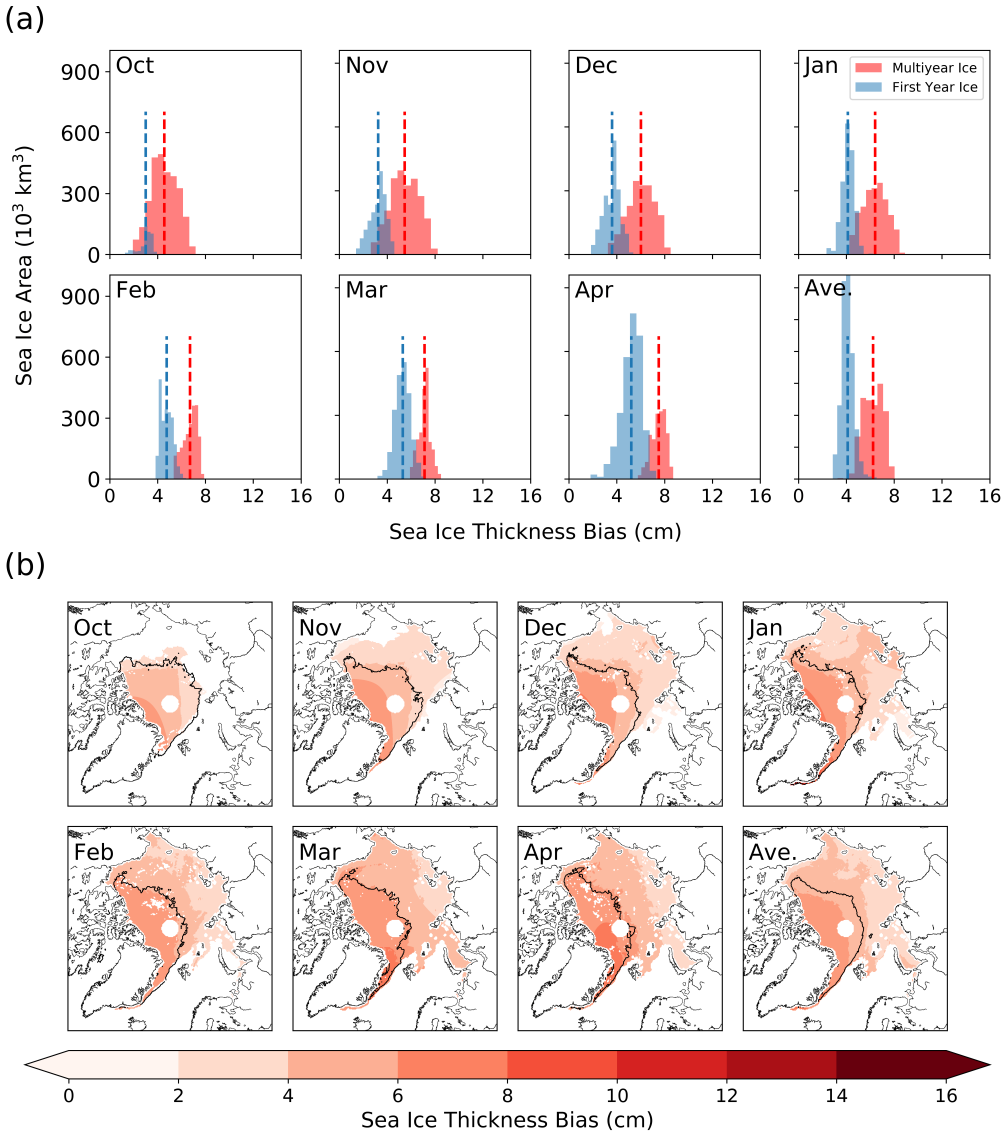

Figure S7: Monthly differences in sea ice thickness from the use of $\delta h = 0.22Z$ and $\delta h = 0.25Z$ for the propagation by AWI and CPOM respectively.

Supplement to Chapter 3

S3 Snow's impact on conventional sea ice thickness retrievals can be characterised solely by its snow water equivalent

Using the expression of ice freeboard from Armitage and Ridout (2015):

$$\text{Ice Freeboard} = \text{Radar Freeboard} + \text{Propagation Correction} \tag{S6}$$

And using the expression of the propagation correction from Tilling et al. (2018):

$$h_i = h_r + h_s(c/c_s - 1) \tag{S7}$$

Where h_s is snow depth, c is the speed of light in free space and c_s is the speed of light in snow. Numerous empirical expressions for c_s exist, in this work we use the expression for the permittivity of dry snow from Matzler et al. (2006):

$$\varepsilon_{ds} = \left(1 + 0.5194\rho_s\right)^3 \tag{S8}$$

Relating the radar wave speed to the permittivity using $c_s = c/\sqrt{\varepsilon}$ (Ulaby and Long, 2014):

$$c_s = c\left(1 + 0.5194\rho_s\right)^{-3/2} \tag{S9}$$

The conversion of h_i to SIT then invokes the floe's hydrostatic equilibrium and Archimedes' principle. Like the freeboard correction for slower radar pulse

propagation in snow, this operation requires a priori knowledge of the depth and density of the snow cover.

$$SIT = h_i \frac{\rho_w}{\rho_w - \rho_i} + h_s \frac{\rho_s}{\rho_w - \rho_i} \qquad \text{(Tilling et al. 2018)} \tag{S10}$$

Separating h_i into its h_r and δh_{prop} components using Eq. (S7), we can express SIT for a given ice type as a linear combination of the radar freeboard and snow properties.

$$SIT = h_r \frac{\rho_w}{\rho_w - \rho_i} + h_s \frac{\rho_w}{\rho_w - \rho_i} \left[\frac{c}{c_s} - 1 \right] + h_s \frac{\rho_s}{\rho_w - \rho_i} \tag{S11}$$

$$SIT = h_r \frac{\rho_w}{\rho_w - \rho_i} + h_s \frac{\rho_w}{\rho_w - \rho_i} \left(\left[\frac{c}{c_s} - 1 \right] + \frac{\rho_s}{\rho_w} \right) \tag{S12}$$

The equation $y = c/c_s - 1$ where c_s is a function of ρ_s as in Eq (S9) is highly linear as a function of ρ_s as follows:

$$\frac{c}{c_s} - 1 = 8.36 \times 10^{-4} \times \rho_s \tag{S13}$$

This linearity is visualised in Fig. (S8) and allows the second term in Eq. (S12) to be written to a close approximation:

$$SIT = h_r \frac{\rho_w}{\rho_w - \rho_i} + m_s \frac{\rho_w}{\rho_w - \rho_i} \left((8.36 \times 10^{-4}) + \frac{1}{\rho_w} \right) \tag{S14}$$

Where m_s represents the mass of snow per unit area. This can be reformulated by setting $\rho_w = 1023$ kgm^{-3} as:

$$SIT = h_r \frac{\rho_w}{\rho_w - \rho_i} + m_s \frac{\rho_w}{\rho_w - \rho_i} \times 1.81 \times 10^{-3} \tag{S15}$$

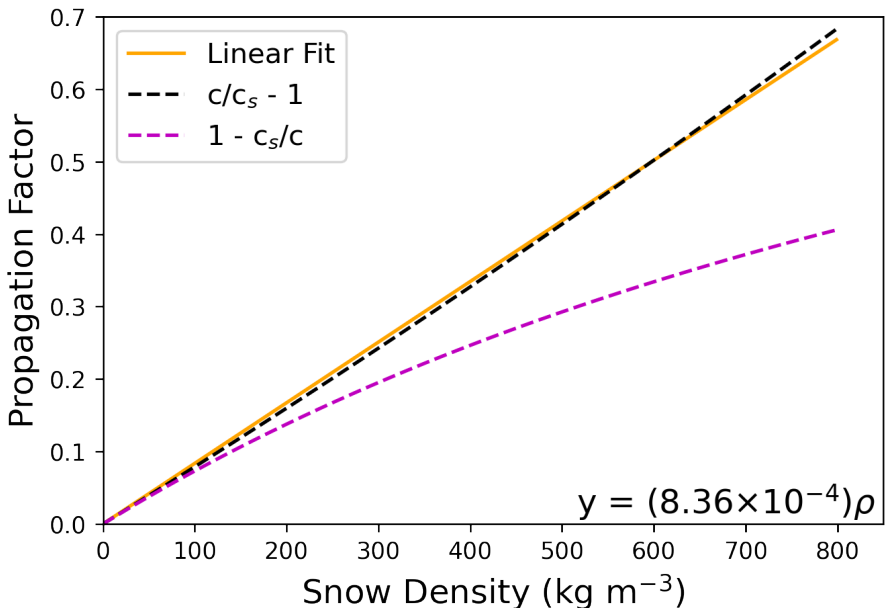

Figure S8: Value of the propagation factor used to convert radar freeboard to ice freeboard, plotted as a function of snow density. This function is highly linear and is approximated as such in this work. The factor is multiplied by the snow depth to generate the total correction.

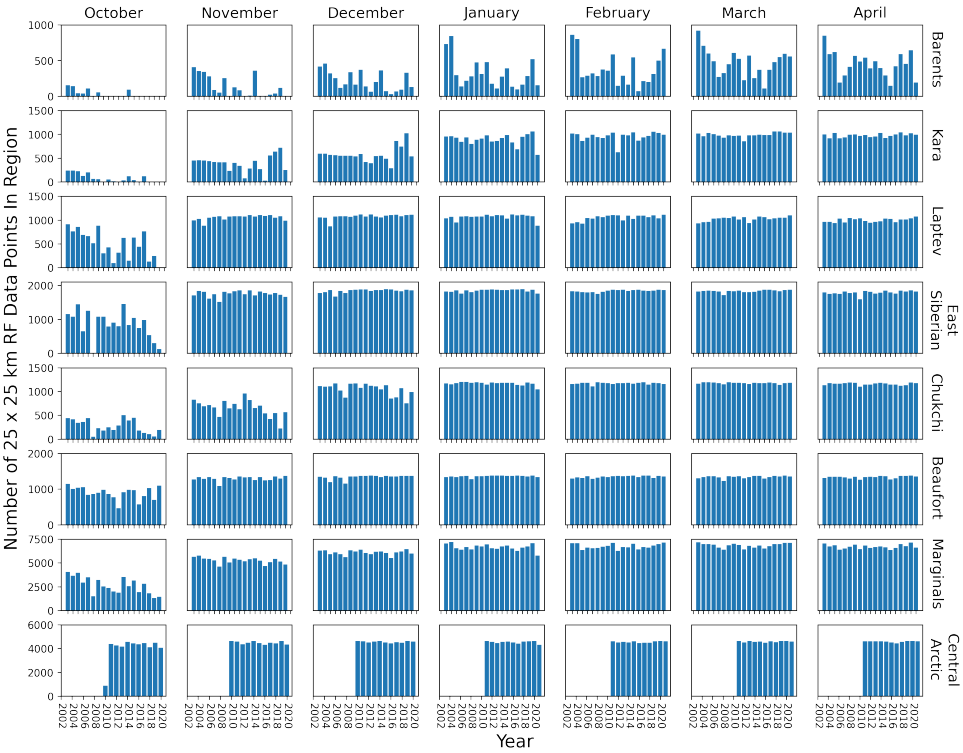

Figure S9: The number of $\overline{RF}$ 25×25 km data points in each region for each month. We were not able to compute $\overline{RF}$ in the Kara Sea for October 2009 or 2012. Nor were we able to calculate it in the Barents Sea in October after 2008 (with the exception of 2011 and 2014).

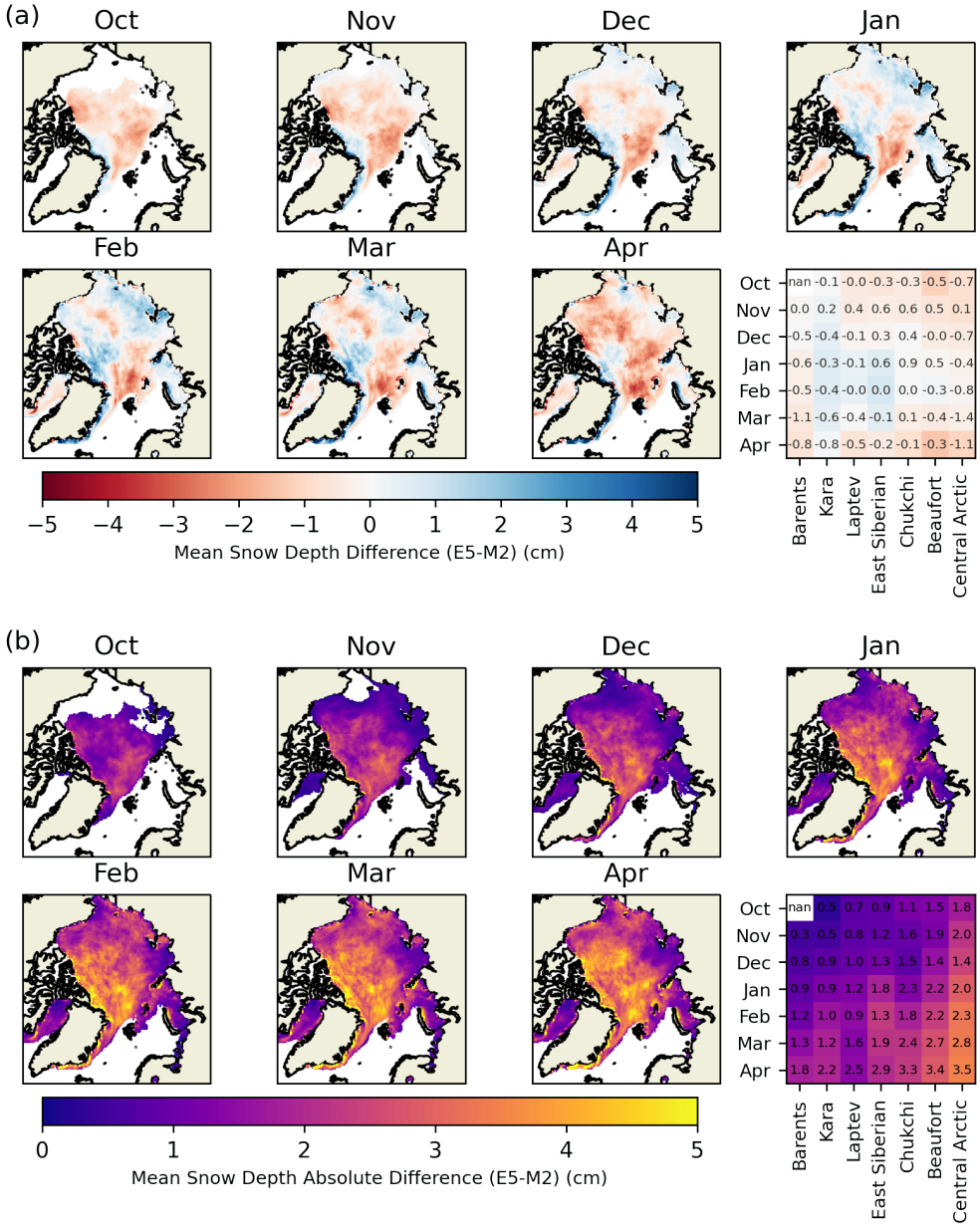

Figure S10: (a) difference in snow depth in SnowModel-LG when driven by ERA5 and Merra2 reanalysis data at each 25x25 km pixel on the EASE grid averaged over the period 2002-2021. (b) time average of absolute differences in SnowModel-LG when driven by ERA5 and Merra2 reanalysis data. We note that (b) is not the absolute value of (a), but instead the time-average of the absolute values of monthly differences.

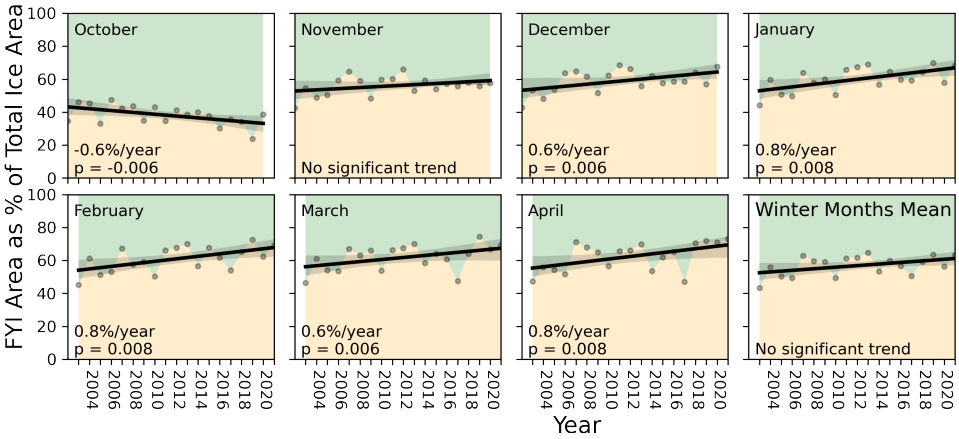

Figure S11: Basinwide trends in first year ice extent as a fraction of total extent from 2003-2021. Statistically significant trends exist in October (declining) and January (increasing). When trends of any significance are considered, all months show positive slopes barring October, which shows distinct decline. The October trend is due to later freeze-ups, the other positive trends fit in with established trends of increasing FYI dominance. Shaded regions represent the 95% confidence level for the linear regression.

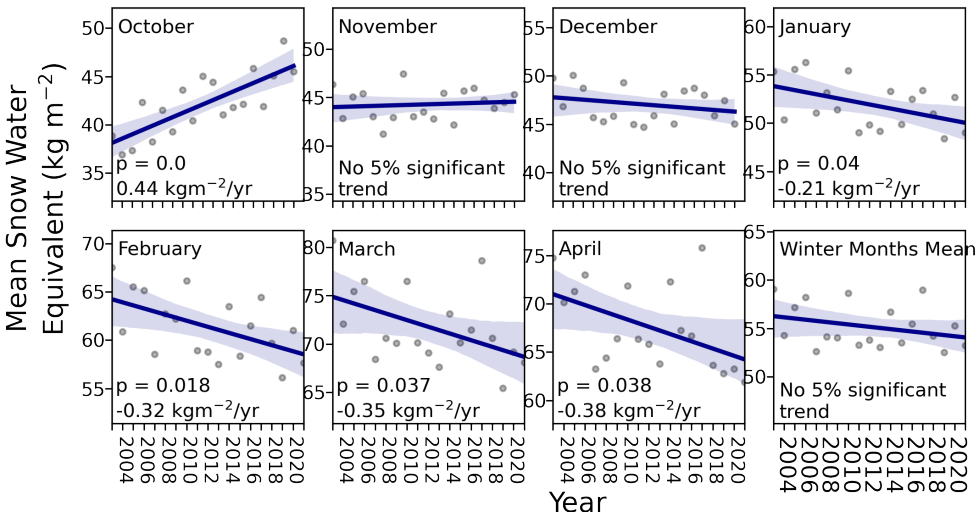

Figure S12: Basinwide trends in mW99 SWE fields from 2003-2021. A statistically significant trend only exists in October, where SWE is increasing due to the increasing dominance of MYI in the month due to later freeze-ups. Shaded regions represent the 95% confidence level for the linear regression.

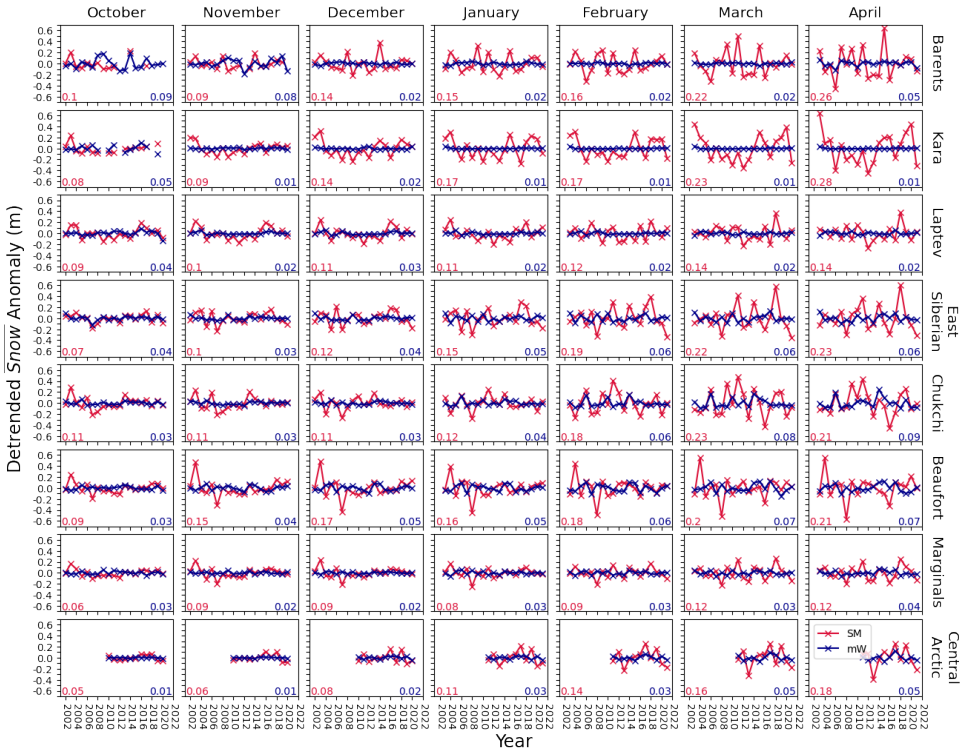

Figure S13: Detrended timeseries of spatially averaged snow contributions to sea ice thickness (Snow) by region from W99 (blue) and SnowModel-LG (red). Standard deviation values are displayed for SnowModel-LG (lower left, red), and mW99 (lower right, blue)

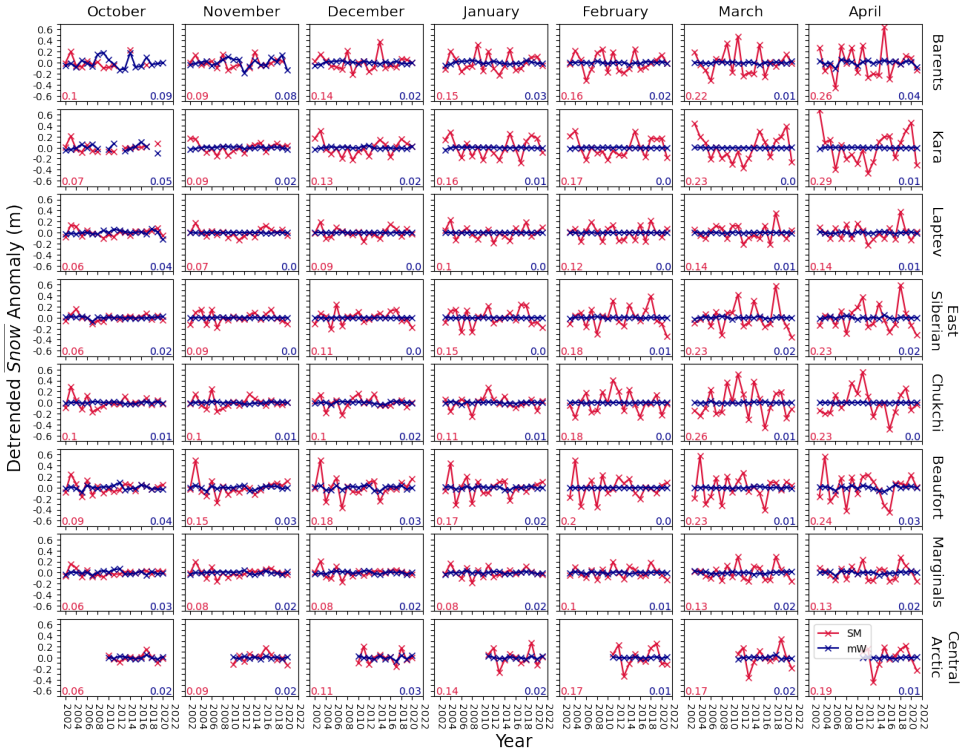

Figure S14: Detrended timeseries of spatially averaged snow contribution to sea ice thickness ($\overline{Snow}$) from W99 (blue) and SnowModel-LG (red) **over first year ice**. SnowModel-LG is significantly more variable from year to year than W99, which only varies due to shifting dominance of ice types. This increased variability propagates through to sea ice thickness, but is moderated by its covariance with radar freeboard variability. The standard deviations of the two timeseries are displayed in the lower corners of each panel.

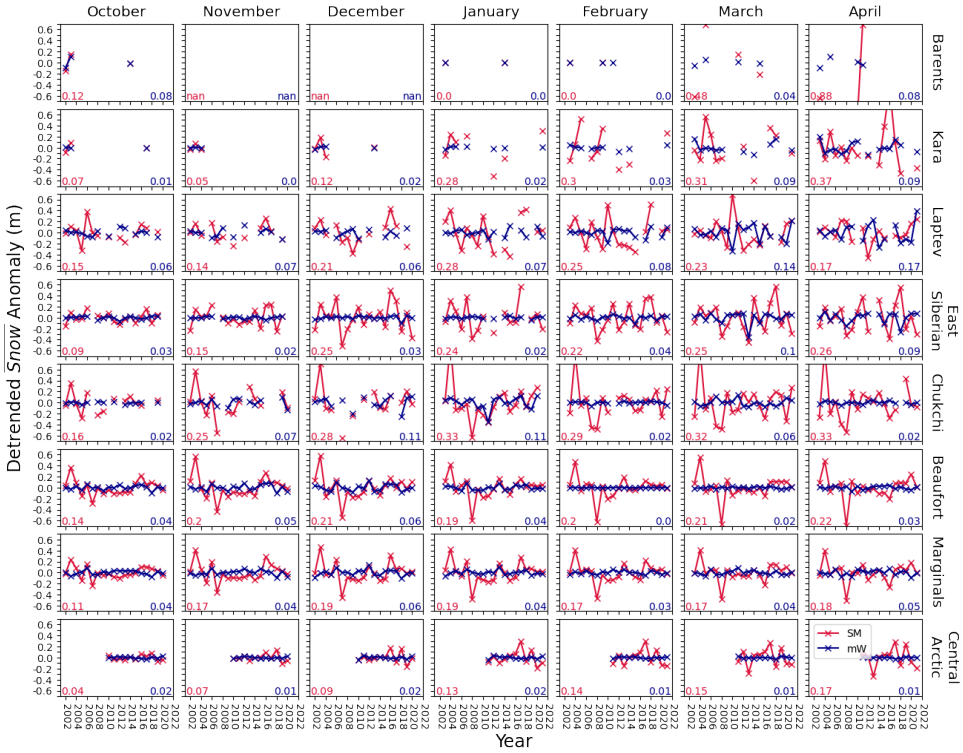

Figure S15: Detrended timeseries of spatially averaged snow contribution to sea ice thickness ($\overline{Snow}$) from W99 (blue) and SnowModel-LG (red) **over multiyear ice** (MYI). SnowModel-LG is significantly more variable from year to year than W99, which only varies due to shifting dominance of ice types. This increased variability propagates through to sea ice thickness, but is moderated by its covariance with radar freeboard variability. A substantial number of data points are missing from some panels - these absences reflect months where no MYI is present in the relevant region. The standard deviations of the two timeseries are displayed in the lower corners of each panel.

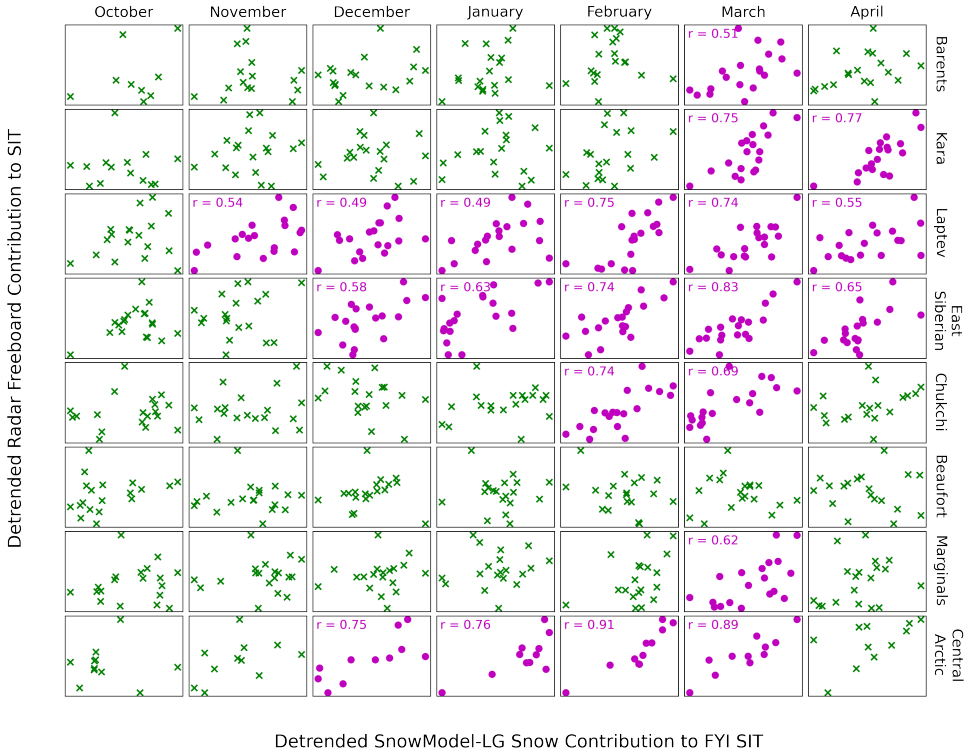

Figure S16: FYI correlations between radar freeboard and snow contributions to sea ice thickness, where the snow contribution is calculated using SnowModel-LG. All statistically significant correlations are positive (i.e. years with more snow exhibit higher radar freeboards). A persistent, positive correlation exists in the Central Arctic and the East Siberian Sea in the last five months of winter. The Barents and Kara Seas both exhibit significant correlations in the last two months of winter. The Beaufort sea exhibits no months of statistically significant correlation between radar freeboard and snow contributions.

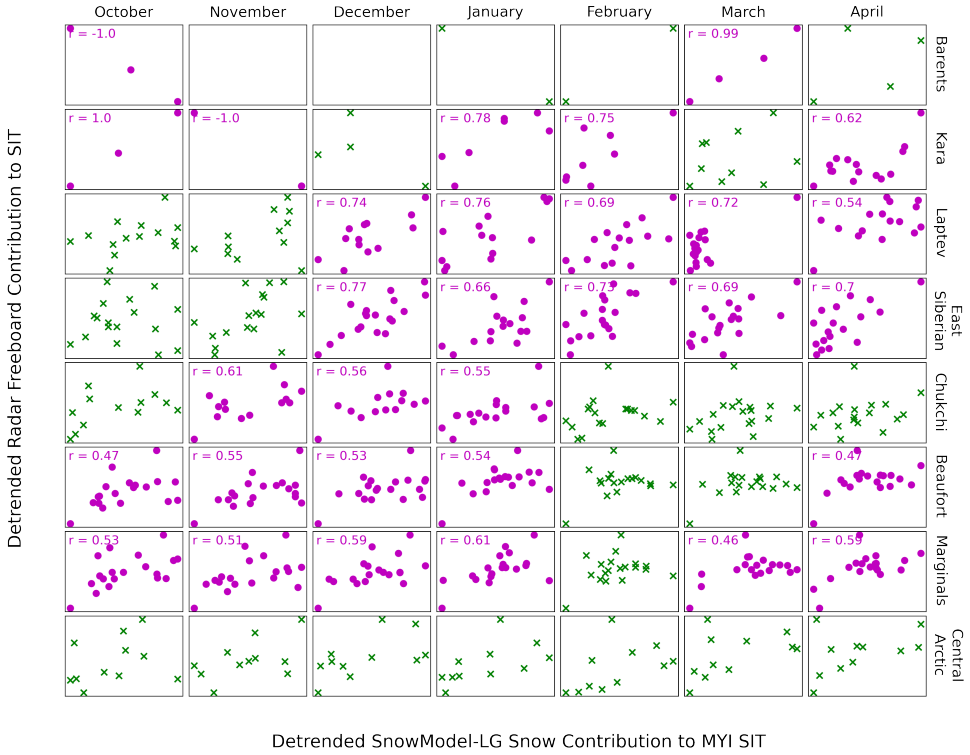

Figure S17: MYI correlations between radar freeboard and snow contributions to sea ice thickness, where the snow contribution is calculated using SnowModel-LG. Fewer correlations exist for MYI than for FYI. The Central Arctic and Chukchi Sea exhibit no correlations between snow and radar freeboard contributions.

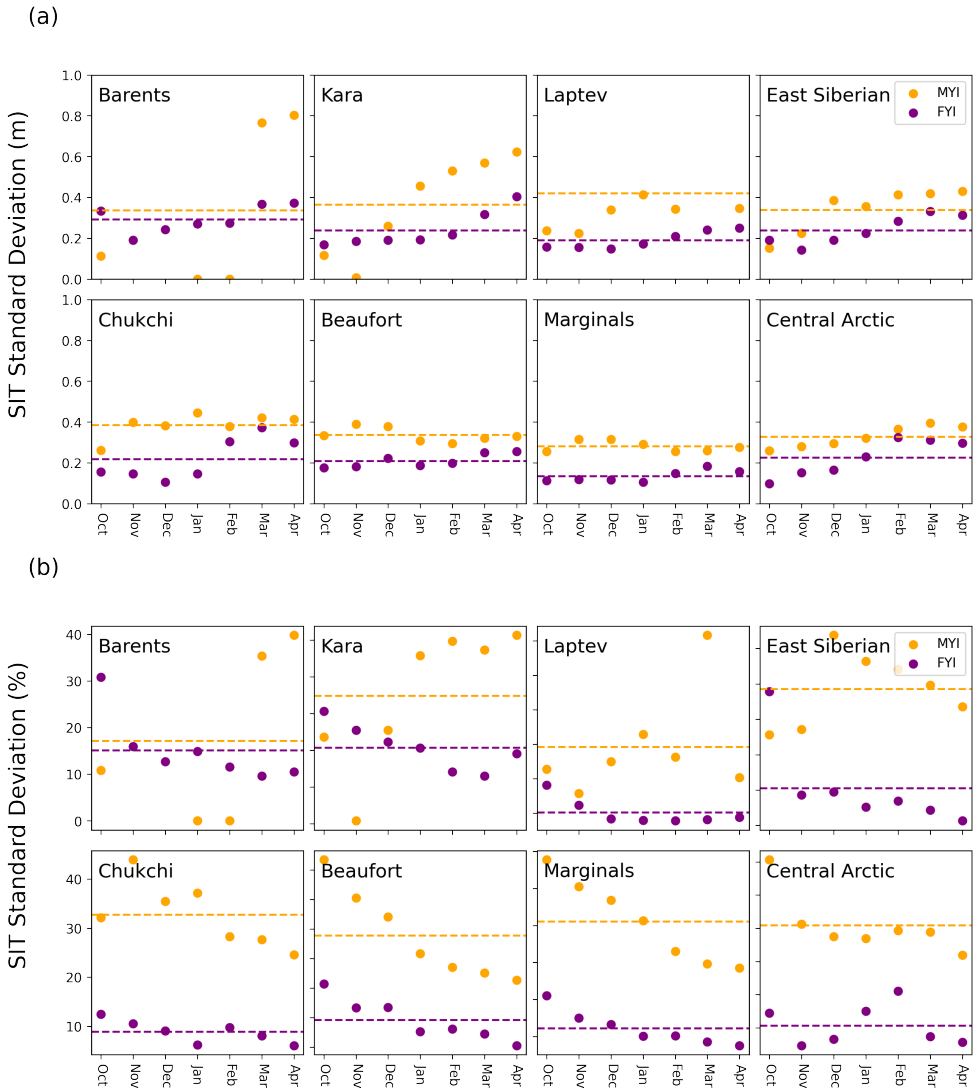

Figure S18: Regional IAV displayed by ice type. MYI represented by orange points, FYI represented by purple. When averaging over the growth season in a given region, MYI is more variable in all the marginal seas.

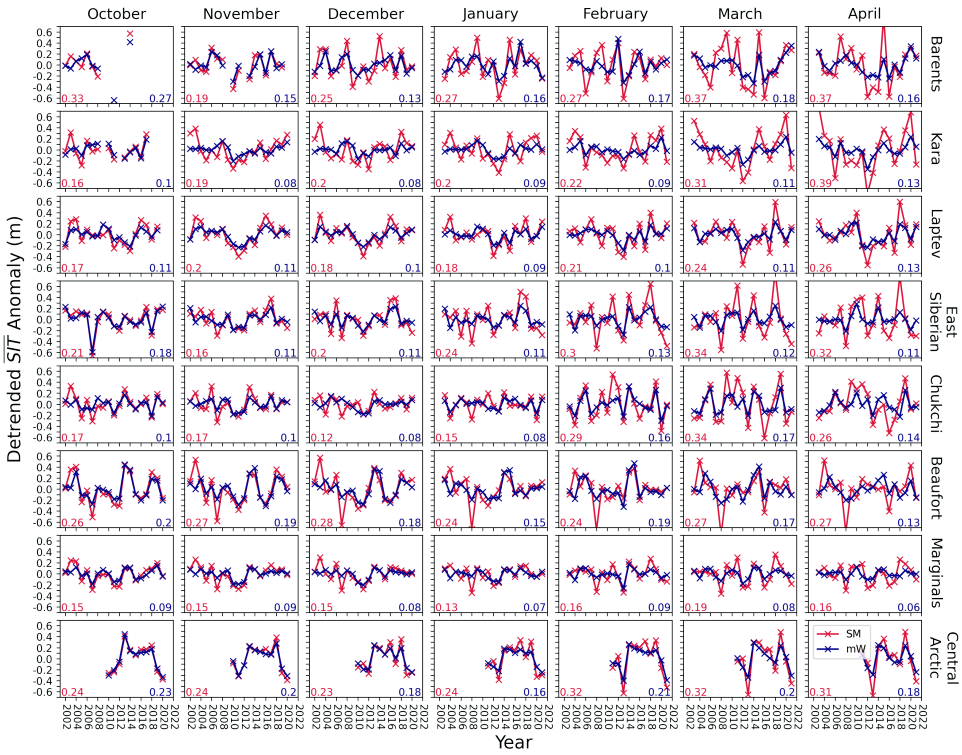

Figure S19: Detrended timeseries of spatially averaged sea ice thickness ($\overline{SIT}$) by region from W99 (blue) and SnowModel-LG (red) for **all ice types**. Standard deviation values are displayed for SnowModel-LG (lower left, red), and mW99 (lower right, blue).

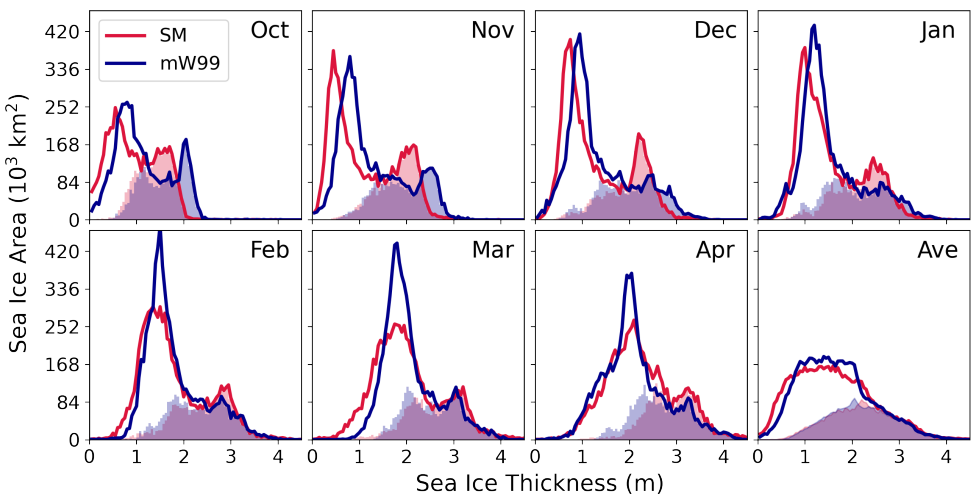

Figure S20: 2010-2021 basin-wide sea ice thickness distribution calculated using both mW99 and SnowModel-LG data expressed as total sea ice area of all grid cells falling into a specific SIT bin. Bin size is 5 cm. Shaded areas represent the area constituted by the Central Arctic.

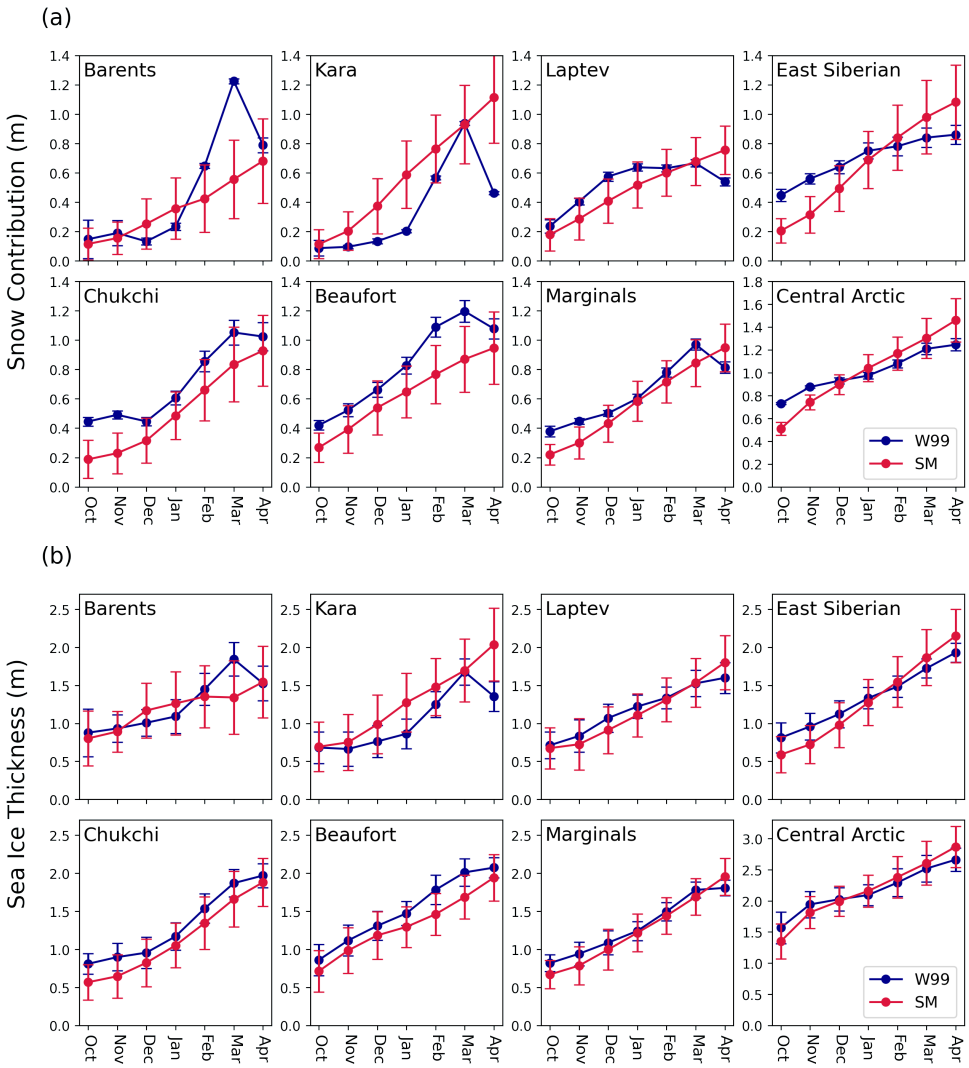

Figure S21: Seasonal evolution of (a) snow thickness and (b) sea ice thickness by region. All regions calculated over 2002-2021 with the exception of the Central Arctic, which is 2010-2021. Note different y-axis scales for Central Arctic panels. 'Error bars' represent the one standard-deviation range either side of the mean value for the timeseries. The SnowModel-LG contribution starts lower but ends higher in the Central Arctic, the region that dominates Pan-Arctic statistics. This is also true for the Marginal Seas grouping, but not necessarily true for the individual constituent regions. This corresponds to faster thickness increase than would be calculated with W99.

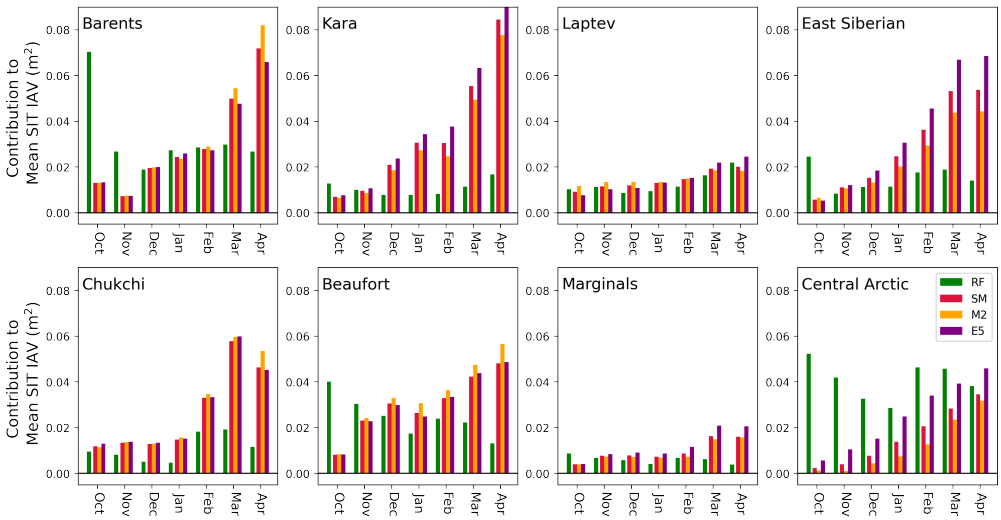

Figure S22: Interannual variability of SnowModel-LG contribution to σ^2_{SIT} (σ^2_{Snow}) when forced by two different reanalysis data sets. MERRA2 (orange) and ERA5 (green) produce very similar variability.

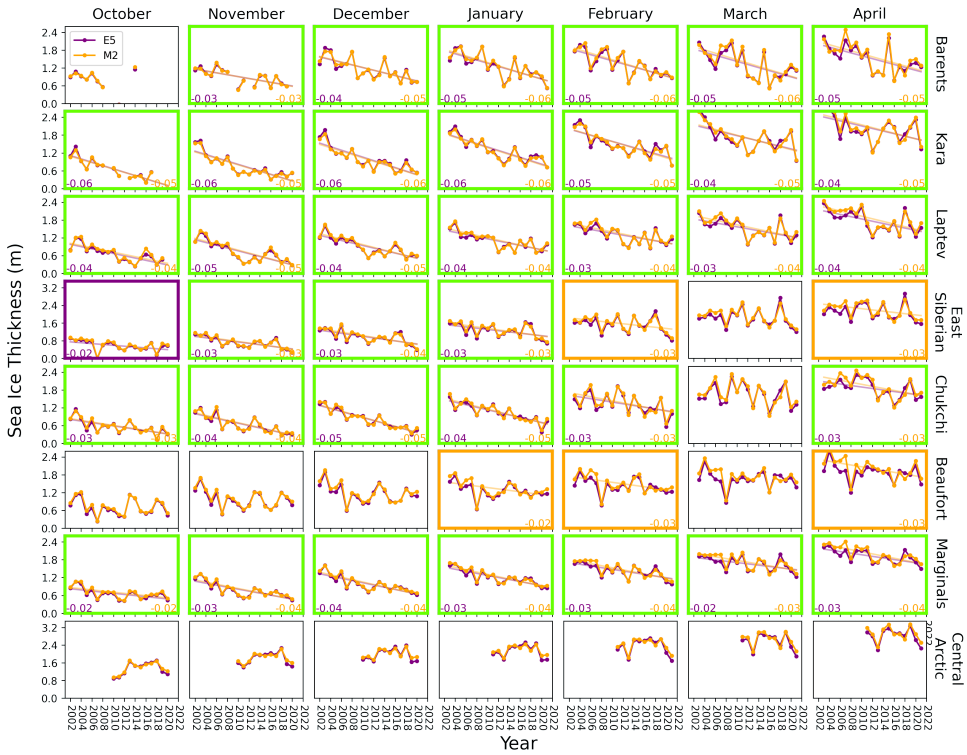

Figure S23: Trends in sea ice thickness (2002-2021) by region, when calculated using SnowModel-LG runs using two different sources of reanalysis (ERA5, Purple; MERRA2, Orange). Panels are framed with green where statistically significant trends exist independent of reanalysis choice. Purple (orange) frames represent month/region pairs where statistically significant trends are only present with ERA5 (MERRA2). Slope values are given where significant in the lower corners. All significant trends in the marginal seas are negative, all significant trends in the Central Arctic are positive. In the Central Arctic, two of the four statistically significant increasing trends are only evident with ERA5 reanalysis. In the Marginal Seas, the decline in some months is only statistically significant with MERRA2.

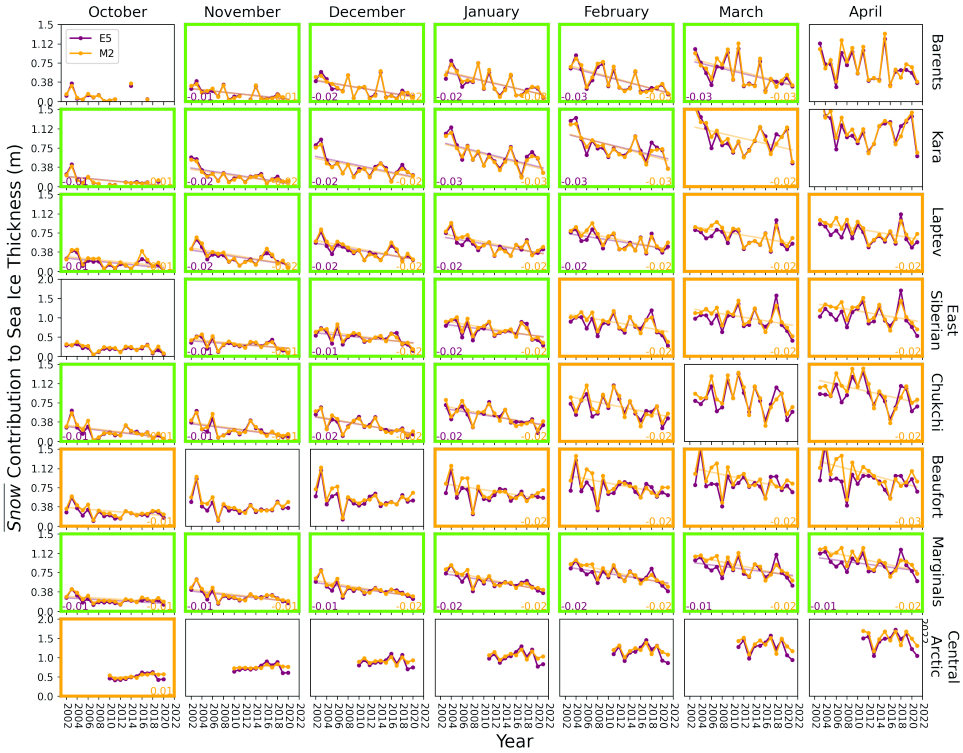

Figure S24: Trends in snow contribution to sea ice thickness ($\overline{Snow}$; 2002-2021) by region, when calculated using SnowModel-LG runs using two different sources of reanalysis (ERA5, Purple; MERRA2, Orange). Panels are framed with green where statistically significant trends exist independent of reanalysis choice. Purple (orange) frames represent month/region pairs where statistically significant trends are only present with ERA5 (MERRA2). Slope values are given where significant in the lower corners.

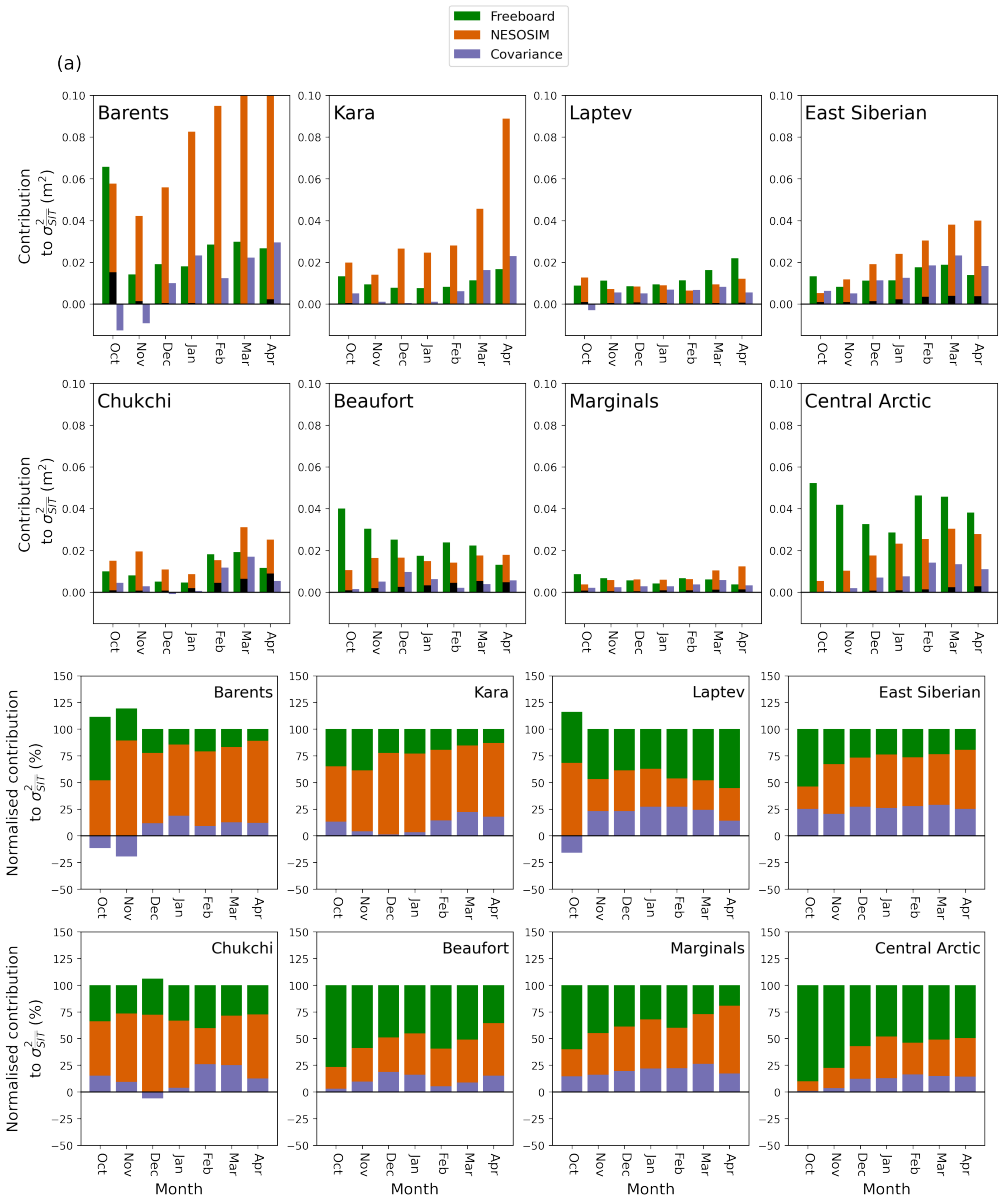

Figure S25: Interannual variability of NESOSIM data's contribution to SIT, shown as (a) absolute contribution to SIT variability, and (b) relative contribution. Variability from snow is of a similar magnitude to that of SnowModel-LG, although regional differences exist between the corresponding plots, particularly in the Barents Sea. As well as differences in the snow accumulation scheme, the two data sets differ in spatial resolution and the timespan over which they are analysed.

Figure S26: Timeseries of the thickness contributions of radar freeboards ($\overline{RF}$) and snow ($\overline{Snow}$) over all ice types. Orange framed boxes indicate statistically significant decline in both $\overline{RF}$ and $\overline{Snow}$. The red framed box indicates statistically significant decline in $\overline{Snow}$ only. No boxes feature a statistically significant decline in $\overline{RF}$ without a concomitant decline in $\overline{Snow}$. All statistically significant trends in both $\overline{Snow}$ and $\overline{RF}$ are negative.

Supplement to Chapter 4

S4 Best-fit statistics for log-normal and gamma distributions

Figure 3 of the main paper shows that the skew normal distribution has a superior fit to the observed data than the log-normal or gamma distributions. Here we provide the parameters of best fit for all three distributions for comparative purposes. For completeness, we restate that for the skew normal curve described in Eq. 2 of the main paper, the parameters of best-fit were a = 2.54, ξ = -1.11 & ω = 1.50.

The log-normal distribution is described as follows:

$$f(x,s) = \frac{1}{sx\sqrt{2\pi}}\exp\left(-\frac{\log^2(x)}{2s^2}\right) \tag{S16}$$

For $x > 0$ & $s > 0$. Analogous to the skew normal distribution described in the main manuscript, two more locating and scaling parameters (ξ & ω) are applied during the fit, such that x in the above equation can be represented by $(\sigma_D - \xi)/\omega$. The corresponding best-fit parameters for the log-normal distribution are s = 0.17, ξ = -5.82, ω = 5.73. The gamma distribution is described as follows:

$$f(x,a) = \frac{x^{a-1}e^{-x}}{\Gamma(a)} \tag{S17}$$

for $x \geq 0$, $a > 0$, and $\Gamma(a)$ being the gamma function. As with the skew normal and log-normal distributions, locating and scaling parameters are applied such that $x = (\sigma_D - \xi)/\omega$. The parameters of best-fit for the Gamma distribution are a = 26.15, ξ = -5.06 & ω = 0.19.

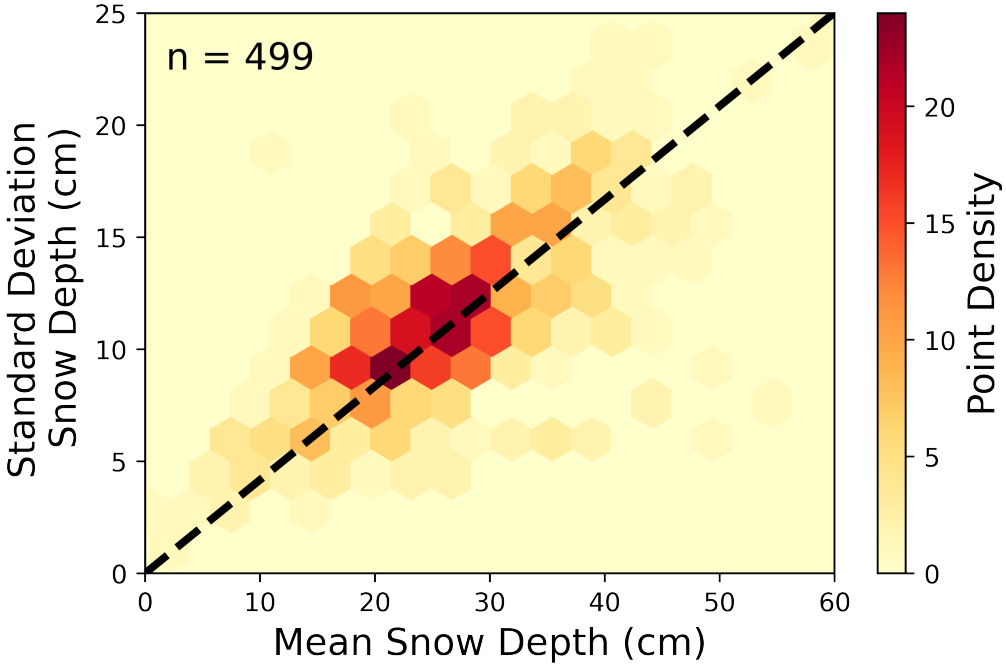

Figure S27: Point density plot corresponding to Fig. 2a of the main paper, and the regression (black dash line) between mean and standard deviation of the snow depth. The Pearson r value of the correlation is 0.66.

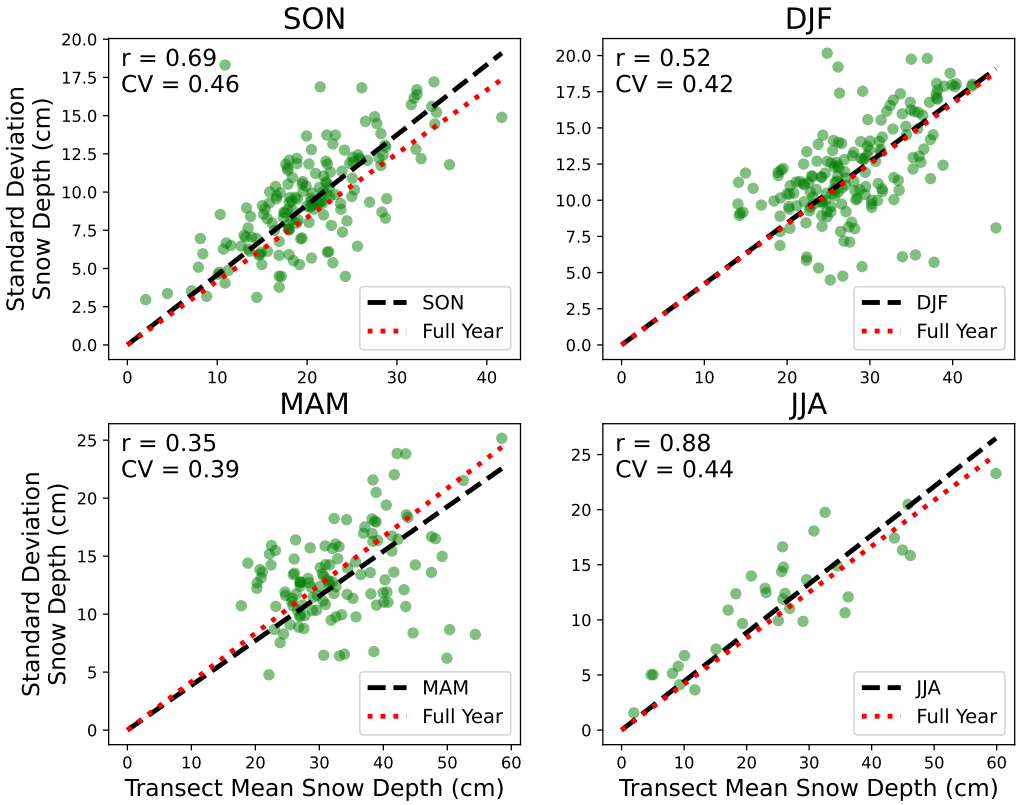

Figure S28: Seasonal relationships between snow depth transect standard deviation and means. Black dashed lines indicates the seasonal relationship, red dotted line indicates the relationship used in the main chapter generated from the whole year. All regression lines are forced through the origin. Seasonal coefficient of variation is higher than the annual average for SON, and lower for MAM.

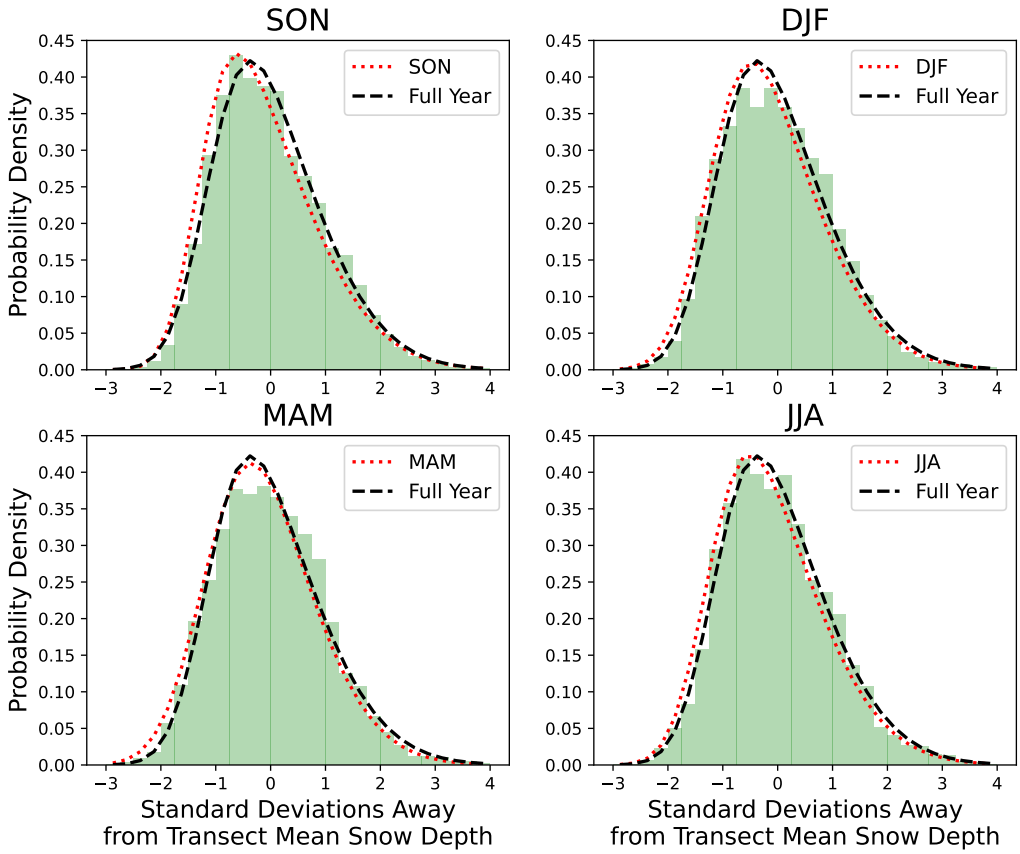

Figure S29: Seasonal distribution of all 33,535 snow depth measurements expressed in standard deviations from their transect mean. Black dashed line indicates the skew normal fit described in the main chapter. Red dotted lines indicate a bespoke skew-normal fit based on the data shown in the panel. The largest discrepancy between the bespoke and full-year fits is in September/October/November, where the bepsoke fit is more sharply peaked, and more strongly positively skewed.

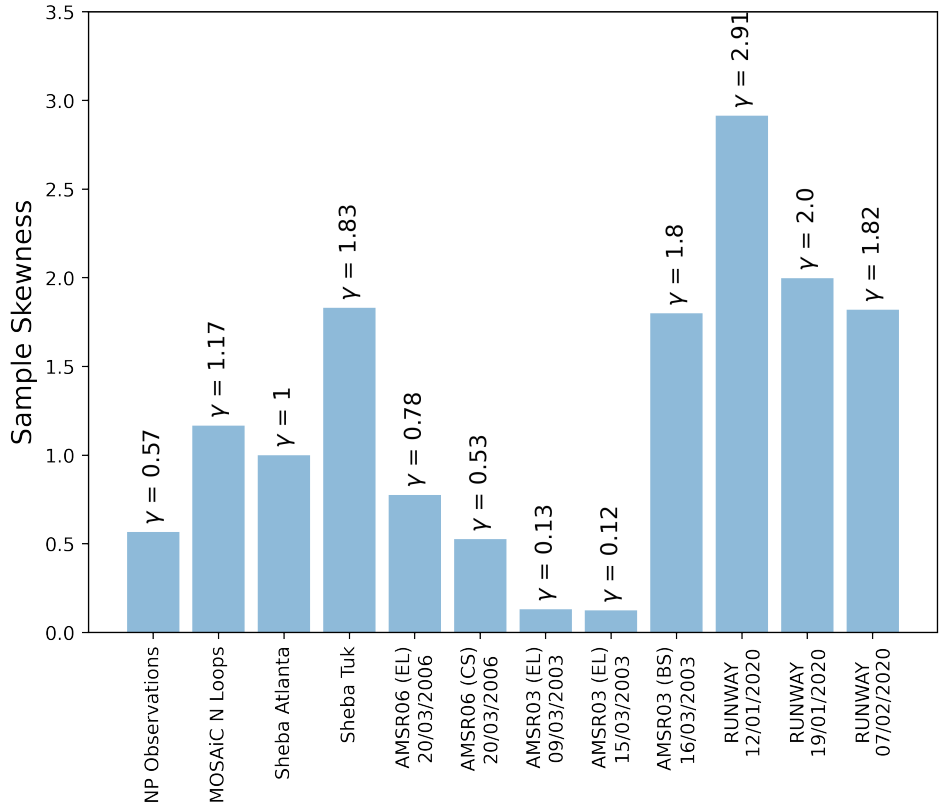

Figure S30: Sample skewness (γ) for all observational data considered in this study. Note that sample skewness is different to the skewness parameter of the skew normal distribution (a), although the two variables have the same sign.

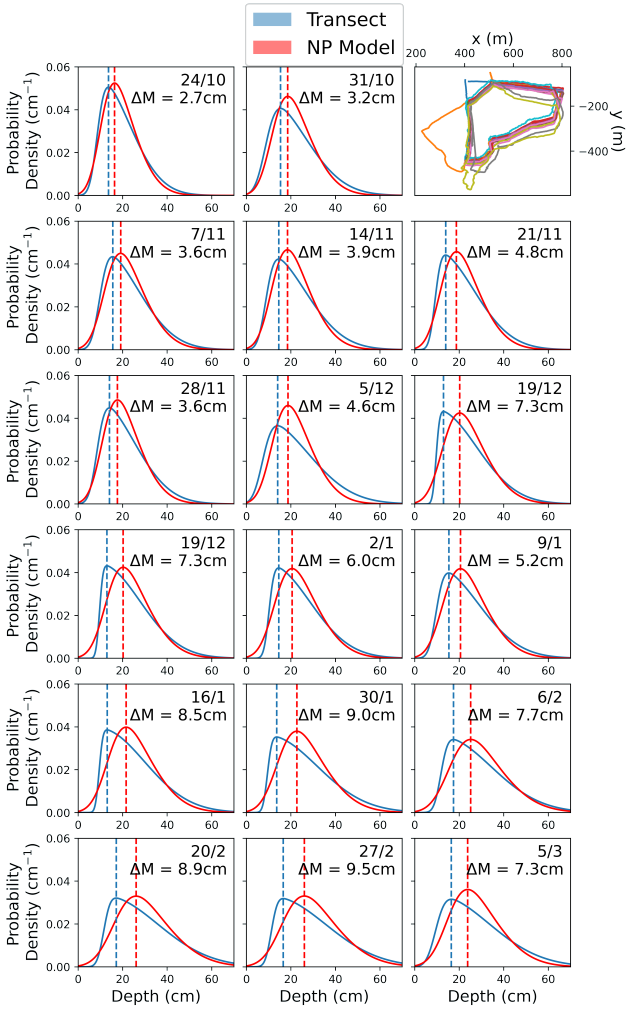

Figure S31: Comparison of the NP model when initialised by the mean snow depth of each transect (red curves), with a skew normal curve fitted to the observed data. The NP model consistently overestimates the modal value of the snow depth by comparison to the skew normal curve of best fit. This discrepancy grows over the course of the measurements, from 2.7 centimetres at the end of October to 9.5 centimetres at the end of February. ΔM indicates the mismatch in the mode of the two distributions.

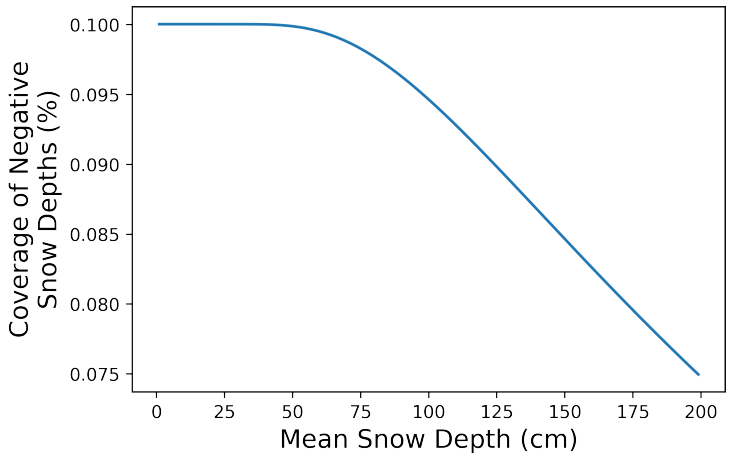

Figure S32: Areal coverage of negative snow depths in the NP model as a function of mean snow depth.

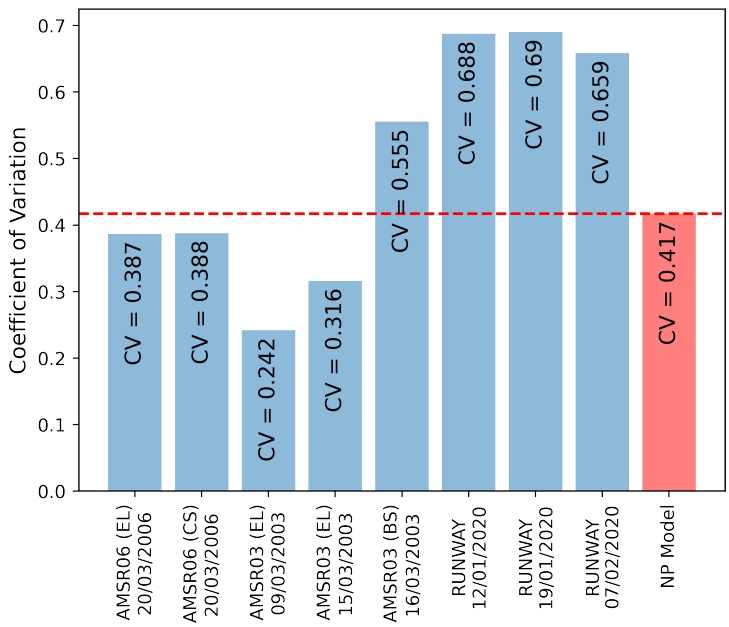

Figure S33: Coefficient of variation for the six FYI data sets considered in this paper, compared to that generated from the NP data.

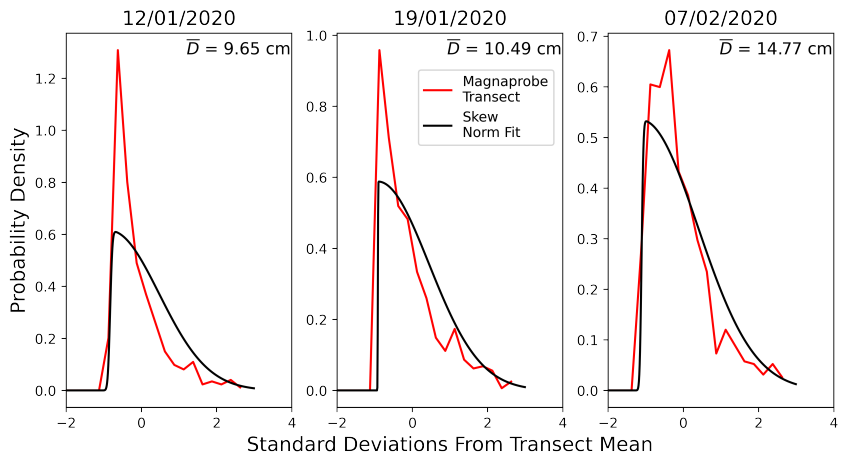

Figure S34: Distribution of snow depths measured on the "Runway" transect of the MOSAiC expedition (red). Black lines indicate the best-fit skew-normal curves, which have a poor quality of fit. $\overline{D}$ indicates the mean depth of the transect.

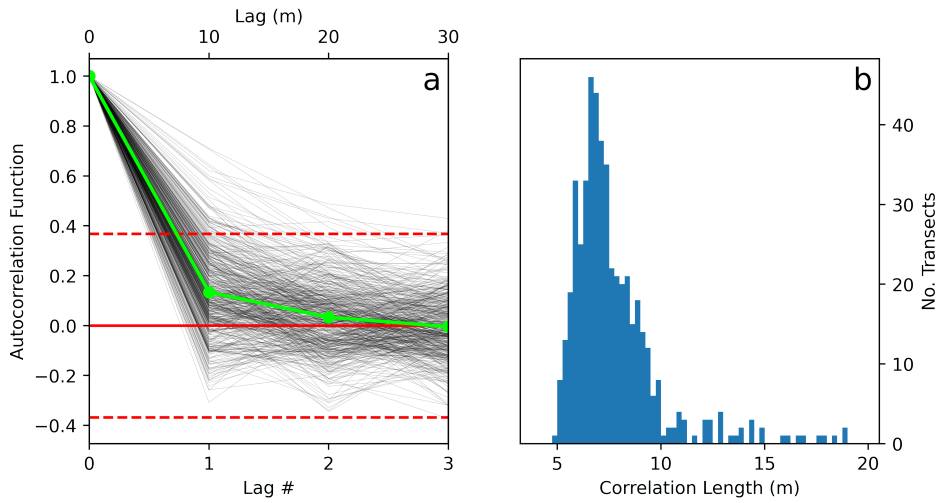

Figure S35: (a) Autocorrelation functions of 499 transects (black lines). The mean of these autocorrelation functions is shown in green. Red dashed lines indicate a value of $\pm 1/e$, the positive value of which corresponds to the threshold for the 'autocorrelation length'. (b) Distribution of transect correlation lengths with a bin size of 25 cm.

Supplement to Chapter 5

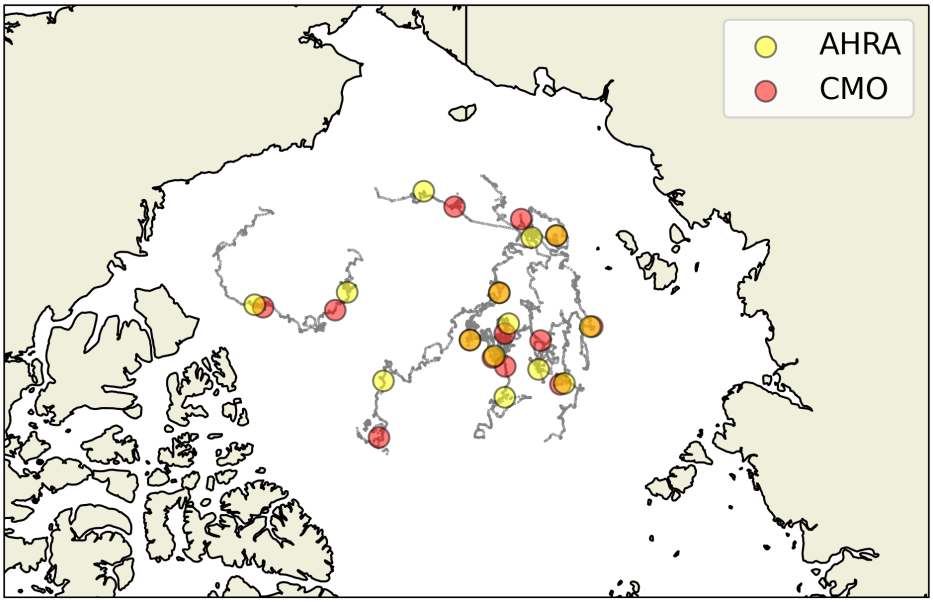

Figure S36: Positions of NP stations on the dates when they drift through a pixel of a satellite melt onset product that indicates melt onset. Because the products differ, the positions of the NP stations when they experience melt onset per the satellite products also differ.

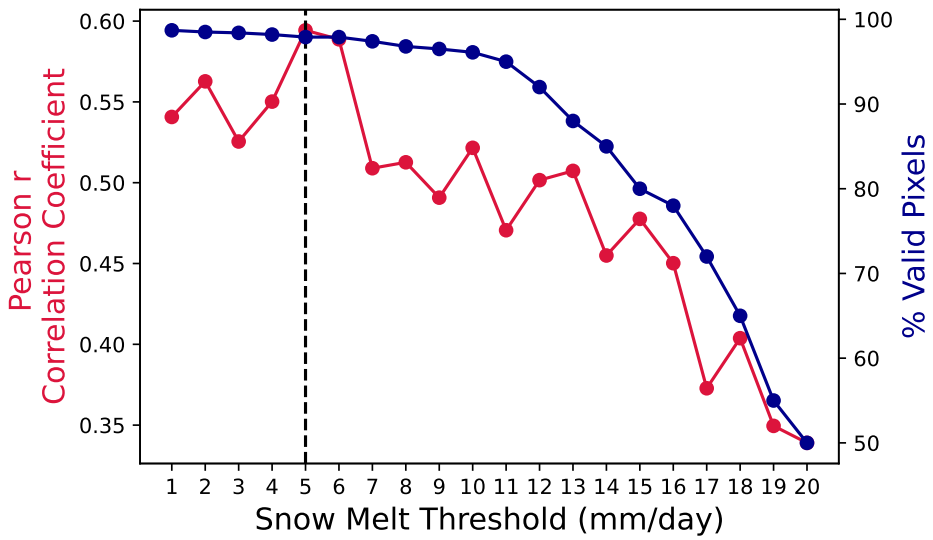

Figure S37: Results of a sensitivity analysis performed over the Central Arctic region (defined consistently with this thesis, as per Meier et al. (2007)). Dark blue line shows how the number of pixels that exceed the threshold in a given season decreases at higher thresholds. This effect means that melt onset cannot be determined in some regions for higher threshold values. Red line indicates the correlation coefficient for the regional mean timing of threshold-excedance and the satellite-based CMO product of Markus et al. (2009). This correlation coefficient is highest for a threshold value of 5 mm/per day. One caveat to this analysis is that for lower thresholds the bias *increases*, i.e. melt onset timing as determined by the SnowModel-LG snow melt threshold gets earlier at lower values, moving *away* from the timing in the satellite melt onset product. This is related to the early-bias of SnowModel-LG as documented elsewhere in Chapter 5. While the bias increases with lower thresholds, the skill in terms of the interannual variability representation (reflected by the correlation coefficient) also increases up to a value at 5 mm/day. Lower correlation coefficients at thresholds less than 5 mm may be related to 'spurious' early triggering of the threshold by warm events earlier in the season that are either not picked up by satellite radiometers, or not actually reflective of the real world and only present in SnowModel-LG.

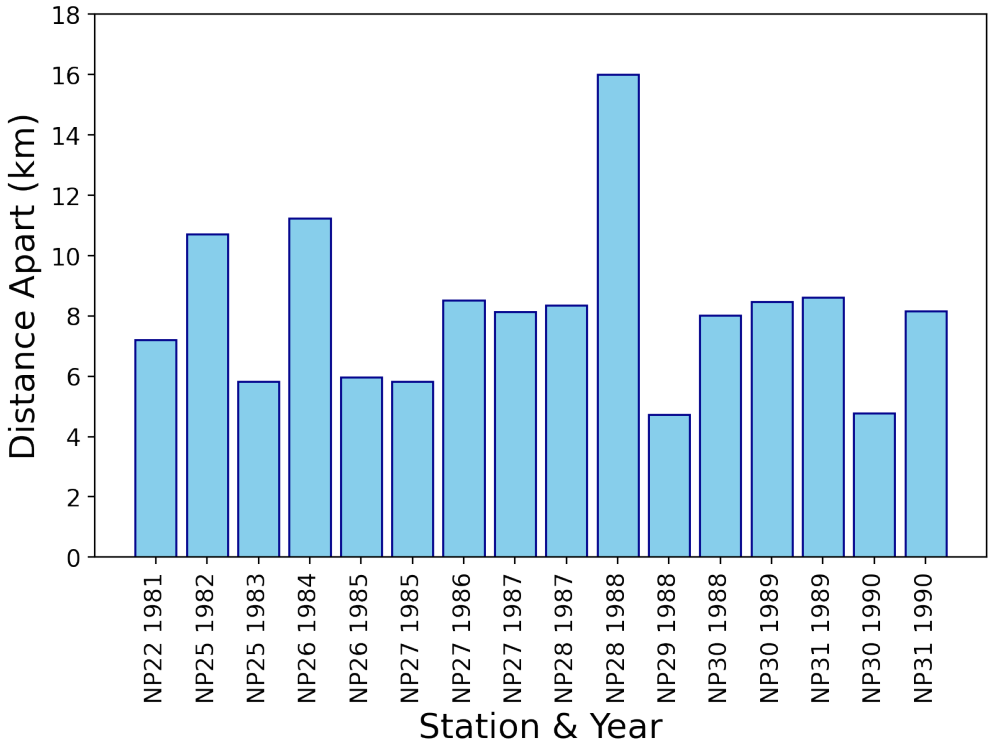

Figure S38: Distances between NP stations and their paired SnowModel-LG parcels on the 100th day of year.

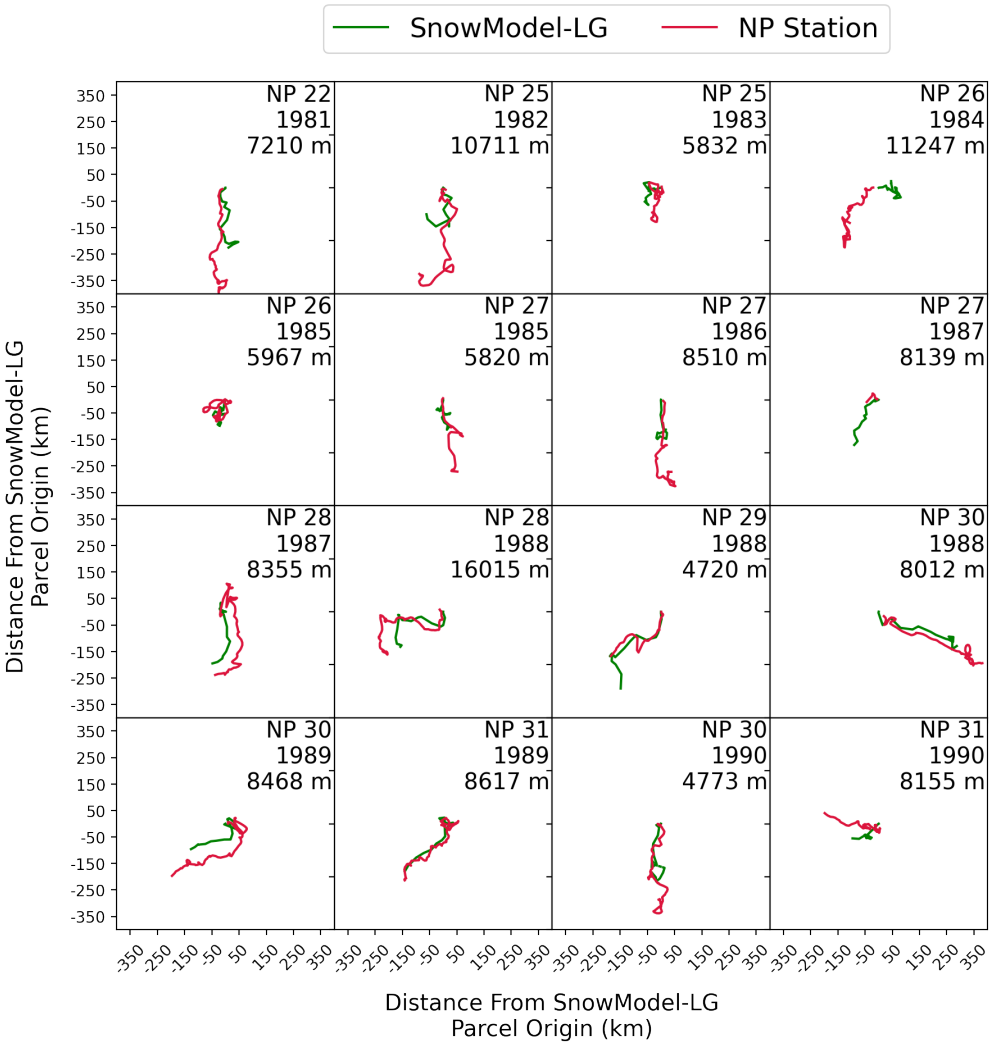

Figure S39: Trajectories in space between NP stations and paired SnowModel-LG parcels in the melt onset period (day-of-year 100 to 214, the first of August). Lower line of annotation indicates the initial distance between the two tracks.

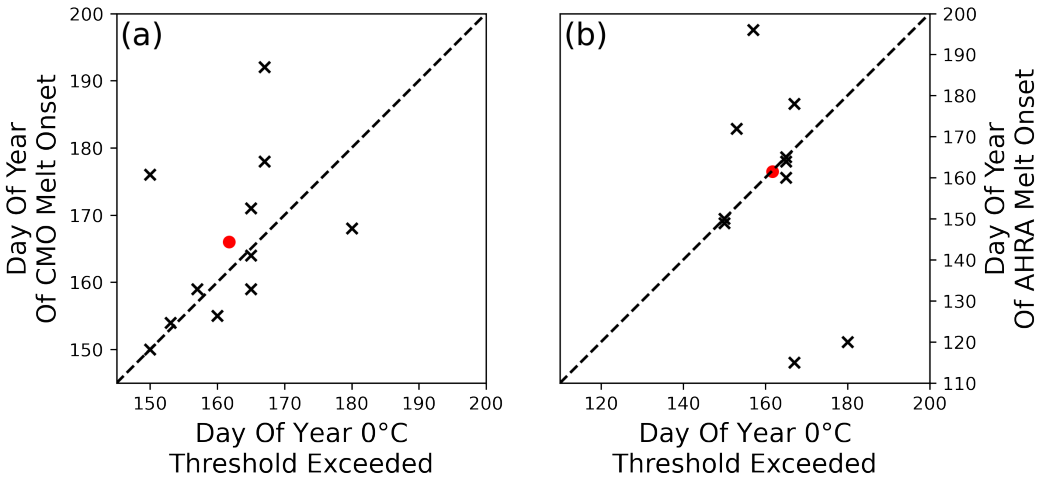

Figure S40: (a) Differences between the continuous melt onset product of Markus et al. (2009) and the date on which 0°C is exceeded for the first time. (b) Same as panel a, but for the Advanced Horizontal Range Algorithm of Drobot and Anderson (2001). Red data points indicate the centroids of the distribution. Note different scales between the panels.

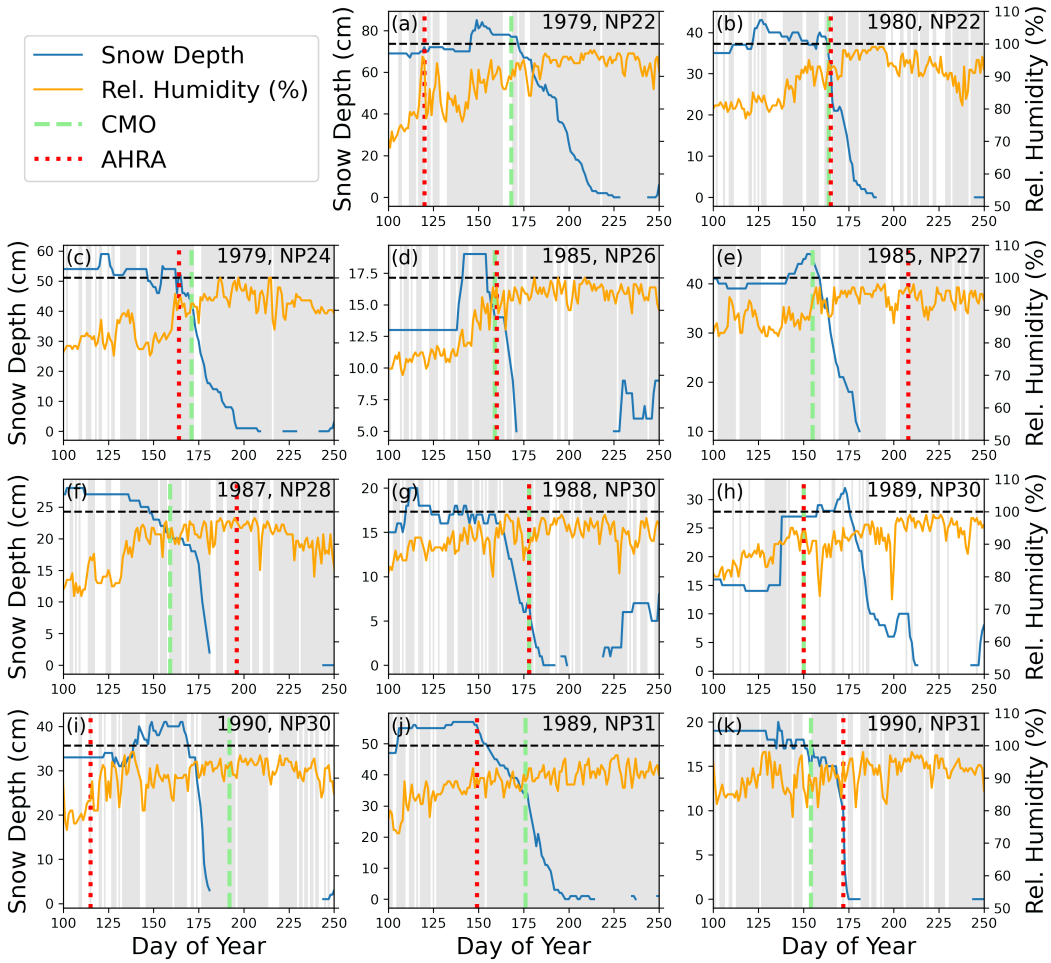

Figure S41: Co-evolution of relative humidity (orange lines, %) and snow depth (blue lines, cm) at the eleven NP stations that were both observed by satellite radiometers during the period of melt onset and took daily snow depth observations consistently. Vertical green lines indicate the melt onset timing per the Continuous Melt Onset product of Markus et al. (2009), red lines indicate the timing per the Advanced Horizontal Range Algorithm product first described by Drobot and Anderson (2001). Horizontal black dashed line indicates the 100% value of total water vapor saturation. Grey banding represents >5/10 total cloud coverage.

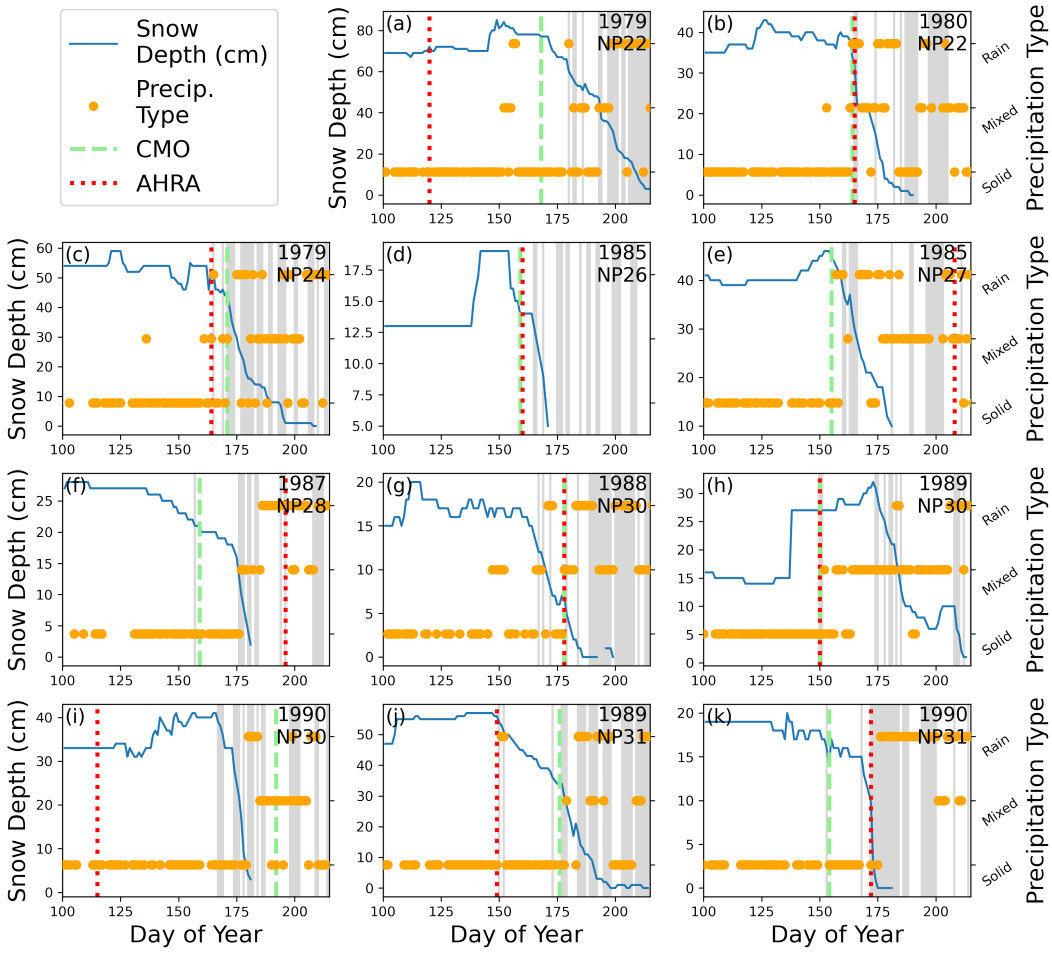

Figure S42: Co-evolution of precipitation type (orange markers) and snow depth (blue lines, cm) at the eleven NP stations that were both observed by satellite radiometers during the period of melt onset and took daily snow depth observations consistently. Vertical green lines indicate the melt onset timing per the Continuous Melt Onset product of Markus et al. (2009), red lines indicate the timing per the Advanced Horizontal Range Algorithm product first described by Drobot and Anderson (2001). Grey banding represents periods where the daily average surface air temperature was greater than or equal to 0°C.

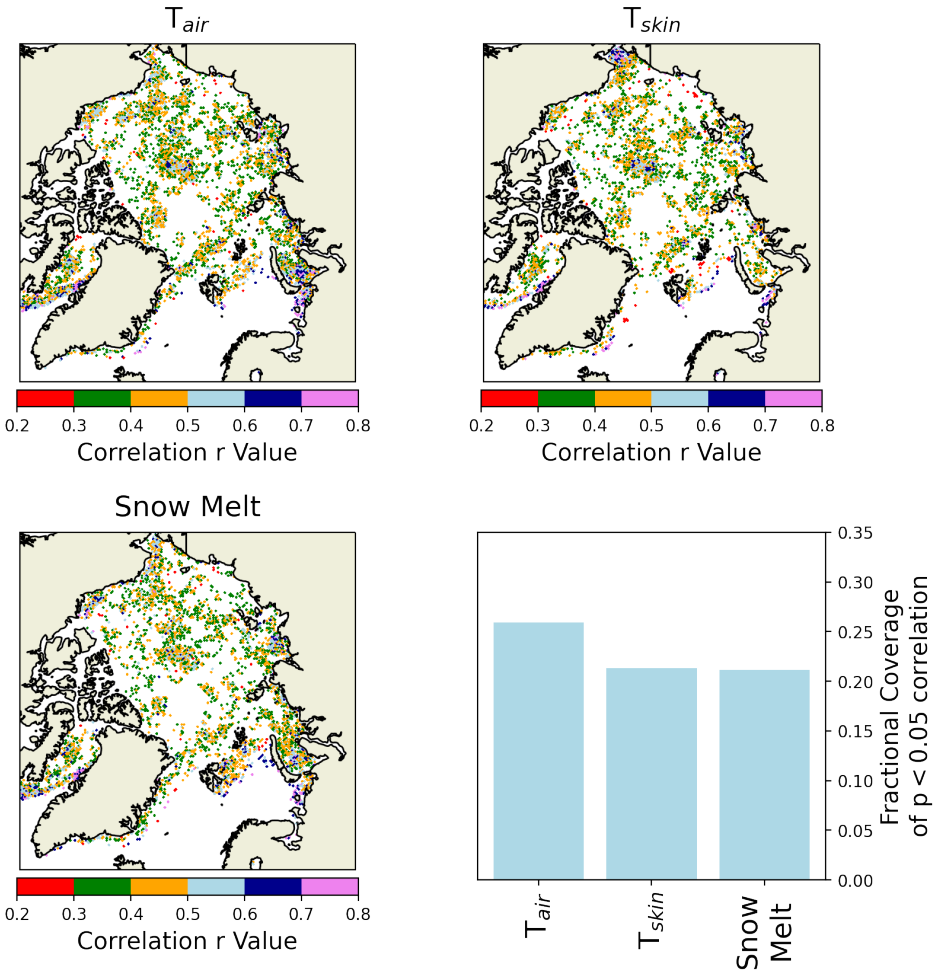

Figure S43: (a - c) Pixel-scale correlations of three melt onset timing diagnostics with radiometry-derived melt onset timings from the CMO product of Markus et al. (2009). (d) The relative coverage of statistically significant correlations the Arctic Ocean (as defined in the chapter text) for the three diagnostics. Correlations are most widespread with the surface air temperature diagnostic.

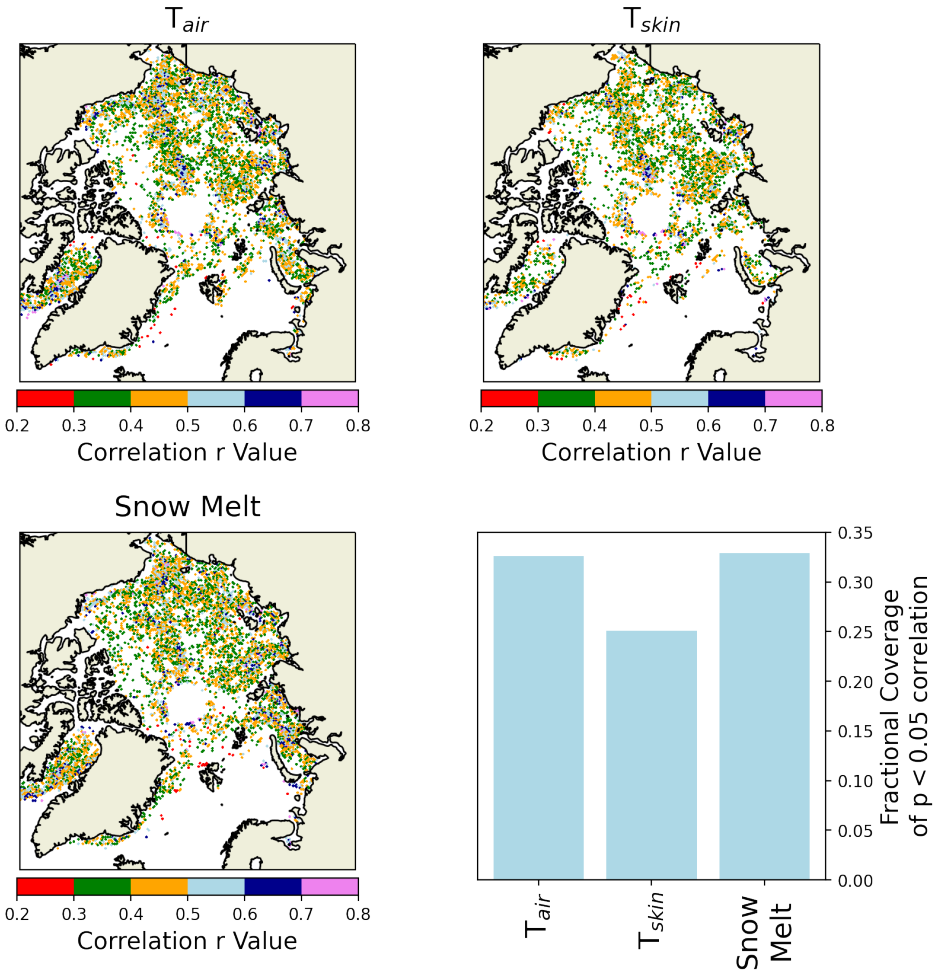

Figure S44: (a - c) Pixel-scale correlations of three melt onset timing diagnostics with radiometry-derived melt onset timings from the AHRA product of Drobot and Anderson (2001). (d) The relative coverage of statistically significant correlations the Arctic Ocean (as defined in the chapter text) for the three diagnostics. Correlations are most widespread with the surface air temperature diagnostic.

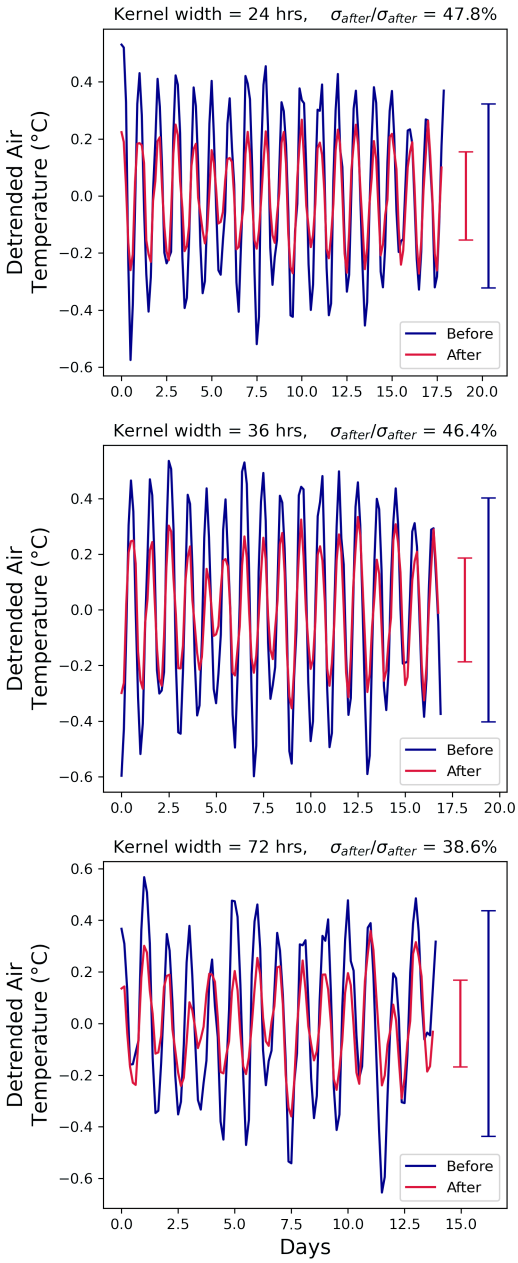

Figure S45: Differences in the amplitude of the diurnal temperature oscillations before and after the reference day of ablation (40% threshold). The three panels represent the results of three different high-pass filtering exercises with different kernel widths. In all cases, the oscillations before the reference day of ablation were significantly larger in amplitude than those afterwards.

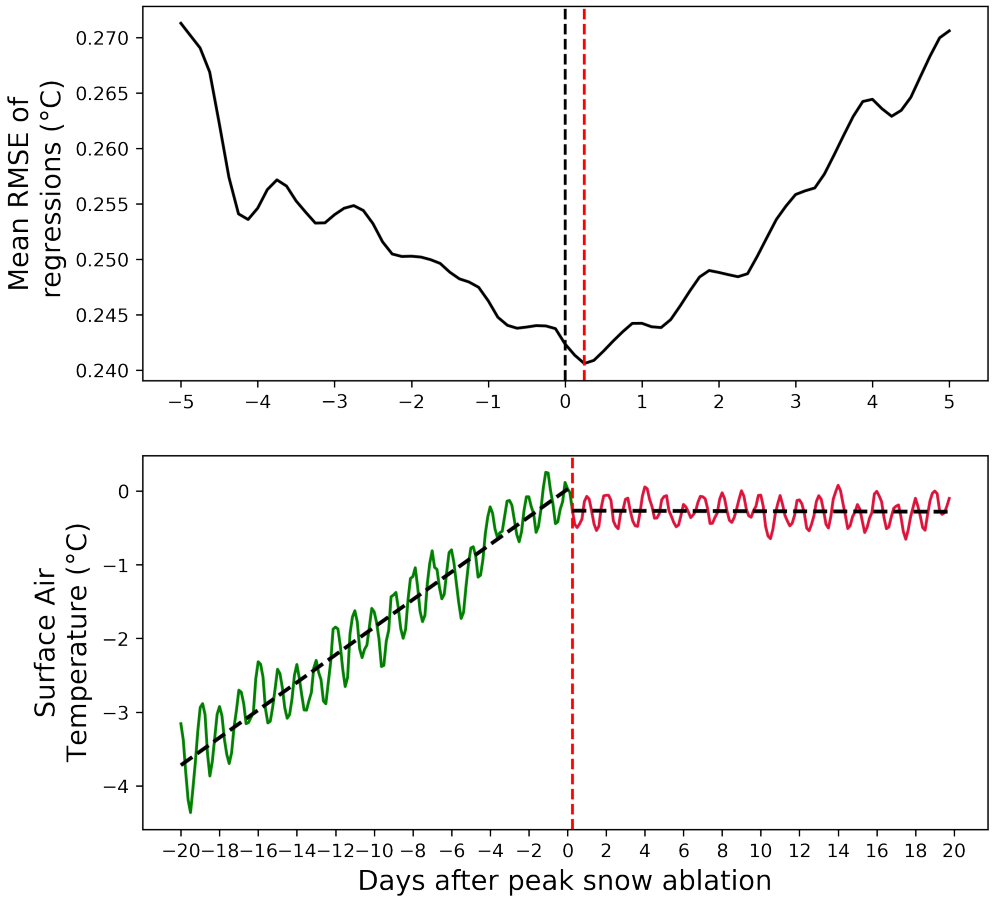

Figure S46: Results of the break-point analysis involving the surface air temperature time-series. Top panel illustrates the process of minimising the mean-RMSE of two linear regressions. The mean error is shown as a function of the position of the breakpoint relative to the reference day of snow ablation. Lower panel illustrates the linear regressions that result from a shifting of the break-point to the position where the mean error of the regressions is minimised.

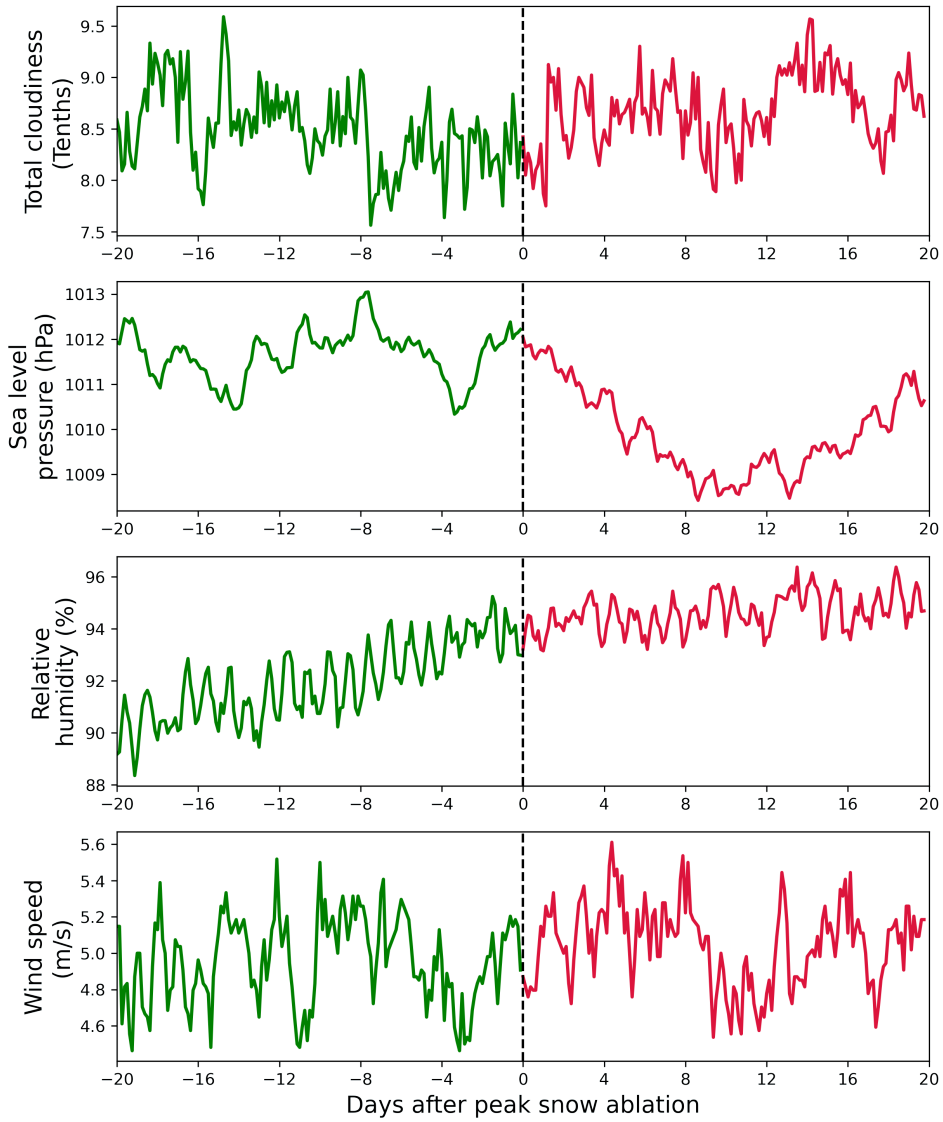

Figure S47: The evolution of four more meteorological variables, shown before and after reference day of snow ablation.

Supplement to Chapter 6

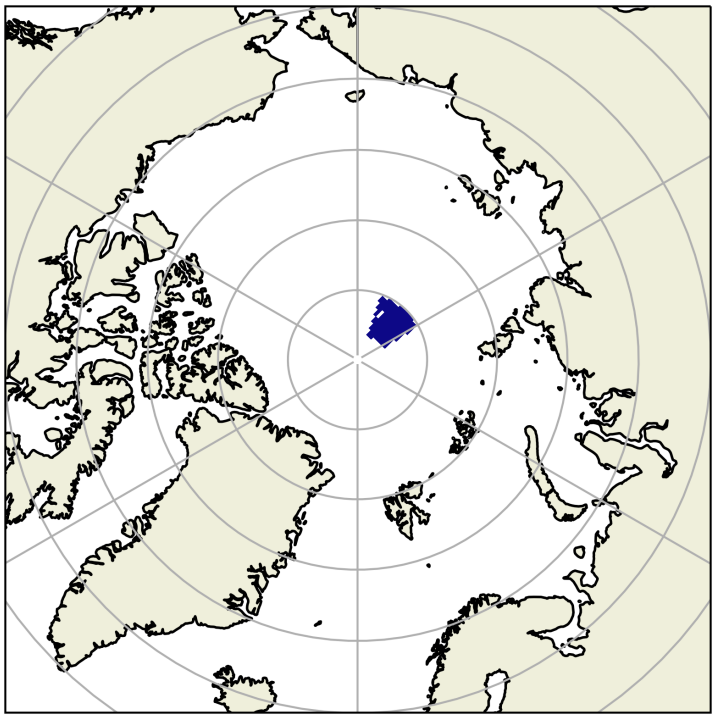

Figure S48: The location (shaded dark blue) of a small test region in which the time-evolution of radar freeboards and snow loading were compared in Chapter 6. The region spans latitudes 85 - 88°N and longitudes 120 - 160°E.

Colophon

Typesetting This PhD thesis was typeset with LaTeX using the Overleaf editor. The bibliography was automatically compiled with BibTex, with the help of the Mendeley reference management software. It is based on a UCL-specific template designed by Ian Kirker and Russel Winder, which can be found here: `https://github.com/UCL/ucl-latex-thesis-templates`

Computer Code All analysis for this thesis was done with the open-source Python programming language. All plots were generated by the Matplotlib software package. Analysis was significantly expedited through the use of the Numpy, Scipy and Pandas packages. All analysis was performed on a Linux machine. My sincere gratitude is owed to the many anonymous and underpaid open-source developers who have made my PhD possible.

NP Station Data Provenance The data analysed in this thesis was supplied in a personal communication from the National Snow and Ice Data Centre in November 2019. While several similar data sets are available online, they generally consist of spatial or temporal averages of the data analysed here. The citation for this data is given here for completeness:

> National Snow and Ice Data Center. 1996. Arctic Ocean Snow and Meteorological Observations from Drifting Stations: 1937, 1950-1991. Version 1.0. CD-ROM. NSIDC, University of Colorado at Boulder.

Bibliography

Aaboe, S. Copernicus Climate Data Records Sea Ice Edge and Sea Ice Type Product User Guide and Specification. Technical report, MET Norway, 2020.

Aaboe, S., Breivik, L.-A., Sørensen, A., Eastwood, S., and Lavergne, T. Global sea ice edge and type product user's manual. *OSI-403-c & EUMETSAT*, 2016.

Abe, M., Nozawa, T., Ogura, T., and Takata, K. Effect of retreating sea ice on Arctic cloud cover in simulated recent global warming. *Atmospheric Chemistry and Physics*, 16(22):14343–14356, 11 2016. ISSN 16807324. doi: 10.5194/ACP-16-14343-2016.

Abraham, C., Steiner, N., Monahan, A., and Michel, C. Effects of subgrid-scale snow thickness variability on radiative transfer in sea ice. *Journal of Geophysical Research: Oceans*, 120(8):5597–5614, 8 2015. ISSN 2169-9291. doi: 10.1002/2015JC010741.

Andersen, O. G. Primary production, chlorophyll, light, and nutrients beneath the Arctic sea ice. *The Arctic seas*, pages 147–191, 1989.

Anderson, M. R. The onset of spring melt in first-year ice regions of the Arctic as determined from scanning multichannel microwave radiometer data for 1979 and 1980. *Journal of Geophysical Research*, 92(C12):13153, 1987. ISSN 0148-0227. doi: 10.1029/JC092IC12P13153.

Aporta, C. The trail as home: Inuit and their pan-arctic network of routes. *Human Ecology*, 37(2):131–146, 1 2009. ISSN 03007839. doi: 10.1007/s10745-009-9213-x.

Aporta, C. The sea, the land, the coast, and the winds: Understanding Inuit sea ice use in context. In *SIKU: Knowing Our Ice: Documenting Inuit Sea Ice Knowledge and Use*, pages 163–180. Springer Netherlands, 2010. ISBN 9789048185863.

Ardyna, M., Mundy, C. J., Mayot, N., Matthes, L. C., Oziel, L., Horvat, C., Leu, E., Assmy, P., Hill, V., Matrai, P. A., Gale, M., Melnikov, I. A., and Arrigo, K. R. Under-Ice Phytoplankton Blooms: Shedding Light on the "Invisible" Part of Arctic Primary Production. *Frontiers in Marine Science*, 7:985, 11 2020. ISSN 22967745. doi: 10.3389/FMARS.2020.608032/BIBTEX.

Armitage, T. W. and Ridout, A. L. Arctic sea ice freeboard from AltiKa and comparison with CryoSat-2 and Operation IceBridge. *Geophysical Research Letters*, 42(16):6724–6731, 2015. ISSN 19448007. doi: 10.1002/2015GL064823.

Armitage, T. W., Manucharyan, G. E., Petty, A. A., Kwok, R., and Thompson, A. F. Enhanced eddy activity in the Beaufort Gyre in response to sea ice loss. *Nature Communications*, 11(1):1–8, 12 2020. ISSN 20411723. doi: 10.1038/s41467-020-14449-z.

Arrigo, K. R. and van Dijken, G. L. Continued increases in Arctic Ocean primary production. *Progress in Oceanography*, 136:60–70, 8 2015. ISSN 0079-6611. doi: 10.1016/J.POCEAN.2015.05.002.

Asbjornsen, H., Årthun, M., Skagseth, O., and Eldevik, T. Mechanisms Underlying Recent Arctic Atlantification. *Geophysical Research Letters*, 47(15): e2020GL088036, 8 2020. ISSN 19448007. doi: 10.1029/2020GL088036.

Azzalini, A. and Capitanio, A. Statistical applications of the multivariate skew normal distribution. *Journal of the Royal Statistical Society: Series B (Statistical Methodology)*, 61(3):579–602, 8 1999. ISSN 1369-7412. doi: 10.1111/1467-9868.00194.

Bailey, H., Hubbard, A., Klein, E. S., Mustonen, K. R., Akers, P. D., Marttila, H., and Welker, J. M. Arctic sea-ice loss fuels extreme European snowfall.

Nature Geoscience 2021 14:5, 14(5):283–288, 4 2021. ISSN 1752-0908. doi: 10.1038/s41561-021-00719-y.

Barnhart, K. R., Overeem, I., and Anderson, R. S. The effect of changing sea ice on the physical vulnerability of Arctic coasts. *Cryosphere*, 8(5):1777–1799, 9 2014. ISSN 19940424. doi: 10.5194/TC-8-1777-2014.

Barnhart, K. R., Miller, C. R., Overeem, I., and Kay, J. E. Mapping the future expansion of Arctic open water. *Nature Climate Change 2015 6:3*, 6(3):280–285, 11 2015. ISSN 1758-6798. doi: 10.1038/nclimate2848.

Barrett, A. P., Stroeve, J. C., and Serreze, M. C. Arctic Ocean Precipitation From Atmospheric Reanalyses and Comparisons With North Pole Drifting Station Records. *Journal of Geophysical Research: Oceans*, 125(1):1–17, 1 2020. ISSN 21699291. doi: 10.1029/2019JC015415.

Barton, B. I., Lenn, Y. D., and Lique, C. Observed atlantification of the Barents Sea causes the Polar Front to limit the expansion of winter sea ice. *Journal of Physical Oceanography*, 48(8):1849–1866, 8 2018. ISSN 15200485. doi: 10.1175/JPO-D-18-0003.1.

Batrak, Y. and Müller, M. On the warm bias in atmospheric reanalyses induced by the missing snow over Arctic sea-ice. *Nature Communications 2019 10:1*, 10(1): 1–8, 9 2019. ISSN 2041-1723. doi: 10.1038/s41467-019-11975-3.

Beaven, S. G., Lockhart, G. L., Gogineni, S. P., Hosseinmostafa, A. R., Jezek, K., Gow, A. J., Perovich, D. K., Fung, A. K., and Tjuatja, S. Laboratory measurements of radar backscatter from bare and snow-covered saline ice sheets. *International Journal of Remote Sensing*, 16(5):851–876, 1995. ISSN 13665901. doi: 10.1080/01431169508954448.

Belchansky, G. I., Douglas, D. C., and Platonov, N. G. Duration of the Arctic sea ice melt season: Regional and interannual variability, 1979-2001. *Journal of Climate*, 17(1), 2004a. ISSN 08948755. doi: 10.1175/1520-0442(2004)017⟨0067:DOTASI⟩2.0.CO;2.

Belchansky, G. I., Douglas, D. C., Mordvintsev, I. N., and Platonov, N. G. Estimating the time of melt onset and freeze onset over Arctic sea-ice area using active and passive microwave data. *Remote Sensing of Environment*, 92(1):21–39, 7 2004b. ISSN 0034-4257. doi: 10.1016/J.RSE.2004.05.001.

Belter, H. J., Krumpen, T., Hendricks, S., Hoelemann, J., Janout, M. A., Ricker, R., and Haas, C. Satellite-based sea ice thickness changes in the Laptev Sea from 2002 to 2017: comparison to mooring observations. *The Cryosphere*, 14(7): 2189–2203, 2020. doi: 10.5194/tc-14-2189-2020.

Bhatt, U. S., Walker, D. A., Walsh, J. E., Carmack, E. C., Frey, K. E., Meier, W. N., Moore, S. E., Parmentier, F.-J. W., Post, E., Romanovsky, V. E., and Simpson, W. R. Implications of Arctic Sea Ice Decline for the Earth System. *Annual Review of Environment and Resources*, 39(1):57–89, 10 2014. ISSN 1543-5938. doi: 10.1146/annurev-environ-122012-094357.

Birchall, J. and Bonnett, N. Thinning sea ice and thawing permafrost: climate change adaptation planning in Nome, Alaska. *Environmental Hazards*, 19(2):152–170, 3 2020. ISSN 18780059. doi: 10.1080/17477891.2019.1637331/FORMAT/EPUB.

Blackwell, E. G. Overview of Differential GPS Methods. *Navigation*, 32(2), 1985. ISSN 21614296. doi: 10.1002/j.2161-4296.1985.tb00895.x.

Bliss, A. C. and Anderson, M. R. Arctic Sea Ice Melt Onset Timing From Passive Microwave-Based and Surface Air Temperature-Based Methods. *Journal of Geophysical Research: Atmospheres*, 123(17):9063–9080, 9 2018. ISSN 2169-8996. doi: 10.1029/2018JD028676.

Blockley, E. W., Peterson, K. A., and Andrew Peterson, K. Improving Met Office seasonal predictions of Arctic sea ice using assimilation of CryoSat-2 thickness. *Cryosphere*, 12(11):3419–3438, 10 2018. ISSN 19940424. doi: 10.5194/tc-12-3419-2018.

Boisvert, L. N., Webster, M. A., Petty, A. A., Markus, T., Bromwich, D. H., and Cullather, R. I. Intercomparison of precipitation estimates over the Arctic ocean

and its peripheral seas from reanalyses. *Journal of Climate*, 31(20):8441–8462, 10 2018. ISSN 08948755. doi: 10.1175/JCLI-D-18-0125.1.

Bradstreet, M., Finley, K., and Sekerak, A. Aspects of the biology of Arctic cod (Boreogadus saida) and its importance in Arctic marine food chains, 1986.

Brodzik, M. J., Billingsley, B., Haran, T., Raup, B., and Savoie, M. H. EASE-Grid 2.0: Incremental but Significant Improvements for Earth-Gridded Data Sets. *ISPRS International Journal of Geo-Information*, 1(1):32–45, 3 2012. ISSN 2220-9964. doi: 10.3390/ijgi1010032.

Brown, C. E. Coefficient of Variation. *Applied Multivariate Statistics in Geohydrology and Related Sciences*, pages 155–157, 1998. doi: 10.1007/978-3-642-80328-4.

Browse, J., Carslaw, K. S., Mann, G. W., Birch, C. E., Arnold, S. R., and Leck, C. The complex response of Arctic aerosol to sea-ice retreat. *Atmospheric Chemistry and Physics*, 14(14):7543–7557, 7 2014. ISSN 16807324. doi: 10.5194/ACP-14-7543-2014.

Bunzel, F., Notz, D., and Pedersen, L. T. Retrievals of Arctic Sea-Ice Volume and Its Trend Significantly Affected by Interannual Snow Variability. *Geophysical Research Letters*, 45(21):751–11, 11 2018. ISSN 19448007. doi: 10.1029/2018GL078867.

Cabaj, A., Kushner, P. J., Fletcher, C. G., Howell, S., and Petty, A. A. Constraining Reanalysis Snowfall Over the Arctic Ocean Using CloudSat Observations. *Geophysical Research Letters*, 47(4):e2019GL086426, 2 2020. ISSN 19448007. doi: 10.1029/2019GL086426.

Calonne, N., Flin, F., Morin, S., Lesaffre, B., Du Roscoat, S. R., and Geindreau, C. Numerical and experimental investigations of the effective thermal conductivity of snow. *Geophysical Research Letters*, 38(23), 12 2011. ISSN 1944-8007. doi: 10.1029/2011GL049234.

Cariou, P., Cheaitou, A., Faury, O., and Hamdan, S. The feasibility of Arctic container shipping: the economic and environmental impacts of ice thickness. *Maritime Economics and Logistics*, pages 1–17, 12 2019. ISSN 1479294X. doi: 10.1057/s41278-019-00145-3.

Carsey, F. D. Prospects for Describing and Monitoring from Space the Elements of the Seasonal Cycle of Sea Ice. *Annals of Glaciology*, 5:37–42, 1984. ISSN 0260-3055. doi: 10.3189/1984AOG5-1-37-42.

Casas-Prat, M. and Wang, X. L. Sea Ice Retreat Contributes to Projected Increases in Extreme Arctic Ocean Surface Waves. *Geophysical Research Letters*, 47(15): e2020GL088100, 8 2020. ISSN 1944-8007. doi: 10.1029/2020GL088100.

Chandler, R. E. and Scott, E. M. *Statistical Methods for Trend Detection and Analysis in the Environmental Sciences*. John Wiley & Sons, 2011. ISBN 9781119991571. doi: 10.1002/9781119991571.

Chemke, R., Polvani, L. M., and Deser, C. The Effect of Arctic Sea Ice Loss on the Hadley Circulation. *Geophysical Research Letters*, 46(2):963–972, 1 2019. ISSN 1944-8007. doi: 10.1029/2018GL081110.

Cheng, B., Vihma, T., Pirazzini, R., and Granskog, M. A. Modelling of superimposed ice formation during the spring snowmelt period in the Baltic Sea. In *Annals of Glaciology*, volume 44, pages 139–146. Cambridge University Press, 2006. doi: 10.3189/172756406781811277.

Chevallier, M. and Salas-Mélia, D. The Role of Sea Ice Thickness Distribution in the Arctic Sea Ice Potential Predictability: A Diagnostic Approach with a Coupled GCM. *Journal of Climate*, 25(8):3025–3038, 4 2012. ISSN 0894-8755. doi: 10.1175/JCLI-D-11-00209.1.

Chung, E.-S., Ha, K.-J., Timmermann, A., Stuecker, M. F., Bodai, T., and Lee, S.-K. Cold-Season Arctic Amplification Driven by Arctic Ocean-Mediated Seasonal Energy Transfer. *Earth's Future*, 9(2):e2020EF001898, 2 2021. ISSN 2328-4277. doi: 10.1029/2020EF001898.

Chung, Y. C., Bélair, S., and Mailhot, J. Blowing snow on arctic sea ice: Results from an improved sea ice-snow-blowing snow coupled system. *Journal of Hydrometeorology*, 12(4):678–689, 8 2011. ISSN 1525755X. doi: 10.1175/2011JHM1293.1.

Cohen, J., Zhang, X., Francis, J., Jung, T., Kwok, R., Overland, J., Ballinger, T. J., Bhatt, U. S., Chen, H. W., Coumou, D., Feldstein, S., Gu, H., Handorf, D., Henderson, G., Ionita, M., Kretschmer, M., Laliberte, F., Lee, S., Linderholm, H. W., Maslowski, W., Peings, Y., Pfeiffer, K., Rigor, I., Semmler, T., Stroeve, J., Taylor, P. C., Vavrus, S., Vihma, T., Wang, S., Wendisch, M., Wu, Y., and Yoon, J. Divergent consensuses on Arctic amplification influence on midlatitude severe winter weather, 1 2020. ISSN 17586798.

Colbeck, S. C. An analysis of water flow in dry snow. *Water Resources Research*, 12(3):523–527, 6 1976. ISSN 1944-7973. doi: 10.1029/WR012I003P00523.

Comiso, J. Bootstrap Sea Ice Concentrations from Nimbus-7 SMMR and DMSP SSM/I, National Snow and Ice Data Center, Boulder, Colorado. Digital media, 2000.

Comiso, J. C., Ackley, S. F., and Gordon, A. L. Antarctic sea ice microwave signatures and their correlation with in situ ice observations (Weddell Sea). *Journal of Geophysical Research*, 89(C1):662–672, 1984. ISSN 01480227. doi: 10.1029/JC089IC01P00662.

Craig, P. C., Griffiths, W. B., Haldorson, L., and McElderry, H. Ecological Studies of Arctic Cod (Boreogadus saida) in Beaufort Sea Coastal Waters, Alaska . *Canadian Journal of Fisheries and Aquatic Sciences*, 39(3), 1982. ISSN 0706-652X. doi: 10.1139/f82-057.

Crawford, A. D., Horvath, S., Stroeve, J., Balaji, R., and Serreze, M. C. Modulation of Sea Ice Melt Onset and Retreat in the Laptev Sea by the Timing of Snow Retreat in the West Siberian Plain. *Journal of Geophysical Research: Atmospheres*, 123 (16):8691–8707, 8 2018. ISSN 2169-8996. doi: 10.1029/2018JD028697.

Cressey, D. Arctic melt opens Northwest passage. *Nature*, 449(7160):267, 9 2007. ISSN 14764687. doi: 10.1038/449267b.

Curry, J. A., Schramm, J. L., and Ebert, E. E. Sea ice-albedo climate feedback mechanism. *Journal of Climate*, 8(2), 1995. ISSN 08948755. doi: 10.1175/1520-0442(1995)008⟨0240:SIACFM⟩2.0.CO;2.

Danabasoglu, G., Lamarque, J. F., Bacmeister, J., Bailey, D. A., DuVivier, A. K., Edwards, J., Emmons, L. K., Fasullo, J., Garcia, R., Gettelman, A., Hannay, C., Holland, M. M., Large, W. G., Lauritzen, P. H., Lawrence, D. M., Lenaerts, J. T., Lindsay, K., Lipscomb, W. H., Mills, M. J., Neale, R., Oleson, K. W., Otto-Bliesner, B., Phillips, A. S., Sacks, W., Tilmes, S., van Kampenhout, L., Vertenstein, M., Bertini, A., Dennis, J., Deser, C., Fischer, C., Fox-Kemper, B., Kay, J. E., Kinnison, D., Kushner, P. J., Larson, V. E., Long, M. C., Mickelson, S., Moore, J. K., Nienhouse, E., Polvani, L., Rasch, P. J., and Strand, W. G. The Community Earth System Model Version 2 (CESM2). *Journal of Advances in Modeling Earth Systems*, 12(2):e2019MS001916, 2 2020. ISSN 1942-2466. doi: 10.1029/2019MS001916.

Dawson, G., Landy, J., Tsamados, M., Komarov, A. S., Howell, S., Heorton, H., and Krumpen, T. A 10-year record of Arctic summer sea ice freeboard from CryoSat-2. *Remote Sensing of Environment*, 268:112744, 1 2022. ISSN 0034-4257. doi: 10.1016/J.RSE.2021.112744.

Day, J. J., Hawkins, E., and Tietsche, S. Will Arctic sea ice thickness initialization improve seasonal forecast skill? *Geophysical Research Letters*, 41(21):7566–7575, 2014.

Debernard, J. Modeling the drift of ridged sea ice: A view from below. *Journal of Geophysical Research: Oceans*, 108(C10):3309, 10 2003. ISSN 2156-2202. doi: 10.1029/2002JC001504.

Denoth, A. The Pendular-Funicular Liquid Transition and Snow Metamorphism.

Journal of Glaciology, 28(99):357–364, 1982. ISSN 0022-1430. doi: 10.3189/S0022143000011692.

Déry, S. J. and Yau, M. K. Large-scale mass balance effects of blowing snow and surface sublimation. *Journal of Geophysical Research: Atmospheres*, 107(D23): 8–1, 12 2002. ISSN 2156-2202. doi: 10.1029/2001JD001251.

Dinnat, E. P. and Brucker, L. Improved Sea Ice Fraction Characterization for L-Band Observations by the Aquarius Radiometers. *IEEE Transactions on Geoscience and Remote Sensing*, 55(3):1285–1304, 3 2017. ISSN 01962892. doi: 10.1109/TGRS.2016.2622011.

Docquier, D. and Koenigk, T. Observation-based selection of climate models projects Arctic ice-free summers around 2035. *Communications Earth & Environment 2021 2:1*, 2(1):1–8, 7 2021. ISSN 2662-4435. doi: 10.1038/s43247-021-00214-7.

Donald, J. R., Soulis, E. D., Kouwen, N., and Pietroniro, A. A Land Cover-Based Snow Cover Representation for Distributed Hydrologic Models. *Water Resources Research*, 31(4):995–1009, 4 1995. ISSN 1944-7973. doi: 10.1029/94WR02973.

Dou, T., Xiao, C., Liu, J., Han, W., Du, Z., Mahoney, A. R., Jones, J., and Eicken, H. A key factor initiating surface ablation of Arctic sea ice: Earlier and increasing liquid precipitation. *Cryosphere*, 13(4):1233–1246, 4 2019. ISSN 19940424. doi: 10.5194/TC-13-1233-2019.

Drobot, S. D. and Anderson, M. R. Spaceborne Microwave Remote Sensing of Arctic Sea Ice During Spring. *Professional Geographer*, 52(2):315–322, 2000. ISSN 14679272. doi: 10.1111/0033-0124.00227.

Drobot, S. D. and Anderson, M. R. An improved method for determining snowmelt onset dates over Arctic sea ice using scanning multichannel microwave radiometer and Special Sensor Microwave/Imager data. *Journal of Geophysical Research Atmospheres*, 106(D20), 2001. ISSN 01480227. doi: 10.1029/2000JD000171.

Dumont, M. and Gascoin, S. Optical Remote Sensing of Snow Cover. *Land Surface Remote Sensing in Continental Hydrology*, pages 115–137, 1 2016. doi: 10.1016/B978-1-78548-104-8.50004-8.

Egli, L., Jonas, T., Grünewald, T., Schirmer, M., and Burlando, P. Dynamics of snow ablation in a small Alpine catchment observed by repeated terrestrial laser scans. *Hydrological Processes*, 26(10):1574–1585, 5 2012. ISSN 1099-1085. doi: 10.1002/HYP.8244.

Eguíluz, V. M., Fernández-Gracia, J., Irigoien, X., and Duarte, C. M. A quantitative assessment of Arctic shipping in 2010-2014. *Scientific Reports*, 6(1):1–6, 8 2016. ISSN 20452322. doi: 10.1038/srep30682.

Ehn, J. K., Granskog, M. A., Papakyriakou, T., Galley, R., and Barber, D. G. Surface albedo observations of Hudson Bay (Canada) landfast sea ice during the spring melt. *Annals of Glaciology*, 44:23–29, 2006. ISSN 0260-3055. doi: 10.3189/172756406781811376.

Eicken, H., Lange, M. A., and Wadhams, P. Characteristics and distribution patterns of snow and meteoric ice in the Weddell Sea and their contribution to the mass balance of sea ice. *Annales Geophysicae*, 12(1):80–93, 1 1994. ISSN 14320576. doi: 10.1007/s00585-994-0080-x.

England, M., Polvani, L. M., Sun, L., and Deser, C. Tropical climate responses to projected Arctic and Antarctic sea-ice loss. *Nature Geoscience*, 13(4):275–281, 4 2020. ISSN 17520908. doi: 10.1038/s41561-020-0546-9.

ESA. ESA'S LIVING PLANET PROGRAMME: SCIENTIFIC ACHIEVEMENTS AND FUTURE CHALLENGES, 2015.

ESA. Sea Ice CCI+ User Requirements Document. Technical report, European Space Agency, 2019.

Farrell, S. L., Kurtz, N., Connor, L. N., Elder, B. C., Leuschen, C., Markus, T., McAdoo, D. C., Panzer, B., Richter-Menge, J., and Sonntag, J. G. A first as-

sessment of IceBridge Snow and Ice thickness data over arctic sea ice. *IEEE Transactions on Geoscience and Remote Sensing*, 50(6):2098–2111, 2012. ISSN 01962892. doi: 10.1109/TGRS.2011.2170843.

Fetterer, F., Savoie, M., Helfrich, S., and Clemente-Colón, P. Multisensor Analyzed Sea Ice Extent - Northern Hemisphere (MASIE-NH), Version 1, 2010.

Filhol, S. and Sturm, M. Snow bedforms: A review, new data, and a formation model. *Journal of Geophysical Research: Earth Surface*, 120(9):1645–1669, 9 2015. ISSN 21699003. doi: 10.1002/2015JF003529.

Forbes, B. C., Kumpula, T., Meschtyb, N., Laptander, R., MacIas-Fauria, M., Zetterberg, P., Verdonen, M., Skarin, A., Kim, K. Y., Boisvert, L. N., Stroeve, J. C., and Bartsch, A. Sea ice, rain-on-snow and tundra reindeer nomadism in Arctic Russia. *Biology Letters*, 12(11):20160466, 11 2016. ISSN 1744957X. doi: 10.1098/rsbl.2016.0466.

Fort, J., Moe, B., Strøm, H., Grémillet, D., Welcker, J., Schultner, J., Jerstad, K., Johansen, K. L., Phillips, R. A., and Mosbech, A. Multicolony tracking reveals potential threats to little auks wintering in the North Atlantic from marine pollution and shrinking sea ice cover. *Diversity and Distributions*, 19(10):1322–1332, 10 2013. ISSN 1472-4642. doi: 10.1111/DDI.12105.

Fox-Kemper, B., Hewitt, H., Xiao, C., Aoalgeirsdottir, G., Drijfhout, S., Edwards, T., Golledge, N., Hemer, M., Kopp, R., Krinner, G., Mix, A., Notz, D., Nowicki, S., Nurhati, I., Ruiz, I., Sallée, J.-B., Slangen, A., and Yu, Y. Ocean, Cryosphere and Sea Level Change. In Masson-Delmotte V., Zhai P., Pirani A., Connors S.L., Péan C., Berger S., Caud N., Chen Y., Goldfarb L., Gomis M.I., Huang M., Leitzell K., Lonnoy E., Matthews J.B.R., Maycock T.K., Waterfield T., Yelekci O., Yuand R., and Zhou B., editors, *Climate Change 2021: The Physical Science Basis. Contribution of Working Group I to the Sixth Assessment Report of the Intergovernmental Panel on Climate Change*, pages 1211–1362. Cambridge University Press, 2021.

Fyke, J., Eby, M., Mackintosh, A., and Weaver, A. Impact of climate sensitivity and

polar amplification on projections of Greenland Ice Sheet loss. *Climate Dynamics*, 43(7-8):2249–2260, 10 2014. ISSN 14320894. doi: 10.1007/S00382-014-2050-7/FIGURES/10.

Galindo, V., Levasseur, M., Mundy, C. J., Gosselin, M., Tremblay, J. E., Scarratt, M., Gratton, Y., Papakiriakou, T., Poulin, M., and Lizotte, M. Biological and physical processes influencing sea ice, under-ice algae, and dimethylsulfoniopropionate during spring in the Canadian Arctic Archipelago. *Journal of Geophysical Research: Oceans*, 119(6):3746–3766, 6 2014. ISSN 2169-9291. doi: 10.1002/2013JC009497.

Gaston, A. J., Gilchrist, H. G., Mallory, M. L., and Smith, P. A. Changes in Seasonal Events, Peak Food Availability, and Consequent Breeding Adjustment in a Marine Bird: A Case of Progressive Mismatching. *https://doi.org/10.1525/cond.2009.080077*, 111(1):111–119, 2 2009. ISSN 0010-5422. doi: 10.1525/COND.2009.080077.

Giles, K. A., Laxon, S. W., and Ridout, A. L. Circumpolar thinning of Arctic sea ice following the 2007 record ice extent minimum. *Geophysical Research Letters*, 35 (22):L22502, 11 2008a. ISSN 00948276. doi: 10.1029/2008GL035710.

Giles, K. A., Laxon, S. W., and Worby, A. P. Antarctic sea ice elevation from satellite radar altimetry. *Geophysical Research Letters*, 35(3):L03503, 2 2008b. ISSN 00948276. doi: 10.1029/2007GL031572.

Gisnas, K., Westermann, S., Vikhamar Schuler, T., Melvold, K., and Etzelmüller, B. Small-scale variation of snow in a regional permafrost model. *Cryosphere*, 10(3): 1201–1215, 6 2016. doi: 10.5194/TC-10-1201-2016.

Glissenaar, I. A., Landy, J. C., Petty, A. A., Kurtz, N. T., and Stroeve, J. C. Impacts of snow data and processing methods on the interpretation of long-term changes in Baffin Bay early spring sea ice thickness. *The Cryosphere*, 15(10):4909–4927, 10 2021. doi: 10.5194/TC-15-4909-2021.

Goosse, H., Kay, J. E., Armour, K. C., Bodas-Salcedo, A., Chepfer, H., Docquier, D., Jonko, A., Kushner, P. J., Lecomte, O., Massonnet, F., Park, H. S., Pithan, F., Svensson, G., and Vancoppenolle, M. Quantifying climate feedbacks in polar regions, 12 2018. ISSN 20411723.

Gordon, A. L. and Schlosser, P. Weddell Sea exploration from ice station. *Eos, Transactions American Geophysical Union*, 74(11):121–126, 3 1993. ISSN 2324-9250. doi: 10.1029/93EO00260.

Gradinger, R. R. and Bluhm, B. A. In-situ observations on the distribution and behavior of amphipods and Arctic cod (Boreogadus saida) under the sea ice of the High Arctic Canada Basin. *Polar Biology*, 27(10):595–603, 10 2004. ISSN 07224060. doi: 10.1007/S00300-004-0630-4/FIGURES/4.

Graham, R. M., Cohen, L., Petty, A. A., Boisvert, L. N., Rinke, A., Hudson, S. R., Nicolaus, M., and Granskog, M. A. Increasing frequency and duration of Arctic winter warming events. *Geophysical Research Letters*, 44(13):6974–6983, 2017.

Granskog, M. A., Assmy, P., and Koç, N. Emerging traits of sea ice in the Atlantic sector of the Arctic. *Climate Change and the White World*, pages 3–10, 10 2019. doi: 10.1007/978-3-030-21679-5{_}1/COVER.

Gricius, G. Conceptualising the Arctic as a Zone of Conflict. *Central European Journal of International and Security Studies*, 15(4):4–30, 12 2021. ISSN 1802548X. doi: 10.51870/CEJISS.A150401.

Guerreiro, K., Fleury, S., Zakharova, E., Rémy, F., and Kouraev, A. Potential for estimation of snow depth on Arctic sea ice from CryoSat-2 and SARAL/AltiKa missions. *Remote Sensing of Environment*, 186:339–349, 2016. ISSN 00344257. doi: 10.1016/j.rse.2016.07.013.

Haas, C. Late-summer sea ice thickness variability in the Arctic Transpolar Drift 1991-2001 derived from ground-based electromagnetic sounding. *Geophysical Research Letters*, 31(9):L09402, 5 2004. ISSN 00948276. doi: 10.1029/2003GL019394.

Hallikainen, M., Ulaby, F., and Abdel-Razik, M. Measurements of the dielectric properties of snow in the 4-18 GHz frequency range. In *1982 12th European Microwave Conference*, pages 151–156, 1982.

Hamilton, C. D., Kovacs, K. M., Ims, R. A., Aars, J., and Lydersen, C. An Arctic predator–prey system in flux: climate change impacts on coastal space use by polar bears and ringed seals. *Journal of Animal Ecology*, 86(5):1054–1064, 9 2017. ISSN 1365-2656. doi: 10.1111/1365-2656.12685.

Hanesiak, J. M., Barber, D. G., and Flato, G. M. Role of diurnal processes in the seasonal evolution of sea ice and its snow cover. *Journal of Geophysical Research: Oceans*, 104(C6):13593–13603, 6 1999. ISSN 21699291. doi: 10.1029/1999JC900054.

He, M., Hu, Y., Chen, N., Wang, D., Huang, J., and Stamnes, K. High cloud coverage over melted areas dominates the impact of clouds on the albedo feedback in the Arctic. *Scientific Reports 2019 9:1*, 9(1):1–11, 7 2019. ISSN 2045-2322. doi: 10.1038/s41598-019-44155-w.

Hellmer, H. H., Schröder, M., Haas, C., Dieckmann, G. S., and Spindler, M. The ISPOL drift experiment. *Deep Sea Research Part II: Topical Studies in Oceanography*, 55(8-9):913–917, 4 2008. ISSN 0967-0645. doi: 10.1016/J.DSR2.2008.01.001.

Hendricks, S. and Ricker, R. Product User Guide & Algorithm Specification: AWI CryoSat-2 Sea Ice Thickness (version 2.2), 2019.

Hendricks, S. and Ricker, R. Product User Guide & Algorithm Specification: AWI CryoSat-2 Sea Ice Thickness (version 2.3), 2020.

Hendricks, S., Paul, S., and Rinne, E. Northern hemisphere sea ice thickness from the CryoSat-2 satellite on a monthly grid (L3C), v2.0, 2018.

Hersbach, H., Bell, B., Berrisford, P., Hirahara, S., Horányi, A., Muñoz-Sabater, J., Nicolas, J., Peubey, C., Radu, R., Schepers, D., Simmons, A., Soci, C., Abdalla,

S., Abellan, X., Balsamo, G., Bechtold, P., Biavati, G., Bidlot, J., Bonavita, M., Chiara, G., Dahlgren, P., Dee, D., Diamantakis, M., Dragani, R., Flemming, J., Forbes, R., Fuentes, M., Geer, A., Haimberger, L., Healy, S., Hogan, R. J., Hólm, E., Janisková, M., Keeley, S., Laloyaux, P., Lopez, P., Lupu, C., Radnoti, G., Rosnay, P., Rozum, I., Vamborg, F., Villaume, S., and Thépaut, J. The ERA5 global reanalysis. *Quarterly Journal of the Royal Meteorological Society*, 146 (730):1999–2049, 7 2020. ISSN 0035-9009. doi: 10.1002/qj.3803.

Holland, M. M., Clemens-Sewall, D., Landrum, L., Light, B., Perovich, D., Polashenski, C., Smith, M., and Webster, M. The influence of snow on sea ice as assessed from simulations of CESM2. *Cryosphere*, 15(10):4981–4998, 10 2021. ISSN 19940424. doi: 10.5194/TC-15-4981-2021.

Hop, H., Poltermann, M., Lønne, O. J., Falk-Petersen, S., Korsnes, R., and Budgell, W. P. Ice amphipod distribution relative to ice density and under-ice topography in the northern Barents Sea. *Polar Biology 2000 23:5*, 23(5):357–367, 2000. ISSN 1432-2056. doi: 10.1007/S003000050456.

Horvath, S., Stroeve, J., Rajagopalan, B., and Jahn, A. Arctic sea ice melt onset favored by an atmospheric pressure pattern reminiscent of the North American-Eurasian Arctic pattern. *Climate Dynamics*, 57(7-8):1771–1787, 10 2021. ISSN 14320894. doi: 10.1007/S00382-021-05776-Y/FIGURES/11.

Howell, S. E., Small, D., Rohner, C., Mahmud, M. S., Yackel, J. J., and Brady, M. Estimating melt onset over Arctic sea ice from time series multi-sensor Sentinel-1 and RADARSAT-2 backscatter. *Remote Sensing of Environment*, 229:48–59, 8 2019. ISSN 0034-4257. doi: 10.1016/J.RSE.2019.04.031.

Huang, S., Huang, Y., and Sun, J. Experimental investigations on snow cover effect on the navigating resistance of an icebreaker. In *Proceedings of the International Offshore and Polar Engineering Conference*, volume 1, 2019.

Huntington, H. P., Gearheard, S., Holm, L. K., Noongwook, G., Opie, M., and Sanguya, J. Sea ice is our beautiful garden: Indigenous perspectives on sea ice in

the Arctic. In *Sea Ice: Third Edition*, pages 583–599. John Wiley & Sons, Ltd, Chichester, UK, 12 2016. ISBN 9781118778371. doi: 10.1002/9781118778371.ch25.

Hurley, R. C. The Problem of Short period measurements of Snow Ablation. *Journal of Glaciology*, 2(16):437–440, 1954. ISSN 0022-1430. doi: 10.3189/002214354793702542.

Iacozza, J. and Barber, D. G. Ablation patterns of snow cover over smooth first-year sea ice in the Canadian Arctic. *Hydrological Processes*, 15(18):3559–3569, 12 2001. ISSN 1099-1085. doi: 10.1002/HYP.1037.

Iacozza, J. and Barber, D. G. An examination of the distribution of snow on sea-ice. *Atmosphere - Ocean*, 37(1):21–51, 1999. ISSN 14809214. doi: 10.1080/07055900.1999.9649620.

IPCC. Summary for Policymakers. In Masson-Delmotte, V., Zhai, P., Pirani, A., Connors, S., Péan, C., Berger, S., Caud, N., Chen, Y., Goldfarb, L., Gomis, M., Huang, M., Leitzell, K., Lonnoy, E., Matthews, J., Maycock, T., Waterfield, T., Yelekçi, O., Yu, R., and Zhou, B., editors, *Climate Change 2021: The Physical Science Basis. Contribution of Working Group I to the Sixth Assessment Report of the Intergovernmental Panel on Climate Change*. Cambridge University Press, 2021.

Itkin, P., Webster, M., Hendricks, S., Oggier, M., Jaggi, M., Ricker, R., Arndt, S., Divine, D. V., von Albedyll, L., Raphael, I., Rohde, J., and Liston, G. E. Magnaprobe snow and melt pond depth measurements from the 2019-2020 MOSAiC expedition, 2021.

Ivanov, V., Alexeev, V., Koldunov, N. V., Repina, I., Sandø, A. B., Smedsrud, L. H., and Smirnov, A. Arctic Ocean Heat Impact on Regional Ice Decay: A Suggested Positive Feedback. *Journal of Physical Oceanography*, 46(5):1437–1456, 5 2016. ISSN 0022-3670. doi: 10.1175/JPO-D-15-0144.1.

Ji, R., Jin, M., and Varpe, O. Sea ice phenology and timing of primary production pulses in the Arctic Ocean. *Global Change Biology*, 19(3):734–741, 3 2013. ISSN 1365-2486. doi: 10.1111/GCB.12074.

Jordan, R. E. A one-dimensional temperature model for a snow cover: technical documentation for SNTHERM.89. *Cold Regions Research and Engineering Laboratory Special Report*, 1991.

Jutila, A., Hendricks, S., Ricker, R., Von Albedyll, L., Krumpen, T., and Haas, C. Retrieval and parameterisation of sea-ice bulk density from airborne multi-sensor measurements. *Cryosphere*, 16(1):259–275, 1 2022. ISSN 19940424. doi: 10.5194/TC-16-259-2022.

Kapsch, M. L., Eicken, H., and Robards, M. Sea ice distribution and ice use by indigenous walrus hunters on St. Lawrence Island, Alaska. In *SIKU: Knowing Our Ice: Documenting Inuit Sea Ice Knowledge and Use*, pages 115–144. Springer Netherlands, 2010. ISBN 9789048185863. doi: 10.1007/978-90-481-8587-05.

Karnovsky, N. J. and Gavrilo, M. V. A feathered perspective: the influence of sea ice on Arctic marine birds. *Sea Ice: Third Edition*, pages 556–569, 11 2016. doi: 10.1002/9781118778371.CH23.

Kashiwase, H., Ohshima, K. I., Nihashi, S., and Eicken, H. Evidence for ice-ocean albedo feedback in the Arctic Ocean shifting to a seasonal ice zone. *Scientific Reports 2017 7:1*, 7(1):1–10, 8 2017. ISSN 2045-2322. doi: 10.1038/s41598-017-08467-z.

Katlein, C., Arndt, S., Nicolaus, M., Perovich, D. K., Jakuba, M. V., Suman, S., Elliott, S., Whitcomb, L. L., McFarland, C. J., Gerdes, R., Boetius, A., and German, C. R. Influence of ice thickness and surface properties on light transmission through Arctic sea ice. *Journal of Geophysical Research: Oceans*, 120(9): 5932–5944, 9 2015. ISSN 2169-9275. doi: 10.1002/2015JC010914.

Kern, M., Cullen, R., Berruti, B., Bouffard, J., Casal, T., Drinkwater, M. R., Gabriele, A., Lecuyot, A., Ludwig, M., Midthassel, R., Navas Traver, I., Parrinello, T.,

Ressler, G., Andersson, E., Martin-Puig, C., Andersen, O., Bartsch, A., Farrell, S., Fleury, S., Gascoin, S., Guillot, A., Humbert, A., Rinne, E., Shepherd, A., van den Broeke, M. R., and Yackel, J. The Copernicus Polar Ice and Snow Topography Altimeter (CRISTAL) high-priority candidate mission. *The Cryosphere*, 14(7): 2235–2251, 7 2020. doi: 10.5194/tc-14-2235-2020.

Kern, S., Khvorostovsky, K., Skourup, H., Rinne, E., Parsakhoo, Z. S., Djepa, V., Wadhams, P., and Sandven, S. The impact of snow depth, snow density and ice density on sea ice thickness retrieval from satellite radar altimetry: Results from the ESA-CCI Sea Ice ECV Project Round Robin Exercise. *Cryosphere*, 9(1): 37–52, 2015. ISSN 19940424. doi: 10.5194/tc-9-37-2015.

Kern, S., Khvorostovsky, K., and Skourup, H. Sea Ice Climate Change Initiative: Phase 2 D4.1 Product Validation & Intercomparison Report (PVIR). Technical report, European Space Agency, 2018.

Kilic, L., Prigent, C., Aires, F., Boutin, J., Heygster, G., Tonboe, R. T., Roquet, H., Jimenez, C., and Donlon, C. Expected Performances of the Copernicus Imaging Microwave Radiometer (CIMR) for an All-Weather and High Spatial Resolution Estimation of Ocean and Sea Ice Parameters. *Journal of Geophysical Research: Oceans*, 123(10):7564–7580, 10 2018. ISSN 2169-9291. doi: 10.1029/2018JC014408.

King, J., Skourup, H., Hvidegaard, S. M., Rösel, A., Gerland, S., Spreen, G., Polashenski, C., Helm, V., and Liston, G. E. Comparison of Freeboard Retrieval and Ice Thickness Calculation From ALS, ASIRAS, and CryoSat-2 in the Norwegian Arctic to Field Measurements Made During the N-ICE2015 Expedition. *Journal of Geophysical Research: Oceans*, 123(2):1123–1141, 2018. ISSN 21699291. doi: 10.1002/2017JC013233.

King, J., Howell, S., Brady, M., Toose, P., Derksen, C., Haas, C., and Beckers, J. Local-scale variability of snow density on Arctic sea ice. *The Cryosphere*, 14(12): 4323–4339, 12 2020. ISSN 1994-0424. doi: 10.5194/tc-14-4323-2020.

Kinnard, C., Zdanowicz, C. M., Fisher, D. A., Isaksson, E., De Vernal, A., and Thompson, L. G. Reconstructed changes in Arctic sea ice over the past 1,450 years. *Nature*, 479(7374):509–512, 11 2011. ISSN 00280836. doi: 10.1038/nature10581.

Koh, G. and Jordan, R. Sub-surface melting in a seasonal snow cover. *Journal of Glaciology*, 41(139):474–482, 1995. ISSN 0022-1430. doi: 10.3189/S002214300003481X.

Kokhanovsky, A. A. Light penetration in snow layers. *Journal of Quantitative Spectroscopy and Radiative Transfer*, 278:108040, 2 2022. ISSN 0022-4073. doi: 10.1016/J.JQSRT.2021.108040.

Kontorovich, A. E., Solomentsev, Y., Fugarov, D. D., Eder, L. V., and Filimonova, I. V. Paradigm oil and gas complex of Russia at the present stage Paradigm oil and gas complex of Russia at the present stage. *IOP Conf. Series: Earth and Environmental Science*, 84:12010, 2017. doi: 10.1088/1755-1315/84/1/012010.

Kopec, B. G., Feng, X., Michel, F. A., and Posmentiera, E. S. Influence of sea ice on Arctic precipitation. *Proceedings of the National Academy of Sciences of the United States of America*, 113(1):46–51, 1 2016. ISSN 10916490.

Kovacs, K. M., Lydersen, C., Overland, J. E., and Moore, S. E. Impacts of changing sea-ice conditions on Arctic marine mammals. *Marine Biodiversity*, 41(1):181–194, 3 2011. ISSN 18671616. doi: 10.1007/S12526-010-0061-0/TABLES/1.

Kubny, H. First two-way winter-crossing of the Northeast Passage, Polar Journal, 2 2021.

Kuchment, L. S. and Gelfan, A. N. The determination of the snowmelt rate and the meltwater outflow from a snowpack for modelling river runoff generation. *Journal of Hydrology*, 179(1-4):23–36, 5 1996. ISSN 0022-1694. doi: 10.1016/0022-1694(95)02878-1.

Kurtz, N. T., Galin, N., and Studinger, M. An improved CryoSat-2 sea ice freeboard

retrieval algorithm through the use of waveform fitting. *Cryosphere*, 8(4):1217–1237, 7 2014. ISSN 19940424. doi: 10.5194/tc-8-1217-2014.

Kurtz, N. T. and Farrell, S. L. Large-scale surveys of snow depth on Arctic sea ice from Operation IceBridge. *Geophysical Research Letters*, 38(20), 10 2011. ISSN 00948276. doi: 10.1029/2011GL049216.

Kwok, R. Simulated effects of a snow layer on retrieval of CryoSat-2 sea ice freeboard. *Geophysical Research Letters*, 41(14), 2014. ISSN 19448007. doi: 10.1002/2014GL060993.

Kwok, R. Arctic sea ice thickness, volume, and multiyear ice coverage: Losses and coupled variability (1958-2018). *Environmental Research Letters*, 13(10):105005, 2018. ISSN 17489326. doi: 10.1088/1748-9326/aae3ec.

Kwok, R. and Cunningham, G. F. Variability of arctic sea ice thickness and volume from CryoSat-2. *Philosophical Transactions of the Royal Society A: Mathematical, Physical and Engineering Sciences*, 373(2045):20140157, 2015. ISSN 1364503X. doi: 10.1098/rsta.2014.0157.

Kwok, R. and Markus, T. Potential basin-scale estimates of Arctic snow depth with sea ice freeboards from CryoSat-2 and ICESat-2: An exploratory analysis. *Advances in Space Research*, 62(6):1243–1250, 2018. ISSN 18791948. doi: 10.1016/j.asr.2017.09.007.

Kwok, R. and Rothrock, D. A. Decline in Arctic sea ice thickness from submarine and ICESat records: 1958-2008. *Geophysical Research Letters*, 36(15):L15501, 8 2009. ISSN 00948276. doi: 10.1029/2009GL039035.

Kwok, R., Cunningham, G. F., Wensnahan, M., Rigor, I., Zwally, H. J., and Yi, D. Thinning and volume loss of the Arctic Ocean sea ice cover: 2003-2008. *Journal of Geophysical Research: Oceans*, 114(7):2003–2008, 7 2009. ISSN 21699291. doi: 10.1029/2009JC005312.

Kwok, R., Panzer, B., Leuschen, C., Pang, S., Markus, T., Holt, B., and Gogineni, S. Airborne surveys of snow depth over Arctic sea ice. *Journal of Geophysical Research: Oceans*, 116(11):C11018, 11 2011. ISSN 21699291. doi: 10.1029/2011JC007371.

Kwok, R., Spreen, G., and Pang, S. Arctic sea ice circulation and drift speed: Decadal trends and ocean currents. *Journal of Geophysical Research: Oceans*, 118(5):2408–2425, 5 2013. ISSN 21699275. doi: 10.1002/jgrc.20191.

Kwok, R., Cunningham, G. F., Kacimi, S., Webster, M. A., Kurtz, N. T., and Petty, A. A. Decay of the Snow Cover Over Arctic Sea Ice From ICESat-2 Acquisitions During Summer Melt in 2019. *Geophysical Research Letters*, 47 (12):e2020GL088209, 6 2020a. ISSN 1944-8007. doi: 10.1029/2020GL088209.

Kwok, R., Kacimi, S., Webster, M. A., Kurtz, N. T., and Petty, A. A. Arctic Snow Depth and Sea Ice Thickness From ICESat-2 and CryoSat-2 Freeboards: A First Examination. *Journal of Geophysical Research: Oceans*, 125(3):1–19, 3 2020b. ISSN 21699291. doi: 10.1029/2019JC016008.

Kwok, R. and Cunningham, G. F. ICESat over Arctic sea ice: Estimation of snow depth and ice thickness. *Journal of Geophysical Research: Oceans*, 113(8): C08010, 8 2008. ISSN 21699291. doi: 10.1029/2008JC004753.

Kwok, R. and Kacimi, S. Three years of sea ice freeboard, snow depth, and ice thickness of the weddell sea from operation icebridge and cryosat-2. *Cryosphere*, 12(8):2789–2801, 2018. ISSN 19940424. doi: 10.5194/tc-12-2789-2018.

Landy, J. C., Ehn, J. K., Babb, D. G., Thériault, N., and Barber, D. G. Sea ice thickness in the Eastern Canadian Arctic: Hudson Bay Complex & Baffin Bay. *Remote Sensing of Environment*, 200, 2017. ISSN 00344257. doi: 10.1016/j.rse.2017.08.019.

Landy, J. C., Tsamados, M., and Scharien, R. K. A Facet-Based Numerical Model for Simulating SAR Altimeter Echoes from Heterogeneous Sea Ice Surfaces. *IEEE*

Transactions on Geoscience and Remote Sensing, 57(7):4164–4180, 7 2019. ISSN 15580644. doi: 10.1109/TGRS.2018.2889763.

Landy, J. C., Petty, A. A., Tsamados, M., and Stroeve, J. C. Sea ice roughness overlooked as a key source of uncertainty in CryoSat-2 ice freeboard retrievals. *Journal of Geophysical Research: Oceans*, 44(0):1–36, 5 2020. ISSN 2169-9275. doi: 10.1029/2019jc015820.

Landy, J. C., Dawson, G. J., Tsamados, M., Bushuk, M., Stroeve, J. C., Howell, S. E. L., Krumpen, T., Babb, D. G., Komarov, A. S., Heorton, H. D. B. S., Belter, H. J., and Aksenov, Y. A year-round satellite sea-ice thickness record from CryoSat-2. *Nature 2022 609:7927*, 609(7927):517–522, 9 2022. ISSN 1476-4687. doi: 10.1038/s41586-022-05058-5.

Langleben, M. P. On the factors affecting the rate of ablation of sea ice. *Canadian Journal of Earth Sciences*, 3(4), 1966. ISSN 0008-4077. doi: 10.1139/e66-032.

Langleben, M. P. Albedo and Degree of Puddling of a Melting Cover of Sea Ice. *Journal of Glaciology*, 8(54):407–412, 1969. ISSN 0022-1430. doi: 10.3189/S002214300002699X.

Langlois, A., Mundy, C., and Barber, D. G. On the winter evolution of snow thermophysical properties over land-fast first-year sea ice. *Hydrological Processes: An International Journal*, 21(6):705–716, 2007.

Lannuzel, D., Tedesco, L., van Leeuwe, M., Campbell, K., Flores, H., Delille, B., Miller, L., Stefels, J., Assmy, P., Bowman, J., Brown, K., Castellani, G., Chierici, M., Crabeck, O., Damm, E., Else, B., Fransson, A., Fripiat, F., Geilfus, N. X., Jacques, C., Jones, E., Kaartokallio, H., Kotovitch, M., Meiners, K., Moreau, S., Nomura, D., Peeken, I., Rintala, J. M., Steiner, N., Tison, J. L., Vancoppenolle, M., Van der Linden, F., Vichi, M., and Wongpan, P. The future of Arctic sea-ice biogeochemistry and ice-associated ecosystems. *Nature Climate Change 2020 10:11*, 10(11):983–992, 10 2020. ISSN 1758-6798. doi: 10.1038/s41558-020-00940-4.

Lasserre, F. and Têtu, P.-L. Extractive Industry: The Growth Engine of Arctic Shipping? In Lackenbauer, P. W. and Nicol, H., editors, *Whole of Government through and Arctic Lens*, pages 239–268. 2017. ISBN 9781775077435.

Lavergne, T., Kern, S., Aaboe, S., Derby, L., Dybkjaer, G., Garric, G., Heil, P., Hendricks, S., Holfort, J., Howell, S., Key, J., Lieser, J. L., Maksym, T., Maslowski, W., Meier, W., Muñoz-Sabater, J., Nicolas, J., Özsoy, B., Rabe, B., Rack, W., Raphael, M., De Rosnay, P., Smolyanitsky, V., Tietsche, S., Ukita, J., Vichi, M., Wagner, P., Willmes, S., and Zhao, X. A New Structure for the Sea Ice Essential Climate Variables of the Global Climate Observing System. *Bulletin of the American Meteorological Society*, 103(6):E1502–E1521, 6 2022. ISSN 0003-0007. doi: 10.1175/BAMS-D-21-0227.1.

Lawrence, I. R., Tsamados, M. C., Stroeve, J. C., Armitage, T. W., and Ridout, A. L. Estimating snow depth over Arctic sea ice from calibrated dual-frequency radar freeboards. *Cryosphere*, 12(11):3551–3564, 11 2018. ISSN 19940424. doi: 10.5194/tc-12-3551-2018.

Laxon, S., Peacock, H., and Smith, D. High interannual variability of sea ice thickness in the Arctic region. *Nature*, 425(6961):947–950, 10 2003. ISSN 00280836. doi: 10.1038/nature02050.

Laxon, S., Giles, K. A., Ridout, A. L., Wingham, D. J., Willatt, R., Cullen, R., Kwok, R., Schweiger, A., Zhang, J., Haas, C., Hendricks, S., Krishfield, R., Kurtz, N., Farrell, S., and Davidson, M. CryoSat-2 estimates of Arctic sea ice thickness and volume. *Geophysical Research Letters*, 40(4):732–737, 2 2013. ISSN 19448007. doi: 10.1002/grl.50193.

Lecomte, O., Fichefet, T., Vancoppenolle, M., Domine, F., Massonnet, F., Mathiot, P., Morin, S., and Barriat, P. On the formulation of snow thermal conductivity in large-scale sea ice models. *Journal of Advances in Modeling Earth Systems*, 5(3): 542–557, 7 2013. ISSN 1942-2466. doi: 10.1002/JAME.20039.

Ledley, T. S. Snow on sea ice: competing effects in shaping climate. *Journal*

of Geophysical Research, 96(D9):17195–17208, 9 1991. ISSN 01480227. doi: 10.1029/91jd01439.

Leningrad. *Manual for hydrometeorological stations and posts, Issue 3 (meteorological observations at stations), Part 1: Main meteorological observations (In Russian)*. 1969.

Leonard, K. C. and Maksym, T. The importance of wind-blown snow redistribution to snow accumulation on Bellingshausen Sea ice. *Annals of Glaciology*, 52(57): 271–278, 2011. ISSN 0260-3055. doi: 10.3189/172756411795931651.

Li, M., Ke, C., Shen, X., Cheng, B., and Li, H. Investigation of the Arctic Sea ice volume from 2002 to 2018 using multi-source data. *International Journal of Climatology*, page joc.6972, 12 2020a. ISSN 0899-8418. doi: 10.1002/joc.6972.

Li, Z., Zhao, J., Su, J., Li, C., Cheng, B., Hui, F., Yang, Q., and Shi, L. Spatial and temporal variations in the extent and thickness of arctic landfast ice. *Remote Sensing*, 12(1):64, 1 2020b. ISSN 20724292. doi: 10.3390/RS12010064.

Libois, Q., Picard, G., France, J. L., Arnaud, L., Dumont, M., Carmagnola, C. M., and King, M. D. Influence of grain shape on light penetration in snow. *Cryosphere*, 7(6):1803–1818, 11 2013. ISSN 19940416. doi: 10.5194/TC-7-1803-2013.

Liston, G., Stroeve, J., and Itkin, P. Lagrangian Snow Distributions for Sea-Ice Applications, Version 1. *NASA National Snow and Ice Data Center Distributed Active Archive Center*, 2021.

Liston, G. E., Polashenski, C., Rösel, A., Itkin, P., King, J., Merkouriadi, I., and Haapala, J. A Distributed Snow-Evolution Model for Sea-Ice Applications (SnowModel). *Journal of Geophysical Research: Oceans*, 123(5):3786–3810, 5 2018. ISSN 21699291. doi: 10.1002/2017JC013706.

Liston, G. E., Itkin, P., Stroeve, J., Tschudi, M., Stewart, J. S., Pedersen, S. H., Reinking, A. K., and Elder, K. A Lagrangian Snow-Evolution System for Sea-Ice Applications (SnowModel-LG): Part I – Model Description. *Journal of*

Geophysical Research: Oceans, 125(10):e2019JC015913, 8 2020. ISSN 2169-9275. doi: 10.1029/2019jc015913.

Liu, J., Zhang, Y., Cheng, X., and Hu, Y. Retrieval of snow depth over Arctic Sea ice using a deep neural network. *Remote Sensing*, 11(23):2864, 12 2019. ISSN 20724292. doi: 10.3390/rs11232864.

Liu, Y., Key, J. R., Liu, Z., Wang, X., and Vavrus, S. J. A cloudier Arctic expected with diminishing sea ice. *Geophysical Research Letters*, 39(5):5705, 3 2012. ISSN 1944-8007. doi: 10.1029/2012GL051251.

Luce, C. H. and Tarboton, D. G. The application of depletion curves for parameterization of subgrid variability of snow. *Hydrological Processes*, 18(8):1409–1422, 6 2004. ISSN 1099-1085. doi: 10.1002/HYP.1420.

Maccario, L., Carpenter, S. D., Deming, J. W., Vogel, T. M., and Larose, C. Sources and selection of snow-specific microbial communities in a Greenlandic sea ice snow cover. *Scientific Reports 2019 9:1*, 9(1):1–14, 2 2019. ISSN 2045-2322. doi: 10.1038/s41598-019-38744-y.

MacGilchrist, G. A., Naveira Garabato, A. C., Tsubouchi, T., Bacon, S., Torres-Valdés, S., and Azetsu-Scott, K. The Arctic Ocean carbon sink. *Deep Sea Research Part I: Oceanographic Research Papers*, 86:39–55, 4 2014. ISSN 0967-0637. doi: 10.1016/J.DSR.2014.01.002.

Major, D. C., Blaschke, P., Gornitz, V., Hosek, E., Lehmann, M., Lewis, J., Loehr, H., Major-Ex, G. A., Pedersen Zari, M., Vásquez Vargas, M. J., Watterson, E., and Wejs, A. Adaptation to climate change in small island settlements. *Ocean & Coastal Management*, 212:105789, 10 2021. ISSN 0964-5691. doi: 10.1016/J.OCECOAMAN.2021.105789.

Mallett, R., Mallett, R. D. C., Stroeve, J. C., Tsamados, M., Willatt, R., Newman, T., Nandan, V., Landy, J. C., Itkin, P., Oggier, M., Jaggi, M., and Perovich, D. Sub-kilometre scale distribution of snow depth on Arctic sea ice from Soviet

drifting stations. *Journal of Glaciology*, pages 1–13, 4 2022. ISSN 0022-1430. doi: 10.1017/JOG.2022.18.

Mallett, R. D. C., Stroeve, J. C., Tsamados, M., Landy, J. C., Willatt, R., Nandan, V., and Liston, G. E. Faster decline and higher variability in the sea ice thickness of the marginal Arctic seas when accounting for dynamic snow cover. *The Cryosphere*, 15(5):2429–2450, 6 2021. ISSN 1994-0424. doi: 10.5194/tc-15-2429-2021.

Mallett, R. D. C., Lawrence, I. R., Stroeve, J. C., Landy, J. C., and Tsamados, M. Brief communication: Conventional assumptions involving the speed of radar waves in snow introduce systematic underestimates to sea ice thickness and seasonal growth rate estimates. *Cryosphere*, 14(1):251–260, 1 2020. ISSN 19940424. doi: 10.5194/tc-14-251-2020.

Marchand, W.-D. and Killingtveit, Å. Statistical properties of spatial snow cover in mountainous catchments in Norway. *Hydrology Research*, 35(2):101–117, 4 2004. ISSN 0029-1277. doi: 10.2166/NH.2004.0008.

Marcovecchio, A., Behrangi, A., Dong, X., Xi, B., and Huang, Y. Precipitation influence on and response to early and late Arctic sea ice melt onset during melt season. *International Journal of Climatology*, 42(1):81–96, 1 2022. ISSN 1097-0088. doi: 10.1002/JOC.7233.

Markus, T., Stroeve, J. C., and Miller, J. Recent changes in Arctic sea ice melt onset, freezeup, and melt season length. *Journal of Geophysical Research: Oceans*, 114: C12024, 12 2009. doi: 10.1029/2009JC005436.

Marshunova, M. S. and Mishin, A. Handbook of the Radiation Regime of the Arctic Basin (Results from the Drift Stations). Technical report, 1994.

Martin, S. and Munoz, E. A. Properties of the Arctic 2-meter air temperature field for 1979 to the present derived from a new gridded dataset. *Journal of Climate*, 10 (6):1428–1440, 1997. ISSN 08948755. doi: 10.1175/1520-0442(1997)010⟨1428: POTAMA⟩2.0.CO;2.

Massom, R. A., Drinkwater, M. R., and Haas, C. Winter snow cover on sea ice in the Weddell Sea. *Journal of Geophysical Research: Oceans*, 102(C1):1101–1117, 1 1997. ISSN 01480227. doi: 10.1029/96JC02992.

Maykut, G. A., Untersteiner, N., MAYKUT GA, and UNTERSTEINER N. Some results from a time- dependent thermodynamic model of sea ice. *J Geophys Res*, 76(6):1550–1575, 2 1971. doi: 10.1029/jc076i006p01550.

Meier, W. N., Stroeve, J., and Fetterer, F. Whither Arctic sea ice? A clear signal of decline regionally, seasonally and extending beyond the satellite record. *Annals of Glaciology*, 46:428–434, 2007. ISSN 0260-3055. doi: 10.3189/172756407782871170.

Meier, W. N., Hovelsrud, G. K., Van Oort, B. E., Key, J. R., Kovacs, K. M., Michel, C., Haas, C., Granskog, M. A., Gerland, S., Perovich, D. K., Makshtas, A., and Reist, J. D. Arctic sea ice in transformation: A review of recent observed changes and impacts on biology and human activity. *Reviews of Geophysics*, 52 (3):185–217, 9 2014. ISSN 1944-9208. doi: 10.1002/2013RG000431.

Melia, N., Haines, K., and Hawkins, E. Sea ice decline and 21st century trans-Arctic shipping routes. *Geophysical Research Letters*, 43(18):9720–9728, 9 2016. ISSN 19448007. doi: 10.1002/2016GL069315.

Melia, N., Haines, K., Hawkins, E., and Day, J. J. Towards seasonal Arctic shipping route predictions. *Environmental Research Letters*, 12(8):084005, 7 2017. ISSN 17489326. doi: 10.1088/1748-9326/aa7a60.

Meredith, M., Sommerkorn, M., Cassotta, S., Derksen, C., Ekaykin, A., Hollowed, A., Kofinas, G., Mackintosh, A., Melbourne-Thomas, J., Muelbert, M., Ottersen, G., Pritchard, H., and Schuur, E. Polar Regions. In Portner, H.-O., Roberts, D., Masson-Delmotte, V., Zhai, P., Tignor, M., Poloczanska, E., Mintenbeck, K., Alegria, A., Nicolai, M., Okem, A., Petzold, J., Rama, B., and Weyer, N., editors, *IPCC Special Report on the Ocean and Cryosphere in a Changing Climate*, pages 203–320. IPCC, 2019.

Merkouriadi, I., Liston, G. E., Graham, R. M., and Granskog, M. A. Quantifying the Potential for Snow-Ice Formation in the Arctic Ocean. *Geophysical Research Letters*, 47(4):e2019GL085020, 2 2020. ISSN 19448007. doi: 10.1029/2019GL085020.

Moon, W., Nandan, V., Scharien, R. K., Wilkinson, J., Yackel, J. J., Barrett, A., Lawrence, I., Segal, R. A., Stroeve, J., Mahmud, M., Duke, P. J., and Else, B. Physical length scales of wind-blown snow redistribution and accumulation on relatively smooth Arctic first-year sea ice. *Environmental Research Letters*, 14 (10):104003, 2019. ISSN 1748-9326. doi: 10.1088/1748-9326/ab3b8d.

Mortin, J., Svensson, G., Graversen, R. G., Kapsch, M. L., Stroeve, J. C., and Boisvert, L. N. Melt onset over Arctic sea ice controlled by atmospheric moisture transport. *Geophysical Research Letters*, 43(12):6636–6642, 6 2016. ISSN 1944-8007. doi: 10.1002/2016GL069330.

Müller, M., Kelder, T., and Palerme, C. Decline of sea-ice in the Greenland Sea intensifies extreme precipitation over Svalbard. *Weather and Climate Extremes*, 36:100437, 6 2022. ISSN 2212-0947. doi: 10.1016/J.WACE.2022.100437.

Mundy, C. J. and Meiners, K. M. Ecology of Arctic Sea Ice. *Arctic Ecology*, pages 261–288, 2 2021. doi: 10.1002/9781118846582.CH10.

Mundy, C. J., Barber, D. G., and Michel, C. Variability of snow and ice thermal, physical and optical properties pertinent to sea ice algae biomass during spring. *Journal of Marine Systems*, 58(3-4):107–120, 12 2005. ISSN 09247963. doi: 10.1016/j.jmarsys.2005.07.003.

Musselman, K. N., Clark, M. P., Liu, C., Ikeda, K., and Rasmussen, R. Slower snowmelt in a warmer world. *Nature Climate Change 2017 7:3*, 7(3):214–219, 2 2017. ISSN 1758-6798. doi: 10.1038/nclimate3225.

Nandan, V., Geldsetzer, T., Yackel, J., Mahmud, M., Scharien, R., Howell, S., King, J., Ricker, R., and Else, B. Effect of Snow Salinity on CryoSat-2 Arctic First-Year

Sea Ice Freeboard Measurements. *Geophysical Research Letters*, 44(20):419–426, 10 2017. ISSN 19448007. doi: 10.1002/2017GL074506.

Nicolaus, M., Katlein, C., Maslanik, J., and Hendricks, S. Changes in Arctic sea ice result in increasing light transmittance and absorption. *Geophysical Research Letters*, 39(24), 2012a. ISSN 19448007. doi: 10.1029/2012GL053738.

Nicolaus, M., Katlein, C., Maslanik, J., and Hendricks, S. Changes in Arctic sea ice result in increasing light transmittance and absorption. *Geophysical Research Letters*, 39(24), 2012b. doi: 10.1029/2012GL053738.

Nicolaus, M., Haas, C., Bareiss, J., and Willmes, S. A model study of differences of snow thinning on Arctic and Antarctic first-year sea ice during spring and summer. *Annals of Glaciology*, 44:147–153, 2006. ISSN 02603055. doi: 10.3189/172756406781811312.

Nicolaus, M., Hoppmann, M., Arndt, S., Hendricks, S., Katlein, C., Nicolaus, A., Rossmann, L., Schiller, M., and Schwegmann, S. Snow Depth and Air Temperature Seasonality on Sea Ice Derived From Snow Buoy Measurements. *Frontiers in Marine Science*, 8:377, 4 2021. ISSN 2296-7745. doi: 10.3389/fmars.2021.655446.

Nicolaus, M., Perovich, D. K., Spreen, G., Granskog, M. A., von Albedyll, L., Angelopoulos, M., Anhaus, P., Arndt, S., Jakob Belter, H., Bessonov, V., Birnbaum, G., Brauchle, J., Calmer, R., Cardellach, E., Cheng, B., Clemens-Sewall, D., Dadic, R., Damm, E., de Boer, G., Demir, O., Dethloff, K., Divine, D. V., Fong, A. A., Fons, S., Frey, M. M., Fuchs, N., Gabarró, C., Gerland, S., Goessling, H. F., Gradinger, R., Haapala, J., Haas, C., Hamilton, J., Hannula, H. R., Hendricks, S., Herber, A., Heuzé, C., Hoppmann, M., Høyland, K. V., Huntemann, M., Hutchings, J. K., Hwang, B., Itkin, P., Jacobi, H. W., Jaggi, M., Jutila, A., Kaleschke, L., Katlein, C., Kolabutin, N., Krampe, D., Kristensen, S. S., Krumpen, T., Kurtz, N., Lampert, A., Lange, B. A., Lei, R., Light, B., Linhardt, F., Liston, G. E., Loose, B., Macfarlane, A. R., Mahmud, M., Matero, I. O., Maus, S., Morgenstern,

A., Naderpour, R., Nandan, V., Niubom, A., Oggier, M., Oppelt, N., Pätzold, F., Perron, C., Petrovsky, T., Pirazzini, R., Polashenski, C., Rabe, B., Raphael, I. A., Regnery, J., Rex, M., Ricker, R., Riemann-Campe, K., Rinke, A., Rohde, J., Salganik, E., Scharien, R. K., Schiller, M., Schneebeli, M., Semmling, M., Shimanchuk, E., Shupe, M. D., Smith, M. M., Smolyanitsky, V., Sokolov, V., Stanton, T., Stroeve, J., Thielke, L., Timofeeva, A., Tonboe, R. T., Tavri, A., Tsamados, M., Wagner, D. N., Watkins, D., Webster, M., and Wendisch, M. Overview of the MOSAiC expedition: Snow and sea ice. *Elementa*, 10(1), 2 2022. ISSN 23251026. doi: 10.1525/ELEMENTA.2021.000046/119791.

Nomura, D., Yoshikawa-Inoue, H., Toyota, T., and Shirasawa, K. Effects of snow, snowmelting and refreezing processes on air–sea-ice CO2 flux. *Journal of Glaciology*, 56(196):262–270, 6 2010. ISSN 0022-1430. doi: 10.3189/002214310791968548.

Notz, D. and SIMIP Community. Arctic Sea Ice in CMIP6. *Geophysical Research Letters*, 47(10):e2019GL086749, 5 2020. ISSN 19448007. doi: 10.1029/2019GL086749.

Odgaard, L. Russia's Arctic Designs and NATO. *https://doi.org/10.1080/00396338.2022.2103259*, 64(4):89–104, 2022. ISSN 14682699. doi: 10.1080/00396338.2022.2103259.

O'Hagan, A. and Leonard, T. Bayes estimation subject to uncertainty about parameter constraints. *Biometrika*, 63(1):201–203, 1 1976. ISSN 0006-3444. doi: 10.1093/biomet/63.1.201.

Overeem, I., Anderson, R. S., Wobus, C. W., Clow, G. D., Urban, F. E., and Matell, N. Sea ice loss enhances wave action at the Arctic coast. *Geophysical Research Letters*, 38(17):17503, 9 2011. ISSN 00948276. doi: 10.1029/2011GL048681.

Overland, J. E., Ballinger, T. J., Cohen, J., Francis, J. A., Hanna, E., Jaiser, R., Kim, B. M., Kim, S. J., Ukita, J., Vihma, T., Wang, M., and Zhang, X. How

do intermittency and simultaneous processes obfuscate the Arctic influence on midlatitude winter extreme weather events?, 4 2021. ISSN 17489326.

Oxford Analytica. Russia's militarisation of the Arctic will grow. *Emerald Expert Briefings*, 2015. ISSN 2633-304X. doi: 10.1108/OXAN-ES199536.

Pagano, A. M. and Williams, T. M. Physiological consequences of Arctic sea ice loss on large marine carnivores: unique responses by polar bears and narwhals. *Journal of Experimental Biology*, 224(Suppl_1), 2 2021. ISSN 14779145. doi: 10.1242/JEB.228049/237178.

Parmentier, F. J. W., Christensen, T. R., Sørensen, L. L., Rysgaard, S., Mcguire, A. D., Miller, P. A., and Walker, D. A. The impact of lower sea-ice extent on Arctic greenhouse-gas exchange. *Nature Climate Change 2013 3:3*, 3(3):195–202, 2 2013. ISSN 1758-6798. doi: 10.1038/nclimate1784.

Paul, S., Hendricks, S., Ricker, R., Kern, S., and Rinne, E. Empirical parametrization of Envisat freeboard retrieval of Arctic and Antarctic sea ice based on CryoSat-2: progress in the ESA Climate Change Initiative. *The Cryosphere*, 12(7):2437–2460, 7 2018. ISSN 1994-0424. doi: 10.5194/tc-12-2437-2018.

Peng, G., Steele, M., Bliss, A. C., Meier, W. N., and Dickinson, S. Temporal Means and Variability of Arctic Sea Ice Melt and Freeze Season Climate Indicators Using a Satellite Climate Data Record. *Remote Sensing 2018, Vol. 10, Page 1328*, 10(9): 1328, 8 2018. doi: 10.3390/RS10091328.

Perovich, D. K., Grenfell, T. C., Light, B., and Hobbs, P. V. Seasonal evolution of the albedo of multiyear Actic sea ice. *Journal of Geophysical Research C: Oceans*, 107(10), 10 2002. ISSN 01480227. doi: 10.1029/2000jc000438.

Perovich, D. K., Jones, K. F., Light, B., Eicken, H., Markus, T., Stroeve, J., and Lindsay, R. Solar partitioning in a changing Arctic sea-ice cover. *Annals of Glaciology*, 52(57 PART 2), 2011. ISSN 02603055. doi: 10.3189/172756411795931543.

Perovich, D. K. and Polashenski, C. Albedo evolution of seasonal Arctic sea ice. *Geophysical Research Letters*, 39(8):8501, 4 2012. ISSN 1944-8007. doi: 10.1029/2012GL051432.

Perovich, D. K., Grenfell, T. C., Richter-Menge, J. A., Light, B., Tucker, W. B., and Eicken, H. Thin and thinner: Sea ice mass balance measurements during SHEBA. *Journal of Geophysical Research: Oceans*, 108(C3):8050, 3 2003. ISSN 2156-2202. doi: 10.1029/2001JC001079.

Persson, O., Fairall, G., Andreas, E. L., Guest, P. S., and Perovich, D. K. Measurements near the Atmospheric Surface Flux Group tower at SHEBA: Near-surface conditions and surface energy budget. *Journal of Geophysical Research: Oceans*, 107(C10):21–1, 10 2002. ISSN 2156-2202. doi: 10.1029/2000JC000705.

Persson, P. O. G. Onset and end of the summer melt season over sea ice: Thermal structure and surface energy perspective from SHEBA. *Climate Dynamics*, 39 (6):1349–1371, 9 2012. ISSN 09307575. doi: 10.1007/S00382-011-1196-9/FIGURES/17.

Petrich, C., Eicken, H., Polashenski, C. M., Sturm, M., Harbeck, J. P., Perovich, D. K., and Finnegan, D. C. Snow dunes: A controlling factor of melt pond distribution on Arctic sea ice. *Journal of Geophysical Research: Oceans*, 117(9), 2012. ISSN 21699291. doi: 10.1029/2012JC008192.

Petrick, S., Riemann-Campe, K., Hoog, S., Growitsch, C., Schwind, H., Gerdes, R., and Rehdanz, K. Climate change, future Arctic Sea ice, and the competitiveness of European Arctic offshore oil and gas production on world markets. *Ambio*, 46 (3):410–422, 12 2017. ISSN 16547209. doi: 10.1007/s13280-017-0957-z.

Petty, A. A., Hutchings, J. K., Richter-Menge, J. A., and Tschudi, M. A. Sea ice circulation around the Beaufort Gyre: The changing role of wind forcing and the sea ice state. *Journal of Geophysical Research: Oceans*, 121(5):3278–3296, 5 2016. ISSN 2169-9275. doi: 10.1002/2015JC010903.

Petty, A. A., Holland, M. M., Bailey, D. A., and Kurtz, N. T. Warm Arctic, Increased Winter Sea Ice Growth? *Geophysical Research Letters*, 45(23):922–930, 12 2018a. ISSN 0094-8276. doi: 10.1029/2018GL079223.

Petty, A. A., Webster, M., Boisvert, L., and Markus, T. The NASA Eulerian Snow on Sea Ice Model (NESOSIM) v1.0: Initial model development and analysis. *Geoscientific Model Development*, 11(11):4577–4602, 11 2018b. ISSN 19919603. doi: 10.5194/gmd-11-4577-2018.

Petty, A. A., Kurtz, N. T., Kwok, R., Markus, T., and Neumann, T. A. Winter Arctic Sea Ice Thickness From ICESat-2 Freeboards. *Journal of Geophysical Research: Oceans*, 125(5), 5 2020. ISSN 21699291. doi: 10.1029/2019JC015764.

Picard, G., Sandells, M., and Löwe, H. SMRT: an active–passive microwave radiative transfer model for snow with multiple microstructure and scattering formulations (v1.0). *Geoscientific Model Development*, 11(7):2763–2788, 7 2018. ISSN 1991-9603. doi: 10.5194/gmd-11-2763-2018.

Pistone, K., Eisenman, I., and Ramanathan, V. Observational determination of albedo decrease caused by vanishing Arctic sea ice. *Proceedings of the National Academy of Sciences of the United States of America*, 111(9):3322–3326, 3 2014. ISSN 00278424. doi: 10.1073/PNAS.1318201111/SUPPLFILE/PNAS.201318201SI.PDF.

Polashenski, C., Perovich, D., and Courville, Z. The mechanisms of sea ice melt pond formation and evolution. *Journal of Geophysical Research: Oceans*, 117 (C1):1001, 1 2012. ISSN 2156-2202. doi: 10.1029/2011JC007231.

Pomeroy, J. W., Gray, D. M., Shook, K. R., Toth, B., Essery, R. L. H., Pietroniro, A., and Hedstrom, N. An evaluation of snow accumulation and ablation processes for land surface modelling. *Hydrological Processes*, 12(15):2339–2367, 1998.

Post, E., Bhatt, U. S., Bitz, C. M., Brodie, J. F., Fulton, T. L., Hebblewhite, M., Kerby, J., Kutz, S. J., Stirling, I., and Walker, D. A. Ecological consequences of sea-ice decline. *Science*, 341(6145):519–524, 8 2013. ISSN 10959203.

Previdi, M., Smith, K. L., and Polvani, L. M. Arctic amplification of climate change: a review of underlying mechanisms. *Environmental Research Letters*, 16(9): 093003, 9 2021. ISSN 1748-9326. doi: 10.1088/1748-9326/AC1C29.

Pringle, D. J., Eicken, H., Trodahl, H. J., and Backstrom, L. G. Thermal conductivity of landfast Antarctic and Arctic sea ice. *Journal of Geophysical Research: Oceans*, 112(C4):4017, 4 2007. ISSN 2156-2202. doi: 10.1029/2006JC003641.

Qi, D., Ouyang, Z., Chen, L., Wu, Y., Lei, R., Chen, B., Feely, R. A., Anderson, L. G., Zhong, W., Lin, H., Polukhin, A., Zhang, Y., Zhang, Y., Bi, H., Lin, X., Luo, Y., Zhuang, Y., He, J., Chen, J., and Cai, W.-J. Climate change drives rapid decadal acidification in the Arctic Ocean from 1994 to 2020. *Science*, 377 (6614):1544–1550, 9 2022. ISSN 0036-8075. doi: 10.1126/SCIENCE.ABO0383/SUPPL{_}FILE/SCIENCE.ABO0383{_}SM.PDF.

Rainville, L., Lee, C. M., and Woodgate, R. A. Impact of wind-driven mixing in the Arctic Ocean. *Oceanography*, 24(3):136–145, 9 2011. ISSN 10428275. doi: 10.5670/OCEANOG.2011.65.

Rampal, P., Weiss, J., and Marsan, D. Positive trend in the mean speed and deformation rate of Arctic sea ice, 1979-2007. *Journal of Geophysical Research: Oceans*, 114(5):C05013, 5 2009. ISSN 21699291. doi: 10.1029/2008JC005066.

Rantanen, M., Karpechko, A. Y., Lipponen, A., Nordling, K., Hyvärinen, O., Ruosteenoja, K., Vihma, T., and Laaksonen, A. The Arctic has warmed nearly four times faster than the globe since 1979. *Communications Earth & Environment 2022 3:1*, 3(1):1–10, 8 2022. ISSN 2662-4435. doi: 10.1038/s43247-022-00498-3.

Richards, F. S. G. A Method of Maximum-Likelihood Estimation. *Journal of the Royal Statistical Society: Series B (Methodological)*, 23(2):469–475, 7 1961. ISSN 2517-6161. doi: 10.1111/J.2517-6161.1961.TB00430.X.

Ricker, R., Hendricks, S., Helm, V., Skourup, H., and Davidson, M. Sensitivity of CryoSat-2 Arctic sea-ice freeboard and thickness on radar-waveform

interpretation. *Cryosphere*, 8(4):1607–1622, 8 2014. ISSN 19940424. doi: 10.5194/tc-8-1607-2014.

Ricker, R., Hendricks, S., Perovich, D. K., Helm, V., and Gerdes, R. Impact of snow accumulation on CryoSat-2 range retrievals over Arctic sea ice: An observational approach with buoy data. *Geophysical Research Letters*, 42(11):4447–4455, 2015. ISSN 19448007. doi: 10.1002/2015GL064081.

Ricker, R., Hendricks, S., Girard-Ardhuin, F., Kaleschke, L., Lique, C., Tian-Kunze, X., Nicolaus, M., and Krumpen, T. Satellite-observed drop of Arctic sea ice growth in winter 2015–2016. *Geophysical Research Letters*, 44(7):3236–3245, 2017. ISSN 19448007. doi: 10.1002/2016GL072244.

Rigor, I. G., Colony, R. L., and Martin, S. Variations in surface air temperature observations in the Arctic, 1979-97. *Journal of Climate*, 13(5), 2000. ISSN 08948755. doi: 10.1175/1520-0442(2000)013⟨0896:VISATO⟩2.0.CO;2.

Rösel, A., Itkin, P., King, J., Divine, D., Wang, C., Granskog, M. A., Krumpen, T., and Gerland, S. Thin Sea Ice, Thick Snow, and Widespread Negative Freeboard Observed During N-ICE2015 North of Svalbard. *Journal of Geophysical Research: Oceans*, 123(2):1156–1176, 2018. ISSN 21699291. doi: 10.1002/2017JC012865.

Rostosky, P., Spreen, G., Farrell, S. L., Frost, T., Heygster, G., and Melsheimer, C. Snow Depth Retrieval on Arctic Sea Ice From Passive Microwave Radiometers—Improvements and Extensions to Multiyear Ice Using Lower Frequencies. *Journal of Geophysical Research: Oceans*, 123(10):7120–7138, 10 2018. ISSN 21699291. doi: 10.1029/2018JC014028.

Rothrock, D. A., Percival, D. B., and Wensnahan, M. The decline in arctic sea-ice thickness: Separating the spatial, annual, and interannual variability in a quarter century of submarine data. *Journal of Geophysical Research: Oceans*, 113(5): C05003, 5 2008. ISSN 21699291. doi: 10.1029/2007JC004252.

Sallila, H., Farrell, S. L., McCurry, J., and Rinne, E. Assessment of contemporary

satellite sea ice thickness products for Arctic sea ice. *The Cryosphere*, 13(4): 1187–1213, 4 2019. ISSN 1994-0424. doi: 10.5194/tc-13-1187-2019.

Schröder, D., Feltham, D. L., Tsamados, M., Ridout, A., and Tilling, R. New insight from CryoSat-2 sea ice thickness for sea ice modelling. *The Cryosphere*, 13(1): 125–139, 1 2019. ISSN 1994-0424. doi: 10.5194/tc-13-125-2019.

Schweiger, A. J. Unified Sea Ice Thickness Climate Data Record, Polar Science Center, Applied Physics Laboratory, University of Washington. http://psc.apl.uw.edu/sea_ice_cdr, 2017.

Schweiger, A. J., Wood, K. R., and Zhang, J. Arctic Sea Ice volume variability over 1901-2010: A model-based reconstruction. *Journal of Climate*, 32(15):4731–4752, 7 2019. ISSN 08948755. doi: 10.1175/JCLI-D-19-0008.1.

Sergunin, A. A. International Cooperation in the Arctic. *The Handbook of the Arctic*, pages 1–21, 2022. ISSN 00368075. doi: 10.1007/978-981-16-9250-5{_}3-1/COVER.

Sévellec, F., Fedorov, A. V., and Liu, W. Arctic sea-ice decline weakens the Atlantic meridional overturning circulation. *Nature Climate Change*, 7(8):604, 2017.

Shakhova, N., Semiletov, I., Sergienko, V., Lobkovsky, L., Yusupov, V., Salyuk, A., Salomatin, A., Chernykh, D., Kosmach, D., Panteleev, G., Nicolsky, D., Samarkin, V., Joye, S., Charkin, A., Dudarev, O., Meluzov, A., and Gustafsson, O. The East Siberian Arctic Shelf: towards further assessment of permafrost-related methane fluxes and role of sea ice. *Philosophical Transactions of the Royal Society A: Mathematical, Physical and Engineering Sciences*, 373(2052), 10 2015. ISSN 1364503X. doi: 10.1098/RSTA.2014.0451.

Singarayer, J. S., Bamber, J. L., and Valdes, P. J. Twenty-First-Century Climate Impacts from a Declining Arctic Sea Ice Cover. *Journal of Climate*, 19(7):1109–1125, 4 2006. ISSN 0894-8755. doi: 10.1175/JCLI3649.1.

Skaugen, T. Modelling the spatial variability of snow water equivalent at the catchment scale. *Hydrology and Earth System Sciences*, 11(5):1543–1550, 2007. doi: 10.5194/HESS-11-1543-2007.

Skaugen, T. and Melvold, K. Modeling the Snow Depth Variability With a High-Resolution Lidar Data Set and Nonlinear Terrain Dependency. *Water Resources Research*, 55(11):9689–9704, 11 2019. ISSN 1944-7973. doi: 10.1029/2019WR025030.

Sledd, A. and L'Ecuyer, T. S. A Cloudier Picture of Ice-Albedo Feedback in CMIP6 Models. *Frontiers in Earth Science*, 9:1067, 12 2021. ISSN 22966463. doi: 10.3389/FEART.2021.769844/BIBTEX.

Smith, A., Jahn, A., and Wang, M. Seasonal transition dates can reveal biases in Arctic sea ice simulations. *Cryosphere*, 14(9):2977–2997, 9 2020. ISSN 19940424. doi: 10.5194/TC-14-2977-2020.

Smith, A., Jahn, A., Burgard, C., and Notz, D. Improving model-satellite comparisons of sea ice melt onset with a satellite simulator. *The Cryosphere*, 16(8): 3235–3248, 8 2022a. ISSN 1994-0424. doi: 10.5194/TC-16-3235-2022.

Smith, D. M. Observation of perennial Arctic sea ice melt and freeze-up using passive microwave data. *Journal of Geophysical Research: Oceans*, 103(C12): 27753–27769, 11 1998. ISSN 2156-2202. doi: 10.1029/98JC02416.

Smith, M. M., Light, B., Macfarlane, A. R., Perovich, D. K., Holland, M. M., and Shupe, M. D. Sensitivity of the Arctic Sea Ice Cover to the Summer Surface Scattering Layer. *Geophysical Research Letters*, 49(9):e2022GL098349, 5 2022b. ISSN 1944-8007. doi: 10.1029/2022GL098349.

Sommer, C. G., Wever, N., Fierz, C., and Lehning, M. Investigation of a wind-packing event in Queen Maud Land, Antarctica. *Cryosphere*, 12(9):2923–2939, 9 2018. ISSN 19940424. doi: 10.5194/TC-12-2923-2018.

Statham, S., Ford, J., Berrang-Ford, L., Lardeau, M. P., Gough, W., and Siewierski, R. Anomalous climatic conditions during winter 2010–2011 and vulnerability of the traditional Inuit food system in Iqaluit, Nunavut. *Polar Record*, 51(3):301–317, 5 2015. ISSN 0032-2474. doi: 10.1017/S0032247414000151.

Steele, M., Bliss, A. C., Peng, G., Meier, W. N., and Dickinson, S. Arctic Sea Ice Seasonal Change and Melt/Freeze Climate Indicators from Satellite Data, Version 1, 2019.

Steiner, N. S., Cheung, W. W., Cisneros-Montemayor, A. M., Drost, H., Hayashida, H., Hoover, C., Lam, J., Sou, T., Sumaila, U. R., Suprenand, P., Tai, T. C., and VanderZwaag, D. L. Impacts of the changing ocean-sea ice system on the key forage fish arctic cod (Boreogadus saida) and subsistence fisheries in the Western Canadian arctic-evaluating linked climate, ecosystem and economic (CEE) models. *Frontiers in Marine Science*, 6(APR):179, 4 2019. ISSN 22967745. doi: 10.3389/fmars.2019.00179.

Stewart, E. J., Dawson, J., Howell, S. E., Johnston, M. E., Pearce, T., and Lemelin, H. Local-level responses to sea ice change and cruise tourism in Arctic Canada's Northwest Passage. *Polar Geography*, 36(1-2):142–162, 3 2013. ISSN 1088937X. doi: 10.1080/1088937X.2012.705352.

Stone, M. Cross-validation: a review. *Series Statistics*, 9(1):127–139, 1 1978. ISSN 0323-3944. doi: 10.1080/02331887808801414.

Stroeve, J., Markus, T., Boisvert, L., Miller, J., and Barrett, A. Changes in Arctic melt season and implications for sea ice loss. *Geophysical Research Letters*, 41 (4):1216–1225, 2 2014. ISSN 00948276. doi: 10.1002/2013GL058951.

Stroeve, J. and Notz, D. Changing state of Arctic sea ice across all seasons. *Environmental Research Letters*, 13(10):103001, 2018. ISSN 17489326. doi: 10.1088/1748-9326/aade56.

Stroeve, J., Markus, T., Meier, W. N., and Miller, J. Recent changes in the Arctic

melt Season. *Annals of Glaciology*, 44:367–374, 2006. ISSN 0260-3055. doi: 10.3189/172756406781811583.

Stroeve, J., Liston, G. E., Buzzard, S., Zhou, L., Mallett, R., Barrett, A., Tschudi, M., Tsamados, M., Itkin, P., and Stewart, J. S. A Lagrangian Snow-Evolution System for Sea Ice Applications (SnowModel-LG): Part II - Analyses. *Journal of Geophysical Research: Oceans*, 125(10):e2019JC015900, 9 2020a. ISSN 2169-9275. doi: 10.1029/2019JC015900.

Stroeve, J., Nandan, V., Willatt, R., Tonboe, R., Hendricks, S., Ricker, R., Mead, J., Mallett, R., Huntemann, M., Itkin, P., Schneebeli, M., Krampe, D., Spreen, G., Wilkinson, J., Matero, I., Hoppmann, M., and Tsamados, M. Surface-based Ku- and Ka-band polarimetric radar for sea ice studies. *The Cryosphere*, 14(12): 4405–4426, 12 2020b. ISSN 1994-0424. doi: 10.5194/tc-14-4405-2020.

Stroeve, J., Vancoppenolle, M., Veyssiere, G., Lebrun, M., Castellani, G., Babin, M., Karcher, M., Landy, J., Liston, G. E., and Wilkinson, J. A Multi-Sensor and Modeling Approach for Mapping Light Under Sea Ice During the Ice-Growth Season. *Frontiers in Marine Science*, 7:1253, 2 2021. ISSN 22967745. doi: 10.3389/fmars.2020.592337.

Stroeve, J. C., Schroder, D., Tsamados, M., and Feltham, D. Warm winter, thin ice? *The Cryosphere*, 12(5):1791–1809, 2018.

Sturm, M. and Holmgren, J. Differences in compaction behavior of three climate classes of snow. *Annals of Glaciology*, 26:125–130, 1998. ISSN 0260-3055. doi: 10.3189/1998AOG26-1-125-130.

Sturm, M. and Holmgren, J. An Automatic Snow Depth Probe for Field Validation Campaigns. *Water Resources Research*, 54(11):9695–9701, 11 2018. ISSN 1944-7973. doi: 10.1029/2018WR023559.

Sturm, M. and Massom, R. A. Snow in the sea ice system: Friend or foe? *Sea Ice: Third Edition*, pages 65–109, 12 2016. doi: 10.1002/9781118778371.ch3.

Sturm, M., Holmgren, J., and Perovich, D. K. Winter snow cover on the sea ice of the Arctic Ocean at the Surface Heat Budget of the Arctic Ocean (SHEBA): Temporal evolution and spatial variability. *Journal of Geophysical Research C: Oceans*, 107(10):1–17, 10 2002a. ISSN 01480227. doi: 10.1029/2000jc000400.

Sturm, M., Perovich, D. K., and Holmgren, J. Thermal conductivity and heat transfer through the snow on the ice of the Beaufort Sea. *Journal of Geophysical Research - Oceans*, 107:19–1, 10 2002b.

Sturm, M., Maslanik, J. A., Perovich, D. K., Stroeve, J. C., Richter-Menge, J., Markus, T., Holmgren, J., Heinrichs, J. F., and Tape, K. Snow depth and ice thickness measurements from the Beaufort and Chukchi Seas collected during the AMSR-Ice03 Campaign. *IEEE Transactions on Geoscience and Remote Sensing*, 44(11):3009–3019, 11 2006. ISSN 01962892. doi: 10.1109/TGRS.2006.878236.

Taverniers, P. Weather variability and changing sea ice use in Qeqertaq, West Greenland, 1987-2008. *SIKU: Knowing Our Ice: Documenting Inuit Sea Ice Knowledge and Use*, pages 31–44, 2010. doi: 10.1007/978-90-481-8587-02/FIGURES/10.

Thomson, J., Fan, Y., Stammerjohn, S., Stopa, J., Rogers, W. E., Girard-Ardhuin, F., Ardhuin, F., Shen, H., Perrie, W., Shen, H., Ackley, S., Babanin, A., Liu, Q., Guest, P., Maksym, T., Wadhams, P., Fairall, C., Persson, O., Doble, M., Graber, H., Lund, B., Squire, V., Gemmrich, J., Lehner, S., Holt, B., Meylan, M., Brozena, J., and Bidlot, J. R. Emerging trends in the sea state of the Beaufort and Chukchi seas. *Ocean Modelling*, 105:1–12, 9 2016. ISSN 1463-5003. doi: 10.1016/J.OCEMOD.2016.02.009.

Tilling, R. L., Ridout, A., Shepherd, A., and Wingham, D. J. Increased Arctic sea ice volume after anomalously low melting in 2013. *Nature Geoscience*, 8(8):643–646, 2015. ISSN 17520908. doi: 10.1038/ngeo2489.

Tilling, R. L., Ridout, A., and Shepherd, A. Estimating Arctic sea ice thickness and

volume using CryoSat-2 radar altimeter data. *Advances in Space Research*, 62(6): 1203–1225, 2018. ISSN 18791948. doi: 10.1016/j.asr.2017.10.051.

Timmermans, M. L. The impact of stored solar heat on Arctic sea ice growth. *Geophysical Research Letters*, 42(15):6399–6406, 8 2015. ISSN 1944-8007. doi: 10.1002/2015GL064541.

Timmermans, M.-L. and Toole, J. M. The Arctic Ocean's Beaufort Gyre. *Annual Review of Marine Science*, 12, 2022. doi: 10.1146/annurev-marine-032122.

Tiuri, M., Sihvola, A., Nyfors, E. G., and Hallikaiken, M. The complex dielectric constant of snow at microwave frequencies. *IEEE Journal of oceanic Engineering*, 9(5):377–382, 1984.

Tomé, A. R. and Miranda, P. M. Piecewise linear fitting and trend changing points of climate parameters. *Geophysical Research Letters*, 31(2), 1 2004. ISSN 00948276. doi: 10.1029/2003GL019100.

Tschudi, M. A., Meier, W. N., and Scott Stewart, J. An enhancement to sea ice motion and age products at the National Snow and Ice Data Center (NSIDC). *Cryosphere*, 14(5):1519–1536, 5 2020. ISSN 19940424. doi: 10.5194/tc-14-1519-2020.

Tseng, P. H., Zhou, A., and Hwang, F. J. Northeast passage in Asia-Europe liner shipping: an economic and environmental assessment. *https://doi.org/10.1080/15568318.2020.1741747*, 15(4):273–284, 2020. ISSN 15568334. doi: 10.1080/15568318.2020.1741747.

Turner, J., Holmes, C., Caton Harrison, T., Phillips, T., Jena, B., Reeves-Francois, T., Fogt, R., Thomas, E. R., and Bajish, C. C. Record Low Antarctic Sea Ice Cover in February 2022. *Geophysical Research Letters*, 49(12):e2022GL098904, 6 2022. ISSN 1944-8007. doi: 10.1029/2022GL098904.

Ulaby, F. and Long, D. *Microwave Radar and Radiometric Remote Sensing*. The University of Michigan Press, 2014. ISBN 9780472119356 0472119354. doi: 10.3998/0472119356.

Ulaby, F. T., Moore, R. K., and Fung, A. K. *Microwave remote sensing: Active and passive. Volume 3-From theory to applications*. Artech House, 1986.

Uttal, T., Curry, J. A., McPhee, M. G., Perovich, D. K., Moritz, R. E., Maslanik, J. A., Guest, P. S., Stern, H. L., Moore, J. A., Turenne, R., and others. Surface heat budget of the Arctic Ocean. *Bulletin of the American Meteorological Society*, 83(2):255–276, 2002.

Vancoppenolle, M., Meiners, K. M., Michel, C., Bopp, L., Brabant, F., Carnat, G., Delille, B., Lannuzel, D., Madec, G., Moreau, S., Tison, J. L., and van der Merwe, P. Role of sea ice in global biogeochemical cycles: Emerging views and challenges. *Quaternary Science Reviews*, 79:207–230, 2013. ISSN 02773791. doi: 10.1016/j.quascirev.2013.04.011.

Vanin, F., Laberinti, P., Donlon, C., Fiorelli, B., Barat, I., Sole, M. P., Palladino, M., Eggers, P., Rudolph, T., and Galeazzi, C. Copernicus Imaging Microwave Radiometer (CIMR): System Aspects and Technological Challenges. *International Geoscience and Remote Sensing Symposium (IGARSS)*, pages 6535–6538, 9 2020. doi: 10.1109/IGARSS39084.2020.9324259.

Vella, D. and Wettlaufer, J. S. Explaining the patterns formed by ice floe interactions. *Journal of Geophysical Research*, 113(C11):C11011, 11 2008. ISSN 0148-0227. doi: 10.1029/2008JC004781.

Vérin, G., Domine, F., Babin, M., Picard, G., and Arnaud, L. Metamorphism of snow on Arctic sea ice during the melt season: impact on spectral albedo and radiative fluxes through snow. *The Cryosphere*, 16(9):3431–3449, 9 2022. doi: 10.5194/TC-16-3431-2022.

Vihma, T. Effects of Arctic Sea Ice Decline on Weather and Climate: A Review. *Surveys in Geophysics*, 35(5):1175–1214, 8 2014. ISSN 15730956. doi: 10.1007/S10712-014-9284-0/FIGURES/7.

Vivier, F., Hutchings, J. K., Kawaguchi, Y., Kikuchi, T., Morison, J. H., Lourenço, A., and Noguchi, T. Sea ice melt onset associated with lead opening dur-

ing the spring/summer transition near the North Pole. *Journal of Geophysical Research: Oceans*, 121(4):2499–2522, 4 2016. ISSN 2169-9291. doi: 10.1002/2015JC011588.

Wang, K., Deser, C., Sun, L., and Tomas, R. A. Fast Response of the Tropics to an Abrupt Loss of Arctic Sea Ice via Ocean Dynamics. *Geophysical Research Letters*, 45(9):4264–4272, 5 2018. ISSN 1944-8007. doi: 10.1029/2018GL077325.

Wang, Q., Wekerle, C., Wang, X., Danilov, S., Koldunov, N., Sein, D., Sidorenko, D., von Appen, W. J., and Jung, T. Intensification of the Atlantic Water Supply to the Arctic Ocean Through Fram Strait Induced by Arctic Sea Ice Decline. *Geophysical Research Letters*, 47(3):e2019GL086682, 2 2020. ISSN 19448007. doi: 10.1029/2019GL086682.

Warren, S. G. Optical properties of ice and snow. *Philosophical Transactions of the Royal Society A: Mathematical, Physical and Engineering Sciences*, 377(2146), 2019. ISSN 1364503X. doi: 10.1098/rsta.2018.0161.

Warren, S. G., Rigor, I. G., Untersteiner, N., Radionov, V. F., Bryazgin, N. N., Aleksandrov, Y. I., and Colony, R. Snow depth on Arctic sea ice. *Journal of Climate*, 12(6):1814–1829, 1999. ISSN 08948755. doi: 10.1175/1520-0442(1999)012⟨1814:SDOASI⟩2.0.CO;2.

Webster, M., Gerland, S., Holland, M., Hunke, E., Kwok, R., Lecomte, O., Massom, R., Perovich, D., and Sturm, M. Snow in the changing sea-ice systems. *Nature Climate Change*, 8(11):946–953, 11 2018. ISSN 17586798. doi: 10.1038/s41558-018-0286-7.

Webster, M. A., Rigor, I. G., Nghiem, S. V., Kurtz, N. T., Farrell, S. L., Perovich, D. K., Sturm, M., Webster, M. A., Rigor, I. G., Nghiem, S. V., Kurtz, N. T., Farrell, S. L., Perovich, D. K., and Sturm, M. Interdecadal changes in snow depth on Arctic sea ice. *Journal of Geophysical Research : Oceans*, 119(8):5395–5406, 8 2014. doi: 10.1002/2014JC009985.Received.

Webster, M. A., Rigor, I. G., Perovich, D. K., Richter-Menge, J. A., Polashenski, C. M., and Light, B. Seasonal evolution of melt ponds on Arctic sea ice. *Journal of Geophysical Research: Oceans*, 120(9):5968–5982, 9 2015. ISSN 21699291. doi: 10.1002/2015JC011030.

Webster, M. A., Holland, M., Wright, N. C., Hendricks, S., Hutter, N., Itkin, P., Light, B., Linhardt, F., Perovich, D. K., Raphael, I. A., Smith, M. M., Von Albedyll, L., and Zhang, J. Spatiotemporal evolution of melt ponds on Arctic sea ice: MOSAiC observations and model results. *Elementa*, 10(1), 5 2022. ISSN 23251026. doi: 10.1525/ELEMENTA.2021.000072/169460.

Wei, T., Yan, Q., Qi, W., Ding, M., and Wang, C. Projections of Arctic sea ice conditions and shipping routes in the twenty-first century using CMIP6 forcing scenarios. *Environmental Research Letters*, 15(10), 10 2020. ISSN 17489326. doi: 10.1088/1748-9326/abb2c8.

Wever, N., Rossmann, L., Maaß, N., Leonard, K. C., Kaleschke, L., Nicolaus, M., and Lehning, M. Version 1 of a sea ice module for the physics-based, detailed, multi-layer SNOWPACK model. *Geoscientific Model Development*, 13(1):99–119, 1 2020. ISSN 19919603. doi: 10.5194/gmd-13-99-2020.

Willatt, R., Laxon, S., Giles, K., Cullen, R., Haas, C., and Helm, V. Ku-band radar penetration into snow cover on Arctic sea ice using airborne data. *Annals of Glaciology*, 52(57 PART 2):197–205, 2011. ISSN 02603055. doi: 10.3189/172756411795931589.

Willatt, R. C., Giles, K. A., Laxon, S. W., Stone-Drake, L., and Worby, A. P. Field investigations of Ku-band radar penetration into snow cover on antarctic sea ice. *IEEE Transactions on Geoscience and Remote Sensing*, 48(1):365–372, 1 2010. ISSN 01962892. doi: 10.1109/TGRS.2009.2028237.

Wilson, P. Society, steward or security actor? Three visions of the Arctic Council:. *Cooperation and Conflict*, 51(1):55–74, 7 2015. ISSN 14603691. doi: 10.1177/0010836715591711.

Winebrenner, E. D. and West, R. D. Observation of melt onset on multiyear Arctic sea ice using the ERS 1 synthetic aperture radar. *Journal of Geophysical Research*, 99(C11), 1994. ISSN 01480227. doi: 10.1029/94JC01268.

Wingham, D. J., Francis, C. R., Baker, S., Bouzinac, C., Brockley, D., Cullen, R., de Chateau-Thierry, P., Laxon, S. W., Mallow, U., Mavrocordatos, C., Phalippou, L., Ratier, G., Rey, L., Rostan, F., Viau, P., and Wallis, D. W. CryoSat: A mission to determine the fluctuations in Earth's land and marine ice fields. *Advances in Space Research*, 37(4):841–871, 2006. ISSN 02731177. doi: 10.1016/j.asr.2005.07.027.

WMO. The 2022 GCOS Implementation Plan. Technical report, World Meteorological Organisation, 2022a.

WMO. The 2022 GCOS ECVs Requirements. Technical report, World Meteorological Organisation, 2022b.

Xia, W. and Xie, H. Assessing three waveform retrackers on sea ice freeboard retrieval from Cryosat-2 using Operation IceBridge Airborne altimetry datasets. *Remote Sensing of Environment*, 204:456–471, 2018.

Yaremchuk, M., Townsend, T., Panteleev, G., Hebert, D., and Allard, R. Advancing Short-Term Forecasts of Ice Conditions in the Beaufort Sea. *Journal of Geophysical Research: Oceans*, 124(2):807–820, 2019.

Zhang, J. and Rothrock, D. A. Modeling global sea ice with a thickness and enthalpy distribution model in generalized curvilinear coordinates. *Monthly Weather Review*, 131(5), 2003. ISSN 00270644. doi: 10.1175/1520-0493(2003)131⟨0845:MGSIWA⟩2.0.CO;2.

Zhang, Z., Huisingh, D., and Song, M. Exploitation of trans-Arctic maritime transportation, 3 2019. ISSN 09596526.

Zhou, L., Stroeve, J., Xu, S., Petty, A., Tilling, R., Winstrup, M., Rostosky, P., Lawrence, I. R., Liston, G. E., Ridout, A., Tsamados, M., and Nandan, V. Intercomparison of snow depth over Arctic sea ice from reanalysis reconstructions

and satellite retrieval. *Cryosphere*, 15(1):345–367, 1 2021. ISSN 19940424. doi: 10.5194/tc-15-345-2021.

Zygmuntowska, M., Rampal, P., Ivanova, N., and Smedsrud, L. H. Uncertainties in Arctic sea ice thickness and volume: New estimates and implications for trends. *Cryosphere*, 8(2):705–720, 4 2014. ISSN 19940424. doi: 10.5194/tc-8-705-2014.

UCL Research Paper Declaration Form: referencing the doctoral candidate's own published work(s)

Please use this form to declare if parts of your thesis are already available in another format, e.g. if data, text, or figures:

- have been uploaded to a preprint server;
- are in submission to a peer-reviewed publication;
- have been published in a peer-reviewed publication, e.g. journal, textbook.

This form should be completed as many times as necessary. For instance, if you have seven thesis chapters, two of which containing material that has already been published, you would complete this form twice.

1. For a research manuscript that has already been published (if not yet published, please skip to section 2)**:**		
a) Where was the work published? (e.g. journal name)	**The Cryosphere**	
b) Who published the work? (e.g. Elsevier/Oxford University Press):	**Copernicus Publications**	
c) When was the work published?	17/1/2022	
d) Was the work subject to academic peer review?	Yes	
e) Have you retained the copyright for the work?	Yes	
[If no, please seek permission from the relevant publisher and check the box next to the below statement]:		
☐	*I acknowledge permission of the publisher named under 1b to include in this thesis portions of the publication named as included in 1a.*	
2. For a research manuscript prepared for publication but that has not yet been published (if already published, please skip to section 3)**:**		
a) Has the manuscript been uploaded to a preprint server? (e.g. medRxiv):	Please select.	**If yes, which server?** Click or tap here to enter text.
b) Where is the work intended to be published? (e.g. names of journals that you are planning to submit to)	Click or tap here to enter text.	
c) List the manuscript's authors in the intended authorship order:	Click or tap here to enter text.	
d) Stage of publication	Please select.	
3. For multi-authored work, please give a statement of contribution covering all authors (if single-author, please skip to section 4**):**		

RDCM proposed the study, carried out the analysis and wrote the paper, with continued input from all authors. In addition to paper input, JCS and JCL contributed data to aid analysis and MCT contributed to the processing code.			
4. In which chapter(s) of your thesis can this material be found?			
Chapter 2			
5. e-Signatures confirming that the information above is accurate (this form should be co-signed by the supervisor/ senior author unless this is not appropriate, e.g. if the paper was a single-author work):			
Candidate:	Robbie Mallett	**Date:**	18/9/22
Supervisor/ Senior Author (where appropriate)**:**	Julienne Stroeve	**Date:**	18/9/22

UCL Research Paper Declaration Form: referencing the doctoral candidate's own published work(s)

Please use this form to declare if parts of your thesis are already available in another format, e.g. if data, text, or figures:

- have been uploaded to a preprint server;
- are in submission to a peer-reviewed publication;
- have been published in a peer-reviewed publication, e.g. journal, textbook.

This form should be completed as many times as necessary. For instance, if you have seven thesis chapters, two of which containing material that has already been published, you would complete this form twice.

1. For a research manuscript that has already been published (if not yet published, please skip to section 2)**:**		
a) Where was the work published? (e.g. journal name)	**The Cryosphere**	
b) Who published the work? (e.g. Elsevier/Oxford University Press):	**Copernicus Publications**	
c) When was the work published?	4/6/2021	
d) Was the work subject to academic peer review?	Yes	
e) Have you retained the copyright for the work?	Yes	
[If no, please seek permission from the relevant publisher and check the box next to the below statement]:		
☐	*I acknowledge permission of the publisher named under 1b to include in this thesis portions of the publication named as included in 1a.*	
2. For a research manuscript prepared for publication but that has not yet been published (if already published, please skip to section 3)**:**		
a) Has the manuscript been uploaded to a preprint server? (e.g. medRxiv):	Please select.	**If yes, which server?** Click or tap here to enter text.
b) Where is the work intended to be published? (e.g. names of journals that you are planning to submit to)	Click or tap here to enter text.	
c) List the manuscript's authors in the intended authorship order:	Click or tap here to enter text.	
d) Stage of publication	Please select.	
3. For multi-authored work, please give a statement of contribution covering all authors (if single-author, please skip to section 4)**:**		

JCS and JCL proposed the study. RDCM carried out the analysis. VN and GEL provided extensive feedback on the manuscript, and GEL provided the SnowModel-LG data. All authors contributed to the write-up.			
4. In which chapter(s) of your thesis can this material be found?			
Chapter 3			
5. e-Signatures confirming that the information above is accurate (this form should be co-signed by the supervisor/ senior author unless this is not appropriate, e.g. if the paper was a single-author work):			
Candidate:	Robbie Mallett	**Date:**	18/9/2022
Supervisor/ Senior Author (where appropriate)**:**	Julienne Stroeve	**Date:**	18/9/2022

UCL Research Paper Declaration Form: referencing the doctoral candidate's own published work(s)

Please use this form to declare if parts of your thesis are already available in another format, e.g. if data, text, or figures:

- have been uploaded to a preprint server;
- are in submission to a peer-reviewed publication;
- have been published in a peer-reviewed publication, e.g. journal, textbook.

This form should be completed as many times as necessary. For instance, if you have seven thesis chapters, two of which containing material that has already been published, you would complete this form twice.

1. For a research manuscript that has already been published (if not yet published, please skip to section 2)**:**		
a) Where was the work published? (e.g. journal name)	**Journal of Glaciology**	
b) Who published the work? (e.g. Elsevier/Oxford University Press):	**Cambridge University Press**	
c) When was the work published?	4/4/2022	
d) Was the work subject to academic peer review?	Yes	
e) Have you retained the copyright for the work?	Yes	
[If no, please seek permission from the relevant publisher and check the box next to the below statement]:		
☐	*I acknowledge permission of the publisher named under 1b to include in this thesis portions of the publication named as included in 1a.*	
2. For a research manuscript prepared for publication but that has not yet been published (if already published, please skip to section 3)**:**		
a) Has the manuscript been uploaded to a preprint server? (e.g. medRxiv):	Please select.	**If yes, which server?** Click or tap here to enter text.
b) Where is the work intended to be published? (e.g. names of journals that you are planning to submit to)	Click or tap here to enter text.	
c) List the manuscript's authors in the intended authorship order:	Click or tap here to enter text.	
d) Stage of publication	Please select.	
3. For multi-authored work, please give a statement of contribution covering all authors (if single-author, please skip to section 4)**:**		

RM developed the NP model in consultation with JS, MT, RW and VN. JL, PI, MO, MJ and DP were involved in collecting, providing and advising on the evaluation data. All authors contributed to and provided feedback on the manuscript.			
4. In which chapter(s) of your thesis can this material be found?			
Chapter 4			
5. e-Signatures confirming that the information above is accurate (this form should be co-signed by the supervisor/ senior author unless this is not appropriate, e.g. if the paper was a single-author work):			
Candidate:	Robbie Mallett	**Date:**	18/9/2022
Supervisor/ Senior Author (where appropriate)**:**	Julienne Stroeve	**Date:**	18/9/2022